

# **Leading-colour two-loop QCD corrections for top-quark pair production in association with a jet at a lepton collider**

Dissertation

zur Erlangung des akademischen Grades

doctor rerum naturalium (Dr. rer. nat.)

im Fach Physik:

Spezialisierung: Theoretische Physik

eingereicht an der

Mathematisch-Naturwissenschaftlichen Fakultät der Humboldt-Universität zu Berlin

von

M. Sc. Sascha Peitzsch

Präsidentin der Humboldt-Universität zu Berlin

Prof. Dr. Julia von Blumenthal

Dekanin der Mathematisch-Naturwissenschaftlichen Fakultät

Prof. Dr. Caren Tischendorf

Gutachter/innen:

1. Prof. Dr. Peter Uwer
2. Prof. Dr. Christophe Grojean
3. Prof. Dr. Gudrun Heinrich

Tag der mündlichen Prüfung: 05.12.2022



# Selbständigkeitserklärung

Ich erkläre, dass ich die Dissertation selbständig und nur unter Verwendung der von mir gemäß § 7 Abs. 3 der Promotionsordnung der Mathematisch-Naturwissenschaftlichen Fakultät, veröffentlicht im Amtlichen Mitteilungsblatt der Humboldt-Universität zu Berlin Nr. 42/2018 am 11.07.2018 angegebenen Hilfsmittel angefertigt habe.

Berlin, den 23.06.2022

Sascha Peitzsch



# Abstract

In this work, the calculation of the leading-colour two-loop QCD corrections for top-quark pair production with an additional jet at a lepton collider is presented. The matrix element is decomposed into vector and axial-vector currents and the currents are further decomposed into Dirac spinor structures and form factors. The form factors are extracted with projectors. The Feynman integrals are reduced to a quasi-finite basis in  $6 - 2\epsilon$  dimensions using IBP identities and dimension-shift transformations.

The majority of master integrals belong to a double-box integral family. The master integrals are computed by numerically solving systems of differential equations in the kinematic invariants. Asymptotic expansions of the master integrals in the top-quark mass variable are used to calculate initial conditions for the numerical differential equation solutions. The leading terms of the expansion are obtained with the expansion by regions and the higher orders are calculated by solving a system of equations obtained from applying the differential equation onto an ansatz of the expansion.

The renormalized form factors and the leading-colour two-loop amplitude are evaluated numerically to high precision at a benchmark phase space point. The results are cross-checked with electroweak Ward identities and by numerically comparing the IR singularities with the expected singularity structure.



# Zusammenfassung

In dieser Arbeit wird die Berechnung der farbführenden Zweischleifen-QCD-Korrekturen für die Top-Quark-Paarproduktion mit einem zusätzlichen Jet an einem Lepton-Collider präsentiert. Das Matrixelement wird in Vektor- und Axial-Vektorströme zerlegt und die Ströme werden weiter in Dirac-Spinorstrukturen und Formfaktoren zerlegt. Die Formfaktoren werden mit Projektoren extrahiert. Die auftretenden Feynmanintegrale werden mittels IBP-Identitäten und Dimensionsverschiebungstransformationen durch eine Basis quasi-finiten Masterintegrale in  $6-2\epsilon$  Dimensionen ausgedrückt.

Die Mehrheit der Feynmanintegrale gehört zu einer Doppelbox-Integralfamilie. Die Berechnung der Masterintegrale erfolgt durch numerisches Lösen von Differentialgleichungen in kinematischen Invarianten. Asymptotische Reihenentwicklungen der Masterintegrale in der Top-Quarkmasse werden verwendet, um die Anfangsbedingungen für die numerischen Lösungen der Differentialgleichungen zu bestimmen. Die führenden Terme dieser Entwicklung werden mit der Expansion-by-Regions-Methode berechnet. Höhere Reihenkoeffizienten werden durch die Anwendung einer Differentialgleichung auf einen Ansatz für die Reihenentwicklung bestimmt.

Die renormierten Formfaktoren und die farbführende Zweischleifenamplitude werden an einem Referenzphasenraumpunkt zu hoher Präzision numerisch ausgewertet. Die Resultate werden mit elektroschwachen Ward-Identitäten und durch numerische Vergleiche der IR-Singularitäten mit der erwarteten Singularitätsstruktur überprüft.





# Contents

<b>1. Introduction</b>	<b>11</b>
<b>2. Notation and definitions</b>	<b>17</b>
2.1. Kinematics . . . . .	17
2.2. Amplitudes and currents . . . . .	18
2.3. Estimated renormalization scale dependence at NNLO QCD . . . . .	20
2.4. Feynman integrals . . . . .	21
2.4.1. Introduction . . . . .	21
2.4.2. Tensor integral reduction . . . . .	23
2.4.3. Parametric representations . . . . .	23
2.4.4. Dimension-shift transformations . . . . .	24
2.4.5. IBP reductions and quasi-finite master integrals . . . . .	25
2.4.6. Differential equations . . . . .	26
<b>3. Projection procedure</b>	<b>29</b>
3.1. Introduction . . . . .	29
3.2. Construction of the projectors . . . . .	30
3.3. Introductory example: $\gamma^* \rightarrow q\bar{q}$ . . . . .	32
3.4. Construction of the spinor structures . . . . .	35
3.5. Electroweak Ward identities . . . . .	38
<b>4. Evaluation of the master integrals</b>	<b>43</b>
4.1. Introduction . . . . .	43
4.2. Asymptotic expansion . . . . .	47
4.2.1. Introduction . . . . .	47
4.2.2. Calculating the leading terms with the expansion by regions . . . . .	48
4.2.3. Calculation of higher-order terms . . . . .	54
4.2.4. Results of the asymptotic expansion . . . . .	55
4.3. Numerical solutions of the differential equations . . . . .	58
4.3.1. Introduction . . . . .	58
4.3.2. Preparation and implementation of the ODE system . . . . .	59
4.3.3. Singularities and contour deformation . . . . .	62
4.3.4. Estimation of uncertainties of the numerical ODE solutions . . . . .	66
4.3.5. Calculation of a grid in $x$ and $z$ . . . . .	69
4.3.6. Cross-checks of the results . . . . .	71
<b>5. Amplitude evaluation and numerical results</b>	<b>81</b>
5.1. Overview of the calculation . . . . .	81
5.1.1. General work-flow . . . . .	81
5.1.2. Leading-order and one-loop amplitudes . . . . .	82
5.2. Renormalization . . . . .	83
5.3. Cross-checks . . . . .	86
5.3.1. Electroweak Ward identities . . . . .	86
5.3.2. Analytic structure of the singularity . . . . .	88

5.4. Numerical results . . . . .	91
<b>6. Conclusion</b>	<b>95</b>
<b>A. Additional calculations</b>	<b>99</b>
A.1. Determination of the benchmark phase space point . . . . .	99
A.2. Brief overview of the Tarasov method . . . . .	101
A.3. Calculating derivatives of Feynman integrals . . . . .	103
A.3.1. Derivatives in the parametric representation . . . . .	103
A.3.2. Derivatives in the momentum representation . . . . .	104
A.4. Axial-vector current spinor structures . . . . .	107
A.5. Restoring the renormalization scale dependence of the finite remainder . . . . .	107
<b>B. Master integral calculation</b>	<b>111</b>
B.1. Leading-colour two-loop master integrals . . . . .	111
B.2. Asymptotic expansions . . . . .	112
B.3. Singularities of the differential equations . . . . .	121
<b>C. Numerical results</b>	<b>123</b>
C.1. Numerical results for the master integrals at the benchmark phase space point . . . . .	123
C.2. Numerical results for the projection coefficients at the benchmark phase space point . . . . .	128
C.3. Numerical results at a special phase space point . . . . .	133
<b>Bibliography</b>	<b>137</b>

# 1. Introduction

In the previous years, the field of high-energy physics saw tremendous progress both on the experimental and theoretical side, which was especially driven by the experiments at the Large Hadron Collider (LHC). This progress, however, was built on a foundation stemming from a long line of particle physics experiments which over the course of many decades discovered the building blocks of the Standard Model of Elementary Particle Physics (SM). This includes for instance the observation of the  $W$  and  $Z$  bosons at the UA1 and UA2 experiments at the Sp $\bar{p}$ S accelerator in 1983 [1–4] as well as the discovery of the top quark at the Tevatron in 1995 [5, 6]. The Higgs boson was finally discovered by ATLAS and CMS in 2012 [7, 8] as the last remaining particle of the SM. This discovery, in a manner of speech, completed the SM and was undoubtedly one of the most important events in particle physics in the last decades.

Moreover, almost all current experimental observations at the LHC and other high energy physics experiments are in very good agreement with theoretical SM predictions. It is particularly noteworthy that the theoretical foundations of the SM, in particular the Glashow-Weinberg-Salam theory [9–11] of the electroweak interaction as well as the symmetry breaking mechanism which explains the generation of gauge boson masses in the SM [12–15], were formulated in the 1960s and still describe current experiments to astonishing precision.

However, it is well known on a very fundamental level that the SM is incomplete since there are several observations which the SM cannot explain. For example, the SM does not include gravity, offers no explanation for the nature of dark matter and dark energy, cannot explain the origins of the Baryon asymmetry, and provides no theoretical description of neutrino masses. Furthermore, there are issues such as the Hierarchy problem, the Strong CP problem, and the origin of the SM parameter values, which could arguably indicate that the SM is part of a more fundamental theory.

A multitude of theories and models that could explain these observations have been proposed over the years. However, no physics beyond the Standard Model (BSM) has been observed so far at the LHC and other experiments, despite being extensively studied and searched for with great effort. At most, the experiments observed as of now unexplained tensions with SM predictions. For example, the experimental measurement and the SM prediction of the anomalous magnetic moment of the muon exhibit a tension with a  $4.2\sigma$  significance [16, 17]. Measurements of rare  $B$  hadron decays, in particular at the BaBar, Belle, and LHCb experiments, also exhibit tensions with the SM predictions [18–32]. This might point to a violation of lepton flavour universality. Recently published measurements of the  $W$  boson mass at the CDF II experiment at the Tevatron collider [33] also exhibit a significant tension with the SM prediction.

This raises the question: How to proceed from here? It goes without saying that no consensus on the answer has formed yet. However, it is very likely that further experimental input will play a major role in answering this question.

This raises the related question: What experiments will succeed the LHC? Currently, there are several proposed future experiments implementing different experimental approaches. Proposed lepton collider experiments include, for example, CLIC [34], the CPEC [35, 36], the FCC-ee [37], and the ILC [38]. Hadron colliders, such as the FCC-hh [39] and the SPPC [35, 36] experiments, also have been proposed. Hadron colliders generally allow to reach higher collision energies compared to lepton colliders, which would allow to observe potential new physics at these energy scales by direct production of BSM particles. Lepton colliders, on the other hand, typically allow

## 1. Introduction

for more precise measurements due to cleaner initial states and smaller backgrounds compared to hadron colliders, which makes it possible to search for BSM physics by looking for very small discrepancies from the SM prediction. Lepton colliders hence effectively allow to indirectly probe higher energy scales than their collision energy since heavy BSM particles would most likely manifest themselves in corrections to lower-energy SM processes. This also means that lepton collider experiments in particular require high-precision predictions for SM processes.

The central piece of theoretical modelling is the perturbative calculation of the hard scattering process. Currently, next-to-leading order (NLO) precision in QCD is the standard at the LHC while next-to-next-to-leading order (NNLO) QCD corrections, NLO electroweak corrections, or even higher-order corrections are available for many important processes. Yet, there is still a great demand for further higher-order corrections for many processes [40]. The LHC is expected to record an integrated luminosity of  $350\text{ fb}^{-1}$  by the end of Run 3 and the subsequent high-luminosity LHC phase could yield an integrated luminosity of up to  $4000\text{ fb}^{-1}$  [41]. This will correspondingly reduce statistical uncertainties. Systematic effects, which are not affected by increased luminosity, might as a result become the dominant uncertainty contribution. Going beyond NLO QCD precision will consequently become mandatory in the future to ensure that the theoretical predictions match the decreased experimental uncertainties.

Let us now come back to the topic of lepton collider experiments. The major purposes of the proposed lepton colliders are precision measurements of Higgs boson properties, tests of electroweak symmetry breaking in the SM, searches for BSM physics, and precision studies of the top quark. The top quark is the heaviest known elementary particle with a mass close to the electroweak symmetry breaking scale and the largest Yukawa coupling of all particles. It plays hence a special role in the SM as well as in many BSM scenarios. Because of its unique properties, it is often hypothesized that new physics might be observed first in processes involving top quarks. Hence, it is a promising approach to search for new physics which might manifest itself in top-quark observables through slight deviations from SM predictions. In the SM, top quarks are predominantly produced in top-antitop-quark pairs. The proposed lepton colliders would be able to determine the top-quark mass with unprecedented accuracy by scanning the production threshold of the top-antitop-quark pair production process and by measuring the process at higher energies in the continuum. The measurement in the continuum allows not only to determine the top-quark mass in a complementary way to the threshold measurement but also to precisely test the electroweak interaction vertices and is therefore especially well suited for searches of new physics modifying these couplings [42, 43].

Top-quark pair production at lepton colliders has consequently received a lot of attention since future lepton colliders were proposed, e. g. ref. [44, 45].

In this work, I am studying the top-quark pair production with an additional jet at the ILC with a collision energy of  $500\text{ GeV}$ . This process is an important part of the inclusive top-quark pair production process and is hence sensitive to the top-quark mass. Additionally, it can be used to search for anomalous gluon couplings [46] and modified vector boson couplings to the top quark [47, 48]. Furthermore, the ratio of this cross section with respect to the inclusive top-quark pair production cross section can be used to determine the coupling constant of the strong interaction  $\alpha_s$ . Moreover, this measurement can serve as a test of flavour universality of the strong interaction by comparing with the coupling constant for light quark flavours, which can be determined, for example, by measuring the three-jet production process [49]. Both three-jet production and the here studied process are very well suited to extract the coupling constant of the strong interaction as their cross sections are already at LO proportional to  $\alpha_s$ .

Three-jet production at lepton colliders, which has proven to be a key process for high-precision studies of QCD and jet physics at LEP, also highlights the importance of higher-order corrections. The NNLO QCD corrections [50–53], especially in combination with event-shape observ-

ables [54–61], significantly improved the  $\alpha_s$  measurement with this process and changed the  $\alpha_s$  prediction by 10% compared to the extraction using only NLO accuracy [62].

NLO QCD accuracy will not be sufficient to match the experimental precision of future lepton colliders since expected experimental uncertainties for cross-section measurements are typically below 1%. Limiting factors for ILC measurements of the top-quark pair production cross section are expected to be theory uncertainties and experimental systematic uncertainties rather than statistical uncertainties [44].

Consider, for example, the top-quark pair production process at the ILC. The NNLO QCD corrections, which are known for both the inclusive cross section and differential distributions of this process [63–66], yield estimated theory uncertainties of roughly 1%. Theoretical predictions at N<sup>3</sup>LO accuracy for the inclusive cross section are available by means of conformal transformations and Padé approximations [67, 68], reducing the estimated theory uncertainties to 0.3% [44]. Additionally, one-loop electroweak corrections are known and are comparable in size [69]. Near the threshold, the N<sup>3</sup>LO QCD corrections for top-quark pair production are available [70]. Cross-section measurements at the ILC with a collision energy of  $\sqrt{s} = 500$  GeV have in comparison expected statistical uncertainties of approximately 0.5% [45].

In contrast, top-quark pair production in association with a jet is known to NLO QCD [49, 71–75] so far and the cross section is subject to an estimated uncertainty of a few percent due to missing higher-order corrections [49]. The NNLO QCD corrections would further reduce the uncertainties to approximately 1 – 2%, as estimated in sec. 2.3. The order of magnitude of the statistical uncertainties of the corresponding ILC measurements can be estimated by comparison to the inclusive top-quark pair production process. The number of events for the  $e^+e^- \rightarrow t\bar{t}$  process is, very roughly, 10 times larger than the number of events for the process  $e^+e^- \rightarrow t\bar{t}j$  according to ref. [49]. This puts the expected statistical uncertainty for the cross-section measurement of the  $e^+e^- \rightarrow t\bar{t}j$  process also in the 1% to 2% range, which is comparable to the estimated theory uncertainties at NNLO QCD.

Hence, I am investigating in this work two-loop contributions to top-quark pair production with an additional jet at the ILC in order to improve the theoretical predictions for this important process. This work is confined to the leading-colour two-loop QCD amplitude. The leading-colour terms are expected to give the most significant numerical contribution to the NNLO QCD corrections. A major building block of this work is the calculation of the relevant Feynman integrals of the leading-colour amplitude, which are almost entirely part of a massive planar double-box integral family.

Top-quark pair production in association with a jet is not only interesting from a phenomenological point of view but also offers great opportunities for exploring and extending two-loop calculation technologies. The ‘simple’ initial state, which is not modified by the QCD corrections, reduces the  $2 \rightarrow 3$  process effectively to an  $1 \rightarrow 3$  process. However, the combination of 4 involved kinematic scales with relatively complicated Feynman integral topologies makes this calculation challenging, which is reflected by the fact that analytic results for the loop integrals are currently not known. This process is in this sense at the current frontier of multi-loop calculations.

When striving for high precision in phenomenological calculations, the task of computing one-loop, two-loop, or even higher loop Feynman integrals, generally referred to as multi-loop Feynman integrals, naturally arises. Although many different techniques for multi-loop calculations already exist, there is no general way or algorithm that works for all cases in practice. Common limiting factors are the number of involved kinematic scales and complicated especially non-planar topologies.

Sector decomposition [76], for example, can be used to numerically evaluate general Feynman

## 1. Introduction

integrals. Moreover, this technique has been implemented in several publicly available programs such as **Fiesta** [77–80], **SecDec**, and **pySecDec** [76, 81–85] and it has been very successfully applied to a large number of processes. This technique is discussed in detail, for example, in ref. [86]. However, the application of sector decomposition can become computationally very challenging due to several factors. Sector decomposition can give rise to a large number of sectors and consequently a large number of numerical integrations. Precision demands might require a large number of sampling points for the numerical integrations. Furthermore, integrals must be numerically evaluated for each phase space point individually.

Another very successfully applied approach is based on Mellin-Barnes representations of Feynman integrals. The Mellin-Barnes representation is obtained by introducing auxiliary integrations, which allows to perform the integration over the loop-momenta in a universal manner. The remaining Mellin-Barnes integrals can be computed either numerically or analytically by determining the residues and then evaluating the resulting nested sums [87–92].

Many phenomenological calculations require the evaluation of a large number of linearly dependent Feynman integrals. These integrals are often first expressed as linear combinations of basis integrals, the so-called master integrals. This reduction is obtained by constructing integration-by-parts (IBP) identities and Lorentz identities [93, 94] involving integrals of the same integral family with different propagator exponents. The resulting system of equations is then solved for the master integrals. This idea is applied systematically in the Laporta algorithm [95], which is implemented in several publicly available programs [96–105].

The major advantage of this approach is that only the master integrals need to be calculated instead of a typically much larger number of Feynman integrals occurring in intermediate steps. Especially tensor reduction techniques, which express tensor Feynman integrals with scalar Feynman integrals, are notorious for increasing the number of occurring integrals.

Moreover, master integrals obey systems of coupled differential equations [106–110], which can be used for calculating Feynman integrals. This approach received in the past a lot of attention and was applied very successfully for a large number of integrals. In some cases, a so-called canonical master integral basis [111] can be obtained [112–114], which greatly simplifies the differential equations and allows to evaluate the integrals directly as iterated integrals corresponding to generalized polylogarithms [115, 116]. General reviews on differential equations can be found in ref. [117, 118].

However, it is not always possible to obtain a canonical form for differential equations and not all integrals can be expressed by means of multiple polylogarithms (MPLs). Moreover, it is currently not known to which function class general two-loop or multi-loop Feynman integrals belong. Promising candidates for such function spaces are elliptic generalizations of polylogarithms such as elliptic polylogarithms [119–124]. A famous and intensively studied example of a Feynman diagram requiring elliptic integrals is the massive two-loop sunrise diagram [125–140]. In addition, elliptic integrals appear in many phenomenological multi-loop calculations, e. g. in top-quark and Higgs boson production at hadron colliders [141–149].

In this work, the differential equations are solved numerically, which allows to evaluate Feynman integrals directly without determining and implementing the necessary mathematical functions and without requiring the differential equation system to assume a special form. This approach was investigated in ref. [128, 150–155] and has already been used in several non-trivial applications [151, 152, 156, 157]. However, solving differential equations numerically requires initial conditions, which are in this work determined by expanding the master integrals asymptotically in the small-mass limit.

Asymptotic expansions are power-logarithmic expansions and are extensively discussed, for example, in ref. [158, 159]. There are several commonly applied approaches to calculate asymptotic

expansions, including in particular an expansion using Mellin-Barnes (MB) representations, the expansion by subgraphs, and the expansion by regions.

The expansion in the Mellin-Barnes representation is, for example, described in ref. [159]. The remaining coefficients can be evaluated numerically, which is, for example, implemented in the **Mathematica** package **MB.m** [87], or they can be evaluated analytically by deriving expressions containing nested sums [90–92, 160, 161]. Another numerical approach described in ref. [162] and implemented in **Fiesta** [79] and **HepLib** [163] combines Mellin-Barnes techniques and sector decomposition.

Asymptotic expansions can also be calculated with the expansion by subgraphs [158, 159, 164–168], where the asymptotic expansion is obtained by summing over certain subgraphs of a graph. This method can be applied to limits typically associated with Euclidean space, which includes, for example, the large-mass limit and the off-shell large-momentum limit.

In this work, the expansion by regions is applied. This method can be used for more general kinematical limits than the expansion by subgraphs, i.e. limits that can be formulated in Minkowski space. Although the expansion by regions is well motivated [169] and proven to work for certain Euclidean limits, there is no general formal proof that this method always yields the correct results. The expansion by regions is hence often referred to as ‘experimental mathematics’ [170] in the literature but also has been successfully applied numerous times. The expansion by subgraphs, in contrast, is generally proven to give the correct result [158, 167].

The non-trivial task of determining all relevant regions is implemented in the **Mathematica** package **asy.m** [171] and in the further improved versions **asy2.m** [172] and **asy2.1.m**. These programs, in a nutshell, determine the regions by virtue of homogeneity conditions which are reformulated as the geometric problem of finding a convex hull of a set of points for which **Qhull** [173] is used. Both **Fiesta** and **pySecDec** also implement expansion by regions based on the same geometric approach combined with sector decomposition [79, 85]. An alternative approach to determine the regions is presented in ref. [174, 175].

This work is structured as follows. In chapter 2, the notation and definitions used in this work are summarized, which includes in particular the kinematics in sec. 2.1, the decomposition of the amplitude into currents in sec. 2.2, and a summary of Feynman-integral-related definitions in sec. 2.4. The renormalization scale dependence of the NNLO QCD cross section is estimated in sec. 2.3. Chapter 3 gives an extensive review of the projection procedure. The calculation of the master integrals of the leading-colour two-loop amplitude is presented in chapter 4. The asymptotic expansions of the master integrals are first calculated in sec. 4.2 and are then used as initial conditions for numerical solutions of systems of differential equations in sec. 4.3. In chapter 5, an overview of the calculation of the amplitude is given and numerical results for the leading-colour two-loop amplitude as well as cross-checks of the results are presented. Conclusions are drawn in chapter 6.





## 2. Notation and definitions

### 2.1. Kinematics

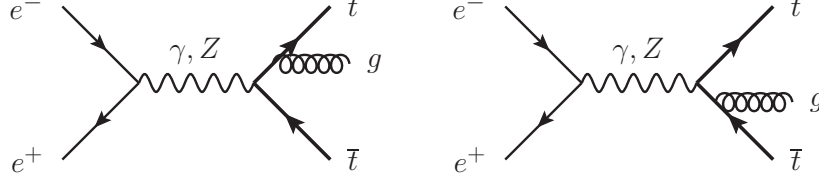


**Figure 2.1.:** Leading-order Feynman diagrams for  $e^+e^- \rightarrow t\bar{t}j$ .

The top-quark pair production process with an additional jet at an electron-positron collider with centre-of-mass energy  $\sqrt{s}$  is depicted at leading order in fig. 2.1. At the parton level, the leading-order kinematics is given by

$$e^+(p_a) + e^-(p_b) \rightarrow \gamma^*/Z^*(p_4) \rightarrow t(p_1) + \bar{t}(p_2) + g(p_3), \quad (2.1)$$

where the electron and positron are considered massless particles and the massive top quarks are on-shell. Hence, the conditions

$$p_a^2 = p_b^2 = 0, \quad p_4^2 = (p_a + p_b)^2 = s, \quad p_1^2 = p_2^2 = m_t^2, \quad p_3^2 = 0 \quad (2.2)$$

are imposed on the external momenta. Momentum conservation yields

$$p_a + p_b = p_4 = p_1 + p_2 + p_3. \quad (2.3)$$

The dimensionless and independent variables

$$m = \frac{m_t^2}{s}, \quad x = \frac{(p_1 + p_3)^2 - m_t^2}{s} = \frac{2p_1 \cdot p_3}{s}, \quad z = \frac{(p_2 + p_3)^2 - m_t^2}{s} = \frac{2p_2 \cdot p_3}{s} \quad (2.4)$$

are used together with the variable  $s$  throughout this work. The variable

$$y = \frac{(p_1 + p_2)^2 - 2m_t^2}{s} = \frac{2p_1 \cdot p_2}{s} = 1 - 2m - x - z \quad (2.5)$$

is not independent due to momentum conservation. The mass dimension only enters through the variable  $s$ , which is often set to one. This effectively reduces the number of independent variables from four to three. The dependence on  $s$  is restored afterwards by dimensional analysis. In this work, the short-hand notation  $\{x_i\} = \{s, x, z, m\}$  for the set of all four variables is used.

Furthermore, many calculations in this work are performed numerically using the reference values

$$s = (500 \text{ GeV})^2, \quad x = \frac{1}{5}, \quad z = \frac{1}{20}, \quad m = \frac{289}{2500}. \quad (2.6)$$

## 2. Notation and definitions

For calculations requiring external momenta, the corresponding benchmark phase space point

$$\begin{aligned}
p_a &= (250, 0, 0, 250) \text{ GeV}, \\
p_b &= (250, 0, 0, -250) \text{ GeV}, \\
p_1 &= (237.5, 7.5 \sqrt{489}, 0, 0) \text{ GeV}, \\
p_2 &= \left( 200, -6940/(3 \sqrt{489}), 250 \sqrt{11/489}/3, 0 \right) \text{ GeV}, \\
p_3 &= \left( 62.5, -8125/(6 \sqrt{489}), -250 \sqrt{11/489}/3, 0 \right) \text{ GeV}
\end{aligned} \tag{2.7}$$

is used. This phase space point is determined in app. A.1 by applying the parameterization of a three-particle phase space given in ref. [176] to the kinematic constraints of the process at hand. The physical phase space region is given by a positive Gram determinant, i. e.

$$\Delta_3(p_1, p_2, p_3) = -\frac{s^3}{4} \left( m(x+z)^2 - xz(1-x-z) \right) \geq 0. \tag{2.8}$$

## 2.2. Amplitudes and currents

The amplitude  $\mathcal{M}$  is split into the electron-positron initial state as well as vector and axial-vector currents according to the coupling structure of the intermediately produced photon and  $Z$  boson. The subamplitude  $\mathcal{M}_\gamma$  containing the virtual photon only involves vector currents. The subamplitude  $\mathcal{M}_Z$  only involves diagrams with a virtual  $Z$  boson and contains both vector and axial-vector currents. The complete amplitude is given by

$$\begin{aligned}
\mathcal{M} &= \mathcal{M}_\gamma + \mathcal{M}_Z \\
&= 4\pi\alpha_e(-ig_s)t_{tt}^g \left( \frac{Q_e}{s} \cdot \epsilon_4^\mu \left( Q_t \cdot V_{t,\mu} + \sum_q Q_q \cdot V_{q,\mu} \right) \right. \\
&\quad + \frac{1}{\sin^2 \theta_w \cos^2 \theta_w} \cdot \frac{1}{s - m_Z^2} \cdot [g_V^e \cdot \epsilon_4^\mu - g_A^e \cdot \tilde{\epsilon}_4^\mu] \times \\
&\quad \left. \times \left[ g_V^t \cdot V_{t,\mu} - g_A^t \cdot A_{t,\mu} + \sum_q g_V^q \cdot V_{q,\mu} - \sum_q g_A^q \cdot A_{q,\mu} \right] \right). \tag{2.9}
\end{aligned}$$

The electron-positron initial state is not modified by the QCD corrections that are studied in this work. The initial state is hence substituted by  $\epsilon_4^\mu$  and  $\tilde{\epsilon}_4^\mu$ , i. e.

$$\epsilon_4^\mu = \bar{v}(p_a)\gamma^\mu u(p_b), \quad \tilde{\epsilon}_4^\mu = \bar{v}(p_a)\gamma^\mu \gamma^5 u(p_b), \tag{2.10}$$

which are effectively treated as polarization vectors of an off-shell photon or  $Z$  boson. The initial state is restored when implementing the amplitudes.

The flavour-dependent coupling of the quarks to the virtual photon or  $Z$  boson gives naturally rise to the following distinct currents:

- $V_t^\mu$  includes all terms proportional to the vector coupling of the top quark to the  $\gamma$  or  $Z$  boson,
- $A_t^\mu$  includes all terms proportional to the axial-vector coupling of the top quark to the  $Z$  boson,
- $V_q^\mu$  and  $A_q^\mu$  are the corresponding vector and axial-vector currents where the massless quarks  $q \in \{d, u, s, c, b\}$  couple to the  $\gamma$  or  $Z$  boson respectively.

The currents  $V_q^\mu$  and  $A_q^\mu$  only consist of diagrams where the photon or  $Z$  boson couples to closed fermion loops of massless quarks. The currents  $V_t^\mu$  and  $A_t^\mu$  in contrast contain diagrams where

the photon or  $Z$  boson couples to the external top-quark line as well as to closed top-quark loops.

The vector and axial-vector couplings  $g_V^f$  and  $g_A^f$  of the  $Z$  boson to the fermions  $f \in \{e, t, q\}$  are given by [177]

$$g_V^f = \frac{1}{2} \left( T_f^3 - 2Q_f \sin^2 \theta_w \right), \quad g_A^f = \frac{1}{2} T_f^3. \quad (2.11)$$

The relevant couplings for the process at hand are

$$\begin{aligned} Q_e &= -1, & Q_{u,c,t} &= \frac{2}{3}, & Q_{d,s,b} &= -\frac{1}{3}, \\ g_V^e &= -\frac{1}{4} + \sin^2 \theta_w, & g_V^{u,c,t} &= \frac{1}{4} - \frac{2}{3} \sin^2 \theta_w, & g_V^{d,s,b} &= -\frac{1}{4} + \frac{1}{3} \sin^2 \theta_w, \\ g_A^e &= -\frac{1}{4}, & g_A^{u,c,t} &= \frac{1}{4}, & g_A^{d,s,b} &= -\frac{1}{4}. \end{aligned} \quad (2.12)$$

The colour structure of the amplitude is rather simple as the entire amplitude is proportional to one single colour factor given by  $|c\rangle = t_{\bar{t}t}^g$ , i. e. a generator of the  $SU(N_c)$  in the fundamental representation where the colour indices of the external particles are denoted with  $t$ ,  $\bar{t}$ , and  $g$ . This also holds for all loop corrections.

The unrenormalized amplitude is expanded perturbatively as

$$\begin{aligned} \mathcal{M}_{\text{bare}} \left( \alpha_s^0, \{x_i^0\}, \epsilon \right) &= \mathcal{M}_{\text{bare}}^{(0)} \left( \{x_i^0\}, \epsilon \right) + \mathcal{M}_{\text{bare}}^{(1)} \left( \{x_i^0\}, \epsilon \right) \left( \frac{\alpha_s^0}{2\pi} \right) \\ &+ \mathcal{M}_{\text{bare}}^{(2)} \left( \{x_i^0\}, \epsilon \right) \left( \frac{\alpha_s^0}{2\pi} \right)^2 + \mathcal{O} \left( \alpha_s^3 \right), \end{aligned} \quad (2.13)$$

where the index 0 indicates ‘bare’ quantities. Note that the unrenormalized top-quark mass enters in  $\{x_i^0\}$ . The unrenormalized amplitude contains UV and IR singularities, which are regularized dimensionally by setting the space-time dimension to  $d = 4 - 2\epsilon$ . The conventional dimensional regularization (CDR) scheme, where all external particles have  $d$ -dimensional degrees of freedom, is adopted.

The UV divergences are cancelled by multiplicative renormalization, which is discussed in detail in sec. 5.2. The renormalized gluon wave function  $A_\mu^a$  and top-quark wave function  $\psi^t$ , which are defined by

$$A_{0\mu}^a = Z_g^{1/2} A_\mu^a, \quad \psi_0^t = Z_t^{1/2} \psi^t, \quad (2.14)$$

appear as global factors in the renormalized amplitude

$$\mathcal{M}_{\text{ren}} (\alpha_s, \{x_i\}, \epsilon) = Z_t^{-1} Z_g^{-\frac{1}{2}} \mathcal{M}_{\text{bare}} \left( \alpha_s^0, \{x_i^0\}, \epsilon \right). \quad (2.15)$$

The renormalized quantities are denoted without any index. The mass renormalization, defined by  $m_t^0 = Z_{m_t} m_t$ , enters through the variable  $m$ . The renormalized coupling constant of the strong interaction in an  $\overline{\text{MS}}$  scheme with  $n_l$  active flavours is defined by

$$\alpha_s^0 = \left( \frac{\mu^2 e^{\gamma_E}}{4\pi} \right)^\epsilon Z_{\alpha_s}^{(n_l)} \alpha_s^{(n_l)}(\mu). \quad (2.16)$$

The prefactor fixes the mass dimension of the dimensionally regularized amplitude and follows similar conventions in the literature, e. g. ref. [178]. The number of quark flavours is

## 2. Notation and definitions

denoted with  $n_f$ , the number of heavy quark flavours is  $n_h$ , and the number of light quark flavours is  $n_l$ . Throughout this work, the renormalization scale  $\mu$  is set to the top-quark mass, i. e.  $\mu^2 = m_t^2 = m \cdot s$ . The renormalization scale dependence can be restored with the renormalization group equation (RGE) [179, 180].

A corresponding perturbative expansion is also introduced for the vector and axial-vector currents and the leading-order, one-loop, and two-loop coefficients are similarly denoted with  $V_t^{(0)}$ ,  $V_t^{(1)}$ ,  $V_t^{(2)}$  and  $A_t^{(0)}$ ,  $A_t^{(1)}$ ,  $A_t^{(2)}$  respectively.

The amplitude is further expanded in the number of colours  $N_c$ . The leading-order amplitude is proportional to  $N_c^0$ . The one-loop amplitude contains terms proportional to  $N_c^{-1}$ ,  $N_c^0$ ,  $N_c$  and the two-loop amplitude consists of terms proportional to  $N_c^{-2}$ ,  $\dots$ ,  $N_c^2$ .

In this work, only the leading-colour terms of the two-loop amplitude, i. e. terms of order  $N_c^2$ , are calculated. The leading-colour terms are expected to be the numerically most significant part of the two-loop amplitude due to the colour prefactor. This simplifies the calculation since only 74 Feynman diagrams contribute to the leading-colour two-loop vector current as opposed to 414 Feynman diagrams if all colour coefficients are included. The leading-colour two-loop amplitude only involves planar Feynman diagrams, which are expected to be easier to calculate than non-planar Feynman diagrams.

## 2.3. Estimated renormalization scale dependence at NNLO QCD

The uncertainties of theory predictions are estimated by varying the renormalization scale  $\mu$  around a central scale  $\mu_0$  by a factor of 2. Although the NNLO QCD cross section is not fully known yet, it is possible to compute the renormalization scale dependence with the RGE. The renormalization scale dependence for the process at hand assumes the form

$$\begin{aligned} \sigma = \alpha_s(\mu) & \left[ \sigma_0^{(0)} + \left( \frac{\alpha_s(\mu)}{4\pi} \right) \left( \sigma_0^{(1)} + \sigma_1^{(1)} \ln \left( \frac{\mu^2}{\mu_0^2} \right) \right) \right. \\ & \left. + \left( \frac{\alpha_s(\mu)}{4\pi} \right)^2 \left( \sigma_0^{(2)} + \sigma_1^{(2)} \ln \left( \frac{\mu^2}{\mu_0^2} \right) + \sigma_2^{(2)} \ln^2 \left( \frac{\mu^2}{\mu_0^2} \right) \right) \right] + \mathcal{O}(\alpha_s^4). \end{aligned} \quad (2.17)$$

The cross section to all orders in  $\alpha_s$  must be independent of  $\mu$ , i. e.

$$\mu^2 \frac{d\sigma}{d\mu^2} = 0. \quad (2.18)$$

Calculating the left-hand side of eq. (2.18) by applying

$$\mu^2 \frac{d\alpha_s}{d\mu^2} = -\alpha_s \left( \beta_0 + \frac{\alpha_s}{4\pi} \beta_1 + \mathcal{O}(\alpha_s^2) \right) \quad (2.19)$$

and expanding in  $\alpha_s$  gives a system of equations, which yields the identities

$$\sigma_1^{(1)} = \beta_0 \sigma_0^{(0)}, \quad \sigma_1^{(2)} = \beta_1 \sigma_0^{(0)} + 2\beta_0 \sigma_0^{(1)}, \quad \sigma_2^{(2)} = \beta_0^2 \sigma_0^{(0)}. \quad (2.20)$$

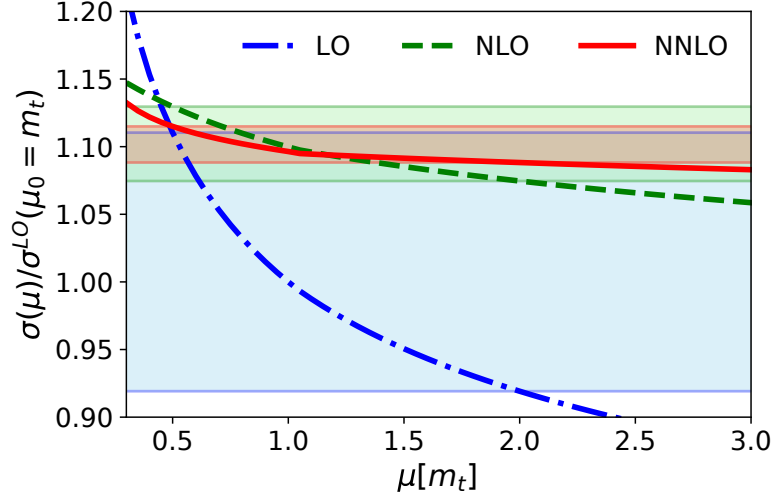


**Figure 2.2.:** Estimated renormalization scale dependence of the LO (blue), NLO (green), and NNLO (red) QCD cross sections. The corresponding scale variation between  $0.5m_t$  and  $2m_t$  is highlighted with horizontal bands.

The required coefficients of the QCD beta function [181, 182] are

$$\begin{aligned}\beta_0 &= \frac{11}{3}C_A - \frac{4}{3}T_F n_f, \\ \beta_1 &= \frac{34}{3}C_A^2 - \frac{20}{3}C_A T_F n_f - 4C_F T_F n_f\end{aligned}\tag{2.21}$$

with  $C_F = \frac{N_c^2 - 1}{2N_c}$ ,  $C_A = N_c$ ,  $T_F = \frac{1}{2}$ , and  $n_f = 6$ .

The full renormalization scale dependence can be restored by calculating  $\sigma_0^{(0)}$ ,  $\sigma_0^{(1)}$ , and  $\sigma_0^{(2)}$ . The theory uncertainty for the NNLO QCD cross section is estimated by making the following assumptions: the coefficient  $\sigma_0^{(1)}$  is chosen such that the NLO QCD corrections are positive and amount to approximately 10% of the LO cross section and  $\sigma_0^{(2)}$  is assumed to have a comparable size to  $\sigma_0^{(1)}$ . The results of this estimate are shown in fig. 2.2.

The leading-order cross section is, strictly speaking, independent of  $\mu$ . The one-loop running of the coupling constant  $\alpha_s$  is used for a rudimentary uncertainty estimate, yielding uncertainties of approximately 10%. This gives the blue curve in fig. 2.2. The scale variation is reduced to approximately 4% by the NLO QCD corrections, as indicated with the dashed green line in fig. 2.2. The NNLO QCD cross section, which is shown in red, has an even smaller scale dependence corresponding to an uncertainty of approximately 1% to 2%.

## 2.4. Feynman integrals

### 2.4.1. Introduction

The notations and definitions regarding Feynman integrals that are used in this work are summarized in the following. When performing loop calculations, one typically encounters tensor Feynman integrals of the form

$$\left( \prod_{i=1}^L \int \frac{d^d k_i}{i\pi^{d/2}} \right) k_1^{\mu_1} k_1^{\mu_2} \dots k_2^{\nu_1} k_2^{\nu_2} \dots \prod_{j=1}^t \frac{1}{P_j^{n_j}}\tag{2.22}$$

## 2. Notation and definitions

in intermediate expressions. For this general  $L$ -loop Feynman integral, the integration is performed over the  $L$  loop momenta  $k_i$ , which in the case of tensor Feynman integrals can also appear in tensor structures in the numerator. The tensor structure in eq. (2.22) is indicated by  $(k_1^{\mu_1} \dots k_2^{\nu_1} \dots)$ . The propagators are given by  $P_j = l_j^2 - m_j^2 + i\varepsilon$ , where  $l_j$  is a linear combination of loop momenta  $k_i$  and external momenta  $p_i$  and the mass of the virtual loop particle is  $m_j$ . The exponents of the propagators, which are denoted by  $n_i$  in this formula, are integers. The number of propagators with positive exponents is  $t$ . Feynman integrals are in general divergent in  $d = 4$  space-time dimensions. The singularities manifest themselves in dimensional regularization, where the dimension is typically set to  $d = 4 - 2\epsilon$ , as poles in  $\epsilon$ .

Evaluating tensor Feynman integrals directly is possible. For example, see ref. [183–185] for references of appropriate methods and their applications. This approach typically requires the numerical evaluation of a comparatively small number of integrals, but the numerical evaluation has to be performed for each phase space point separately.

Very often it is beneficial to express the tensor integrals with scalar Feynman integrals with positive propagator exponents  $n_i$ , which is known as tensor reduction. Although the tensor integrals are typically replaced by a larger number of scalar integrals in intermediate expressions, the resulting scalar integrals are usually easier to handle and can be reduced to master integrals using IBP relations.

After performing a tensor reduction, only scalar Feynman integrals of the form

$$I^{(d)}(\{s_i\}, \{m_i^2\}) = \left( \prod_{i=1}^L \int \frac{d^d k_i}{i\pi^{d/2}} \right) \prod_{j=1}^N \frac{1}{P_j^{n_j}}, \quad (2.23)$$

which are functions of the kinematic invariants  $\{s_i\}$  and the internal masses  $\{m_i^2\}$ , remain in the amplitude.

In intermediary steps, scalar Feynman integrals of this form with negative exponents can also occur. Negative exponents can arise in Feynman integrals when scalar products involving external and loop momenta in the numerator of tensor integrals are replaced with linear combinations of inverse propagators and kinematic invariants. The number of independent scalar products involving loop momenta for a given  $L$ -loop Feynman integral with  $E$  external momenta is

$$N = LE + \frac{L(L+1)}{2}. \quad (2.24)$$

Typically, the number of independent propagators  $t$  in a given Feynman integral will be smaller than  $N$  and hence  $N - t$  auxiliary propagators need to be introduced in order to uniquely express all possible scalar products with inverse propagators. When working with Feynman integrals, so-called integral families, which are essentially sets of  $N$  independent propagators and auxiliary propagators, are often defined. Integrals of a given integral family can be identified by listing their exponents and can be denoted with  $I_{n_1, n_2, \dots, n_N}^{(d)}$ .

For example, the process at hand involves 3 independent external momenta and hence one-loop integral families consist of 4 propagators and two-loop integral families consist of 9 propagators. The most complicated Feynman integrals which occur in the one-loop calculation in sec. 5.1.2 are box integrals, i.e. Feynman integrals with 4 propagators and 4 external legs, for which no auxiliary propagators are required. The leading-colour two-loop master integrals which are calculated in chapter 4 involve double-box integral topologies with 7 propagators and two auxiliary propagators.

Furthermore, the number of propagators with positive exponents  $t$ , the sum of all positive

exponents  $r$ , and the sum of all negative exponents  $s$  are given by

$$t = \sum_{j=1}^N \Theta\left(n_j - \frac{1}{2}\right), \quad r = \sum_{j=1}^N n_j \Theta\left(n_j - \frac{1}{2}\right), \quad s = -\sum_{j=1}^N n_j \Theta\left(\frac{1}{2} - n_j\right), \quad (2.25)$$

where  $\Theta(x)$  refers to the Heaviside step function. This notation follows common definitions in the literature [102, 104, 105, 186]. In addition, the sector  $S$  of a Feynman integral is defined by

$$S = \sum_{j=1}^n 2^{j-1} \Theta\left(n_j - \frac{1}{2}\right), \quad (2.26)$$

which effectively assigns a number to a set of propagators. Any sector  $S'$  corresponding to a subset of the propagators of sector  $S$  is referred to as a subsector of  $S$ .

### 2.4.2. Tensor integral reduction

At the one-loop level, the Passarino-Veltman method [187], one of the first tensor reduction schemes ever developed, is still often used for the reduction of tensor Feynman integrals. Moreover, extensions and modifications of this method as well as entirely different approaches were developed in particular to include tensor integrals with more than four external legs and to avoid numerical instabilities that are often associated with vanishing Gram determinants in denominators. Furthermore, there are several software packages available that can numerically evaluate one-loop tensor integrals or automatically perform the reduction to scalar integrals. See for extensive discussions and references to the tensor reduction methods, for example, ref. [183, 185, 188]. However, the Passarino-Veltman method cannot be applied beyond the one-loop level.

A tensor reduction method that can also be applied to multi-loop Feynman integrals was developed by Tarasov [189]. A very short overview of this method is given in app. A.2. In this method, tensor integrals are reduced to scalar integrals in equal or increased space-time dimensions and with increased propagator exponents. Dimension-shift transformations can be used to transform the scalar integrals to the desired dimensionality and IBP relations can be used to reduce the integrals with increased propagator exponents to master integrals.

As explained in app. A.2, each loop momentum in the numerator gives rise to operators increasing the sum of propagator exponents  $r$  by 1 at one-loop level and by 2 at two-loop level. For example, the tensor integrals with a maximal tensor rank of 5 appearing in the leading-colour two-loop amplitude would be reduced to scalar integrals in  $d, d+2, \dots, d+10$  dimensions with  $r$  being increased by up to 10.

The tensor reduction in this work was not performed with the Tarasov method but with projectors and subsequent IBP reduction. In this approach, form factors of tensor structures are extracted with projectors, as explained in sec. 3. After the projection, only scalar products involving external and loop momenta remain in the tensor structure. The scalar products are then subsequently replaced with linear combinations of inverse propagators and kinematic invariants. The inverse propagators decrease propagator exponents or give rise to negative propagator exponents. The resulting integrals are then reduced to master integrals.

### 2.4.3. Parametric representations

In many circumstances, it is beneficial to work with Feynman integrals in parametric representations, where additional parametric integrations are introduced allowing to perform the loop

## 2. Notation and definitions

integrations in a universal manner. Momenta, i.e. Lorentz vectors, are in the resulting expressions replaced by invariants, i.e. Lorentz scalars. Commonly used representations are the Feynman parameter representation, Schwinger parameter representation, Lee-Pomeransky representation [190], Baikov representation [191], and the Mellin-Barnes representation [192–194]. The Schwinger parameter representation is obtained, assuming only positive propagator exponents, by applying the transformation

$$\frac{1}{P_i^{n_i}} = \frac{(-1)^{n_i}}{\Gamma(n_i)} \int_0^\infty dx_i x_i^{n_i-1} \exp(x_i P_i) \quad (2.27)$$

to all propagators in eq. (2.23). The Feynman integral can then be transformed to a  $(d \times L)$ -dimensional Gaussian integral in the loop momenta by virtue of loop-momentum shifts. This results in the Schwinger parameter representation

$$I^{(d)} = \prod_{i=1}^N \left( \int_0^\infty dx_i \frac{(-1)^{n_i} x_i^{n_i-1}}{\Gamma(n_i)} \right) \mathcal{U}^{-d/2} e^{-\mathcal{F}/\mathcal{U}}. \quad (2.28)$$

The first and second Symanzik polynomials  $\mathcal{U}(\{x_i\})$  and  $\mathcal{F}(\{x_i\}, \{s_i\}, \{m_i^2\})$  are homogeneous of degree  $L$  and  $L + 1$  in the Schwinger parameters respectively. They can also be constructed from the topology of the graphs associated with the Feynman diagrams, as described in detail in ref. [86], for example.

Another representation is obtained by introducing Feynman parameters for the propagators, i.e.

$$\frac{1}{P_1^{n_1} \dots P_N^{n_N}} = \Gamma(n) \prod_{i=1}^N \left( \int_0^\infty dx_i \frac{(-1)^{n_i} x_i^{n_i-1}}{\Gamma(n_i)} \right) \delta \left( 1 - \sum_{l=1}^N x_l \right) \left( \sum_i x_i P_i \right)^{-n}, \quad (2.29)$$

where the sum of all exponents is  $n = \sum_i n_i$ . Integrating the loop momenta gives the Feynman parameter representation

$$I^{(d)} = \Gamma \left( n - \frac{Ld}{2} \right) \prod_{i=1}^N \left( \int_0^\infty dx_i \frac{(-1)^{n_i} x_i^{n_i-1}}{\Gamma(n_i)} \right) \delta \left( 1 - \sum_{l=1}^N x_l \right) \frac{\mathcal{U}^{n-(L+1)d/2}}{\mathcal{F}^{n-Ld/2}}. \quad (2.30)$$

### 2.4.4. Dimension-shift transformations

It can be convenient to perform calculations in different space-time dimensions. In this work, for example, master integrals in  $d = 6 - 2\epsilon$  dimensions are used. Hence, dimension-shift operators  $\mathbf{D}_+$  and  $\mathbf{D}_-$  which change the space-time dimensionality of the Feynman integrals by 2, i.e.

$$\mathbf{D}_+ I^{(d)} = I^{(d+2)}, \quad \mathbf{D}_- I^{(d)} = I^{(d-2)}, \quad (2.31)$$

are introduced. When working with Feynman integrals in Schwinger representation, the dimension-shift operators are given by

$$\mathbf{D}_+ = \mathcal{U}^{-1}, \quad \mathbf{D}_- = \mathcal{U} \quad (2.32)$$

on the level of the integrand since the space-time dimension in eq. (2.28) only enters in the exponent of  $\mathcal{U}$ .

Furthermore, the operator  $\mathbf{i}^+$  which increases the power of the  $i$ th propagator by one is intro-



duced. In the Schwinger representation, this operator is at the integrand level given by

$$\mathbf{i}^+ = -\frac{x_i}{n_i}. \quad (2.33)$$

The dimension-shift operator  $\mathbf{D}_-$  can be expressed in terms of  $\mathbf{i}^+$  operators since  $\mathcal{U}$  is composed of Schwinger parameters. Hence, one obtains

$$\mathbf{D}_- = \mathcal{U} = \sum_{i_1, \dots, i_L} u_{i_1, \dots, i_L} x_1^{i_1} \dots x_L^{i_L} = \sum_{i_1, \dots, i_L} \tilde{u}_{i_1, \dots, i_L} (\mathbf{1}^+)^{i_1} \dots (\mathbf{L}^+)^{i_L}, \quad (2.34)$$

where  $u_{i_1, \dots, i_L}$  are the integer coefficients of  $\mathcal{U}$  and where the coefficients  $\tilde{u}_{i_1, \dots, i_L}$  absorb the dependence on the exponents  $n_i$  when replacing  $x_i$  with eq. (2.33). Using this relation when applying both  $\mathbf{D}_+$  and  $\mathbf{D}_-$  to a  $d$ -dimensional master integral  $I_i^{(d)}$  gives

$$I_i^{(d)} = \mathbf{D}_- \mathbf{D}_+ I_i^{(d)} = \mathbf{D}_- I_i^{(d+2)} = \sum_{i_1, \dots, i_L} \tilde{u}_{i_1, \dots, i_L} (\mathbf{1}^+)^{i_1} \dots (\mathbf{L}^+)^{i_L} I_i^{(d+2)}, \quad (2.35)$$

where the master integral in  $d$  dimensions is expressed as a linear combination of  $(d+2)$ -dimensional integrals with increased propagator powers. Subsequently applying IBP relations to reduce the integrals on the right-hand side to  $(d+2)$ -dimensional master integrals gives a linear relation between the master integrals in  $d$  and  $d+2$  dimensions, i.e.

$$\vec{I}^{(d)} = D \cdot \vec{I}^{(d+2)}, \quad (2.36)$$

where  $D$  is a matrix.

#### 2.4.5. IBP reductions and quasi-finite master integrals

Typically, a large number of related scalar Feynman integrals occurs in multi-loop calculations. Especially tensor reductions often give rise to a comparatively large number of scalar integrals. These related Feynman integrals can be expressed through a smaller set of integrals, i.e. the master integrals, by virtue of so-called integration-by-parts (IBP) identities [93, 94]. The existence of IBP identities is a direct consequence of the fact that dimensionally regulated integrals over total derivatives vanish. This yields equations of the form

$$\left( \prod_{i=1}^L \int \frac{d^d k_i}{i\pi^{d/2}} \right) \frac{\partial}{\partial k_i^\mu} \left[ v^\mu \prod_{j=1}^N \frac{1}{P_j^{n_j}} \right] = 0, \quad (2.37)$$

where  $v^\mu$  is a loop or external momentum. This equation gives relations among integrals with different propagator exponents. An over-constrained system of equations can be constructed by calculating sufficiently many IBP relations. This system can be solved for the master integrals. Additional albeit redundant relations can be constructed from Lorentz-invariance [110, 195].

A systematic construction and solution of systems of IBP equations is formulated in the Laporta algorithm [95], which is implemented, for example, in **AIR** [96], **FIRE** [97–100], **Kira** [104, 105], **LiteRed** [103], and **Reduze** [101, 102].

Applying IBP relations also allows to deliberately choose master integrals to simplify calculations. For example, it can make sense to choose integrals which are well suited for the evaluation techniques at hand.

In this work, a quasi-finite basis as described in ref. [196] is used. Quasi-finite Feynman integrals do not contain any subdivergences, which means that the corresponding Feynman parameter integration is free of divergences. Quasi-finite integrals might at most possess trivial poles in  $\epsilon$

## 2. Notation and definitions

arising from gamma function prefactors. This implies in particular that all UV and IR divergences of the amplitude manifest themselves explicitly in the IBP reduction and in dimension-shift transformations.

Quasi-finite bases were developed in particular to be applied together with analytical evaluation techniques for Feynman integrals as, for example, implemented in **HyperInt** [197]. **HyperInt** can express suitable convergent integrals as MPLs, which makes a resolution of singularities beforehand necessary. When using quasi-finite integrals as integral basis, no additional singularity resolution is necessary.

Using quasi-finite integrals can also be beneficial for direct numerical evaluation. When evaluating Feynman integrals with sector decomposition algorithms [76, 198], subdivergences are treated by dividing the integration domain, applying suitable transformations in each sector, and then integrating the resulting convergent integrals numerically. Dividing the integration domain can give rise to spurious transcendental functions [196, 199], and numerically reconstructing these spurious functions can have adverse effects on the performance of the numerical integration. However, these spurious transcendental functions can be avoided by using quasi-finite integrals and hence an improvement of numerical convergence of the respective integrals is plausible. According to ref. [196], it is possible to numerically evaluate quasi-finite integrals in the Euclidean region without further preparation except for a possible treatment of logarithmic endpoint singularities.

A quasi-finite basis can be obtained from a generic integral basis by applying regulating dimension-shift transformations and increasing propagator powers.

The two-loop master integrals relevant for this work are most likely not entirely expressible with MPLs, which prevents a direct calculation with **HyperInt**. The application of a quasi-finite basis is nevertheless still advantageous when calculating asymptotic expansions with the expansion by regions with the help of **HyperInt** as explained in sec. 4.2.2.

### 2.4.6. Differential equations

IBP reductions can also be used to derive differential equations for master integrals. In the following, the shorthand notation  $\partial_a = \frac{\partial}{\partial a}$  is used for derivatives. The derivative of a master integral  $I_i$  with respect to some invariant  $a$  can be expressed as sum of Feynman integrals of the same integral family, denoted here by  $\tilde{I}_j$ , which can be subsequently reduced to master integrals, i. e.

$$\partial_a I_i = \sum_j \tilde{c}_{ij}^a \tilde{I}_j = \sum_j A_{ij}^a I_j. \quad (2.38)$$

This yields differential equations of the general form

$$\partial_a \vec{I} = A_a \cdot \vec{I}, \quad (2.39)$$

where  $\vec{I}$  is a vector of master integrals and  $A_a$  is a matrix. For the process at hand, the master integrals obey a system of four differential equations, which are

$$\partial_x \vec{I} = A_x \cdot \vec{I}, \quad \partial_z \vec{I} = A_z \cdot \vec{I}, \quad \partial_m \vec{I} = A_m \cdot \vec{I}, \quad \partial_s \vec{I} = A_s \cdot \vec{I}. \quad (2.40)$$

The entries of the matrices are rational functions in  $x$ ,  $z$ ,  $m$ ,  $s$ , and  $\epsilon$ . The derivatives with respect to invariants can be calculated in the momentum representation or in a parametric representation, as explained in app. A.3. In the momentum representation, the derivatives

assume the form

$$\partial_a = \sum_{i,j} c_{ij}^a p_i^\mu \partial_{p_j^\mu} + \sum_i c_i^a \partial_{m_i}, \quad (2.41)$$

where  $p_i$  and  $m_i$  are the external momenta and masses of the involved particles. Differentiation in the parametric representation is straightforward since the invariants appear directly in  $\mathcal{F}$ . Differentiating the Schwinger representation can, however, give rise to Feynman integrals in shifted dimensions, which can be subsequently transformed back to  $d$  dimensions with dimension-shift operators.

The equality of mixed partial derivatives of  $\vec{I}$  gives rise to the integrability condition

$$\left( \frac{\partial A_{x_k}}{\partial x_j} - \frac{\partial A_{x_j}}{\partial x_k} \right) - [A_{x_j}, A_{x_k}] = 0, \quad (2.42)$$

where  $x_j, x_k \in \{x, z, m, s\}$ . This condition can be used as a consistency check of the obtained differential equation system. When the differential equation system is denoted by

$$d\vec{I} = A \cdot \vec{I}, \quad (2.43)$$

where  $A$  is the one-form

$$A = \sum_{x_i} A_{x_i} dx_i, \quad (2.44)$$

the integrability condition assumes the form

$$dA - A \wedge A = 0. \quad (2.45)$$

The integral basis can be transformed by applying

$$\vec{J} = T(\epsilon, \{x_i\}) \cdot \vec{I}, \quad (2.46)$$

which transforms the differential equation as

$$\partial_m \vec{J} = (T A_m T^{-1} - T \partial_m T^{-1}) \vec{J}. \quad (2.47)$$

Transformations are typically applied to simplify the differential equation systems. For example, in the so-called canonical or  $\epsilon$  form [111] the one-form in eq. (2.44) assumes the form

$$A(\epsilon, \{x_i\}) = \epsilon d\tilde{A}(\{x_i\}) = \epsilon \sum_i \tilde{A}_i d \ln(L_i(\{x_i\})), \quad (2.48)$$

where the so-called letters  $L_i$  are rational functions and  $\tilde{A}_i$  are matrices. The master integrals can be straightforwardly evaluated as iterated integrals when the differential equation assumes this form.



## 3. Projection procedure

### 3.1. Introduction

The vector currents defined in eq. (2.9) assume in the two-loop calculation the general form

$$V_t^\mu = \epsilon_{3\nu}^* \sum_i F_i \bar{u}(p_1) \Gamma_i^{\mu\nu\alpha_1\dots\alpha_{t_1}\beta_1\dots\beta_{t_2}} v(p_2) \cdot I_{i;\alpha_1,\dots,\alpha_{t_1};\beta_1,\dots,\beta_{t_2}}^{(d)}. \quad (3.1)$$

The two-loop tensor Feynman integrals  $I_{i;\alpha_1,\dots,\alpha_{t_1};\beta_1,\dots,\beta_{t_2}}^{(d)}$  are contracted with Lorentz structures  $\Gamma_i^{\mu\nu\alpha_1\dots\alpha_{t_1}\beta_1\dots\beta_{t_2}}$ , which are composed of Dirac matrices, external momenta, and polarization vectors. All remaining terms in eq. (3.1) are absorbed into the scalar coefficients  $F_i$ . The leading-colour two-loop amplitude contains tensor Feynman integrals with a maximal tensor rank of 5. This gives rise to a relatively large number of Lorentz structures and tensor integrals. The current in eq. (3.1) is not well suited for direct numerical evaluation. For instance, the spinor structures

$$\bar{u}(p_1) \Gamma_i^{\mu\nu\alpha_1\dots\alpha_{t_1}\beta_1\dots\beta_{t_2}} v(p_2) \quad (3.2)$$

are not linearly independent and there are also relations among the Feynman integrals. This gives rise to highly non-trivial cancellations, which could spoil the numerical stability.

The goal of this chapter is to simplify eq. (3.1) by expressing the currents as linear combinations of spinor structure  $S_i$ ,  $\tilde{S}_i$  and form factors  $C_i$ ,  $\tilde{C}_i$ , i.e.

$$\begin{aligned} V_t^\mu &= \sum_i C_i \cdot S_i^\mu = \sum_i C_i \cdot \epsilon_{3\nu}^* \bar{u}(p_1) \Gamma_i^{\mu\nu} v(p_2), \\ A_t^\mu &= \sum_i \tilde{C}_i \cdot \tilde{S}_i^\mu = \sum_i \tilde{C}_i \cdot \epsilon_{3\nu}^* \bar{u}(p_1) \tilde{\Gamma}_i^{\mu\nu} v(p_2). \end{aligned} \quad (3.3)$$

The spinor structures  $S_i$  are rather short and compact functions that only depend on the momenta and helicities of the external particles. For the process at hand, they assume the general form

$$S_i = \epsilon_{4\mu} \epsilon_{3\nu}^* \bar{u}(p_1) \Gamma_i^{\mu\nu} v(p_2). \quad (3.4)$$

The Lorentz tensor  $\Gamma_i^{\mu\nu}$  is composed of Dirac matrices, the metric tensor, and external momenta. The spinor structures  $\tilde{S}_i$  of the axial-vector current contain one  $\gamma^5$  matrix due to the axial-vector coupling. The scalar coefficients  $C_i$  or  $\tilde{C}_i$  are independent of the helicities of the external particles and absorb all the remaining complexity of the calculation, in particular they contain the Feynman integrals.

This form-factor decomposition can be obtained by first performing a tensor reduction and then simplifying the spinor structures by systematically making use of the Clifford algebra. In this work, however, the form factors  $C_i$  are extracted directly with projectors. This approach has the advantage of projecting the amplitude onto a minimal set of linearly independent spinor structures  $\{S_i\}$ , which prevents spurious cancellations among linearly dependent terms. The tensor reduction is also straightforward in this procedure. The tensor Feynman integrals are after the

### 3. Projection procedure

projection contained in the form factors  $C_i$  and consequently only involve scalar products of loop momenta and external momenta in the numerator. These scalar products can then be replaced with inverse propagators, which gives rise to scalar Feynman integrals with negative exponents. The resulting scalar Feynman integrals are then reduced to master integrals using IBP relations. Projectors have been applied successfully in the past to calculate numerous processes [51, 200–204] and are still the subject of further studies and improvements [205–207].

In the following, the projection procedure is outlined in sec. 3.2 and illustrated with a simple example in sec. 3.3. Afterwards, a set of independent spinor structures for the process  $\gamma^* \rightarrow t\bar{t}g$  is constructed by making a generic ansatz for all possible structures in sec. 3.4. Electroweak Ward identities for the projection coefficients are derived in sec. 3.5.

### 3.2. Construction of the projectors

Let  $\{S_i\}$  be a set of  $N$  independent spinor structures for an arbitrary process. This set  $\{S_i\}$  is constructed from the helicity states and momenta of the external particles while being compatible with Lorentz, gauge, and other symmetries. The coefficient  $C_j$  of the spinor structure  $S_j$  is obtained by applying the projection operator  $\mathcal{P}_j$  to the amplitude, i. e.

$$\mathcal{P}_j \circ \left( \sum_i C_i \cdot S_i \right) = \sum_{\text{pol}} \mathcal{P}_j \left( \sum_i C_i \cdot S_i \right) = C_j. \quad (3.5)$$

This definition of the projector  $\mathcal{P}_j$  includes the term  $\mathcal{P}_j$ , for which the ansatz

$$\mathcal{P}_j = \sum_k A_{jk} S_k^+ \quad (3.6)$$

is made. The application of the projector is denoted with  $\circ$ . The entries of the matrix  $A$  are rational functions of the kinematic invariants, i. e. masses and scalar products of external momenta, and the space-time dimension  $d$ . The projectors are applied by summing over all polarizations of the external particles. For this process, this means summing over the helicities of the two top quarks, the gluon and the  $Z$  boson or photon. When performing this sum, the polarization vectors and quark spinors are replaced with polarization sums chosen to be consistent with gauge symmetries and the regularization scheme. In the standard projection approach, which is applied in this work, all external particles and hence also all resulting Lorentz and Dirac structures are regarded as  $d$ -dimensional objects. This corresponds to adopting CDR as regularization scheme. When performing the polarization sum, the quark spinors are hence replaced with

$$\sum_{\text{pol}} u(p_1) \bar{u}(p_1) = \not{p}_1 + m_t, \quad \sum_{\text{pol}} v(p_2) \bar{v}(p_2) = \not{p}_2 - m_t, \quad (3.7)$$

and the  $d$ -dimensional trace in Dirac space is taken. For the external gluon, the polarization sum

$$\sum_{\text{pol}} \epsilon_3^\mu \cdot \epsilon_3^{*\nu} = -g^{\mu\nu} + \frac{p_3^\mu n^\nu + p_3^\nu n^\mu}{p_3 \cdot n} = -g^{\mu\nu} + \frac{p_3^\mu Q^\nu + p_3^\nu Q^\mu}{p_3 \cdot Q} - \frac{Q^2}{(p_3 \cdot Q)^2} p_3^\mu p_3^\nu \quad (3.8)$$

is used and the massive reference vector  $Q = p_4 = p_1 + p_2 + p_3$  is chosen. This polarization sum only includes the physical polarizations of the gluon, i. e. the two physical transverse polarization states of the on-shell gluon. External QCD ghost fields hence do not have to be included in the calculation. This polarization sum follows from the polarization sum associated with the axial

gauge, which is also given in eq. (3.8). Choosing the massless reference vector  $n^\mu = Q^\mu - p_3^\mu \frac{Q^2}{2Q \cdot p_3}$  with an arbitrary massive vector  $Q$  leads to the polarization sum given on the right-hand side of eq. (3.8), which is typically associated with the so-called temporal gauge.

For the polarization sum of the initial-state vector,

$$\sum_{\text{pol}} \epsilon_4^\mu \cdot \epsilon_4^{*\nu} = -g^{\mu\nu} \quad (3.9)$$

is used. This corresponds to setting  $\xi_Z = 1$  in the  $R_\xi$  gauge, which is also often colloquially referred to as 't Hooft-Feynman gauge. Since the initial-state polarization vector  $\epsilon_4$  corresponds to an off-shell photon or  $Z$  boson, the transverse as well as the longitudinal polarization states need to be included. This polarization sum actually also includes the unphysical time-like polarization, which is kept as a superfluous degree of freedom for the sake of simplicity. However, this increases the number of spinor structures appearing in the calculation slightly and gives rise to relations among the projection coefficients when imposing electroweak Ward identities as done in sec. 3.5.

The matrix  $A$  in the ansatz of eq. (3.6) is determined by applying  $\mathcal{P}_j$  to  $S_i$ , which by definition gives a Kronecker delta, i. e.

$$\mathcal{P}_j \circ S_i = \sum_{\text{pol}} \mathcal{P}_j S_i = \sum_k A_{jk} (S_k^+ \circ S_i) = \delta_{ji}. \quad (3.10)$$

The coefficient matrix  $A$  of the projectors is consequently the inverse of the matrix  $(S^+ \circ S)$ , i. e.

$$A = (S^+ \circ S)^{-1}. \quad (3.11)$$

The matrix  $(S^+ \circ S)$  must be invertible if the spinor structures of a given set  $\{S_i\}$  are independent. The rank of the matrix can hence be used to check for linear independence of the spinor structures.

The computer algebra system **Fermat** [208] was used to calculate the rank and the inverse of  $(S^+ \circ S)$ . For the process at hand, the vector and vector-axial currents only require the inversion of two  $18 \times 18$  matrices, which did not pose any problems. But for other processes, this inversion could be problematic since the number of independent spinor structures can grow rapidly with the number of external particles. This could effectively render this method infeasible for high-multiplicity processes. This is worsened by the fact that in CDR more independent spinor structures tend to emerge than in 4 dimensions. The spurious structures, in the literature also sometimes referred to as irrelevant structures, are not independent in 4 dimensions and hence can be expressed with the remaining independent structures in 4 dimensions. While for up to four-parton amplitudes typically only  $\mathcal{O}(10)$  independent structures occur, already five-parton amplitudes can possess more than a hundred structures when using CDR.

For example, the four-gluon amplitude possesses 10 independent structures in  $d$  dimensions according to ref. [207] of which 8 are independent in 4 dimensions. For this process, only 8 of the  $2^4 = 16$  helicity configurations are independent since processes with up to four legs exhibit trivial behaviour under parity transformations [207]. The five-gluon amplitude, however, already possesses 142 independent spinor structures in  $d$  dimensions according to ref. [205] of which only 32 are independent in 4 dimensions. To mitigate this effect, techniques applying ‘physical’ projectors were proposed in ref. [205–207] with which the number of independent spinor structures is reduced to the number of independent helicity configurations of external particles. Essentially, the ‘physical’ projectors impose 4-dimensional external states, i. e. only take physical polarizations of external particles into account, while only virtual particles are  $d$ -dimensional. This corresponds to adopting the ‘t Hooft-Veltman regularization scheme [209].

### 3. Projection procedure

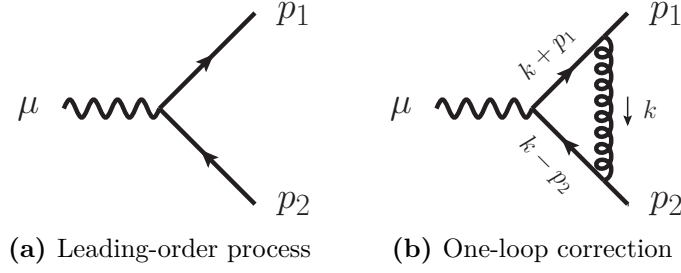


**Figure 3.1.:** Introductory example: off-shell photon decaying into two massless quarks.

In this work, the standard projector approach is chosen and the CDR scheme is adopted since the number of independent spinor structures is still manageable with the tools at hand.

### 3.3. Introductory example: $\gamma^* \rightarrow q\bar{q}$

The previously defined projectors are illustrated in this section with a simple introductory example: an off-shell photon decaying into two massless quarks, i. e.

$$\gamma^*(p_1 + p_2) \rightarrow q(p_1) + \bar{q}(p_2), \quad (3.12)$$

which is at leading order depicted in fig. 3.1a. The kinematics of this process are given by

$$p_1^2 = p_2^2 = 0, \quad (p_1 + p_2)^2 = 2p_1 \cdot p_2 = s. \quad (3.13)$$

At leading order, the amplitude is proportional to the vector current

$$V^{(0)} = \epsilon_\mu \bar{u}(p_1) \gamma^\mu v(p_2). \quad (3.14)$$

All possible spinor structures for this process obey the form  $\epsilon_\mu \bar{u}(p_1) \Gamma^\mu v(p_2)$ , where  $\Gamma^\mu$  denotes all possible products of Dirac matrices and momenta with one uncontracted Lorentz index  $\mu$ . The three possible structures are

$$S_1 = \epsilon_\mu \bar{u}(p_1) \gamma^\mu v(p_2), \quad S_2 = \epsilon_\mu p_1^\mu \bar{u}(p_1) v(p_2), \quad S_3 = \epsilon_\mu p_2^\mu \bar{u}(p_1) v(p_2), \quad (3.15)$$

where  $S_1$  is proportional to the leading-order amplitude. Note that the spinor structures do not contain  $\not{p}_1$  and  $\not{p}_2$  due to the Dirac equation. The corresponding hermitian conjugates

$$S_1^+ = \epsilon_\mu^* \bar{v}(p_2) \gamma^\mu u(p_1), \quad S_2^+ = \epsilon_\mu^* p_1^\mu \bar{v}(p_2) u(p_1), \quad S_3^+ = \epsilon_\mu^* p_2^\mu \bar{v}(p_2) u(p_1) \quad (3.16)$$

are used to calculate the matrix  $(S^+ \circ S)$ . The projection operation  $\circ$  is applied by summing over all polarizations and replacing the polarization sums by

$$\sum_{\text{pol}} u(p_1) \bar{u}(p_1) = \not{p}_1, \quad \sum_{\text{pol}} v(p_2) \bar{v}(p_2) = \not{p}_2, \quad \sum_{\text{pol}} \epsilon_\mu \epsilon_\nu^* = -g_{\mu\nu}, \quad (3.17)$$

followed by taking the trace in  $d$  dimensions. The non-zero components of  $(S^+ \circ S)$  are

$$\begin{aligned} S_1^+ \circ S_1 &= \sum_{\text{pol}} S_1^+ S_1 = \sum_{\text{pol}} \epsilon_\mu^* \epsilon_\nu \bar{v}(p_2) \gamma^\mu u(p_1) \bar{u}(p_1) \gamma^\nu v(p_2) \\ &= -g_{\mu\nu} \text{Tr} \left( \not{p}_2 \gamma^\mu \not{p}_1 \gamma^\nu \right) = 2(d-2)s \end{aligned} \quad (3.18)$$



and

$$\begin{aligned} S_3^+ \circ S_2 &= S_2^+ \circ S_3 = \sum_{\text{pol}} S_2^+ S_3 = \sum_{\text{pol}} \epsilon_\mu^* \epsilon_\nu \bar{v}(p_2) p_1^\mu u(p_1) \bar{u}(p_1) p_3^\nu v(p_2) \\ &= -(p_1 \cdot p_2) \text{Tr}(\not{p}_2 \not{p}_1) = -s^2, \end{aligned} \quad (3.19)$$

while all remaining coefficients vanish, e. g.

$$S_1^+ \circ S_2 = \sum_{\text{pol}} S_1^+ S_2 = \sum_{\text{pol}} \epsilon_\mu^* \epsilon_\nu \bar{v}(p_2) \gamma^\mu u(p_1) \bar{u}(p_1) p_1^\nu v(p_2) = \text{Tr}(\not{p}_2 \not{p}_1 \not{p}_1) = 0. \quad (3.20)$$

Hence, the matrix is

$$(S^+ \circ S) = \begin{pmatrix} (-4+2d)s & 0 & 0 \\ 0 & 0 & -s^2 \\ 0 & -s^2 & 0 \end{pmatrix} \quad (3.21)$$

and its inverse is

$$A = (S^+ \circ S)^{-1} = \begin{pmatrix} \frac{1}{(-4+2d)s} & 0 & 0 \\ 0 & 0 & \frac{-1}{s^2} \\ 0 & \frac{-1}{s^2} & 0 \end{pmatrix}. \quad (3.22)$$

The spinor structures in eq. (3.15) are indeed independent since the matrix  $(S^+ \circ S)$  is invertible. The number of independent structures is equal or smaller than the number of independent helicity configurations. This process has in total  $2 \cdot 2 \cdot 2 = 8$  helicity configuration. This number is reduced by a factor of 2 since the final-state quarks are massless. Invariance under parity transformation reduces the number of independent helicity configurations by another factor of 2.

Why does this calculation yield three independent spinor structures when there are only two independent helicity amplitudes for this process? The answer lies in the choice of the polarization sum of the photon in eq. (3.17) which, just as the polarization sum of the initial-state vector in eq. (3.9), is simply given by the metric corresponding to the choice of 't Hooft-Feynman gauge. While this slightly simplifies the calculations, the unphysical polarizations give rise to one superfluous spinor structure. Imposing a Ward identity for the photon on the vector current, i. e.

$$\begin{aligned} 0 &= (p_1 + p_2)_\mu V^\mu = C_1 \bar{u}(p_1) (\not{p}_1 + \not{p}_2) v(p_2) + (C_2 + C_3) \frac{s}{2} \bar{u}(p_1) v(p_2) \\ &= (C_2 + C_3) \frac{s}{2} \bar{u}(p_1) v(p_2), \end{aligned} \quad (3.23)$$

results in the relation  $C_2 = -C_3$ , which reduces the number of independent structures to 2.

One option is to perform the projection as described above and check whether  $C_2 = -C_3$  holds for the resulting coefficients. Another possibility is to modify the projection procedure. For example, when applying the polarization sum

$$\sum_{\text{pol}} \epsilon_\mu \epsilon_\nu^* = -g_{\mu\nu} + \frac{(p_1 + p_2)_\mu (p_1 + p_2)_\nu}{s}, \quad (3.24)$$

### 3. Projection procedure

which corresponds to the polarization sum of a massive vector boson and cancels unphysical polarizations, the resulting matrix

$$(S^+ \circ S) = \begin{pmatrix} (-4 + 2d)s & 0 & 0 \\ 0 & \frac{s^2}{2} & -\frac{s^2}{2} \\ 0 & -\frac{s^2}{2} & \frac{s^2}{2} \end{pmatrix} \quad (3.25)$$

is of rank 2. This implies that only two structures are independent. A new set of spinor structures is, for example,

$$S'_1 = \epsilon_\mu \bar{u}(p_1) \gamma^\mu v(p_2), \quad S'_2 = \epsilon_\mu (p_1^\mu - p_2^\mu) \bar{u}(p_1) v(p_2). \quad (3.26)$$

This set already incorporates the Ward identity on the level of individual spinor structures, i. e.

$$S'_i \xrightarrow{\epsilon \rightarrow p_1 + p_2} 0, \quad (3.27)$$

and yields the matrix

$$(S'^+ \circ S') = \begin{pmatrix} (-4 + 2d)s & 0 \\ 0 & 2s^2 \end{pmatrix}. \quad (3.28)$$

The projectors for the three spinor structures in eq. (3.15) with polarization sums defined as in eq. (3.17) are

$$\begin{aligned} \mathcal{P}_1 &= \sum_i A_{1i} S_i^+ = \frac{1}{(2d-4)s} \epsilon_\mu^* \bar{v}(p_2) \gamma^\mu u(p_1), \\ \mathcal{P}_2 &= \sum_i A_{2i} S_i^+ = -\frac{1}{s^2} (p_1 \cdot \epsilon^*) \bar{v}(p_2) u(p_1), \\ \mathcal{P}_3 &= \sum_i A_{3i} S_i^+ = -\frac{1}{s^2} (p_2 \cdot \epsilon^*) \bar{v}(p_2) u(p_1). \end{aligned} \quad (3.29)$$

Equivalent results are obtained when using the two structures in eq. (3.26) with the polarization sum in eq. (3.24), which yields the projectors

$$\begin{aligned} \mathcal{P}'_1 &= \mathcal{P}_1 = \sum_i A'_{1i} S_i'^+ = \frac{1}{(2d-4)s} \epsilon_\mu^* \bar{v}(p_2) \gamma^\mu u(p_1), \\ \mathcal{P}'_2 &= \frac{1}{2} (\mathcal{P}_3 - \mathcal{P}_2) = \sum_i A'_{2i} S_i'^+ = \frac{1}{2s^2} (p_1 - p_2) \cdot \epsilon^* \bar{v}(p_2) u(p_1). \end{aligned} \quad (3.30)$$

Applying the projectors to the leading-order current in eq. (3.14) yields, as expected, the coefficients

$$C_1 = C'_1 = 1, \quad C_2 = C_3 = C'_2 = 0. \quad (3.31)$$

At the one-loop level, only the diagram depicted in fig. 3.1b contributes to the vector current

$$V^{(1)} = \epsilon_\mu \int \frac{d^d k}{i\pi^{d/2}} \frac{\bar{u}(p_1) \gamma^\nu (\not{k} + \not{p}_1) \gamma^\mu (\not{k} - \not{p}_2) \gamma_\nu v(p_2)}{k^2 (k + p_1)^2 (k - p_2)^2}. \quad (3.32)$$

Applying the projectors given in eq. (3.29) yields the coefficients

$$C_1 = \frac{1}{s} \int \frac{d^d k}{i\pi^{d/2}} \frac{(d-4)sk^2 - 2(s - 2(p_1 \cdot k))(2(p_2 \cdot k) + s)}{k^2(k+p_1)^2(k-p_2)^2}, \quad C_2 = C_3 = 0. \quad (3.33)$$

In this one-loop example, the  $C_2$  and  $C_3$  coefficients also vanish. However, this is not the case when quark masses are introduced.

The tensor structures in the numerator of eq. (3.33) have been replaced by scalar products involving the loop momentum. The coefficient  $C_1$  can be further simplified by replacing the scalar products  $k^2$ ,  $p_1 \cdot k$ , and  $p_2 \cdot k$  with inverse propagators, i. e.

$$p_1 \cdot k = \frac{1}{2} [(k+p_1)^2 - k^2], \quad p_2 \cdot k = \frac{1}{2} [k^2 - (k-p_2)^2]. \quad (3.34)$$

The inverse propagators are cancelled with propagators in the denominator or give rise to negative propagator powers, as

$$\begin{aligned} C_1 &= \int \frac{d^d k}{i\pi^{d/2}} \left( \frac{d-8}{(k+p_1)^2(k-p_2)^2} - \frac{2s}{k^2(k+p_1)^2(k-p_2)^2} - \frac{2k^2}{(k+p_1)^2(k-p_2)^2s} \right. \\ &\quad \left. + \frac{2}{k^2(k+p_1)^2} + \frac{2}{k^2(k-p_2)^2} - \frac{2}{k^2s} + \frac{2}{(k+p_1)^2s} + \frac{2}{(k-p_2)^2s} \right) \\ &= 2 \left( \frac{d-8}{2} I_{0,1,1} - s I_{1,1,1} + I_{1,1,0} + I_{1,0,1} - \frac{1}{s} (I_{-1,1,1} + I_{1,0,0} - I_{0,1,0} - I_{0,0,1}) \right) \\ &= \frac{16-7d+d^2}{2(d-4)} I_{0,1,1}. \end{aligned} \quad (3.35)$$

In this formula, the integrals are denoted by

$$I_{\nu_1, \nu_2, \nu_3} = \int \frac{d^d k}{i\pi^{d/2}} \frac{1}{[k^2]^{\nu_1} [(k+p_1)^2]^{\nu_2} [(k-p_2)^2]^{\nu_3}}. \quad (3.36)$$

Furthermore, an IBP reduction obtained with Kira was applied in the last step and scaleless integrals were replaced with zero. The only contributing integral is  $I_{0,1,1}$  for this current. Note that also the triangle integral  $I_{1,1,1}$  can be reduced to  $I_{0,1,1}$  for this specific kinematic.

In this work, the projectors are applied as demonstrated in this example. However, calculations are not explicitly shown in the following due to their complexity. For example,  $A = (S^+ \circ S)^{-1}$  is for the process at hand an  $18 \times 18$  matrix with more complicated entries than the matrix in eq. (3.22).

### 3.4. Construction of the spinor structures

In this section, a set of linearly independent spinor structures  $\{S_i\}$  is constructed for the process  $\gamma^* \rightarrow t\bar{t}g$ . For this purpose, a general ansatz for all relevant spinor structures is made, then a QCD Ward identity for the external gluon is imposed, and the linear independence of the resulting set is checked by calculating the rank of the matrix  $(S^+ \circ S)$ .

According to ref. [210] the number of independent Standard Matrix Elements, which are equivalent to the spinor structures, cannot be larger than the number of independent helicity configurations of the external particles. For the process under investigation, there are  $3 \cdot 2^3 = 24$  possible polarizations of external particles, of which 12 are independent due to trivial behaviour

### 3. Projection procedure

under parity transformations since this process only involves 4 external particles [207]. However, the initial-state vector  $\epsilon_4$  carries 4 instead of 3 polarizations, i. e. the unphysical time-like polarization is additionally included, because of the choice of the corresponding polarization sum. This results in  $4 \cdot 2^3/2 = 16$  spinor structures when applying the projection in  $d = 4$  dimensions. Additionally, an electroweak Ward identity yields 4 relations among the projection coefficients reducing the number of independent spinor structures to 12, as expected.

The spinor structures for currents  $V^\mu$  and  $A^\mu$  as defined in eq. (3.3) can be written as

$$S_i = \epsilon_{4\mu} \epsilon_{3\nu}^* S_i^{\mu\nu} = \epsilon_{4\mu} \epsilon_{3\nu}^* \bar{u}(p_1) \Gamma_i^{\mu\nu} v(p_2), \quad \tilde{S}_i = \epsilon_{4\mu} \epsilon_{3\nu}^* \tilde{S}_i^{\mu\nu} = \epsilon_{4\mu} \epsilon_{3\nu}^* \bar{u}(p_1) \tilde{\Gamma}_i^{\mu\nu} v(p_2). \quad (3.37)$$

This ansatz includes a general tensor structure with two indices in Dirac space  $\Gamma_i^{\mu\nu}$ , which for this process is given by

$$\begin{aligned} \Gamma_i^{\mu\nu} = & \left( c_1 + c_2 \cdot \not{p}_3 \right) \cdot L_1^{\mu\nu} + \left( c_3 \cdot \gamma^\nu + c_4 \cdot \gamma^\nu \not{p}_3 \right) \cdot L_2^\mu \\ & + \left( c_5 \cdot \gamma^\mu + c_6 \cdot \gamma^\mu \not{p}_3 \right) \cdot L_3^\nu + \left( c_7 \cdot \gamma^\mu \gamma^\nu + c_8 \cdot \gamma^\mu \gamma^\nu \not{p}_3 \right). \end{aligned} \quad (3.38)$$

By virtue of the Dirac equation, no  $\not{p}_1$  and  $\not{p}_2$  occur in the ansatz. The Lorentz tensors  $L_1^{\mu\nu}$ ,  $L_2^\mu$  and  $L_3^\nu$  can only contain the momenta  $p_1$ ,  $p_2$ , and  $p_3$  and the metric tensor  $g^{\mu\nu}$ . Furthermore, the condition  $\epsilon_3 \cdot p_3 = 0$  forbids all terms containing  $p_3^\nu$  in  $L_1^{\mu\nu}$  and  $L_3^\nu$ . The Lorentz tensors are hence

$$\begin{aligned} L_1^{\mu\nu} &= c'_1 g^{\mu\nu} + c'_2 p_1^\mu p_1^\nu + c'_3 p_1^\mu p_2^\nu + c'_4 p_2^\mu p_1^\nu + c'_5 p_2^\mu p_2^\nu + c'_6 p_3^\mu p_1^\nu + c'_7 p_3^\mu p_2^\nu, \\ L_2^\mu &= c'_8 p_1^\mu + c'_9 p_2^\mu + c'_{10} p_3^\mu, \\ L_3^\nu &= c'_{11} p_1^\nu + c'_{12} p_2^\nu. \end{aligned} \quad (3.39)$$

Inserting the Lorentz tensors into the ansatz in eq. (3.38) gives 26 structures for the vector current. After relabelling the coefficients, the vector current becomes

$$\begin{aligned} \epsilon_4^\mu \epsilon_3^{*\nu} V_{\mu\nu} = & C_1 \cdot (p_1 \cdot \epsilon_3^*) (p_1 \cdot \epsilon_4) \bar{u}(p_1) v(p_2) & + C_2 \cdot (p_1 \cdot \epsilon_3^*) (p_2 \cdot \epsilon_4) \bar{u}(p_1) v(p_2) \\ & + C_3 \cdot (p_1 \cdot \epsilon_3^*) (p_3 \cdot \epsilon_4) \bar{u}(p_1) v(p_2) & + C_4 \cdot (p_1 \cdot \epsilon_4) (p_2 \cdot \epsilon_3^*) \bar{u}(p_1) v(p_2) \\ & + C_5 \cdot (p_2 \cdot \epsilon_3^*) (p_2 \cdot \epsilon_4) \bar{u}(p_1) v(p_2) & + C_6 \cdot (p_2 \cdot \epsilon_3^*) (p_3 \cdot \epsilon_4) \bar{u}(p_1) v(p_2) \\ & + C_7 \cdot (\epsilon_3^* \cdot \epsilon_4) \bar{u}(p_1) v(p_2) & + C_8 \cdot (p_1 \cdot \epsilon_3^*) (p_1 \cdot \epsilon_4) \bar{u}(p_1) \not{p}_3 v(p_2) \\ & + C_9 \cdot (p_1 \cdot \epsilon_3^*) (p_2 \cdot \epsilon_4) \bar{u}(p_1) \not{p}_3 v(p_2) & + C_{10} \cdot (p_1 \cdot \epsilon_3^*) (p_3 \cdot \epsilon_4) \bar{u}(p_1) \not{p}_3 v(p_2) \\ & + C_{11} \cdot (p_1 \cdot \epsilon_4) (p_2 \cdot \epsilon_3^*) \bar{u}(p_1) \not{p}_3 v(p_2) & + C_{12} \cdot (p_2 \cdot \epsilon_3^*) (p_2 \cdot \epsilon_4) \bar{u}(p_1) \not{p}_3 v(p_2) \\ & + C_{13} \cdot (p_2 \cdot \epsilon_3^*) (p_3 \cdot \epsilon_4) \bar{u}(p_1) \not{p}_3 v(p_2) & + C_{14} \cdot (\epsilon_3^* \cdot \epsilon_4) \bar{u}(p_1) \not{p}_3 v(p_2) \\ & + C_{15} \cdot (p_1 \cdot \epsilon_4) \bar{u}(p_1) \not{\epsilon}_3^* \not{p}_3 v(p_2) & + C_{16} \cdot (p_2 \cdot \epsilon_4) \bar{u}(p_1) \not{\epsilon}_3^* \not{p}_3 v(p_2) \\ & + C_{17} \cdot (p_3 \cdot \epsilon_4) \bar{u}(p_1) \not{\epsilon}_3^* \not{p}_3 v(p_2) & + C_{18} \cdot \bar{u}(p_1) \not{\epsilon}_4 \not{\epsilon}_3^* v(p_2) \\ & + C_{19} \cdot (p_1 \cdot \epsilon_4) \bar{u}(p_1) \not{\epsilon}_3^* v(p_2) & + C_{20} \cdot (p_2 \cdot \epsilon_4) \bar{u}(p_1) \not{\epsilon}_3^* v(p_2) \\ & + C_{21} \cdot (p_3 \cdot \epsilon_4) \bar{u}(p_1) \not{\epsilon}_3^* v(p_2) & + C_{22} \cdot \bar{u}(p_1) \not{\epsilon}_4 \not{\epsilon}_3^* \not{p}_3 v(p_2) \\ & + C_{23} \cdot (p_1 \cdot \epsilon_3^*) \bar{u}(p_1) \not{\epsilon}_4 \not{p}_3 v(p_2) & + C_{24} \cdot (p_2 \cdot \epsilon_3^*) \bar{u}(p_1) \not{\epsilon}_4 \not{p}_3 v(p_2) \\ & + C_{25} \cdot (p_1 \cdot \epsilon_3^*) \bar{u}(p_1) \not{\epsilon}_4 v(p_2) & + C_{26} \cdot (p_2 \cdot \epsilon_3^*) \bar{u}(p_1) \not{\epsilon}_4 v(p_2). \end{aligned} \quad (3.40)$$

Imposing the QCD Ward identity for the external gluon on the vector current, i. e.

$$\epsilon_4^\mu \epsilon_3^{*\nu} V_{\mu\nu} \xrightarrow{\epsilon_3 \rightarrow p_3} \epsilon_4^\mu p_3^\nu V_{\mu\nu} = 0, \quad (3.41)$$

yields

$$\begin{aligned}
 0 = & \bar{u}(p_1)\not{p}_3v(p_2)(p_1 \cdot \epsilon_4)\frac{1}{2s}(2C_{19} + zC_{11} + xC_8) + \bar{u}(p_1)\not{p}_3v(p_2)(p_2 \cdot \epsilon_4)\frac{1}{2s}(2C_{20} + zC_{12} + xC_9) \\
 & + \bar{u}(p_1)\not{p}_3v(p_2)(p_3 \cdot \epsilon_4)\frac{1}{2s}(2C_{21} + 2C_{14} + zC_{13} + xC_{10}) + \bar{u}(p_1)v(p_2)(p_1 \cdot \epsilon_4)\frac{m_t}{4s}(2zC_4 + xC_1) \\
 & + \bar{u}(p_1)v(p_2)(p_2 \cdot \epsilon_4)\frac{m_t}{2s}(zC_5 + xC_2) + \bar{u}(p_1)v(p_2)(p_3 \cdot \epsilon_4)\frac{m_t}{2s}(2C_7 + zC_6 + xC_3) \\
 & + \bar{u}(p_1)\not{\epsilon}_4\not{p}_3v(p_2)\frac{m_t}{2s}(2C_{18} + zC_{24} + xC_{23}) + \bar{u}(p_1)\not{\epsilon}_4v(p_2)\frac{1}{2}(zC_{26} + xC_{25}). \tag{3.42}
 \end{aligned}$$

The 8 spinor structures on the right-hand side are linearly independent, which was checked by calculating the rank of the corresponding  $(S^+ \circ S)$  matrix, and their coefficients must hence vanish. The resulting 8 equations reduce the number of spinor structures to 18.

Relabelling and adjusting the spinor structures yields

$$\begin{aligned}
 S_1 &= \frac{2}{s^2}\bar{u}(p_1)\left(\not{p}_3(p_1 \cdot \epsilon_3^*) - \frac{sx}{2}\not{\epsilon}_3^*\right)v(p_2)(p_1 \cdot \epsilon_4), \\
 S_2 &= \frac{2}{s^2}\bar{u}(p_1)\left(\not{p}_3(p_1 \cdot \epsilon_3^*) - \frac{sx}{2}\not{\epsilon}_3^*\right)v(p_2)(p_2 \cdot \epsilon_4), \\
 S_3 &= \frac{2}{s^2}\bar{u}(p_1)\left(\not{p}_3(p_2 \cdot \epsilon_3^*) - \frac{sz}{2}\not{\epsilon}_3^*\right)v(p_2)(p_1 \cdot \epsilon_4), \\
 S_4 &= \frac{2}{s^2}\bar{u}(p_1)\left(\not{p}_3(p_2 \cdot \epsilon_3^*) - \frac{sz}{2}\not{\epsilon}_3^*\right)v(p_2)(p_2 \cdot \epsilon_4), \\
 S_5 &= \frac{1}{s}\bar{u}(p_1)\left(\not{p}_3(\epsilon_3^* \cdot \epsilon_4) - \not{\epsilon}_3^*(p_3 \cdot \epsilon_4)\right)v(p_2), \\
 S_6 &= \frac{m_t}{s^2}\bar{u}(p_1)\not{\epsilon}_3^*\not{p}_3v(p_2)(p_1 \cdot \epsilon_4), \\
 S_7 &= \frac{m_t}{s^2}\bar{u}(p_1)\not{\epsilon}_3^*\not{p}_3v(p_2)(p_2 \cdot \epsilon_4), \\
 S_8 &= \frac{2m_t}{s^2}\bar{u}(p_1)\left(\not{\epsilon}_4\not{p}_3(p_1 \cdot \epsilon_3^*) - \frac{sx}{2}\not{\epsilon}_4\not{\epsilon}_3^*\right)v(p_2), \\
 S_9 &= 2\frac{m_t}{s^2}\bar{u}(p_1)\left(\not{\epsilon}_4\not{p}_3(p_2 \cdot \epsilon_3^*) - \frac{sz}{2}\not{\epsilon}_4\not{\epsilon}_3^*\right)v(p_2), \\
 S_{10} &= \frac{1}{s}\bar{u}(p_1)\not{\epsilon}_4\not{\epsilon}_3^*\not{p}_3v(p_2), \\
 S_{11} &= \frac{1}{s}\bar{u}(p_1)\left(\not{\epsilon}_4(p_1 \cdot \epsilon_3^*)z - \not{\epsilon}_4(p_2 \cdot \epsilon_3^*)x\right)v(p_2), \\
 S_{12} &= \frac{m_t}{s^2}\bar{u}(p_1)v(p_2)\left((p_1 \cdot \epsilon_3^*)z - (p_2 \cdot \epsilon_3^*)x\right)(p_1 \cdot \epsilon_4), \\
 S_{13} &= \frac{m_t}{s^2}\bar{u}(p_1)\not{\epsilon}_3^*\not{p}_3v(p_2)(p_3 \cdot \epsilon_4), \\
 S_{14} &= \frac{1}{s^2}\bar{u}(p_1)\left(\not{p}_3(p_2 \cdot \epsilon_3^*) - \frac{sz}{2}\not{\epsilon}_3^*\right)v(p_2)(p_3 \cdot \epsilon_4), \\
 S_{15} &= \frac{1}{s^2}\bar{u}(p_1)\left(\not{p}_3(p_1 \cdot \epsilon_3^*) - \frac{sx}{2}\not{\epsilon}_3^*\right)v(p_2)(p_3 \cdot \epsilon_4), \\
 S_{16} &= \frac{m_t}{s^2}\bar{u}(p_1)v(p_2)\left((p_1 \cdot \epsilon_3^*)(p_3 \cdot \epsilon_4) - \frac{sx}{2}(\epsilon_3^* \cdot \epsilon_4)\right), \\
 S_{17} &= \frac{m_t}{s^2}\bar{u}(p_1)v(p_2)\left((p_2 \cdot \epsilon_3^*)(p_3 \cdot \epsilon_4) - \frac{sz}{2}(\epsilon_3^* \cdot \epsilon_4)\right), \\
 S_{18} &= \frac{m_t}{s^2}\bar{u}(p_1)v(p_2)\left((p_1 \cdot \epsilon_3^*)z - (p_2 \cdot \epsilon_3^*)x\right)(p_2 \cdot \epsilon_4). \tag{3.43}
 \end{aligned}$$

The spinor structures were rescaled to have mass dimension zero.

### 3. Projection procedure

All 18 spinor structures are independent when performing the helicity sums in the projection in  $d = 4 - 2\epsilon$  dimensions while only 16 structures remain independent in  $d = 4$  dimensions.

The spinor structures  $\{\tilde{S}_i\}$  for the axial-vector current are obtained in the same way as the structures  $\{S_i\}$  for the vector current. The axial-vector current structures are stated in app. A.4. They are essentially the same structures as in eq. (3.43) with a  $\gamma^5$  matrix inserted at the most left possible position. The projection procedure also remains the same except for the treatment of  $\gamma^5$ .

Dimensional regularization does not preserve chiral invariance. Consequently, it is not possible to define a  $d$ -dimensional Clifford algebra with an anticommuting  $\gamma^5$  and a cyclic trace. This issue, known as the  $\gamma^5$  problem, has received a lot of attention and different approaches for its treatment have emerged as a result [209, 211–217].

For instance, in the 't Hooft-Veltman [209] or Breitenlohner-Maison scheme [211, 212], the cyclicity of the trace is preserved and the anticommutativity of  $\gamma^5$  is given up. This leads to a violation of Ward identities, which are restored by introducing counterterms, as described in ref. [215].

In other schemes, e. g. the scheme described in ref. [213, 214], the anticommuting property is imposed and cyclicity of the trace is sacrificed. The position of Dirac matrices in non-cyclic traces originating from closed fermion loops is ambiguous, which is resolved with a reading point prescription.

For the calculation at hand, the so-called naive dimensional regularization (NDR) scheme [216, 218, 219] is adopted, in which an anticommuting  $\gamma^5$  and a cyclic trace are used. The NDR scheme can be applied under certain conditions despite being algebraically inconsistent. In particular, closed fermion lines with an even number of  $\gamma^5$  matrices can be calculated in NDR [185]. This scheme can be applied in this work since closed fermion lines involving one  $\gamma^5$  do not contribute to the leading-colour amplitude. Only traces with two  $\gamma^5$  matrices occur when applying the projectors derived from the spinor structures  $\{\tilde{S}_i\}$  to the leading-colour axial-vector current. The two  $\gamma^5$  are anticommutated to each other and resolved with  $(\gamma^5)^2 = 1$ . This is also a trivial special case of the anticommuting scheme defined in ref. [213, 214].

## 3.5. Electroweak Ward identities

In addition to the QCD Ward identity, there are also electroweak Ward identities. For the subprocess involving the photon, the QED Ward identity is

$$p_4^\mu \Gamma_\mu^\gamma(p_4) = 0, \quad (3.44)$$

where  $\Gamma_\mu^\gamma(p_4)$  is the one-particle-irreducible vertex function of a photon with external momentum  $p_4$ . Consequently, the vector current  $V^\mu$  must vanish when  $\epsilon_4$  is replaced with  $p_4$ , i. e.

$$\epsilon_{4\mu} V^\mu \xrightarrow{\epsilon_4 \rightarrow p_4} p_{4\mu} V^\mu = 0. \quad (3.45)$$

Replacing  $\epsilon_4$  with  $p_4$  in the spinor structures given in eq. (3.43) results in a term containing the 6 spinor structures

$$\begin{aligned} \bar{u}(p_1) \not{p}_3 \not{\epsilon}_3^* v(p_2), & \quad \bar{u}(p_1) \not{p}_3 v(p_2) (p_1 \cdot \epsilon_3^*), & \quad \bar{u}(p_1) \not{p}_3 v(p_2) (p_2 \cdot \epsilon_3^*), \\ \bar{u}(p_1) \not{\epsilon}_3^* v(p_2), & \quad \bar{u}(p_1) v(p_2) (p_1 \cdot \epsilon_3^*), & \quad \bar{u}(p_1) v(p_2) (p_2 \cdot \epsilon_3^*), \end{aligned} \quad (3.46)$$

which are not independent. The four reduced structures

$$\begin{aligned} S_1^W &= \frac{1}{s} \bar{u}(p_1) v(p_2) (p_1 \cdot \epsilon_3^*), & S_2^W &= \frac{m_t}{s} \bar{u}(p_1) \not{\epsilon}_3^* v(p_2), \\ S_3^W &= \frac{m_t}{s^2} \bar{u}(p_1) \not{p}_3 v(p_2) (p_1 \cdot \epsilon_3^*), & S_4^W &= \frac{1}{s} \bar{u}(p_1) \not{p}_3 \not{\epsilon}_3^* v(p_2) \end{aligned} \quad (3.47)$$

are linearly independent. Hence, the four corresponding coefficients must vanish when applying the associated projectors on  $p_{4\mu} V^\mu = 0$ . This gives the four relations

$$\begin{aligned} 0 &= W_1 = \frac{m_t}{2} (x+z) (-4C_8 + C_{12}(z-1) + C_{16}(x-1) + C_{17} - C_{18}), \\ 0 &= W_2 = -\frac{m_t}{4m} (-2C_1 x(z-1) - 2C_2(x-1)x - 2C_3(z-1)z - 2C_4(x-1)z + 2C_5(x+z) \\ &\quad + 8C_8 m x + 8C_9 m z + 4C_{10} z + C_{14} z(x+z) + C_{15} x(x+z)), \\ 0 &= W_3 = \frac{m_t}{2m} (C_1(2-2z) + C_2(2-2x) + 2C_3(z-1) + 2C_4(x-1) + 8C_8 m - 8C_9 m - 4C_{10} \\ &\quad + 2C_{11}(x+z) + C_{14}(-x-z) + C_{15}(x+z)), \\ 0 &= W_4 = -\frac{m_t}{2} (C_6(1-z) + C_7(1-x) + 2C_8 x + 2C_9 z + C_{13}(x+z)), \end{aligned} \quad (3.48)$$

where the right-hand side of the equation is denoted with  $W_i$ . Hence, the 4 equations reduce the number of linearly independent structures to 14 in  $d$  dimensions and to 12 in 4 dimensions. This agrees with the number of independent helicity configurations for this process.

In this work, the above outlined projection procedure is applied in  $d$  dimensions using all 18 structures, i.e. the electroweak Ward identity is not imposed at the level of spinor structures. The four equations given in eq. (3.48) serve as a non-trivial cross-check of the projection coefficients.

A slightly more complicated Ward identity also holds for the axial-vector current although  $p_{4\mu} A_t^\mu$  does not vanish but rather is proportional to the corresponding Goldstone current  $A_t^{\text{Goldstone}}$ . The Goldstone current is defined similarly to the vector and axial-vector currents in eq. (2.9). The amplitude of the process  $e^+ e^- \rightarrow \varphi_Z \rightarrow t \bar{t} g$ , i.e. the process where the  $Z$  boson is replaced with Goldstone boson  $\varphi_Z$ , is defined as

$$\mathcal{M}_{\varphi_Z} = -\pi \alpha_e (-ig_s) t_{t\bar{t}}^g \frac{1}{\sin^2 \theta_w \cos^2 \theta_w} \cdot \frac{i}{s - m_Z^2} \cdot \frac{m_e}{m_Z} \cdot \bar{u}(p_b) \gamma^5 u(p_a) \cdot \frac{m_t}{m_Z} A_t^{\text{Goldstone}}. \quad (3.49)$$

Note that this subprocess, strictly speaking, does not contribute to the amplitude since the electron and positron are considered massless. Nevertheless,  $A_t^{\text{Goldstone}}$  is necessary to check the Ward identity for the axial-vector current  $A_t^\mu$ . The Ward identity is in general given by [220, 221]

$$p_4^\mu \Gamma_\mu^Z(p_4) = m_Z \Gamma_\mu^{\varphi_Z}(p_4), \quad (3.50)$$

where  $\Gamma_\mu^Z(p_4)$  and  $\Gamma_\mu^{\varphi_Z}(p_4)$  are the one-particle-irreducible vertex functions for the  $Z$  boson and the Goldstone boson with external momentum  $p_4$ . The Ward identity for the axial-vector current then assumes the form

$$\epsilon_{4\mu} A_t^\mu \xrightarrow{\epsilon_4 \rightarrow p_4} p_{4\mu} A_t^\mu = -\frac{1}{2} A_t^{\text{Goldstone}}. \quad (3.51)$$

### 3. Projection procedure

The Goldstone current has the four independent spinor structures

$$\begin{aligned} S_1^{\text{Goldstone}} &= \frac{1}{s} \bar{u}(p_1) \gamma^5 v(p_2) (p_1 \cdot \epsilon_3^*), & S_2^{\text{Goldstone}} &= \frac{m_t}{s} \bar{u}(p_1) \gamma^5 \not{\epsilon}_3^* v(p_2), \\ S_3^{\text{Goldstone}} &= \frac{m_t}{s^2} \bar{u}(p_1) \gamma^5 \not{p}_3 v(p_2) (p_1 \cdot \epsilon_3^*), & S_4^{\text{Goldstone}} &= \frac{1}{s} \bar{u}(p_1) \gamma^5 \not{p}_3 \not{\epsilon}_3^* v(p_2), \end{aligned} \quad (3.52)$$

for which corresponding projectors are defined. Note that these structures correspond to the reduced structures for the vector current in eq. (3.47) with an inserted  $\gamma^5$  matrix. Applying the four projectors on the right-hand side of eq. (3.51) yields the four equations

$$\begin{aligned} C_1^{\text{Goldstone}} &= (x+z)(4\tilde{C}_{11} + \tilde{C}_{12}(z-1) + \tilde{C}_{16}(x-1) + \tilde{C}_{17} - \tilde{C}_{18} - 4\tilde{C}_8) = \tilde{W}_1, \\ C_2^{\text{Goldstone}} &= \frac{1}{2m} (2\tilde{C}_1 x(1-z) + 2\tilde{C}_2(1-x)x + 2\tilde{C}_3 z(1-z) + 2\tilde{C}_4(1-x)z \\ &\quad + 2\tilde{C}_5(x+z) + 4\tilde{C}_{10}z + \tilde{C}_{14}(x+z)z + \tilde{C}_{15}x(x+z)) = \tilde{W}_2, \\ C_3^{\text{Goldstone}} &= \frac{1}{m} (2\tilde{C}_1(z-1) + 2\tilde{C}_2(x-1) + 2\tilde{C}_3(1-z) + 2\tilde{C}_4(1-x) + 4\tilde{C}_{10} \\ &\quad - 2\tilde{C}_{11}(x+z) + \tilde{C}_{14}(x+z) - \tilde{C}_{15}(x+z)) = \tilde{W}_3, \\ C_4^{\text{Goldstone}} &= (\tilde{C}_6(1-z) + \tilde{C}_7(1-x) + 2\tilde{C}_8x + 2\tilde{C}_9z - 4\tilde{C}_{10} + \tilde{C}_{13}(x+z)) = \tilde{W}_4. \end{aligned} \quad (3.53)$$

The right-hand side of these equations, i. e. the linear combination of the projection coefficients, is denoted by  $\tilde{W}_i$ .

Instead of obtaining relations for the coefficients from the Ward identities, it is also possible to construct spinor structures that obey the Ward identities and then to remove the irrelevant structures. In the case of the vector current, redundant coefficients can be removed by using the relations from eq. (3.48) and substituting, for example, the coefficients  $C_5$ ,  $C_{11}$ ,  $C_{13}$ , and  $C_{18}$ . This gives the 14 structures

$$\begin{aligned} S'_1 &= S_{17} + S_{18}, & S'_2 &= S_{16} - (1-x)S_{18}, \\ S'_3 &= \frac{1}{2}(2S_{15} - S_{11} - S_5), & S'_4 &= S_{12} - (1-z)S_{18}, \\ S'_5 &= \frac{1}{2}(S_{11} + 2S_{14} - S_5z), & S'_6 &= S_7 - S_{13} \frac{1-x}{x+z}, \\ S'_7 &= S_8 - 4S_{18} - \frac{2S_{13}x - 4m(S_{11} + S_5x)}{x+z}, & S'_8 &= S_6 - S_{13} \frac{1-z}{x+z}, \\ S'_9 &= S_1 - \frac{(S_{11} + xS_5)(1-z)}{x+z}, & S'_{10} &= S_{10} + 2 \frac{S_{11} - zS_5}{x+z}, \\ S'_{11} &= S_2 - \frac{(S_{11} + xS_5)(1-x)}{x+z}, & S'_{12} &= S_3 + \frac{(S_{11} - zS_5)(1-z)}{x+z}, \\ S'_{13} &= S_4 + \frac{(S_{11} - zS_5)(1-x)}{x+z}, & S'_{14} &= S_9 + 2 \frac{2m(S_{11} - S_5z) - S_{13}z}{x+z}. \end{aligned} \quad (3.54)$$

Each of these structures satisfies the Ward identity individually. Two superfluous structures can be removed if the remaining tensor structures span the entire tensor space of the amplitude. Applying the transformation defined in ref. [207] to the 14 structures in eq. (3.54), i. e.

$$\begin{aligned} \bar{S}_i &= S'_i, & i &= 1, \dots, 12, \\ \bar{S}_i &= S'_i - \sum_{j=1}^{12} (\mathcal{P}_j^{12 \times 12} \circ S'_i) \cdot S'_j, & i &= 13, 14, \end{aligned} \quad (3.55)$$



removes the contributions of the first 12 structures from  $S_{13}$  and  $S_{14}$ . The matrix

$$(\bar{S}^+ \circ \bar{S}) = \begin{pmatrix} (\bar{S}^+ \circ \bar{S})^{12 \times 12} & 0 \\ 0 & (\bar{S}^+ \circ \bar{S})^{2 \times 2} \end{pmatrix} \quad (3.56)$$

acquires a block structure as a result. In this formula,  $(\bar{S}^+ \circ \bar{S})^{12 \times 12}$  denotes the corresponding matrix constructed from the first 12 structures and  $(\bar{S}^+ \circ \bar{S})^{2 \times 2}$  denotes the corresponding matrix constructed from the remaining two structures. Correspondingly, the projectors

$$\mathcal{P}_i^{12 \times 12} = \sum_{j=1}^{12} \left( (\bar{S}^+ \circ \bar{S})^{12 \times 12} \right)_{ij}^{-1} \bar{S}_j \quad (3.57)$$

are constructed using only the first 12 independent spinor structures. Both block matrices can be inverted individually in  $d$  dimensions. Furthermore, the matrix  $(\bar{S}^+ \circ \bar{S})^{2 \times 2}$  vanishes for  $d = 4$  dimensions since both  $(\bar{S}^+ \circ \bar{S})$  and  $(\bar{S}^+ \circ \bar{S})^{12 \times 12}$  have rank 12 in 4 dimensions. The contributions from  $\bar{S}_{13}$  and  $\bar{S}_{14}$  are hence in  $d$  dimensions of order  $\epsilon$ . The projection involving only the first 12 spinor structures in  $d$  dimensions gives consequently the full result up to terms of order  $\epsilon$ .



## 4. Evaluation of the master integrals

### 4.1. Introduction

In the following chapter, the calculation of the leading-colour two-loop master integrals is presented. The master integrals are computed by numerically solving differential equations (DE). The high-precision initial conditions that are needed for the numerical DE solution are calculated in sec. 4.2 by expanding the integrals asymptotically around small  $m$  values. Subsequently, the physical  $m$  value is restored in sec. 4.3 by numerically solving the DE in  $m$ . The integrals are calculated for phase space points on a grid in  $x$  and  $z$  by numerically solving the respective DEs. Results for phase space points between grid points are obtained by interpolation. The remainder of this introduction is dedicated to the master integrals.

The leading-colour two-loop amplitude requires the calculation of the 90 master integrals which are collected in tab. B.1 in app. B.1. All 90 master integrals are  $(6 - 2\epsilon)$ -dimensional and belong to one of the four integral families defined in tab. 4.1. Only the Feynman integrals of the double-box integral family and the ‘crossed’ double-box integral family contain genuine two-loop integrals. Furthermore, both double-box integral families are related by exchanging  $p_1$  and  $p_2$ , as already indicated by the name of the second family. Hence, it is sufficient to calculate only the master integrals of one double-box family and reconstruct the ‘crossed’ master integrals by evaluating the integrals at the corresponding phase space point.

The double-box topology is depicted in fig 4.1. In this figure, massive propagators are indicated with bold lines and the momenta of all propagators are explicitly stated. The shown propagators correspond to the propagators  $P_1, \dots, P_7$  given in tab. 4.1. The two auxiliary propagators  $P_8$

**Table 4.1.:** Integral families for the leading-colour two-loop amplitude.

<b>double-box integral family</b>		
$P_1 = k_1^2 - m_t^2$	$P_2 = k_2^2$	$P_3 = (k_2 + p_1)^2 - m_t^2$
$P_4 = (k_1 - p_1 - p_2 - p_3)^2 - m_t^2$	$P_5 = (k_1 + k_2 - p_2 - p_3)^2$	$P_6 = (k_1 - p_2)^2$
$P_7 = (k_2 - p_3)^2$	$P_8 = (k_2 - p_2)^2 - m_t^2$	$P_9 = (k_1 - p_3)^2 - m_t^2$
<b>‘crossed’ double-box integral family</b>		
$P_1 = k_1^2 - m_t^2$	$P_2 = k_2^2$	$P_3 = (k_2 + p_2)^2 - m_t^2$
$P_4 = (k_1 - p_1 - p_2 - p_3)^2 - m_t^2$	$P_5 = (k_1 + k_2 - p_1 - p_3)^2$	$P_6 = (k_1 - p_1)^2$
$P_7 = (k_2 - p_3)^2$	$P_8 = (k_2 - p_1)^2 - m_t^2$	$P_9 = (k_1 - p_3)^2 - m_t^2$
<b>auxiliary family 1</b>		
$P_1 = k_1$	$P_2 = k_2^2 - m_t^2$	$P_3 = (k_1 + p_2)^2 - m_t^2$
$P_4 = (k_1 - p_1 - p_3)^2 - m_t^2$	$P_5 = (k_1 - k_2 + p_2)^2$	$P_6 = (k_2 - p_1 - p_2 - p_3)^2 - m_t^2$
$P_7 = (k_1 - p_3)^2$	$P_8 = (k_2 - p_2)^2$	$P_9 = (k_2 - p_3)^2$
<b>auxiliary family 2</b>		
$P_1 = k_1^2 - m_t^2$	$P_2 = k_2 - m_t^2$	$P_3 = (k_1 + p_3)^2 - m_t^2$
$P_4 = (k_1 - p_1 - p_2)^2 - m_t^2$	$P_5 = (k_1 - k_2 + p_3)^2$	$P_6 = (k_2 - p_1 - p_2 - p_3)^2 - m_t^2$
$P_7 = (k_2 - p_3)^2$	$P_8 = (k_1 - p_1)^2$	$P_9 = (k_1 - k_2 - p_2)^2$

#### 4. Evaluation of the master integrals

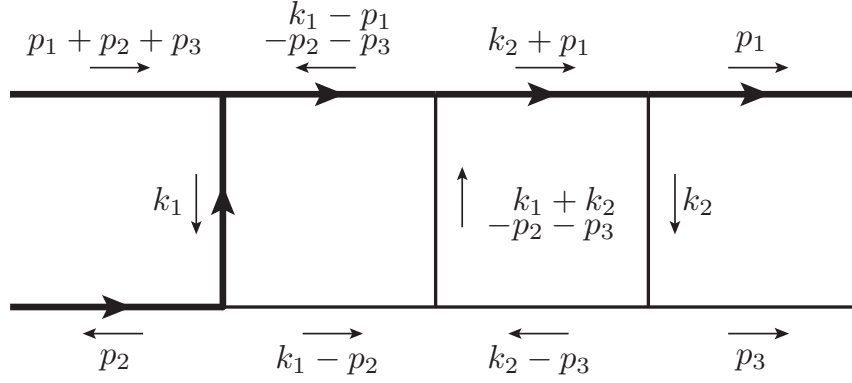


**Figure 4.1.:** Double-box topology with explicitly stated propagator momenta. Bold lines indicate massive propagators.

and  $P_9$  are necessary for the IBP reduction and the tensor reduction. The 54 master integrals of this integral family are depicted in fig. 4.2. Bold lines indicate again massive propagators and each dot on a propagator line indicates an increase of the corresponding propagator exponent by one. For example, one dot means that the corresponding propagator has the exponent  $n_i = 2$ . In addition, two auxiliary integral families are defined. The five associated master integrals are only products of two one-loop integrals as can be seen in fig. 4.3. Some master integrals depicted in fig. 4.2 and fig. 4.3 seem to appear more than once. The respective integrals have different kinematics and are hence regarded as different integrals.

The double-box integrals of sector 127 are presumably not expressible with MPLs alone and require elliptic generalizations of MPLs. Note that, for example, the sunrise Feynman integrals with two massive propagators belonging to sector 21 can be expressed with logarithms and dilogarithms [222].

The discussion in this chapter focuses on the calculation of the 54 master integrals of the double-box integral family. These master integrals are, by explicit choice, independent of the auxiliary propagators. Hence, the notation of Feynman integrals introduced in sec. 2.4.1 is, in this chapter, shortened to

$$I_{n_1, n_2, n_3, n_4, n_5, n_6, n_7} = I_{n_1, n_2, n_3, n_4, n_5, n_6, n_7, 0, 0}^{(6-2\epsilon)}, \quad (4.1)$$

i. e. only the first 7 propagator exponents are stated and the remaining two auxiliary propagator exponents are suppressed. Moreover, the space-time dimension is also suppressed and always assumed to be  $d = 6 - 2\epsilon$  unless specifically stated otherwise. All integrals in this notation belong to the double-box integral family and  $\vec{I}$  denotes the vector of all 54 master integrals of the double-box integral family. The integrals of the ‘crossed’ double-box integral family are similarly denoted with  $I_{n_1, \dots, n_7}^c$  and integrals of the two auxiliary integral families are denoted with  $I_{n_1, \dots, n_9}^{a1}$  and  $I_{n_1, \dots, n_9}^{a2}$ .

The leading-colour master integrals in tab. B.1 are quasi-finite Feynman integrals, which were determined with the help of **Reduze2** [102]. The general motivation for quasi-finite bases is explained in sec. 2.4.5. The master integrals in tab. B.1 are chosen to be in  $d = 6 - 2\epsilon$  dimensions and many integrals acquire rather high propagator exponents. Other choices of quasi-finite integrals are of course possible. The integral basis could, for example, also contain integrals in  $6 - 2\epsilon$  and in  $8 - 2\epsilon$  dimensions. The integrals in tab. B.1 were explicitly chosen to avoid multiple dimensionalities for simpler bookkeeping. Moreover, all master integrals in tab. B.1 are finite.

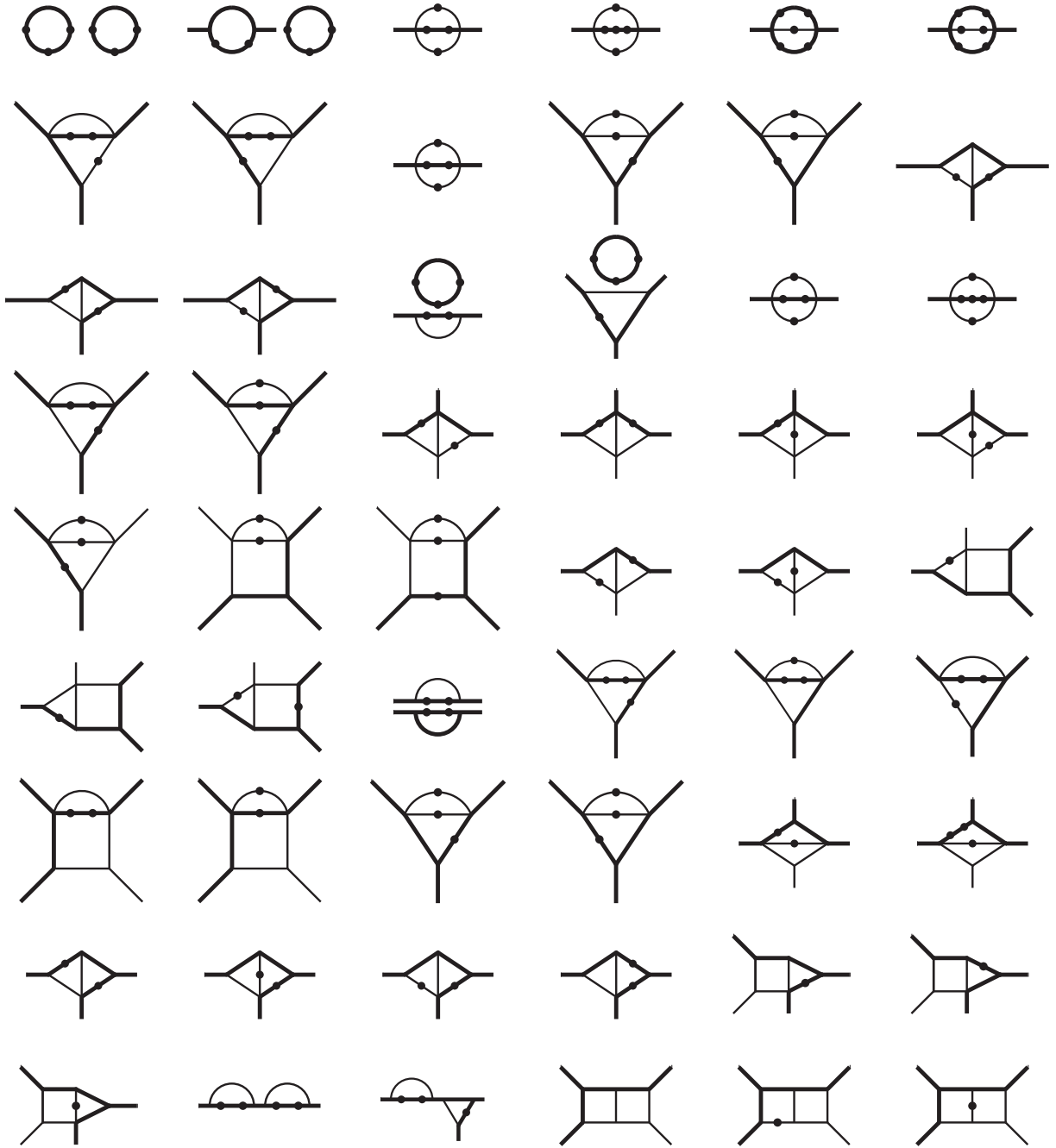


**Figure 4.2.:** The 54 master integrals of the double-box integral family. Bold lines indicate massive propagators and each dot on a propagator line indicates an increase of the corresponding exponent by one.



**Figure 4.3.:** The five master integrals of the two auxiliary integral families.

#### 4. Evaluation of the master integrals

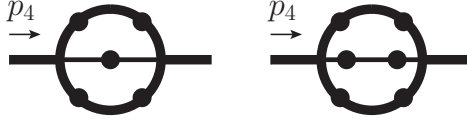


**Figure 4.4.:** The two-loop sunrise integrals with two massive propagators of sector 21. The incoming momentum is  $p_4 = p_1 + p_2 + p_3$ .

Consider the two integrals of sector 21 as a simple example of a quasi-finite basis. This sector corresponds to a two-loop sunrise topology with one massless and two massive propagators as depicted in fig. 4.4. Both integrals only depend on the variables  $s$  and  $m$ .

The master integrals for this sector also have to include the two-loop tadpole integral for the IBP reduction and the dimension-shift transformation. A possible choice of master integrals is

$$I_{1,0,1,0,0,0,0}^{(4-2\epsilon)}, \quad I_{1,0,1,0,1,0,0}^{(4-2\epsilon)}, \quad I_{1,0,1,0,2,0,0}^{(4-2\epsilon)}, \quad (4.2)$$

which, however, have  $\epsilon^{-2}$  poles in  $d = 4 - 2\epsilon$  dimensions. Alternatively, the  $(6 - 2\epsilon)$ -dimensional quasi-finite integrals

$$I_{4,0,4,0,0,0,0}^{(6-2\epsilon)}, \quad I_{3,0,3,0,1,0,0}^{(6-2\epsilon)}, \quad I_{3,0,3,0,2,0,0}^{(6-2\epsilon)} \quad (4.3)$$

can be chosen as master integrals. When expressing the original  $(4 - 2\epsilon)$ -dimensional master integrals with the quasi-finite master integrals,  $\epsilon^{-2}$  poles appear in the IBP reduction and  $\epsilon^{-1}$  poles appear when transforming the  $(4 - 2\epsilon)$ -dimensional basis to the  $(6 - 2\epsilon)$ -dimensional basis. Expressing the integrals in eq. (4.2) with the quasi-finite integrals yields

$$\begin{aligned} I_{1,0,1,0,0,0,0}^{(4-2\epsilon)} &= I_{4,0,4,0,0,0,0}^{(6-2\epsilon)} \left( \frac{36m^4}{\epsilon^2} + \frac{72m^4}{\epsilon} + 108m^4 + \mathcal{O}(\epsilon) \right), \\ I_{1,0,1,0,1,0,0}^{(4-2\epsilon)} &= I_{4,0,4,0,0,0,0}^{(6-2\epsilon)} \left( \frac{36m^3}{\epsilon^2} + \frac{108m^3 - 9m^2}{\epsilon} + 252m^3 - \frac{9m^2}{2} - 9m + \mathcal{O}(\epsilon) \right) \\ &\quad + I_{3,0,3,0,1,0,0}^{(6-2\epsilon)} \left( -2m + \frac{1}{2m} - 3 + \mathcal{O}(\epsilon) \right) \\ &\quad + I_{3,0,3,0,2,0,0}^{(6-2\epsilon)} \left( -8m - \frac{1}{2m} + 4 + \mathcal{O}(\epsilon) \right), \\ I_{1,0,1,0,2,0,0}^{(4-2\epsilon)} &= I_{4,0,4,0,0,0,0}^{(6-2\epsilon)} \left( -\frac{18m^2}{\epsilon^2} + \frac{18m^2 - 18m}{\epsilon} - 54m^2 + 90m - 36 + \mathcal{O}(\epsilon) \right) \\ &\quad + I_{3,0,3,0,1,0,0}^{(6-2\epsilon)} \left( -\frac{1}{\epsilon} \frac{4m - 1}{m} + \frac{2}{m^2} - \frac{10}{m} + 14 + \mathcal{O}(\epsilon) \right) \\ &\quad + I_{3,0,3,0,2,0,0}^{(6-2\epsilon)} \left( -\frac{1}{\epsilon} \frac{8m^2 - 6m + 1}{m} - \frac{2}{m^2} + 16m + \frac{14}{m} - 28 + \mathcal{O}(\epsilon) \right). \end{aligned} \quad (4.4)$$

The poles occur as explicit prefactors of the quasi-finite integrals. Additionally, it can be seen in eq. (4.4) that the  $\epsilon^2$  poles, i.e. the strongest poles, only appear in prefactors of the two-loop tadpole integral  $I_{4,0,4,0,0,0,0}^{(6-2\epsilon)}$ . Stronger poles are also for many other master integrals of the double-box topology shifted into the prefactors of ‘simpler’ integrals, i.e. integrals from subtopologies with fewer propagators. In this example, the tadpole integral  $I_{4,0,4,0,0,0,0}^{(6-2\epsilon)}$  has to be calculated up order  $\epsilon^2$  while  $I_{3,0,3,0,1,0,0}^{(6-2\epsilon)}$  and  $I_{3,0,3,0,2,0,0}^{(6-2\epsilon)}$  only need to be computed up to order  $\epsilon$  to obtain the  $(4 - 2\epsilon)$ -dimensional basis up to order  $\epsilon^0$ .

The dimension-shift transformations for the double-box and the auxiliary integral families are constructed as described in sec. 2.4.4. The reverse transformation, i. e.

$$\vec{I}^{(d+2)} = D^{-1} \cdot \vec{I}^{(d)}, \quad (4.5)$$

can be obtained by inverting the corresponding  $54 \times 54$  matrix  $D$  for the double-box topology and a  $13 \times 13$  matrix for the auxiliary integral families using the computer algebra system *Fermat* [208].

## 4.2. Asymptotic expansion

### 4.2.1. Introduction

Since the initial conditions for the numerical DE solver are only required at one phase space point, which additionally can be chosen more or less freely, it is often useful to choose a convenient kinematical limit and exploit the associated simplifications.

For example, for the process at hand it would be very advantageous if it were possible to use the corresponding massless integrals, i. e. the integrals at  $m = 0$ , as initial conditions and then solve the DE system numerically in  $m$  to obtain the integrals at  $m = 289/2500$ . This would simplify the calculation of the initial conditions tremendously as the master integrals of the corresponding massless process are known and are expressible with MPLs [223]. MPLs have been studied extensively in the past and many techniques and tools for computing and evaluating MPLs are available, e. g. see the reviews in ref. [86, 224]. They are hence from a practical point of view much simpler to handle than elliptic integrals. Unfortunately, this choice of initial conditions is not possible due to singularities in the differential equations at  $m = 0$ . The massless and massive integrals also have different pole structures in  $\epsilon$ .

The small-mass limit, i. e. the limit in which  $m_t^2$  is much smaller than all other involved scales, is chosen instead. One major motivation for this choice is the assumption that the relatively simple function space of the corresponding massless integrals might also be sufficient when approximating the master integrals in the small-mass limit. This assumption turned out to be true.

Asymptotically expanding in the small-mass limit yields the general form

$$I(x, z, m) = \sum_{e=e_{\min}}^{e_{\max}} \sum_{i=i_{\min}}^{\infty} \sum_{j=0}^{e+6} C_{e,i,j}(x, z) \epsilon^e m^i \ln^j(m) \quad (4.6)$$

for all Feynman integrals. The  $s$  dependence is suppressed in this formula and also in the following discussion. Note that the sum over  $e$  starts at  $e_{\min} = -4$  for the transformed quasi-finite integrals. The maximal expansion order  $e_{\max}$  is chosen differently for each master integral due to the numerical solution of the DE, as explained in sec. 4.3.2. Also the expansion typically starts at  $i_{\min} = 0$  although there are exceptions to this.

But how does this simplify the task of calculating the Feynman integrals? The original integrals depend on three independent variables:  $x$ ,  $z$ , and  $m$ . After expanding in powers and logarithms of  $m$ , the coefficients  $C_{e,i,j}$  only depend on  $x$  and  $z$  and are simpler to calculate than the original integrals. But this simplification does not come for free as the number of quantities to calculate increases too, i. e. sufficiently many coefficients of the expansion need to be calculated for an adequate approximation of the integral. Moreover, when using the expansion by regions, the contributions of several regions have to be calculated for every Feynman integral. For example, the contributions of 7 regions have to be calculated for the double-box integrals of sector 127.

Very precise values of the integrals are required since the asymptotic expansions of the master

#### 4. Evaluation of the master integrals

integrals will serve as initial conditions for the following numerical DE solution. The asymptotic expansions were hence calculated to high orders in  $m$ .

In the next section, the expansion by regions is applied to calculate the leading terms of the asymptotic expansion. In sec. 4.2.3, higher orders of the asymptotic expansion are computed by applying the differential equation onto the ansatz given in eq. (4.6) and then solving a system of equations. Results of the asymptotic expansion are presented in sec. 4.2.4.

##### 4.2.2. Calculating the leading terms with the expansion by regions

The leading terms of the asymptotic expansion, i. e. in almost all cases terms of order  $m^0$ , are calculated with the expansion by regions employing the programs `asy2.m` [171,172] to determine the regions and `Mathematica` as well as `HyperInt` [197] to perform the remaining integrations. The expansion by regions is applied in a similar fashion as in ref. [225].

The formulation applied here uses Feynman integrals in Schwinger representation. The Schwinger parameters are in the following denoted with  $x_i$ . When expanding the integral in the small-mass limit, i. e.  $m \ll 1$ , the variable  $m$  is rescaled with a parameter  $\chi$ , i. e.

$$m \rightarrow \chi m. \quad (4.7)$$

The parameter  $\chi$ , which formally controls the small-mass limit, is a technical parameter used in the expansion while  $m$  retains its actual but still small value. The regions, which encompass the various soft, collinear and other limits of the integral, are determined with `asy2.m`. Each region  $r$  is in this formulation represented by a vector  $r = (r_1, r_2, \dots, r_n)$ . The contribution of region  $r$  is obtained by applying the scaling

$$m \rightarrow \chi m, \quad x_i \rightarrow \chi^{r_i} x_i \quad (4.8)$$

to the integrand in Schwinger parameterization and subsequently expanding in  $\chi$ . The set of all regions for a specific integral is denoted with  $R$ . Let the contribution of region  $r$  be denoted by  $I^{(r)}$ . The asymptotic expansion  $I_{\text{AE}}$  of an integral is given by the sum over the contributions of all regions of that integral, i. e.

$$I_{\text{AE}} = \sum_{r \in R} I^{(r)}. \quad (4.9)$$

When applying the scaling in eq. (4.8), the  $\mathcal{U}$  and  $\mathcal{F}$  polynomials obtain a  $\chi$  dependence given by

$$\begin{aligned} \mathcal{U}^{(r)} &= \mathcal{U}_0^{(r)} \chi^{k_{\min}} + \mathcal{U}_1^{(r)} \chi^{k_{\min}+1} + \mathcal{O}(\chi^{k_{\min}+2}), \\ \mathcal{F}^{(r)} &= \mathcal{F}_0^{(r)} \chi^{l_{\min}} + \mathcal{F}_1^{(r)} \chi^{l_{\min}+1} + \mathcal{O}(\chi^{l_{\min}+2}), \end{aligned} \quad (4.10)$$

where the minimal orders in  $\chi$  are  $k_{\min}$  and  $l_{\min}$  respectively. The expansion in  $m$  is obtained by expanding the integrand in  $\chi$  around zero, i. e.

$$\begin{aligned} I^{(r)} &= \left( \prod_{i=1}^n \int_0^\infty \frac{dx_i x_i^{n_i-1}}{\Gamma(n_i)} \right) (\mathcal{U}_0^{(r)})^{-d/2} \exp\left(-\frac{\mathcal{F}_0^{(r)}}{\mathcal{U}_0^{(r)}}\right) \times \\ &\quad \times \left( 1 - \chi \left( \frac{\mathcal{F}_1^{(r)}}{\mathcal{U}_0^{(r)}} + \frac{\mathcal{F}_0^{(r)} \mathcal{U}_1^{(r)}}{\mathcal{U}_0^{(r)2}} - \frac{d\mathcal{U}_1^{(r)}}{2\mathcal{U}_0^{(r)}} \right) + \mathcal{O}(\chi^2) \right) \Big|_{\chi=1}. \end{aligned} \quad (4.11)$$



Afterwards, the expansion in  $m$  is obtained by setting the technical parameter  $\chi$  to one. The parameters  $x_i$  are integrated over the whole integration domain.

It is sufficient to calculate the leading terms  $I_0^{(r)}$ , i. e. the order  $\chi^0$  coefficient in eq. (4.11), for all 54 master integrals and the order  $m$  coefficients for three master integrals explicitly with the expansion by regions. The remaining higher-order coefficients are determined from the leading-order coefficients in sec. 4.2.3. The required contributions of the regions were calculated using **Mathematica** and **HyperInt** [197].

In the following paragraphs, the sunrise integral  $I_{3,0,3,0,1,0,0}$  of sector 21 serves as an example to explain the asymptotic expansion with the expansion by regions.

The integrals of the massive sunrise subtopology of sector 21, shown in fig. 4.4, have the Symanzik polynomials

$$\begin{aligned}\mathcal{U} &= x_1x_2 + x_1x_3 + x_2x_3, \\ \mathcal{F} &= -x_1x_2x_3 + m(x_1 + x_2)(x_1x_2 + x_1x_3 + x_2x_3).\end{aligned}\tag{4.12}$$

This sector possesses the four regions

$$h = (0, 0, 0), \quad a = (0, -1, 0), \quad b = (0, 0, 1), \quad c = (0, 1, 1)\tag{4.13}$$

in the limit  $m \rightarrow \chi m$ . The region  $h = (0, 0, 0)$  is called the hard region and the corresponding scaling is

$$m \rightarrow \chi m, \quad x_1 \rightarrow x_1, \quad x_2 \rightarrow x_2, \quad x_3 \rightarrow x_3.\tag{4.14}$$

The scaling for region  $a$  is, for example, given by

$$m \rightarrow \chi m, \quad x_1 \rightarrow x_1, \quad x_2 \rightarrow \chi^{-1}x_2, \quad x_3 \rightarrow x_3\tag{4.15}$$

and the contributions for region  $b$  are obtained from

$$m \rightarrow \chi m, \quad x_1 \rightarrow x_1, \quad x_2 \rightarrow x_2, \quad x_3 \rightarrow \chi x_3.\tag{4.16}$$

Region  $c = (0, 1, 1)$  is used in the following as an example to explain the steps necessary to compute the contributions of the regions. Applying the corresponding scaling

$$m \rightarrow \chi m, \quad x_1 \rightarrow x_1, \quad x_2 \rightarrow \chi x_2, \quad x_3 \rightarrow \chi x_3\tag{4.17}$$

to the Symanzik polynomials in eq. (4.12) yields

$$\begin{aligned}\mathcal{U}^{(c)} &= \chi x_1(x_2 + x_3) + \chi^2 x_2 x_3, \\ \mathcal{F}^{(c)} &= \chi^2 \left( x_1(-x_2 x_3 + m x_1(x_2 + x_3)) + \chi m x_1 x_2(x_2 + 2x_3) + \chi^2 m x_2^2 x_3 \right).\end{aligned}\tag{4.18}$$

The leading terms  $\mathcal{U}_0^{(c)} = x_1(x_2 + x_3)$  and  $\mathcal{F}_0^{(c)} = x_1(-x_2 x_3 + m x_1(x_2 + x_3))$  involve less terms than the original  $\mathcal{U}$  and  $\mathcal{F}$  polynomials. The leading-order contribution of this region is obtained by inserting  $\mathcal{U}_0^{(c)}$  and  $\mathcal{F}_0^{(c)}$  into the first term of eq. (4.11), which gives

$$I_0^{(c)} = -e^{2\gamma_E \epsilon} \int_0^\infty dx_1 \int_0^\infty dx_2 \int_0^\infty dx_3 \frac{1}{4} x_1^2 x_2^2 (x_1(x_2 + x_3))^{-d/2} \exp\left(-m x_1 + \frac{x_2 x_3}{x_2 + x_3}\right).\tag{4.19}$$

In this expression and in the following examples, the factor  $e^{2\gamma_E \epsilon}$  corresponding to the definition

#### 4. Evaluation of the master integrals

in eq. (2.16) is included to obtain more compact results. In the next step,  $x_1$  can be integrated out directly since it factorizes in the  $\mathcal{U}_0^{(c)}$  polynomial, which yields

$$I_0^{(c)} = -e^{2\gamma_E\epsilon} \Gamma\left(3 - \frac{d}{2}\right) m^{\frac{d}{2}-3} \int_0^\infty dx_2 \int_0^\infty dx_3 \frac{1}{4} x_2^2 (x_2 + x_3)^{-\frac{d}{2}} \exp\left(\frac{x_2 x_3}{x_2 + x_3}\right). \quad (4.20)$$

Similar relations were used in ref. [225]. The result depends on  $x_2 + x_3$  and hence the variable transformation

$$\begin{aligned} x_2 &\rightarrow \lambda x_2, & x_3 &\rightarrow \lambda x_3, & x_2 + x_3 &\rightarrow \lambda, \\ \int_0^\infty dx_2 \int_0^\infty dx_3 &\rightarrow \int_0^\infty d\lambda \lambda \int_0^\infty dx_2 \int_0^\infty dx_3 \delta(1 - x_2 - x_3) \end{aligned} \quad (4.21)$$

is applied. This yields the integral

$$I_0^{(c)} = -e^{2\gamma_E\epsilon} (ms)^{\frac{d-6}{2}} \Gamma\left(3 - \frac{d}{2}\right) \int_0^\infty d\lambda \int_0^\infty dx_2 \int_0^\infty dx_3 \delta(1 - x_2 - x_3) \frac{1}{4} x_2^2 \lambda^{3-\frac{d}{2}} e^{s\lambda x_2 x_3}. \quad (4.22)$$

The dependence on the variable  $s$  is restored in this expression to explain the following calculation. The integration over the variable  $\lambda$  in eq. (4.22) does not converge for  $s > 0$ . Assuming  $s < 0$  while keeping  $ms > 0$  and performing the remaining integrations in  $\lambda$ ,  $x_2$ , and  $x_3$  yields

$$\begin{aligned} I_0^{(c)} &= -e^{2\gamma_E\epsilon} (ms)^{\frac{d-6}{2}} \Gamma\left(3 - \frac{d}{2}\right) \Gamma\left(4 - \frac{d}{2}\right) \int_0^\infty dx_2 \int_0^\infty dx_3 \delta(1 - x_2 - x_3) \frac{1}{4} x_2^2 (-sx_2 x_3)^{\frac{d-8}{2}} \\ &= -e^{2\gamma_E\epsilon} \frac{(-s)^{\frac{d}{2}-4} (ms)^{\frac{d}{2}-3} \Gamma\left(3 - \frac{d}{2}\right) \Gamma\left(4 - \frac{d}{2}\right) \Gamma\left(\frac{d}{2} - 3\right) \Gamma\left(\frac{d}{2} - 1\right)}{4\Gamma(d-4)}. \end{aligned} \quad (4.23)$$

This expression is evaluated for  $s > 0$  using analytic continuation. The imaginary part of the occurring logarithms follows from the Feynman prescription, which is restored by introducing an infinitesimal imaginary part for the variable  $s$ , i.e.  $s \rightarrow s + i\epsilon$ . Expanding the result in  $d = 6 - 2\epsilon$  dimensions yields for  $s = 1$

$$\begin{aligned} I_0^{(c)} &= -\frac{1}{4\epsilon^2} - \frac{1 + i\pi - \ln(m)}{4\epsilon} \\ &\quad - \frac{1}{8} \left(4 - \pi(\pi - 2i) - 2(1 + i\pi) \ln(m) + \ln^2(m)\right) + \mathcal{O}(\epsilon). \end{aligned} \quad (4.24)$$

The spurious  $\epsilon$  poles which appear in this result must cancel when the contributions of all regions are added since the original integral is finite. This example highlights several steps for the calculation of the contributions of the regions. If the  $\mathcal{F}_0^{(r)}$  polynomial contains more Schwinger parameters than the  $\mathcal{U}_0^{(r)}$  polynomial or if Schwinger parameters factorize, as in this example  $x_1$  does, it is possible to integrate out Schwinger parameters directly as done in eq. (4.20).

Furthermore, after this first simplification, the variable transformation

$$\begin{aligned} x_i &\rightarrow \lambda x_i, & \sum_{i=1}^N x_i &\rightarrow \lambda, \\ \prod_{i=1}^N \int_0^\infty dx_i &\rightarrow \int_0^\infty d\lambda \lambda^{N-1} \left( \prod_{i=1}^N \int_0^\infty dx_i \right) \delta\left(1 - \sum_{i=1}^N x_i\right). \end{aligned} \quad (4.25)$$

is applied. This is the general form of the transformation given in eq. (4.21). Subsequently the  $\lambda$  dependence is integrated out. Note that this effectively transforms the integrals from Schwinger to Feynman parameterization.

It is possible to perform the integration of the two remaining variables  $x_2$  and  $x_3$  in eq. (4.24) directly with `Mathematica`. For many integrals, this step is more involved. The remaining parameter integrations are hence in most cases performed with `HyperInt`.

Consider, for example, the hard region  $h = (0, 0, 0)$ . Applying the scaling given in eq. (4.14) gives the Symanzik polynomials

$$\begin{aligned}\mathcal{U}^{(h)} &= x_2 x_3 + x_1(x_2 + x_3), \\ \mathcal{F}^{(h)} &= -x_1 x_2 x_3 + \chi m(x_1 + x_2)(x_2 x_3 + x_1(x_2 + x_3)).\end{aligned}\quad (4.26)$$

Inserting those polynomials into eq. (4.11) gives the leading contribution of the hard region, i. e.

$$\begin{aligned}I_0^{(h)} &= -e^{2\gamma_E \epsilon} \int_0^\infty dx_1 \int_0^\infty dx_2 \int_0^\infty dx_3 \frac{1}{4} x_1^2 x_2^2 (x_1(x_2 + x_3) + x_2 x_3)^{-\frac{d}{2}} \times \\ &\quad \times \exp\left(\frac{x_1 x_2 x_3}{x_1(x_2 + x_3) + x_2 x_3}\right).\end{aligned}\quad (4.27)$$

In contrast to region  $c$ , no Schwinger parameter factorizes in  $\mathcal{U}^{(h)} = \mathcal{U}$  and hence no parameter can be integrated out directly. Consequently, the integral is transformed to Feynman parameters using the transformation given in eq. (4.25), which yields

$$\begin{aligned}I_0^{(h)} &= -e^{2\gamma_E \epsilon} \frac{\Gamma(7-d)}{4} \int_0^\infty dx_1 \int_0^\infty dx_2 \int_0^\infty dx_3 \delta(1 - x_1 - x_2 - x_3) x_1^2 x_2^2 (x_1(x_2 + x_3) + x_2 x_3)^{-\frac{d}{2}} \times \\ &\quad \times \left(-\frac{x_1 x_2 x_3}{x_1(x_2 + x_3) + x_2 x_3}\right)^{d-7}.\end{aligned}\quad (4.28)$$

This integral still contains subdivergences that give rise to  $\epsilon$  poles similarly to the contribution of region  $c$  in eq. (4.24). This prevents a direct evaluation with `HyperInt`. `HyperInt` includes the function `findDivergences` to check integrands for subdivergences. The singularities are resolved with partial integrations as described in ref. [226]. `HyperInt` provides the function `dimregPartial` for this task. For instance, the integral in eq. (4.28) can be made finite by applying

```
dimregPartial(integrand,{1/x1}, -eps),
dimregPartial(integrand,{x1,x3}, -eps)
```

to the integrand, which yields

$$\begin{aligned}I_0^{(h)} &= -e^{2\gamma_E \epsilon} \frac{3\Gamma(2\epsilon + 1)(\epsilon - 1)(3\epsilon - 2)}{4\epsilon^2} \times \\ &\quad \times \int_0^\infty dx_1 \int_0^\infty dx_2 \int_0^\infty dx_3 \delta(1 - x_1 - x_2 - x_3) x_1 x_2 (x_1(x_2 + x_3) + x_2 x_3)^{3\epsilon-4} (-x_1 x_2 x_3)^{1-2\epsilon}.\end{aligned}\quad (4.29)$$

#### 4. Evaluation of the master integrals

The integrand can now be expanded in  $\epsilon$  since the subdivergences are resolved, yielding

$$I_0^{(h)} = -e^{2\gamma_E\epsilon} \int_0^\infty dx_1 \int_0^\infty dx_2 \int_0^\infty dx_3 \delta(1-x_1-x_2-x_3) \frac{x_1^2 x_2^2 x_3}{(x_1(x_2+x_3)+x_2x_3)^4} \left( -\frac{3}{2\epsilon^2} + \frac{3}{4\epsilon} (4\ln(-x_1x_2x_3) - 6\ln(x_1(x_2+x_3)+x_2x_3) + 5) \right) + \mathcal{O}(\epsilon^0). \quad (4.30)$$

The Wu-Cheng theorem [159, 227] allows to change the argument of the  $\delta$  function to the sum of any subset of the variables  $x_i$  while the remaining Feynman parameters are integrated from 0 to  $\infty$ . This can be used to integrate out the  $x_1$  dependence in eq. (4.30) by substituting

$$\delta(1-x_1-x_2-x_3) \rightarrow \delta(1-x_1) \quad (4.31)$$

and then setting  $x_1 = 1$ .

Performing the remaining integrations in  $x_2$  and  $x_3$  with **HyperInt** yields the result

$$I_0^{(h)} = \frac{1}{4\epsilon^2} + \frac{1+i\pi}{2\epsilon} + \frac{1}{24} (36 + 24i\pi - 13\pi^2) + \mathcal{O}(\epsilon). \quad (4.32)$$

The contributions of the remaining regions can be calculated in the same way. The corresponding contributions are

$$I_0^{(a)} = -\frac{1}{4\epsilon^2} - \frac{1+i\pi - \ln(m)}{4\epsilon} - \frac{1}{8} (4 - \pi(\pi - 2i) - 2(1+i\pi)\ln(m) + \ln^2(m)) + \mathcal{O}(\epsilon),$$

$$I_0^{(b)} = \frac{1}{4}\Gamma\left(3 - \frac{d}{2}\right)^2 m^{d-6} = \frac{1}{4\epsilon^2} - \frac{\ln(m)}{2\epsilon} + \frac{1}{2}\ln^2(m) + \frac{\pi^2}{24} + \mathcal{O}(\epsilon). \quad (4.33)$$

The sum over all contributions from all four regions yields the leading term of the asymptotic expansion, which for this integral is

$$I_{\text{AE},0} = I_0^{(h)} + I_0^{(a)} + I_0^{(b)} + I_0^{(c)} = \frac{1}{4} (2 + 2i\pi - \pi^2 + 2(1+i\pi)\ln(m) + \ln^2(m)) + \mathcal{O}(\epsilon). \quad (4.34)$$

The spurious poles cancel in the final result as expected.

In summary, the expansion by regions is performed in this work by applying the following steps for each integral:

- determine the regions with **asy2.m**,
- for each region:
  - apply the  $\chi$  scalings to the  $\mathcal{U}$  and  $\mathcal{F}$  polynomials,
  - expand the integrand in  $\chi$  up to the required expansion order,
  - integrate over Schwinger parameters:
    - \* integrate out factorizing Schwinger parameters,
    - \* transform from Schwinger to Feynman parameterization with eq. (4.25),
    - \* resolve spurious singularities by applying partial integrations,
    - \* expand in  $\epsilon$ ,
    - \* integrate over all remaining Feynman parameters using **HyperInt**,
- sum over contributions from all regions.

The resolution of the singularities and the final Feynman parameter integration with **HyperInt** remain as non-trivial problems.

Several comments on this calculation:

- As already mentioned, the contributions from the relevant regions will in general contain spurious  $\epsilon$  poles, i.e. poles of higher  $\epsilon$  order than the original integral. These spurious

poles cancel after summation over all regions and the expansion has the pole structure of the original integral. This provides a non-trivial test of this calculation.

- It is possible that dimensional regularization is not sufficient to regulate all spurious singularities when applying the expansion by regions. This problem is typically solved by introducing ‘analytic regulators’ [158, 225, 228, 229], where the integer exponents of propagators are replaced by a complex number. In other words, a propagator  $P$  with exponent  $n$  is analytically regulated by adding to the exponent the regulator  $\eta$  as

$$\frac{1}{P^n} \rightarrow \frac{1}{P^{n+\eta}}. \quad (4.35)$$

The regulator must be introduced consistently in the contributions of all regions of an integral. After expanding in the analytic regulator  $\eta$ , the spurious singularities manifest themselves as poles in  $\eta$ . These poles cancel when summing over all regions. Then the limit  $\eta \rightarrow 0$  can be taken.

The calculations presented in this work did not require analytic regulators and hence were performed without.

- The leading-order contribution of the hard region  $h = (0, 0, \dots, 0)$  in the small-mass limit is given by the corresponding massless integral.
- Higher orders of the asymptotic expansion can be calculated by expanding the integrand in eq. (4.11) to higher orders in  $\chi$ . Each new order will be in general more difficult to calculate due to the proliferation of terms in the integrand.
- The sum of the contributions of all regions gives the asymptotic expansion. However, not every region necessarily contributes to the leading order of the asymptotic expansion. I.e. the lowest-order term of the expansion in eq. (4.11) can contribute to higher order terms in the  $m$  expansion.

The above described procedure was used to calculate the leading-order expansions of all 54 master integrals of the double-box topology as well as the 5 remaining integrals of two auxiliary integral families. The details of these calculations are not shown here since they are very lengthy and essentially only repeat the demonstrated steps. Analytic results are also too large to be shown here. Numerical results and a summary of technical details are given in app. B.2.

The systematic determination of higher-order expansions in sec. 4.2.3 requires in addition to the leading-order coefficients also coefficients of order  $m$  of the master integrals  $I_{2,2,1,1,1,0,0}$ ,  $I_{1,1,2,1,1,1,0}$ , and  $I_{2,0,1,1,2,0,1}$ , corresponding to the 12th, 31st, and 44th master integrals in tab. 4.1. This choice is not unique and it is also possible to use the coefficients of order  $m$  of the 26th, 42nd, and 47th master integrals instead.

Almost all contributions to the higher-order coefficients were also calculated as described above except for the hard region of master integral  $I_{1,1,2,1,1,1,0}$ . In this case, the contributions of the hard region were expressed by massless integrals, which were then reduced to the corresponding massless master integrals. The higher-order contributions are obtained by expanding the integrand in eq. (4.11) to higher orders in  $\chi$ . This gives rise to terms containing  $\mathcal{U}_0^{-1}$ , which is interpreted as  $\mathbf{D}_+$  operator, and other terms composed of  $x_i$  parameters, which are interpreted as  $\mathbf{i}^+$  operators. Applying the operators yields massless integrals with increased exponents and increased space-time dimension, which are then reduced to master integrals of the massless topology.

The hard region of master integral  $I_{1,1,2,1,1,1,0}$  in  $6 - 2\epsilon$  dimensions can be reduced to the 7

#### 4. Evaluation of the master integrals

massless quasi-finite master integrals

$$\begin{aligned} \tilde{I}_{0,0,3,0,2,2,0}^{(8-2\epsilon)}, \quad \tilde{I}_{0,2,0,2,2,1,0}^{(8-2\epsilon)}, \quad \tilde{I}_{1,2,0,1,2,1,0}^{(8-2\epsilon)}, \quad \tilde{I}_{2,2,0,1,2,0,0}^{(8-2\epsilon)}, \\ \tilde{I}_{2,2,1,0,1,1,0}^{(8-2\epsilon)}, \quad \tilde{I}_{3,0,3,0,1,0,0}^{(8-2\epsilon)}, \quad \tilde{I}_{3,2,0,0,2,0,0}^{(8-2\epsilon)} \end{aligned} \quad (4.36)$$

in  $8-2\epsilon$  dimensions. Here,  $\tilde{I}$  denotes integrals of the corresponding massless double-box integral family. These massless integrals are then calculated again with **HyperInt**.

A major question about the above described procedure remains: how to efficiently resolve the spurious singularities which arise in the expansion by regions? As already mentioned, **HyperInt** cannot perform integrations involving divergences. The singularities are resolved for each integral individually by applying the function **dimregPartial** ‘by hand’. For this step, it is crucial to use a quasi-finite basis. When expanding quasi-finite integrals, only spurious poles need to be resolved. In contrast, asymptotically expanding divergent Feynman integrals with the expansion by regions yields integrals which contain the spurious singularities on top of the singularity structure of the Feynman integral. Manually resolving a large number of divergences with **dimregPartial** can easily become practically infeasible and might require the additional introduction of analytic regulators.

Moreover, this procedure requires manual work involving trial and error for each region and each order in  $m$  and hence was only applied for the leading coefficients.

Another less severe issue is the determination of an order in which the Feynman parameter integrations can be performed. For this work, this was also done for each integral individually by trial and error. Additionally, some integrations need considerable computational resources. Calculating higher-order expansions in  $m$  in this way would require even more resources due to the proliferation of terms in the integrand in eq. (4.11).

In the future, it would be interesting to study systematic simplifications of the integrands to optimize the integrations. Another interesting question is whether the resolution of subdivergences can be automated for computations with **HyperInt**. Such algorithms could greatly simplify the calculation of Feynman integrals containing subdivergences. These questions are left for future work.

##### 4.2.3. Calculation of higher-order terms

The higher orders of the asymptotic expansions are calculated by applying a differential equation to an ansatz of the asymptotic expansions, which yields a system of linear algebraic equations in the expansion coefficients. This system of equations is then solved and higher-order coefficients are expressed through lower-order coefficients. This approach was pioneered in ref. [109] and has been applied in many calculations [151, 155, 156, 225, 230–232].

The higher-order coefficients are consequently expressed through the coefficients of order  $m^0$  and  $m$  that were calculated in the previous section. The asymptotic expansions can be obtained to very high orders in this way without the need to evaluate integrals.

For all master integrals, an ansatz for asymptotic expansions of the form of eq. (4.6) is made.

Inserting the ansatz into the differential equation  $\partial_m \vec{I} = A_m \cdot \vec{I}$  yields

$$\begin{aligned}
\partial_m \vec{I} &= \partial_m \left( \sum_{e=e_{\min}}^{e_{\max}} \sum_{i=i_{\min}}^{\infty} \sum_{j=0}^{e+6} \vec{C}_{e,i,j} \epsilon^e m^i \ln^j(m) \right) \\
&= \sum_{e=e_{\min}}^{e_{\max}} \sum_{i=i_{\min}}^{\infty} \sum_{j=0}^{e+6} \vec{C}_{e,i,j} \epsilon^e \left( i m^{i-1} \ln^j(m) + j m^{i-1} \ln^{j-1}(m) \right) \\
&\stackrel{!}{=} A_m \vec{I} = \sum_{e=e_{\min}}^{e_{\max}} \sum_{i=i_{\min}}^{\infty} \sum_{j=0}^{e+6} A_m \cdot \vec{C}_{e,i,j} \epsilon^e m^i \ln^j(m).
\end{aligned} \tag{4.37}$$

Note that the matrix  $A_m$  also has a non-trivial  $m$  and  $\epsilon$  dependence. Expanding both sides in  $\epsilon$ ,  $m$ , and  $\ln(m)$  and comparing the coefficients gives a system of linear equations. In eq. (4.37), it can be seen that the equations mix coefficients of order  $m^n$ ,  $m^{n-1}$ , and even higher orders in  $m$  due to the  $m$  dependence of  $A_m$ . Hence, higher-order coefficients can be expressed with lower-order coefficients when solving the system of equations. Assuming that sufficiently many lower-order coefficients, which serve as boundary conditions, are known and assuming a suitable system of equations, it is possible to calculate coefficients theoretically up to any order in  $m$ .

In practice, the maximal expansion order is limited due to the available computational resources as intermediate expression sizes grow with expansion order. The expansions of all 54 master integrals were calculated at least up to order  $m^{13}$ .

The equations obtained from eq. (4.37) and also the expansion coefficients  $\vec{C}_{e,i,j}$  depend on  $x$  and  $z$ . The system of equations is solved for the benchmark phase space point to avoid very large analytical expressions.

Systems of equations are solved for individual sectors and orders in  $\epsilon$  one after another to keep the number of equations small and easily manageable. The systems of equations for individual sectors are solved consecutively since the solution of any given sector depends on the solutions of its subsectors. However, in each step all integrals of a given sector have to be included since they are in general coupled through the differential equation. Similarly, each order in  $\epsilon$  is solved individually starting at the lowest  $\epsilon$  order.

#### 4.2.4. Results of the asymptotic expansion

All 54 master integrals of the double-box topology have been expanded at least up to order  $m^{13}$ . The results of the asymptotic expansion are given in terms of logarithms, polylogarithms, and multiple polylogarithms. This also holds for all higher-order coefficients which were determined from the lower-order coefficients in sec. 4.2.3.

The coefficients are numerically evaluated with *Mathematica*. The MPLs are processed with the *Mathematica* package *PolyLogTools* [233], which uses *HPL* [234, 235] and *GiNaC* [236] for the numerical evaluation of the MPLs.

The results are in general too lengthy to be presented here. Numerical results are given in app. B.2.

#### 4. Evaluation of the master integrals

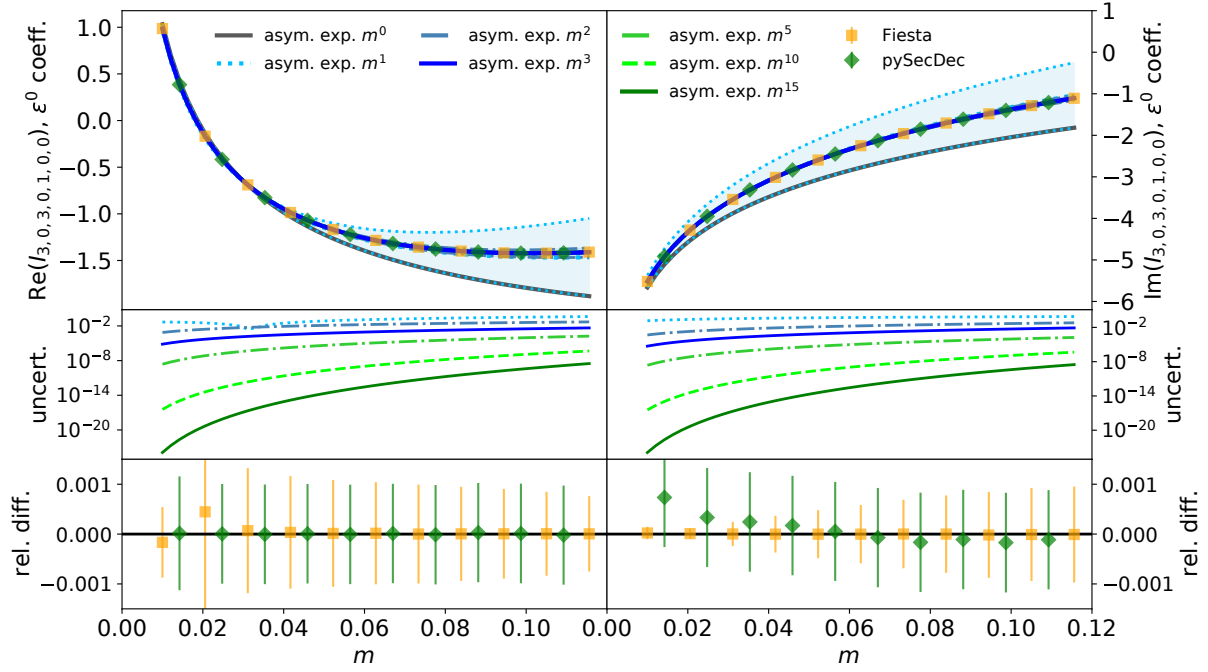


**Figure 4.5.:** The real part (left) and imaginary part (right) of the asymptotic expansion of  $I_{3,0,3,0,1,0,0}$  at order  $\epsilon^0$ . The upper panel shows the results of expansions up to different orders in  $m$  and their estimated uncertainties. Values obtained with **Fiesta** and **pySecDec** are included for comparison. The blue band is the estimated uncertainty of the order  $m^1$  expansion. The middle panel shows the estimated uncertainties of the asymptotic expansions. The lower panel shows the relative difference of the order  $m^{15}$  expansion and the **Fiesta** and **pySecDec** values.

For example, the first terms of the asymptotic expansion of the sunrise integral  $I_{3,0,3,0,1,0,0}$  are

$$\begin{aligned}
 I_{3,0,3,0,1,0,0} = & \frac{1}{4} \left( 2 + 2i\pi - \pi^2 + 2(1 + i\pi) \ln(m) + \ln^2(m) \right) \\
 & + \frac{1}{2} m \left( 2 + \pi^2 - 2i\pi \ln(m) - \ln^2(m) \right) + \frac{1}{2} m^2 (1 - 3i\pi - 3 \ln(m)) \\
 & - \frac{1}{3} m^3 (2 + 5i\pi + 5 \ln(m)) - \frac{1}{12} m^4 (24 + 35i\pi + 35 \ln(m)) \\
 & - \frac{1}{10} m^5 (53 + 63i\pi + 63 \ln(m)) + \mathcal{O}(m^6) + \mathcal{O}(\epsilon). \tag{4.38}
 \end{aligned}$$

This expansion is depicted in fig. 4.5 for  $m$  values from 0.01 up to the physical mass value  $m = 289/2500$  for different expansion orders. The uncertainties of the asymptotic expansion, which are shown in the middle panel of fig. 4.5, are estimated with the last contributing order in  $m$ . The uncertainty bands decrease with increasing expansion order and higher-order expansions lie inside the uncertainty bands of lower-order expansions. This indicates that the expansion converges well for the entire depicted range of  $m$ . The asymptotic expansion gives at least 8 significant decimal digits over the entire plotted range of  $m$  and is even more precise for smaller  $m$  values.

Moreover, fig. 4.5 also includes a comparison with numerical values obtained with **Fiesta** and **pySecDec**. The lower panel shows the relative difference of the **Fiesta** and **pySecDec** results with respect to the expansion. All results agree very well at the permille level with each other



over the entire  $m$  range.

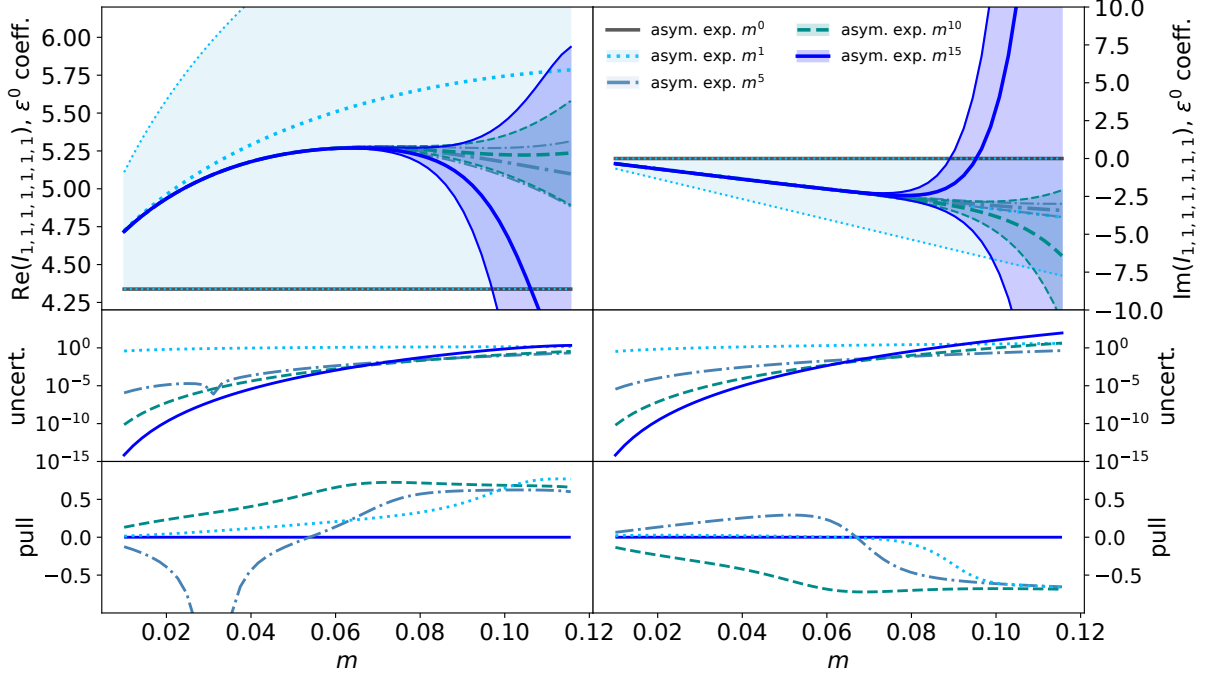


**Figure 4.6.:** The real part (left) and imaginary part (right) of the asymptotic expansion of the double-box integral  $I_{1,1,1,1,1,1,1}$  at order  $\epsilon^0$ . The upper panel shows the results of expansions up to different orders in  $m$  and their estimated uncertainties. The middle panel shows the estimated uncertainties of the asymptotic expansions. The lower panel shows the pull when comparing lower-order expansions with the order  $m^{15}$  expansion.

Studying the results for the asymptotic expansion of  $I_{3,0,3,0,1,0,0}$  raises the question: is the asymptotic expansion sufficient to obtain all master integrals at  $m = 289/2500$ ? After all, for the master integral  $I_{3,0,3,0,1,0,0}$  this seems to be the case.

To answer this question, consider, for example, the double-box integral  $I_{1,1,1,1,1,1,1}$ . The asymptotic expansion of the order  $\epsilon^0$  coefficient of the double-box integral is shown in fig. 4.6. Expansions of different orders up to order  $m^{15}$  are again compared for  $m$  values from 0.01 to  $289/2500$ . The uncertainty of the expansion is again estimated with the last contributing order in  $m$ . The upper panel shows the numerical values of the expansion and its uncertainty bands. The middle panel shows the estimated uncertainties. The lower panel shows the pull of the lower-order expansions and the highest-order expansion. The pull is the difference divided by the combined uncertainty.

The expansion at order  $m^0$  is just a constant while higher-order expansions have a non-trivial  $m$  dependence. The uncertainty bands overlap and the values of different expansion orders agree well with each other within the estimated uncertainty. The middle panel shows that the uncertainties decrease with higher orders up to a value of  $m \approx 0.07$ . However, for larger  $m$  values the uncertainties increase with expansion order and the asymptotic expansion diverges from the true value. The order  $m^{15}$  expansion does not give any meaningful results at the physical mass. In conclusion, it is not possible to use the asymptotic expansion to calculate this integral for the physical  $m$  value. Instead, numerical solutions of the differential equation in  $m$  are used. It can be seen that at  $m = 0.01$  the uncertainty roughly decreases by an order of magnitude with every order in  $m$ . The number of significant decimal digits of the evaluated asymptotic expansions at

#### 4. Evaluation of the master integrals

$m = 0.01$  and  $m = 0.001$  are given in tab. B.3 in app. B.2. The integrals for the larger mass are known for at least 8 decimal digits. The initial conditions are chosen at  $m = 0.001$ , which guarantees an accuracy of at least 22 decimal digits for all integrals while much higher precision is achieved for many integrals. Also note that lower-order coefficients in  $\epsilon$  typically also acquire a higher precision. This very high precision is required for the following numerical DE solution.

### 4.3. Numerical solutions of the differential equations

#### 4.3.1. Introduction

The master integrals obey differential equations in the kinematic variables  $x$ ,  $z$ ,  $m$ , and  $s$  of the form

$$\partial_x \vec{I} = A_x \cdot \vec{I}, \quad \partial_z \vec{I} = A_z \cdot \vec{I}, \quad \partial_m \vec{I} = A_m \cdot \vec{I}, \quad \partial_s \vec{I} = A_s \cdot \vec{I}, \quad (4.39)$$

where  $A_x$ ,  $A_z$ ,  $A_m$ , and  $A_s$  are matrices and  $\vec{I}$  is the vector of all master integrals. The matrices will in general couple the integrals and have entries that are rational functions in  $x$ ,  $z$ ,  $m$ , and  $\epsilon$ . The differential equations in eq. (4.39) are special cases of ordinary differential equations (ODE). For example, a general ODE in  $m$  is given by

$$\partial_m \vec{I} = \vec{f}(\vec{I}, m), \quad (4.40)$$

where the derivative of  $\vec{I}$  with respect to  $m$  is explicitly given by the function  $\vec{f}$ , which depends on  $\vec{I}$  and  $m$ . Numerical solutions to this kind of DE are a very well studied subject.

In the following, the DE in  $m$  is first solved numerically to obtain the integrals at  $m = 289/2500$ . The variables  $x$  and  $z$  are kept fixed in this step. Afterwards, the DEs in  $x$  and  $z$  are solved numerically to obtain the master integrals for different phase space points. In this way, the initial conditions only need to be evaluated for one single phase space point. In other words, the DE systems for the master integrals are solved iteratively as

$$(x_0, z_0, m_0) \xrightarrow{A_m} (x_0, z_0, m) \xrightarrow{A_x} (x, z_0, m) \xrightarrow{A_z} (x, z, m), \quad (4.41)$$

where  $(x_0, z_0, m_0) = (0.2, 0.05, 0.001)$  is the phase space point of the initial conditions.

The following discussion focuses on the calculation of the double-box integral family. The 5 remaining integrals of the two auxiliary integral families are solved essentially in the same way. The DE system for the master integrals of the auxiliary integral families also has to include some master integrals of the double-box and ‘crossed’ double-box topology. The corresponding DE system is hence constructed for the master integrals

$$\begin{aligned} \vec{I}^a = & (I_{1,4,1,1,0,0,1,0,0}^{a1}, I_{0,3,2,1,0,1,1,0,0}^{a1}, I_{1,3,1,1,0,1,1,0,0}^{a1}, I_{0,3,3,1,0,1,0,0,0}^{a2}, I_{0,3,2,1,0,1,0,1,0}^{a2}, \\ & I_{4,0,4,0,0,0,0,0}, I_{3,0,4,1,0,0,0,0}, I_{0,0,4,3,0,1,0}, I_{2,0,4,1,0,1,0}, I_{3,0,3,1,0,0,1}, \\ & I_{0,0,4,3,0,1,0}^c, I_{2,0,4,1,0,1,0}^c, I_{3,0,3,1,0,0,1}^c). \end{aligned} \quad (4.42)$$

These integrals were only solved in  $m$  and no grid results were calculated.

As an introductory example, consider again the double-box integral  $I_{1,1,1,1,1,1}$ . Numerically solving the DE in  $m$  for values between 0.01 and  $m = 289/2500$  yields the results plotted in fig. 4.7. The asymptotic expansions at  $m = 0.01$  are used as initial conditions for this example. This figure also includes a comparison of the ODE results with the asymptotic expansion and

values obtained completely independently with `pySecDec` and `Fiesta` as a cross-check. It can be seen that the asymptotic expansion and the numerical ODE solution agree very well up to roughly  $m \approx 0.06$ . The asymptotic expansion does not converge for larger  $m$  values and cannot be used to obtain meaningful results. The ODE system, however, can be solved numerically for higher masses. The results at the physical value  $m = 289/2500$  have an estimated relative uncertainty of less than  $10^{-7}$ . Additionally, the ODE results agree very well with the numerical `pySecDec` and `Fiesta` results over the entire range of  $m$ .

The details of this calculation are explained in the following. In sec. 4.3.2, the ODE system is prepared for the evaluation. In sec. 4.3.3, the technical details of the ODE solver are summarized and the deformation of the integration contour into the complex plane to avoid singularities is explained. Furthermore, uncertainties of the numerical results are estimated in sec. 4.3.4 and results for the integrals for a grid in  $x$  and  $z$  are presented in sec. 4.3.5. Finally, cross-checks of the results are provided in sec. 4.3.6.

### 4.3.2. Preparation and implementation of the ODE system

The ODE systems were implemented in a C++ program using the numerical ODE solver collection `Odeint` [237], which is part of the `Boost Library` [238], for the numerical calculations. This library provides several commonly used algorithms to numerically solve ODE systems. The calculations are performed with the quadruple-precision floating-point data type `float128` provided by the `Boost Library`. This 128-bit data type provides between 33 and 36 significant decimal digits, which is sufficient for this work. The `Boost Library` provides further data types with even higher numerical precision, including arbitrary-precision data types, which might be necessary for future calculations. All complex numbers are represented with a complex-valued data type derived from `float128`. Suitable parts of the calculation were performed in parallel using `OpenMP`.

In this work, the Bulirsch-Stoer algorithm [239, 240] was used to solve the DEs. This algorithm was, for example, also used in ref. [155] to calculate Feynman integrals. Other calculations applied Runge-Kutta algorithms [153, 241, 242] and multistep methods [151] for this task. The

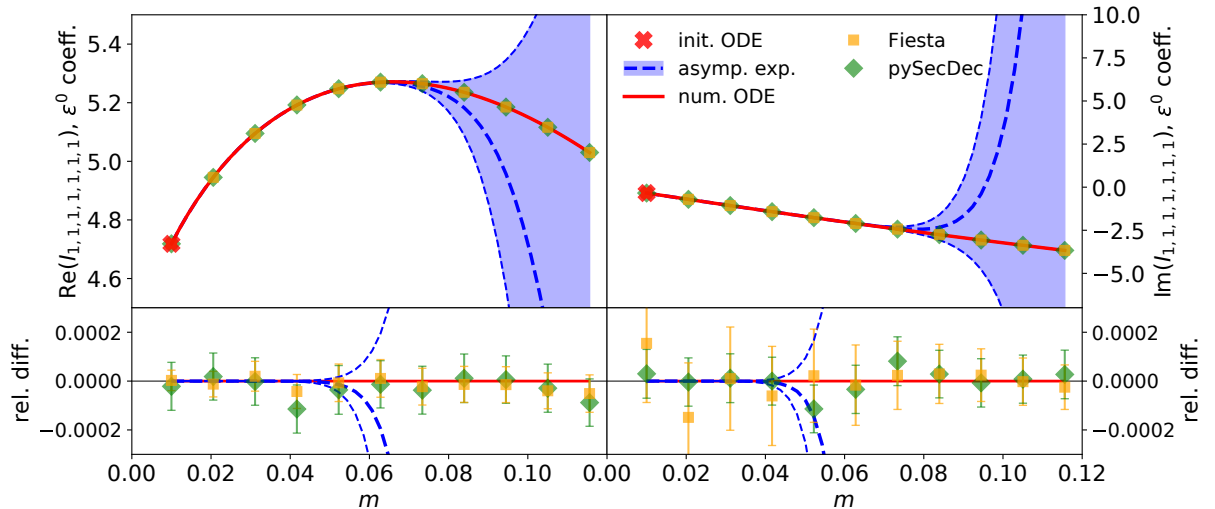


**Figure 4.7.:** Results of the numerical ODE solutions and the asymptotic expansion for the  $\epsilon^0$  coefficient of the real part (left) and imaginary part (right) of the double-box integral  $I_{1,1,1,1,1,1,1}$ . The lower panel compares the asymptotic expansion and `Fiesta` and `pySecDec` results with the numerical ODE solution.

#### 4. Evaluation of the master integrals

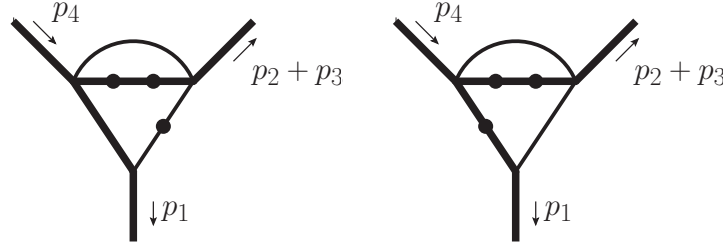


**Figure 4.8.:** The two master integrals  $I_{3,2,1,0,1,0,0}$  and  $I_{3,1,2,0,1,0,0}$  of sector 23.

Bulirsch-Stoer algorithm was chosen in this work because it generally provides stable solutions and good performance for high-precision calculations. A comprehensive discussion of different numerical algorithms for solving general ODE systems, i.e. for computations not confined to the evaluation of Feynman integrals, can be found in ref. [243, 244].

The ODE system needs to be prepared for numerical evaluation. In order to accommodate the  $\epsilon$  dependence, a larger DE system of the expanded integrals and the expanded matrix is constructed. The ODE systems for the leading-colour two-loop master integrals given in tab. B.1 have at most  $\epsilon^{-4}$  poles, i.e.

$$A_m = \epsilon^{-4} A_m^{(-4)} + \epsilon^{-3} A_m^{(-3)} + \dots + A_m^{(0)} + \dots \quad (4.43)$$

For example, the DE for the double-box integral  $I_{1,1,1,1,1,1}$  depends on the tadpole as<sup>1</sup>

$$\partial_m I_{1,1,1,1,1,1} = \mathcal{O}(\epsilon^{-4}) \cdot I_{4,0,4,0,0,0} + \dots \quad (4.44)$$

Since the master integrals are finite, i.e.

$$\vec{I} = \vec{I}^{(0)} + \epsilon \vec{I}^{(1)} + \epsilon^2 \vec{I}^{(2)} + \dots, \quad (4.45)$$

the ODE system assumes the form

$$\partial_m \begin{pmatrix} \vec{I}^{(0)} \\ \vec{I}^{(1)} \\ \vec{I}^{(2)} \\ \vdots \end{pmatrix} = \begin{pmatrix} A^{(0)} & A^{(-1)} & A^{(-2)} & A^{(-3)} & A^{(-4)} & 0 & 0 \\ A^{(1)} & A^{(0)} & A^{(-1)} & A^{(-2)} & A^{(-3)} & A^{(-4)} & 0 \\ A^{(2)} & A^{(1)} & A^{(0)} & A^{(-1)} & A^{(-2)} & A^{(-3)} & A^{(-4)} \\ \vdots & & & & & & \end{pmatrix} \cdot \begin{pmatrix} \vec{I}^{(0)} \\ \vec{I}^{(1)} \\ \vec{I}^{(2)} \\ \vdots \end{pmatrix}. \quad (4.46)$$

The poles in  $\epsilon$  occurring in  $A_m$  but also in  $A_x$  and  $A_z$  prevent a naive numerical implementation since the solution of  $\vec{I}^{(n)}$  depends on certain entries of  $\vec{I}^{(n+1)}$ ,  $\vec{I}^{(n+2)}$ , etc. Hence, a basis transformation that rescales the master integrals with  $\epsilon$  prefactors is applied.

For example, consider sector 23, which contains the master integrals  $I_{3,2,1,0,1,0,0}$  and  $I_{3,1,2,0,1,0,0}$  plotted in fig. 4.8. The corresponding ODE system involves the first 8 master integrals<sup>2</sup>, i.e.

$$\begin{aligned} \vec{I} &= (I_{4,0,4,0,0,0,0}, I_{3,0,4,1,0,0,0}, I_{3,2,0,0,2,0,0}, I_{4,2,0,0,2,0,0}, \\ &\quad I_{3,0,3,0,1,0,0}, I_{3,0,3,0,2,0,0}, I_{3,2,1,0,1,0,0}, I_{3,1,2,0,1,0,0}) \\ &= (I_1, I_2, I_3, I_4, I_5, I_6, I_7, I_8). \end{aligned} \quad (4.47)$$

<sup>1</sup>The complete expression of the  $\epsilon^{-4}$  coefficient is suppressed for this specific example since it is too lengthy.

<sup>2</sup>Master integral  $I_{3,0,4,1,0,0,0}$  actually decouples from sector 23 but is included for simplicity.

The corresponding DE contains poles and is at order  $\epsilon^{-2}$  given by

$$A_m = \frac{1}{\epsilon^2} \frac{1}{(4m - (1 - z)^2)(-1 + 2m + z)} \times$$

$$\times \begin{pmatrix} 0 & 0 & 0 & 0 & 0 & 0 & 0 & 0 \\ \vdots & \vdots & \vdots & \vdots & \vdots & \vdots & \vdots & \vdots \\ 0 & 0 & 0 & 0 & 0 & 0 & 0 & 0 \\ \frac{18m^2(2z+1)}{m+z} & 0 & \frac{m(2z+1)}{m+z} & \frac{3zm(2z+1)}{m+z} & 0 & 0 & 0 & 0 \\ -36m^2 & 0 & -2m & -6mz & 0 & 0 & 0 & 0 \end{pmatrix} + \mathcal{O}(\epsilon^{-1}). \quad (4.48)$$

Consequently, the order  $\epsilon^0$  coefficients of  $I_7$  and  $I_8$  depend on the order  $\epsilon^2$  coefficients of  $I_1$ ,  $I_3$ , and  $I_4$ . The transformation

$$T = \text{diag}(\epsilon^{-2}, 1, \epsilon^{-2}, \epsilon^{-2}, 1, 1, 1, 1), \quad (4.49)$$

rescales these integrals with a factor  $\epsilon^{-2}$ , which then cancels the poles in  $A_m$ .

A transformation for the complete ODE system is constructed in a similar way. The transformation  $T$  has the form

$$T = \text{diag}(\epsilon^{a_1}, \epsilon^{a_2}, \epsilon^{a_3}, \dots) \quad (4.50)$$

and the transformed matrix  $A'_m$  is

$$A'_m = T A_m T^{-1}$$

$$= \text{diag}(\epsilon^{a_1}, \epsilon^{a_2}, \epsilon^{a_3}, \dots) \cdot A_m \cdot \text{diag}(\epsilon^{-a_1}, \epsilon^{-a_2}, \epsilon^{-a_3}, \dots),$$

$$[A'_m]_{ij} = [A_m]_{ij} \epsilon^{a_i - a_j}. \quad (4.51)$$

The exponent  $a_j$  is then chosen to be the order of the strongest  $\epsilon$  pole in the  $j$ th column of  $A_m$  in order to cancel the poles. For the DE system of the double-box integral family, the required exponents are

$$\vec{a} = (-4, -2, -4, -4, -2, -2, -2, -2, -4, -2, -2, 0, 0, 0, -2, -2, -4, -4, -2, -2,$$

$$-2, -2, -2, -2, -1, -1, -1, 0, 0, 0, 0, 0, -1, -2, -2, -2, -2, -2, -2, -2,$$

$$0, -1, -1, -1, -1, -1, 0, 0, 0, -1, -1, 0, 0, 0). \quad (4.52)$$

Technically, this transformation moves the higher-order integral coefficients of  $\vec{I}^{(n+1)}$ ,  $\vec{I}^{(n+2)}$ ,  $\dots$  which are needed to calculate lower-order coefficients of  $\vec{I}^{(n)}$  into the same lower orders. This effectively shifts the poles from the matrix  $A_m$  to the integrals  $\vec{I}$ . After the transformation, the DE has the form

$$\partial_m \begin{pmatrix} \vec{I}^{(-4)} \\ \vec{I}^{(-3)} \\ \vec{I}^{(-2)} \\ \vec{I}^{(-1)} \\ \vec{I}^{(0)} \end{pmatrix} = \begin{pmatrix} A^{(0)} & & & & \\ A^{(1)} & A^{(0)} & & & \\ A^{(2)} & A^{(1)} & A^{(0)} & & \\ A^{(3)} & A^{(2)} & A^{(1)} & A^{(0)} & \\ A^{(4)} & A^{(3)} & A^{(2)} & A^{(1)} & A^{(0)} \end{pmatrix} \cdot \begin{pmatrix} \vec{I}^{(-4)} \\ \vec{I}^{(-3)} \\ \vec{I}^{(-2)} \\ \vec{I}^{(-1)} \\ \vec{I}^{(0)} \end{pmatrix}. \quad (4.53)$$

In the following paragraphs,  $\vec{I}$  denotes the transformed basis unless specifically stated otherwise. Note that  $\vec{I}$  still remains a quasi-finite basis since the poles in eq. (4.53) do not originate from

#### 4. Evaluation of the master integrals

subdivergences.

The  $\epsilon$  expansions of the 54 master integrals of the double-box integral family are calculated up to the maximal orders

$$\vec{e}_{\max} = (0, 0, 0, 0, 0, 0, 0, 0, 0, 1, 1, 1, 1, 1, 1, 0, 0, 0, 0, 0, 0, 0, 0, 0, 2, 1, 1, 1, 1, 0, 0, 0, 0, 0, 0, 0, 0, 0, 1, 1, 1, 1, 0, 0, 0, 0, 1, 1, 1, 1, 0, 0, 0, 0) \quad (4.54)$$

since the corresponding coefficients contribute to the order  $\epsilon^0$  coefficient of the amplitude.

The DE systems for the other master integrals  $\vec{I}^a$  defined in eq. (4.42) do not contain any poles and hence are not transformed. Furthermore, all integrals of  $\vec{I}^a$  are calculated up to order  $\epsilon^1$ .

### 4.3.3. Singularities and contour deformation

The DEs contain singularities in the kinematic variables which manifest in the matrices  $A_m$ ,  $A_x$ , and  $A_z$  as poles in  $x$ ,  $z$ , and  $m$ . All singularities in the kinematic variables for the double-box master integrals are summarized in tab. B.5 in app. B.3. For instance, the master integrals of sector 21 and subsector 5,

$$\vec{I} = (I_{4,0,4,0,0,0,0}, I_{3,0,3,0,1,0,0}, I_{3,0,3,0,2,0,0}), \quad (4.55)$$

obey the DE<sup>3</sup>

$$A_m = \begin{pmatrix} -\frac{2}{m} - \frac{2\epsilon}{m} & 0 & 0 \\ 9 - \frac{18(m-1)\epsilon}{m} & \frac{2m-1}{2m^2} + \frac{(-6m^2+7m-2)\epsilon}{2m^3} & \frac{1-4m}{2m^2} + \frac{(12m^2-11m+2)\epsilon}{2m^3} \\ -\frac{9}{4m-1} + \frac{18(m-1)\epsilon}{m(4m-1)} & \frac{1-2m}{2m^2(4m-1)} + \frac{(10m^2-7m+2)\epsilon}{2m^3(4m-1)} & \frac{-4m^2+4m-1}{2m^2(4m-1)} + \frac{(-8m^3-16m^2+11m-2)\epsilon}{2m^3(4m-1)} \end{pmatrix} + \mathcal{O}(\epsilon^2). \quad (4.56)$$

In this example, the two singularities at  $m = 0$  and  $m = 1/4$  correspond to the massless limit and the production threshold at  $s = 4m_t^2$ . In this work, the Feynman integrals are evaluated for  $0 < m < 1/4$ , i.e. above the production threshold. When calculating the three master integrals of sector 21 above threshold, there is no need for a contour deformation when the initial conditions are also chosen above threshold. However, when calculating the master integrals below threshold while keeping the initial conditions above threshold, a contour deformation in the complex plane is necessary to circumvent the singularity at  $m = 1/4$ .

Another example is given by the DE of sector 23 in eq. (4.48), which contains the three singularities

$$m = -z, \quad m = \frac{1}{2}(1-z), \quad m = \frac{1}{4}(1-z)^2. \quad (4.57)$$

These singularities can, in contrast to the previous example, lie above and below threshold, depending on the phase space point.

Most singularities given in tab. B.5 are located on the real axis when the remaining variables are real valued. For example, the singularity at  $m = \frac{1}{2}(1-z)$  is located at  $m = 0.3$  when numerically solving the DE for  $z = 0.4$ . Moreover, this singularity will always occur for real values of  $m$  in this work since the ODE systems are always solved for fixed and real-valued  $x$  and  $z$ .

The only way in which one of the singularities in tab. B.5 can obtain a complex value in this scenario is by being a complex solution to a quadratic equation. For example, the equation

<sup>3</sup>The transformation given in eq. (4.50) was not applied to this DE.

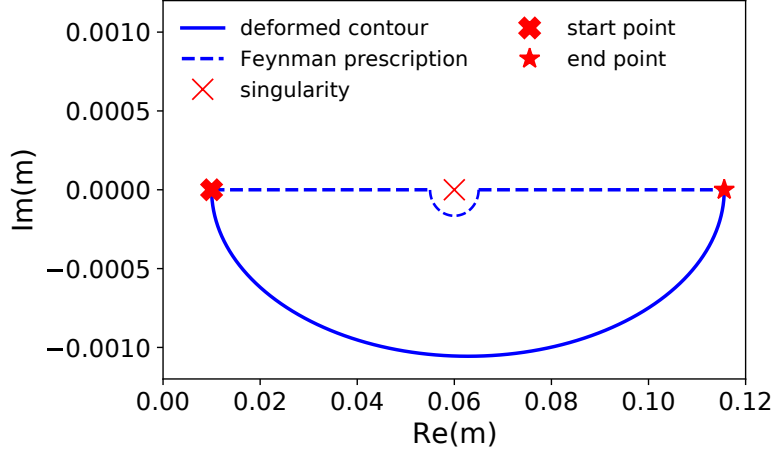


**Figure 4.9.:** Depiction of an example contour for the  $m$  integration. The singularities on the real axis are avoided by using an elliptic contour through the complex plane with a negative imaginary part. The depicted singularity is purely illustrative and does not correspond to an actual singularity of the DE.

$m^2 + x - mx = 0$  has the solutions

$$m = \frac{x}{2} \pm \frac{1}{2} \sqrt{x^2 - 4x}, \quad (4.58)$$

which have non-vanishing imaginary parts for  $0 < x < 4$ .

The numerical integration is done along complex contours for  $x$ ,  $z$ , and  $m$  to circumvent singularities on the real axis. Similarly to ref. [151], the elliptical contour

$$m = (m_1 - m_0) \left( \frac{1}{2} (1 - \cos(t\pi)) + ib \sin(t\pi) \right) + m_0 \quad (4.59)$$

is used. The start value of the contour is  $m_0$ , the end value is  $m_1$ , and the position on the contour is parameterized by  $t \in [0, 1]$ . The deformation into the complex plane is controlled by the parameter  $b$ . This contour is illustrated in fig. 4.9. While this parameterization gives a single, smooth contour, other calculations, e.g. in ref. [153, 241], use contours consisting of multiple parts.

The sign of the deformation parameter  $b$  follows from the Feynman prescription, where propagators are assigned infinitesimal imaginary parts and which is implemented by imposing infinitesimal imaginary parts

$$p_i^2 \rightarrow p_i^2 + i\varepsilon, \quad s_{ij} = (p_i + p_j)^2 \rightarrow s_{ij} + i\varepsilon, \quad m_i \rightarrow m_i - i\varepsilon \quad (4.60)$$

to momenta and masses. The variables  $x$ ,  $z$ , and  $m$  also acquire infinitesimal imaginary parts

$$x \rightarrow x + i\varepsilon, \quad z \rightarrow z + i\varepsilon, \quad m \rightarrow m - i\varepsilon \quad (4.61)$$

as a result. The Feynman prescription separates integration contour and poles on the real axis as indicated for the  $m$  variable by the dashed line in fig. 4.9. This contour can be deformed into the negative complex plane if the area between the two contours is free of singularities with non-vanishing residues. This follows directly from the Cauchy integral theorem. Hence, the deformation parameter  $b$  must be negative for  $m$  and positive for  $x$  and  $z$ .

For the choice of the magnitude of  $b$ , it is important to know the position of all singularities

#### 4. Evaluation of the master integrals

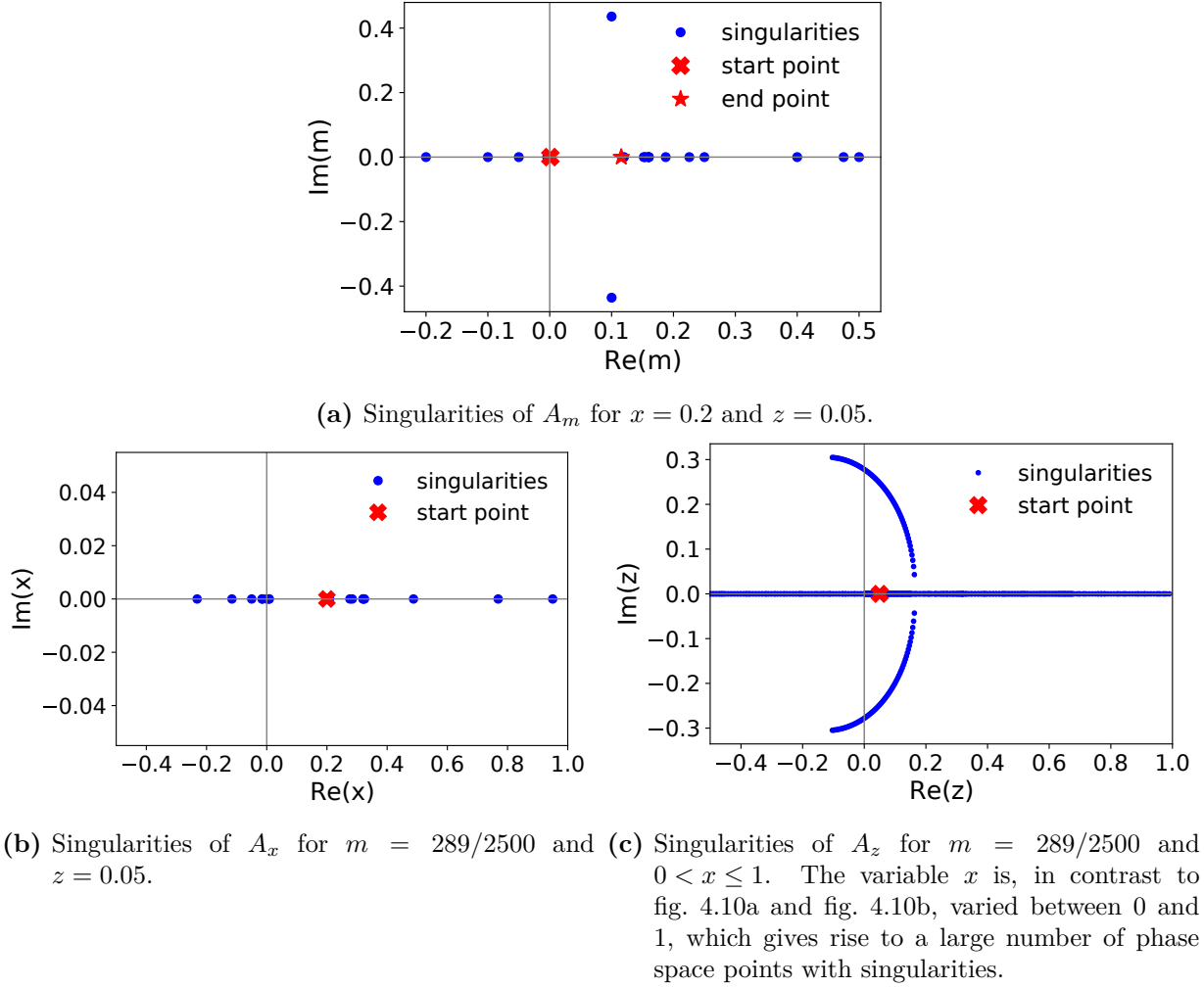


**Figure 4.10.:** Positions of singularities of the different DE systems for the calculation of the grid in  $x$  and  $z$ .

in the complex plane. The singularities for the  $m$  integration with  $x = 0.2$  and  $z = 0.05$  are depicted in fig. 4.10a. It would be possible to set  $b = 0$  since the DE in  $m$  has no poles on the real axis between the chosen start and end points. There are two singularities with non-vanishing imaginary parts since the singularity described by  $m^2 + x - mx = 0$  has the complex solutions given in eq. (4.58). The singularities lie for  $x = 0.2$  and  $z = 0.05$  at  $m \approx 0.1 \pm 0.435i$ . The deformation parameter must be chosen small enough, i.e.  $|b| < 3.8$ , to prevent the deformed contour from crossing the singularity. In this work,  $b = -0.01$  was used for the  $m$  integration. The situation is slightly more complicated for the numerical ODE solutions in  $x$  and  $z$  since integrals are evaluated for many different values of  $x$  and  $z$  and the positions of the singularities depend in general on both values. Fig. 4.10b and fig. 4.10c show the relevant singularities of the DE systems in  $x$  and  $z$  for the calculation of the grid. The singularities of  $A_x$  for  $m = 289/2500$  and  $z = 0.05$  lie on the real axis as shown in fig. 4.10b. In contrast, the singularities of  $A_z$  in fig. 4.10c are depicted for  $m = 289/2500$  and  $0 < x \leq 1$  since the  $z$  integration will be performed for many different  $x$  values. The singularity described by  $m(x+z)^2 - xz(1-x-z) = 0$ , i.e. the boundary of the physical phase space, has complex solutions for  $0.32 < x < 1.68$  when setting  $m = 289/2500$ . A deformation parameter with  $|b| < 0.043$  will avoid all singularities for the depicted setup. For the calculation of the grid,  $b = 0.01$  was used for both the  $x$  and  $z$  integration.



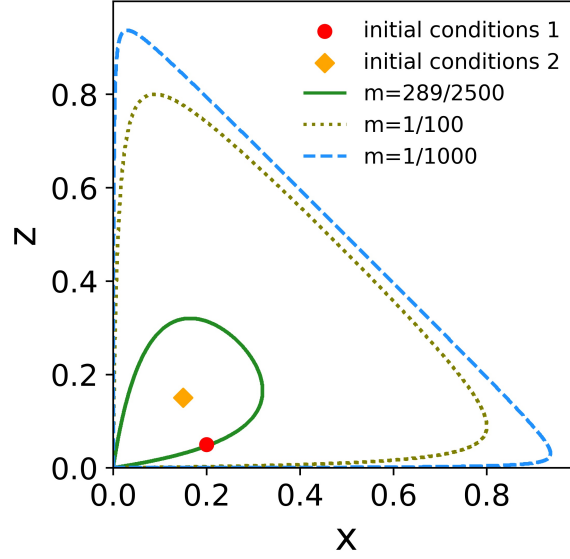


**Figure 4.11.:** Physical phase space regions for different masses. The phase space points of the initial conditions are  $x = 0.2$ ,  $z = 0.05$  and  $x = z = 0.15$ .

The physical phase space region is plotted for different masses in fig. 4.11. The benchmark phase space point at  $x = 0.2$  and  $z = 0.05$  is for  $m = 289/2500$  inside the physical phase space but close to its boundary, which is also a singularity. This is coincidental and it is not expected to have any adverse effect on the numerical calculations. All calculations were as a cross-check also performed with alternative initial conditions at  $x = z = 0.15$ , which are chosen far away from any singularity.

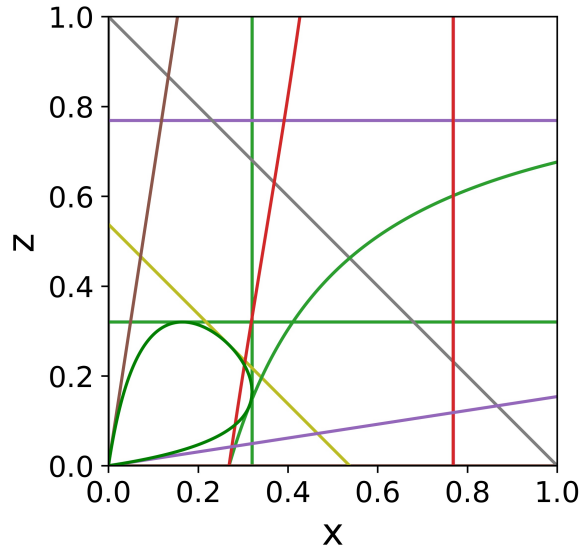


**Figure 4.12.:** Singularities of the differential equations in  $m$ ,  $x$  and  $z$  for  $m = 289/2500$ .

The singularities for  $m = 289/2500$  are shown in fig. 4.12. Singular points also occur inside of the physical phase space. The adoption of complex contours as described above is hence also beneficial even when confining the calculations to the physical region. One alternative approach to the adoption of complex contours could be the usage of multiple initial conditions to avoid crossing any singularities depicted in fig. 4.12.

#### 4. Evaluation of the master integrals

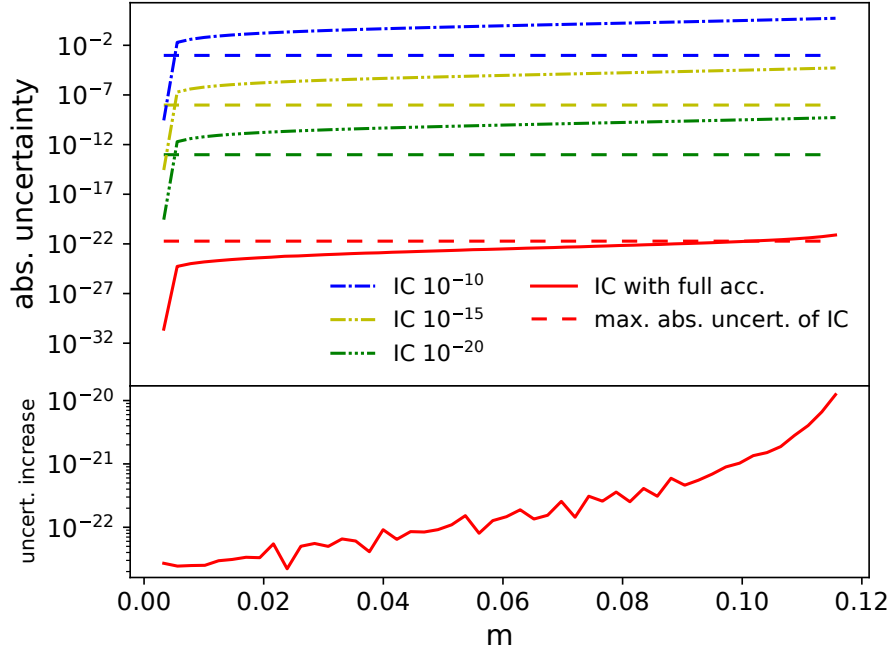


**Figure 4.13.:** Absolute uncertainty of the double-box integral  $I_{1,1,1,1,1,1}$  for initial conditions (IC) with different accuracies. The dashed horizontal lines indicate the maximal absolute uncertainty of all initial-condition integrals. The lower panel shows the uncertainty increase with each integration step of the full-accuracy result.

#### 4.3.4. Estimation of uncertainties of the numerical ODE solutions

There are two main sources of uncertainties, namely the uncertainties of the numerical ODE solver and the uncertainties of the initial conditions.

The numerical uncertainty of the ODE solver is a technical parameter and can be chosen more or less freely. A reduction of the numerical error will in general result in a larger runtime of the calculation. This uncertainty contribution is in the following referred to as numerical uncertainty.

The second contribution originates from the uncertainties of the initial conditions which induce uncertainties of the results of the numerical ODE solution. This contribution is comparable to a systematic uncertainty in an experiment since it is the minimal achievable uncertainty.

This uncertainty contribution is estimated by varying the initial conditions  $\vec{I}_{IC}$  by their uncertainties  $\vec{\sigma}_{IC}$ . In other words, the ODE system is solved with the three initial conditions  $\vec{I}_{IC}$  and  $\vec{I}_{IC} \pm \vec{\sigma}_{IC}$ , corresponding to an uncertainty band with an ‘upper’ and ‘lower’ value around a ‘central’ value<sup>4</sup>. Note that the phase space point of the initial conditions is not varied but only the values of the master integrals. The maximal difference of the three results is used as an estimate for the systematic uncertainties.

The uncertainties of the double-box integral  $I_{1,1,1,1,1,1}$  shown in fig. 4.13 serve as an example to qualitatively study the uncertainties when numerically solving the ODE in  $m$ . The results for initial conditions with the full available precision, shown in red, are compared with the results obtained from initial conditions with simulated uncertainties corresponding to 10, 15, and 20

<sup>4</sup>The labels ‘upper’, ‘lower’, and ‘central’ are used here figuratively. The uncertainty bands will in general not be literal bands for the ODE solutions.

decimal digits precision, shown in blue and green. Initial conditions with different accuracies are simulated with

$$\sigma_{\text{IC},j} = I_{\text{IC},j} \cdot 10^{-\#\text{digits}} \cdot \text{rand}(0,1) \frac{1+i}{\sqrt{2}}. \quad (4.62)$$

The simulated uncertainty for each integral  $I_{\text{IC},j}$  includes a random number  $\text{rand}(0,1)$  between 0 and 1 since otherwise the initial conditions for the ‘lower’, ‘central’, and ‘upper’ uncertainty band would differ effectively by a single constant relative factor for all integrals  $\tilde{I}_{\text{IC}}$ . Due to the linearity of the ODE, this would result in the same factor appearing in the three ODE solutions, which would most likely underestimate the actual uncertainties. Additionally, the factor  $(1+i)/\sqrt{2}$  is included to vary the real and imaginary parts simultaneously. The numerical error of the ODE solver was set to a value much lower than the initial condition uncertainty and hence fig. 4.13 only shows systematic uncertainties.

The uncertainties of the double-box integral increase by roughly 10 orders of magnitude for each initial-condition setting in fig. 4.13. Around 7 decimal digits are lost in the very first step and in the remaining integration, another 3 digits are lost. The lower subplot shows the increase of the absolute uncertainty with each integration step. The growth rate increases with increasing  $m$  as the different solutions diverge.

The apparent ‘jump’ of the uncertainties in the first step originates from the master integrals being coupled by the ODE. The uncertainties of the double-box integral receive contributions from the absolute uncertainties of subsector integrals weighted with the entries of  $A_m$ . Assuming  $A_m$  entries of  $\mathcal{O}(1)$ , this increase is expected to be roughly the maximal absolute uncertainty of the subsector integrals. The maximal absolute uncertainty of all initial-condition values is indicated with the dashed horizontal lines. These dashed lines and the increase of uncertainties in the first step have the same order of magnitude.

Both the results using the simulated and the actual initial-condition uncertainties exhibit qualitative similarities in fig. 4.13, especially the loss of precision when solving the ODE system. In conclusion, more precise end results can be obtained by correspondingly increasing the precision of the initial conditions.

In the previous example, initial conditions at  $m = 0.001$  are used since the asymptotic expansions yield at least 22 significant decimal digits at this  $m$  value. This is much more precise than the initial conditions at  $m = 0.01$ , which only guarantee roughly 8 significant digits.

To motivate both the choice of the error settings of the ODE solver and the choice of initial conditions at  $m = 0.001$ , consider the kite-like integral  $I_{2,2,1,0,1,1,0}$ , for example. This integral belongs to sector 55 and is plotted in fig. 4.14. The integrals of sector 55 lose in certain phase space regions much more accuracy than other integrals. The real part of this integral is shown in fig. 4.15 for  $x = 0.4$  and  $0 < z < 1$ . Using initial conditions at  $m = 0.01$ , which gives the solid green curve, yields problematic behaviour around singular points, especially at  $z \approx 0.14$ . The uncertainty band for the ODE results using initial conditions at  $m = 0.01$  is indicated in green in the upper panel. Close to  $z \approx 0.14$ , the uncertainties are of the same order of magnitude

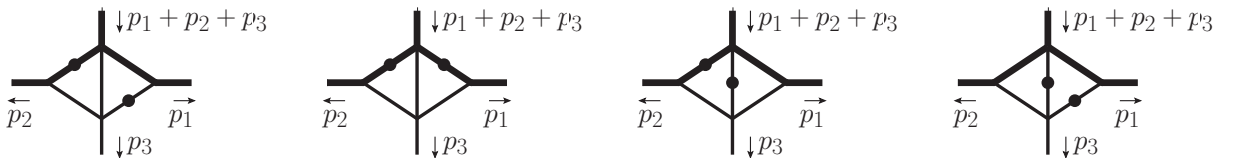


**Figure 4.14.:** The four kite-like master integrals of sector 55.

#### 4. Evaluation of the master integrals

as the actual ODE results. However, the integral calculated with initial conditions chosen at  $m = 0.001$ , depicted as blue dashed-dotted line, does not show this problematic behaviour. Note that this loss of accuracy does not originate from the numerical uncertainty of the ODE solver. The relative numerical uncertainty for the green curve is  $10^{-12}$  in the entire plot. Further reducing the numerical uncertainty of the ODE solver yields the same behaviour for the green curve.

The reason for this behaviour is instead that the results of the numerical integrations become very sensitive to the initial conditions when operating close to the problematic singular points. This results in a large loss of accuracy when solving the DEs in these phase space regions.

The loss of accuracy is illustrated in the lower panel, where the uncertainties for different numerical integration settings are compared. Results of the ODE solution with initial conditions at  $m = 0.01$  are shown in green. The dotted and dashed blue lines and the dashed-dotted red line show the results for initial conditions at  $m = 0.001$  with different numerical uncertainties for the  $m$ ,  $x$ , and  $z$  integrations. The initial conditions of the  $z$  integration are indicated with a grey vertical line. When decreasing the numerical uncertainties of the  $m$  and  $x$  integration, the initial conditions for the  $z$  integration become correspondingly more precise. These more precise

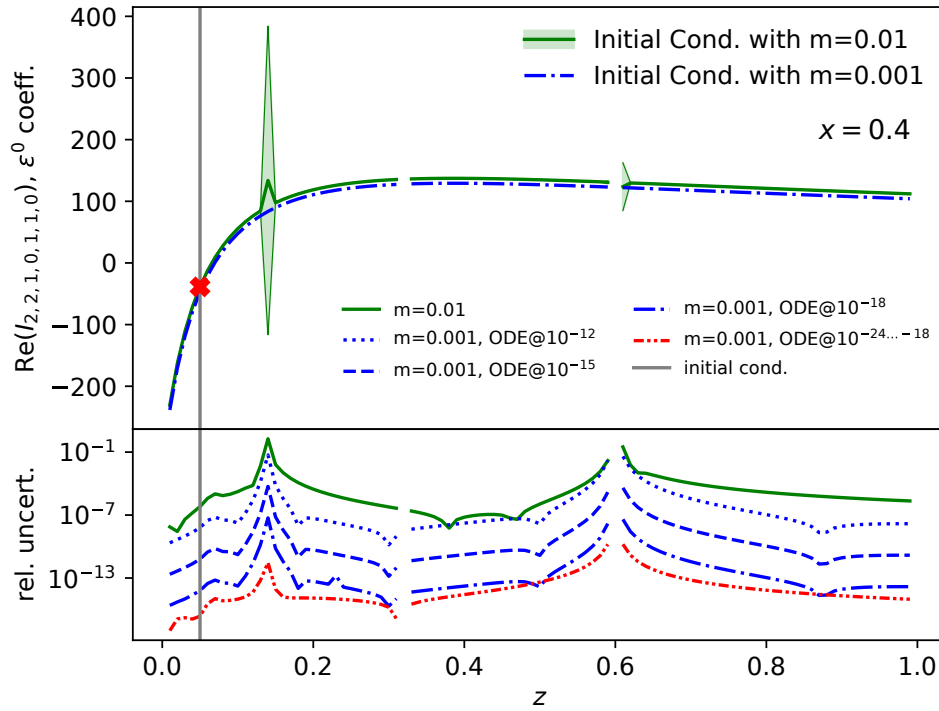


**Figure 4.15.:** Comparison of numerical results for the kite-like Feynman integral  $I_{2,2,1,0,1,1,0}$  for  $x = 0.4$  with different initial conditions and different numerical-precision settings for the ODE solver. The stated uncertainties are the numerical uncertainties of the ODE solver for the  $m$ ,  $x$ , and  $z$  integration. Results with initial conditions at  $m = 0.01$  are shown as solid green line and results for the initial conditions at  $m = 0.001$  are shown in blue and red as dashed and dotted lines. Both lines in the upper panel lie on top of each other, but the blue dashed-dotted line is moved slightly down for better visibility. The lower panel shows the relative uncertainties from the uncertainty band estimate. The red curve in the lower panel indicates the uncertainties when using initial conditions at  $m = 0.001$  with numerical uncertainties of  $10^{-24}$ ,  $10^{-21}$ , and  $10^{-18}$  for the  $m$ ,  $x$ , and  $z$  integration respectively.

initial conditions then yield more precise results of the  $z$  integration. The results at  $z \approx 0.14$  lose for all plotted settings roughly 8 significant digits when comparing with the initial conditions.

The most precise results in fig. 4.15 are given by the dashed-dotted red curve in the lower panel, which uses as numerical uncertainties for the ODE solver  $10^{-24}$  for the  $m$  integration,  $10^{-21}$  for the  $x$  integration, and  $10^{-18}$  for the  $z$  integration. Those settings are also used in the following for the grid. The reason for different choices of numerical accuracy is the propagation of uncertainties and a trade-off between precision and computing time. Numerical uncertainties are for many integrals the dominating uncertainty when solving in  $m$  since the initial conditions have comparatively small uncertainties. Reducing the numerical uncertainties for this step yields negligible additional computational costs since the  $m$  integration is only performed once while many more  $x$  and  $z$  integrations are performed. The numerical uncertainties can be decreased in the following steps since the intermediate results become less precise with each step in general.

The differences of the uncertainty bands can be much smaller than the numerical precision of the ODE solver when solving in  $m$ . The numerical uncertainties are consequently added in quadrature to the uncertainty bands before using the results as initial conditions for the  $x$  integration since it is possible that all three uncertainty bands have the same highly correlated numerical error. However, the numerical uncertainties of the intermediate  $x$  integration are not added before performing the  $z$  integration since this would lead to a strong overestimation of uncertainties for many phase space regions. But the numerical uncertainties of the  $z$  integration are included in the final uncertainty estimate.

Explicitly adding the numerical uncertainties will in general overestimate the uncertainties for many integrals since all master integrals are solved simultaneously. The step size and the uncertainty for each integration step are adjusted by the ODE solver with respect to the entry with the largest uncertainty. Integrals with a better numerical convergence surpass therefore the nominal numerical uncertainty.

#### 4.3.5. Calculation of a grid in $x$ and $z$

All master integrals were computed for a grid in the variables  $x$  and  $z$  by numerically solving the DEs in  $x$  and  $z$  for values between 0.01 and 1.00 with a step size of 0.01 while setting  $m = 289/2500$ . The chosen phase space region deliberately exceeds the physical phase space and hence contains many singularities of the ODE systems shown in fig. 4.10. This serves as a test of the contour deformation. This setup also allows in particular to evaluate the master integrals for phase space regions which are relevant for calculations of other physical processes. Integrals are not calculated for phase space points which lie on or very close to singularities. Phase space cuts around the singularities depicted in fig. 4.12 are applied.

The maximal estimated uncertainties are depicted in fig. 4.16 for the entire calculated phase space. This plot shows for each phase space point the maximal relative uncertainty of all coefficients of the  $\epsilon$  expansion of all master integrals. All relative uncertainties are estimated to be below  $10^{-9}$  for all calculated phase space points. For the majority of phase space points, the integrals have a much lower estimated relative uncertainty. In particular for the physical phase space region, which is indicated with a red line in fig. 4.16, at least double precision is achieved for all integrals. The phase space regions for which no master integrals are calculated due to their proximity to singularities show up as white lines in fig. 4.16. The results have lower precision around certain singular points. In particular, the two parallel bands around singular points described by  $1 = x + z$  and  $4m + x + z = 1$  stand out in this regard.

The master integrals were calculated for 9402 phase space points on the grid. This took in total approximately 267 hours on a computer with 24 physical Intel Xeon cores with 3GHz.

#### 4. Evaluation of the master integrals

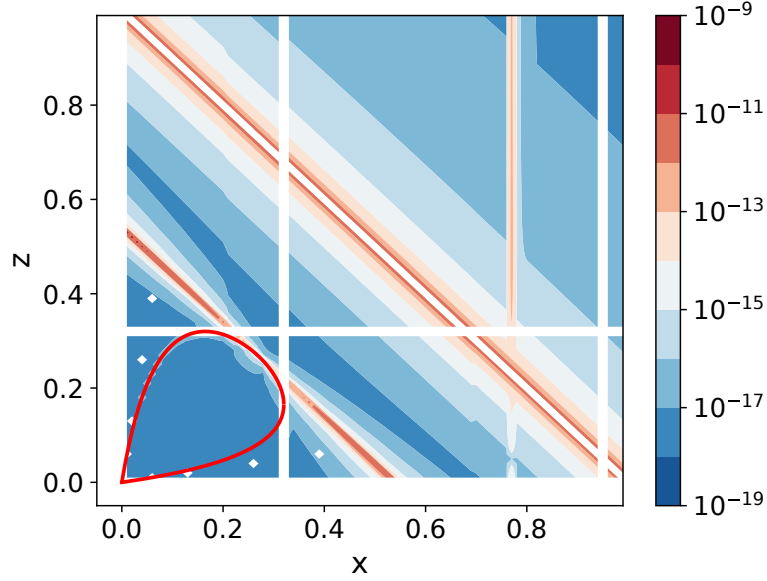


**Figure 4.16.:** Maximal relative uncertainties for all master integrals and for all calculated orders in  $\epsilon$ . The red line marks the physical region of the phase space.

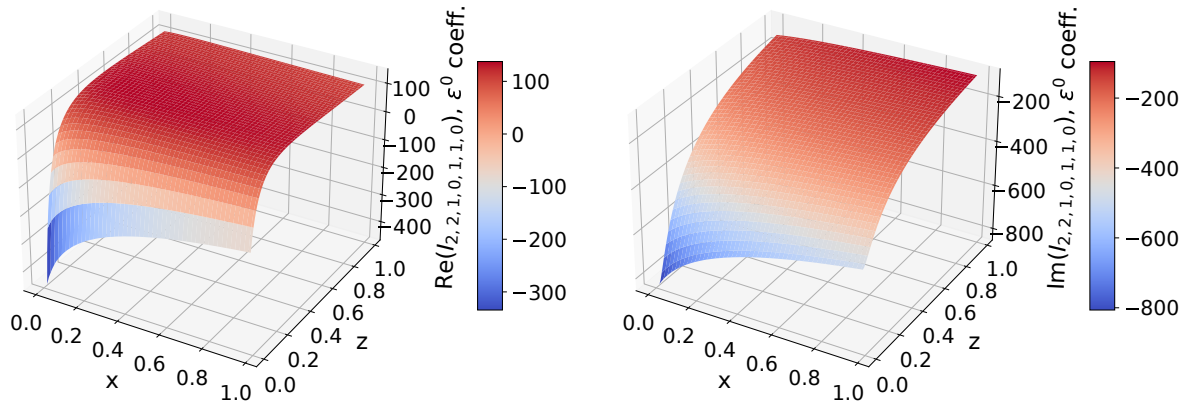


**Figure 4.17.:** The real (left) and imaginary (right) part of the kite-like Feynman integral  $I_{2,2,1,0,1,1,0}$  at order  $\epsilon^0$ .

This means that the calculation of all 54 master integrals for one phase space point required on average 102s with this setup. The first step, i.e. the integration in  $m$  to restore the physical mass, took approximately 5 minutes.

Interpolation techniques are used to obtain the integrals in phase space regions where it is not possible to calculate the master integrals using numerical ODE solvers. In this work, the Clough-Tocher scheme [245,246] implemented in the `scipy` library is used for the interpolation, similarly to ref. [247]. Interpolation makes the master integrals available in the whole physical phase space, which is especially beneficial for phase space integrations using Monte Carlo techniques. This approach also allows to perform the master integral computation for the whole phase space, i.e. a very time consuming part of the cross-section calculation, in advance and to save the results for later use.

Examples of the interpolated grid results are shown in fig. 4.17 for the kite-like integral  $I_{2,2,1,0,1,1,0}$  and in fig. 4.18 for the double-box integral  $I_{1,1,1,1,1,1,1}$ .

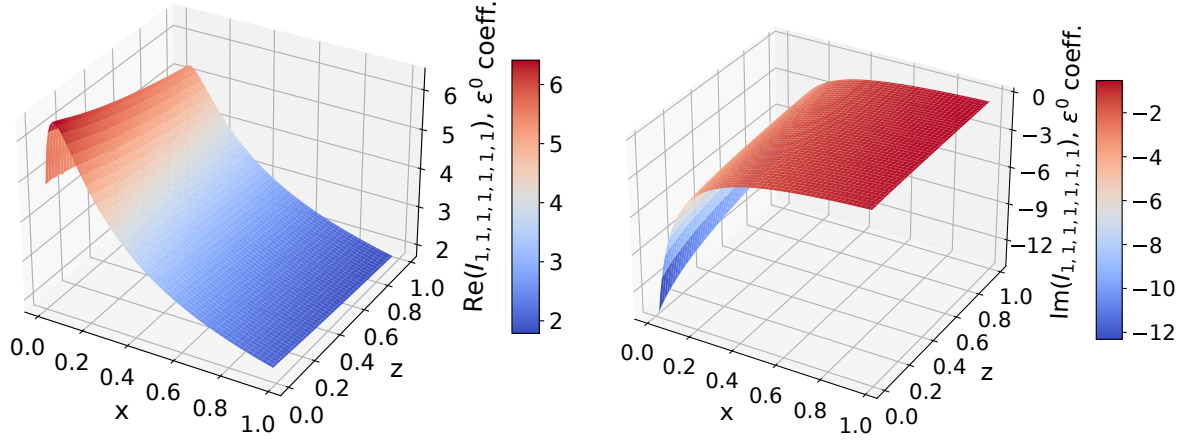


**Figure 4.18.:** The real (left) and imaginary (right) part of the double-box Feynman integral  $I_{1,1,1,1,1,1,1}$  at order  $\epsilon^0$ .

#### 4.3.6. Cross-checks of the results

##### Internal consistency checks

The consistency of the numerical ODE solutions is checked by performing integrations in  $x$  and  $z$  along a closed contour spanned by four points  $(x, z)$  in the order

$$(0.2, 0.05) \rightarrow (0.6, 0.05) \rightarrow (0.6, 0.7) \rightarrow (0.2, 0.7) \rightarrow (0.2, 0.05). \quad (4.63)$$

The numerical precision for the  $x$  and  $z$  integrations is set to  $10^{-21}$  for this check. The uncertainties of the end point values are obtained by adding the uncertainty band estimates and the numerical uncertainty of the ODE solver in quadrature. The initial values and the end values agree within the estimated uncertainties. For example, the double-box integral  $I_{1,1,1,1,1,1,1}$  is given by

$$\begin{aligned} I_{1,1,1,1,1,1,1}^{\text{start}} &= 6.225484058438724375247(2) + \mathcal{O}(\epsilon), \\ I_{1,1,1,1,1,1,1}^{\text{end}} &= 6.22548405843872437(1) + \mathcal{O}(\epsilon). \end{aligned} \quad (4.64)$$

In this expression, all significant digits are stated and the digit in brackets behind the last significant digit indicates the corresponding uncertainty. The end value still has 18 decimal digits of precision although the uncertainty increased by a factor of  $\mathcal{O}(10^4)$ .

The remaining integrals exhibit a comparable level of agreement as shown in the systematic comparison of the  $\epsilon^0$  coefficients for all master integrals in fig. 4.19. The relative difference, which is plotted in the upper panel, is below  $10^{-18}$  for all integrals. The absolute value of the complex-valued difference is plotted for simplicity. All end results have relative uncertainties of less than  $10^{-16}$ . The pull, i.e. the difference divided by the combined uncertainty of both results, is plotted in the lower panel and is smaller than 2. The pull is for many integrals very small since the nominal numerical ODE solver uncertainty of  $10^{-21}$  is explicitly added to the uncertainty estimates of the end results. This overestimates the actual numerical uncertainty for many integrals since all 54 master integrals are solved simultaneously.

The reliability of all grid results and their uncertainties was checked in a similar fashion by changing the integration order of  $x$  and  $z$  and comparing both results. The pull of both results is plotted in fig. 4.20. This plot shows the largest pull value of all coefficients of the  $\epsilon$  expansion of all master integrals and hence indicates the worst disagreement. Both results agree well in



#### 4. Evaluation of the master integrals

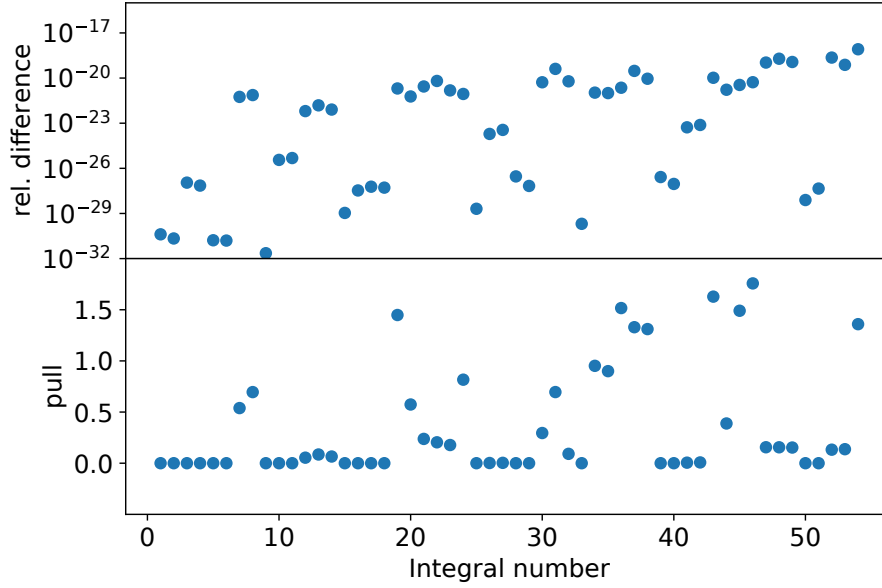


**Figure 4.19.:** Comparison of the start and end point values after performing the numerical integration in eq. (4.63) for all 54 integrals of the double-box topology. The master integrals are numbered according to their order in tab. B.1 and this number is used as identifier on the x-axis. The upper panel shows the relative difference of start and end values and the lower panel shows the pull.

most phase space regions with the pull being below one for the vast majority of phase space points. The uncertainties of both results also have the same order of magnitude. However, the differences are in certain phase space regions larger than the uncertainties. This is most notable close to certain singularities and indicates unreliable uncertainty estimates in these particular regions.

The systematic uncertainties are until this point estimated by calculating an ‘uncertainty band’, i.e. three values for each integral where the initial conditions are varied according to their estimated uncertainties. This estimate, however, depends strongly on the assumption that the uncertainty estimates of the initial conditions are reliable. This approach does not capture effects arising from integrals being coupled by the DE, which might result in uncertainties of different integrals cancelling or enhancing in non-trivial ways. Additionally, the three numerical integrations might have correlated numerical uncertainties since the integrations are performed simultaneously with very similar initial conditions. Hence, the numerical uncertainty is added to the uncertainty band estimate after the  $m$  and  $z$  integration to capture this effect.

The limited numerical resolution and rounding effects of the quadruple-precision data type can also affect the uncertainty estimates. This was observed for certain integrals whose initial conditions have very small uncertainty estimates. For this reason, the so-called machine epsilon of the quadruple-precision data type is added as a ‘rounding error’ contribution to initial condition uncertainties. This adds approximately  $2 \cdot 10^{-34}$  to the relative uncertainties of the initial conditions.

A second grid is calculated using the asymptotic expansions at the phase space point  $x = z = 0.15$  and  $m = 0.001$  as initial conditions. The difference between the two results calculated with initial conditions at different phase space points provides a second uncertainty estimate. The relative difference of the two results is depicted in fig. 4.21 for the entire calculated phase



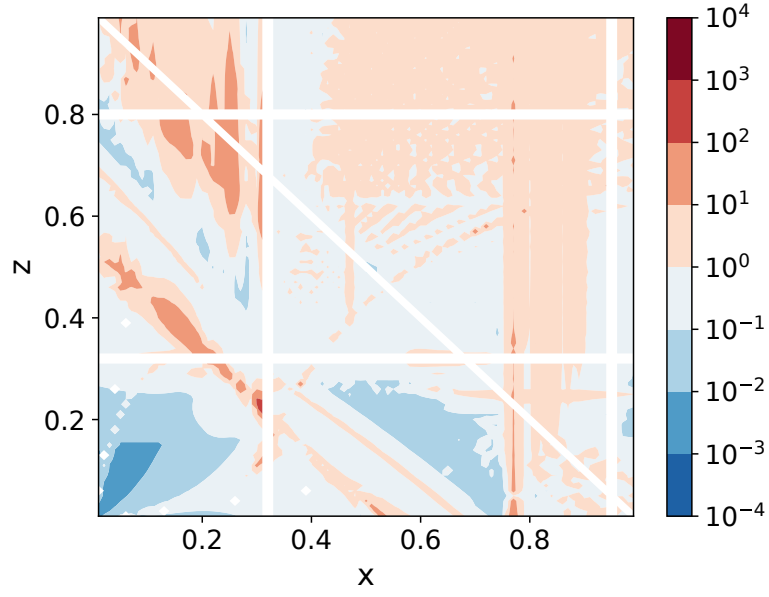


**Figure 4.20.:** Largest pull of two grid results computed with integration orders  $x, z$  and  $z, x$  respectively for each phase space point.

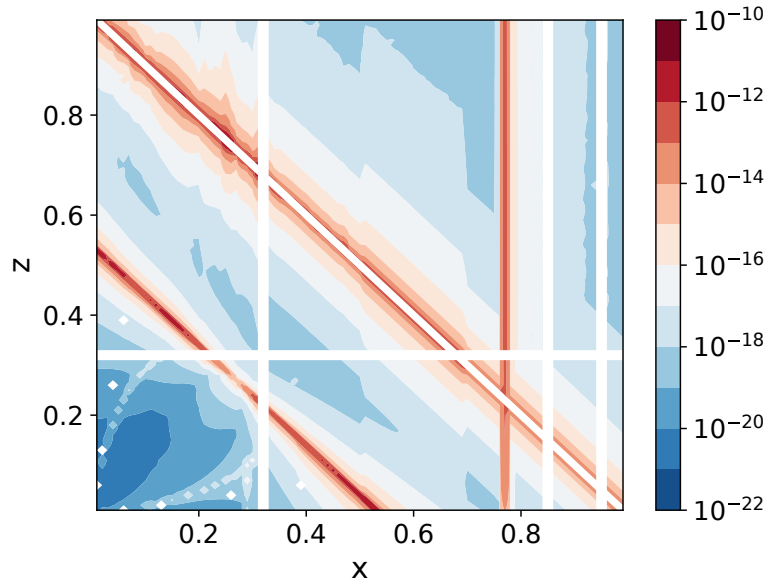
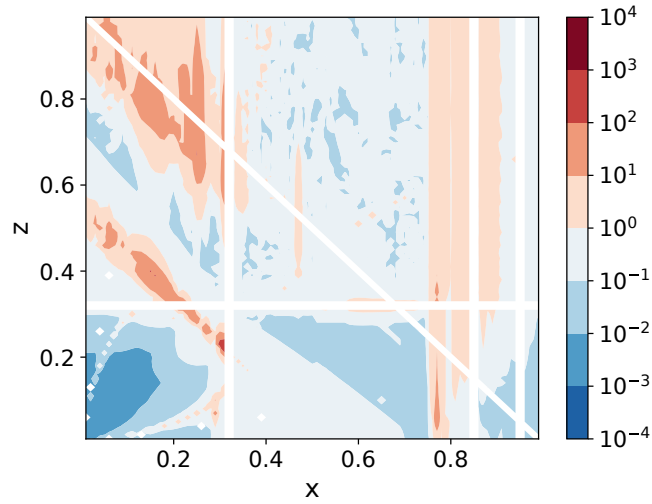
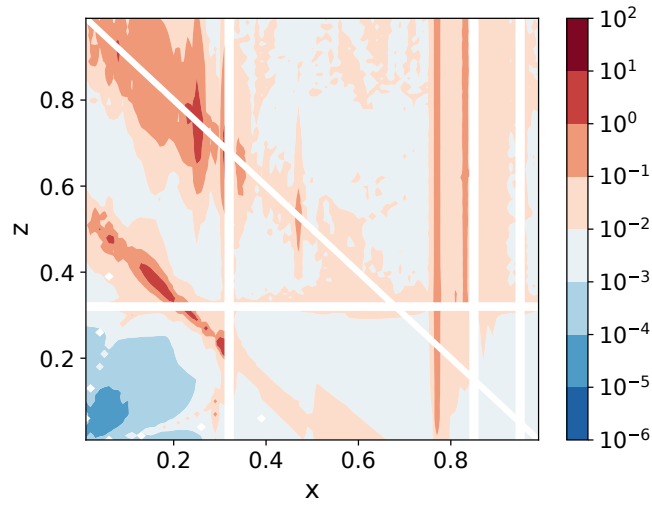


**Figure 4.21.:** Uncertainty estimate by comparing the results of two different initial conditions. The asymptotic expansions at  $m = 0.001$  with  $x = 0.2, z = 0.05$  and with  $x = z = 0.15$  were used as initial conditions.

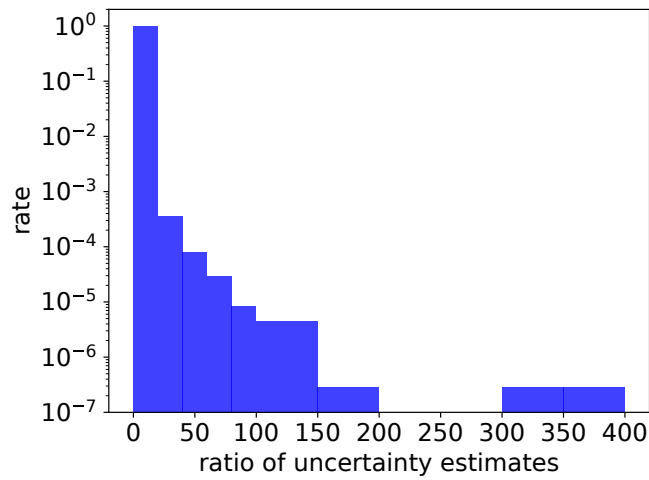
#### 4. Evaluation of the master integrals



(a) Maximal value of the ratio for all integrals and all calculated orders in  $\epsilon$ .



(b) Mean value of the ratio for all integrals and all calculated orders in  $\epsilon$ .



(c) Binned ratios for all integrals, all calculated orders in  $\epsilon$ , and all phase space points.

**Figure 4.22.:** Comparison of the estimated uncertainties obtained from initial conditions at two phase space points and from the uncertainty band estimate. The ratio of both estimates is plotted.

space. This plot shows for each phase space point the maximal relative difference when taking all calculated coefficients of the  $\epsilon$  expansion of all 54 master integrals into account. The absolute value of the complex-valued difference is plotted for the sake of simplicity. This uncertainty estimate reproduces qualitatively the uncertainty band estimate in fig. 4.16 as similar patterns with lower accuracy close to singular points occur. All integrals agree for at least 10 digits with many phase space regions being even more accurate.

The ratio of the two uncertainty estimates, i.e. the difference of the results using initial conditions at two phase space points divided by the combined uncertainty band estimates of both results, is plotted in fig. 4.22. The ratio is calculated for each coefficient of the  $\epsilon$  expansion for all master integrals and the maximal value for each phase space point is plotted in fig. 4.22a. This ratio is in almost all phase space regions of  $\mathcal{O}(1)$  or smaller, which indicates that the uncertainty band estimate is reliable in those phase space regions. However, the ratio being very small indicates that the uncertainty band overestimates the uncertainties. This is a natural consequence of the conservative estimates. It is also possible that varying the phase space point of the initial conditions underestimates the uncertainties since, for example, the same asymptotic expansions are used as initial conditions.

The maximal ratio plotted in fig. 4.22a will naturally overestimate the disagreement. The mean ratio, plotted in fig. 4.22b, is smaller than 10 for all phase space points. The binned ratios for all phase space points in fig. 4.22c also show that the ratio is almost always  $\mathcal{O}(1)$  or smaller. In conclusion, the uncertainty band estimate seems to produce reliable uncertainty estimates for most phase space regions. All consistency checks work in particular very well for integrals in the physical phase space region. But close to singular points, the uncertainty estimates might underestimate the uncertainties for certain coefficients of certain integrals by more than two orders of magnitude. Furthermore, it is worth mentioning that this is an estimate and not an uncertainty interval calculated from first principles.

Another cross-check can be constructed for special phase space points at which the master integral basis becomes degenerate. When setting all three variables to the same value, i.e.  $x = z = m$ , then only 47 master integrals are independent. In particular, the integral  $I_{1,2,1,0,2,1,0}$  belonging to sector 55 can be expressed through reduced master integrals, which yields

$$\begin{aligned}
 I_{1,2,1,0,2,1,0}^{\text{IBP relation}} = & \left( \frac{18m(6m-1)s}{3m-1} + \frac{90m(4m-1)s}{3m-1}\epsilon + \mathcal{O}(\epsilon^2) \right) I_{4,0,4,0,0,0,0} \\
 & + \left( \frac{6m-1}{3m-1} + \frac{16m-1}{3m-1}\epsilon + \mathcal{O}(\epsilon^2) \right) I_{3,2,0,0,2,0,0} \\
 & + \left( \frac{3m(1-6m)s}{3m-1} + \frac{6m(7m-2)s}{3m-1}\epsilon + \mathcal{O}(\epsilon^2) \right) I_{4,2,0,0,2,0,0} \\
 & - \left( \frac{4m^2-8m+1}{(3m-2)m^2} + \frac{8m^3+4m^2-11m+2}{(3m-1)m^2}\epsilon + \mathcal{O}(\epsilon^2) \right) I_{3,0,3,0,1,0,0} \\
 & + \left( \frac{(1-4m)^2s}{(3m-1)m^2} + \frac{(1-4m)^2(m+2)s}{(3m-1)m^3}\epsilon + \mathcal{O}(\epsilon^2) \right) I_{3,0,3,0,2,0,0} \\
 & + (4 + 4\epsilon + \mathcal{O}(\epsilon^2)) I_{3,2,1,0,1,0,0} \\
 & + \left( \frac{2m^2+8m-2}{(3m-1)m}(1+\epsilon) + \mathcal{O}(\epsilon^2) \right) I_{3,1,2,0,1,0,0} \\
 & + 2I_{2,2,1,0,1,1,0} + 2I_{2,1,2,0,1,1,0} + \frac{5m-1}{m}I_{2,1,1,0,2,1,0}.
 \end{aligned} \tag{4.65}$$

#### 4. Evaluation of the master integrals

Inserting the ODE results for  $x = z = m = 289/2500$  into the right-hand side of eq. (4.65) yields

$$\begin{aligned}
I_{1,2,1,0,2,1,0}^{\text{IBP relation}} = & (0(1 \cdot 10^{-23}) + 0(1 \cdot 10^{-23})i) \cdot \epsilon^{-4} \\
& + (0(1 \cdot 10^{-22}) + 0(1 \cdot 10^{-23})i) \cdot \epsilon^{-3} \\
& + (10.452842606973141554070(3) - 21.32903507509364086723619(2)i) \cdot \epsilon^{-2} \\
& + (216.26070825991665818840(9) - 158.4615203262954674859756(1)i) \cdot \epsilon^{-1} \\
& + (1648.58245345727317030(2) - 408.474436586925056729267(2)i) + \mathcal{O}(\epsilon).
\end{aligned} \tag{4.66}$$

Numerical zeros are in this expression denoted with a zero followed by the rounded uncertainty in brackets. This value agrees numerically for 21 digits with the direct ODE result of  $I_{1,2,1,0,2,1,0}$ . Note that this surpasses the nominal relative numerical accuracy of  $10^{-18}$ , which is not included in eq. (4.66) to prevent an overestimation of the uncertainty. The remaining 6 equations for this special phase space point as well as numerical values for the required master integrals are given in app. C.3.

All 7 equations are fulfilled within the estimated uncertainties. The left- and right-hand sides of the 7 equations agree for at least 15 decimal digits. This indicates reliable numerical results and reliably estimated uncertainties.

Eq. (4.65) can also be used to check the interpolation results. Inserting the interpolated master integrals at  $x = z = m = 289/2500$  into the right-hand side of eq. (4.65) yields

$$\begin{aligned}
I_{1,2,1,0,2,1,0}^{\text{IBP relation}} = & (0.0000\mathbf{1} - 0.0002\mathbf{i})\epsilon^{-4} + (0.00\mathbf{1} - 0.002\mathbf{i})\epsilon^{-3} \\
& + (10.4\mathbf{7} - 21.34\mathbf{i})\epsilon^{-2} + (216.4 - 158.5\mathbf{i})\epsilon^{-1} + (164\mathbf{9} - 408.4\mathbf{i}) + \mathcal{O}(\epsilon),
\end{aligned} \tag{4.67}$$

while the direct interpolation of this integral gives

$$\begin{aligned}
I_{1,2,1,0,2,1,0}^{\text{direct}} = & (\mathbf{1} \cdot 10^{-23} - \mathbf{4} \cdot 10^{-23}i)\epsilon^{-4} + (-\mathbf{5} \cdot 10^{-23} + \mathbf{3} \cdot 10^{-22}i)\epsilon^{-3} \\
& + (10.4528\mathbf{3} - 21.33\mathbf{i})\epsilon^{-2} + (216.26\mathbf{9} - 158.48i)\epsilon^{-1} + (1648.\mathbf{7} - 408.6\mathbf{i}) + \mathcal{O}(\epsilon).
\end{aligned} \tag{4.68}$$

In eq. (4.67) and eq. (4.68), bold numerals indicate the digits which differ from the directly calculated ODE solution given in eq. (4.66). The results are rounded at this digit. The value from the IBP relation in eq. (4.67) agrees for roughly 3 digits with the actual result and the direct interpolation in eq. (4.68) agrees for 3 to 4 digits with the actual result.

The relative differences of the left- and right-hand sides of the 6 expressions in eq. (C.1) are

$$1.5 \cdot 10^{-6}, \quad 2.5 \cdot 10^{-6}, \quad 4.5 \cdot 10^{-8}, \quad 1.8 \cdot 10^{-7}, \quad 3.2 \cdot 10^{-7}, \quad 1.3 \cdot 10^{-4} \tag{4.69}$$

when using the interpolated master integrals. These values are the maximal relative differences of all coefficients of the  $\epsilon$  expansion. The corresponding relative differences of the interpolated results for the integrals on the left-hand side of eq. (C.1) and the direct ODE solutions are

$$1.2 \cdot 10^{-4}, \quad 2.1 \cdot 10^{-4}, \quad 7.6 \cdot 10^{-6}, \quad 2.3 \cdot 10^{-5}, \quad 3.7 \cdot 10^{-5}, \quad 1.5 \cdot 10^{-5}. \tag{4.70}$$

This means that the interpolated results are actually less precise than most IBP relations indicate. This might be caused by integrals having very similar interpolation errors.

Two other limits to exploit for a similar cross-check are the singularities at  $1 - x - z = 0$  and  $1 - x - z - 4m = 0$ , where the number of master integrals is reduced to 53. It is again possible to express  $I_{1,2,1,0,2,1,0}$  through the remaining master integrals. However, the integrals have to be obtained by interpolation since these phase space points lie on a singularity. Inserting the

interpolation results for  $m = 289/2500$  and  $x = z = 0.5$  into the corresponding IBP relation for  $1 - x - z = 0$  gives

$$I_{1,2,1,0,2,1,0}^{\text{IBP relation}} = (-0.0000\mathbf{2} + 0.0000\mathbf{2i})\epsilon^{-4} + (-0.000\mathbf{2} + 0.0000\mathbf{2i})\epsilon^{-3} \\ + (6.071\mathbf{1} - 6.926\mathbf{6i})\epsilon^{-2} + (81.33\mathbf{5} - 21.64\mathbf{9i})\epsilon^{-1} + (422.56\mathbf{4} + 71.54\mathbf{5i}) + O(\epsilon), \quad (4.71)$$

while the direct interpolation gives

$$I_{1,2,1,0,2,1,0}^{\text{direct}} = (-\mathbf{2} \cdot 10^{-19} + \mathbf{1} \cdot 10^{-18}\mathbf{i})\epsilon^{-4} + (-\mathbf{1} \cdot 10^{-17} - \mathbf{2} \cdot 10^{-17}\mathbf{i})\epsilon^{-3} \\ + (6.071\mathbf{6} - 6.926\mathbf{4i})\epsilon^{-2} + (81.33\mathbf{7} - 21.64\mathbf{8i})\epsilon^{-1} + (422.56\mathbf{8} + 71.54\mathbf{6i}) + O(\epsilon). \quad (4.72)$$

Bold numerals indicate in this expression the digit where the IBP result and the directly interpolated result differ. The level of agreement is comparable to the interpolation results in eq. (4.67) and eq. (4.68).

The IBP relation at  $1 - x - z - 4m = 0$  for  $m = 289/2500$ ,  $x = 0.5$ , and  $z = 0.0376$  yields

$$I_{1,2,1,0,2,1,0}^{\text{IBP relation}} = (0.00\mathbf{3} + 0.0000\mathbf{5i})\epsilon^{-4} + (0.04 + 0.0\mathbf{3i})\epsilon^{-3} \\ + (9.\mathbf{2} - 22.\mathbf{1i})\epsilon^{-2} + (20\mathbf{7} - 18\mathbf{9i})\epsilon^{-1} + (17\mathbf{24} - 71\mathbf{7i}) + O(\epsilon), \quad (4.73)$$

while the direct interpolation gives

$$I_{1,2,1,0,2,1,0}^{\text{direct}} = (-\mathbf{7} \cdot 10^{-23} - \mathbf{7} \cdot 10^{-22}\mathbf{i})\epsilon^{-4} + (\mathbf{1} \cdot 10^{-20} + \mathbf{1} \cdot 10^{-20}\mathbf{i})\epsilon^{-3} \\ + (9.\mathbf{1} - 22.\mathbf{5i})\epsilon^{-2} + (20\mathbf{8} - 19\mathbf{2i})\epsilon^{-1} + (17\mathbf{38} - 72\mathbf{7i}) + O(\epsilon). \quad (4.74)$$

In this case, the agreement is worse with differences already occurring in the second digit of some coefficients.

These results show that the interpolation is less precise than anticipated. It is possible that the two relations for  $1 - x - z = 0$  and  $1 - x - z - 4m = 0$  overestimate the disagreement due to cancellations in the analytic expressions. However, the comparison of the direct ODE solutions and the interpolation results for  $x = z = m = 289/2500$  shows a comparable level of disagreement. This indicates that the interpolation only yields roughly 3 to 4 decimal digits.

On the other hand, this comparison also serves as a sanity check as the internal cross-checks were able to detect the discrepancies. It is possible that the discrepancies would not have been detected with a numerical comparison with, for example, `pySecDec` or `Fiesta` if numerical results would have been calculated to only permille accuracy.

The uncertainties associated with the interpolation require further thorough investigation. The current results are most likely not suitable for use in a phase space integration. Calculating a denser grid for the physical phase space could improve the interpolation results. Alternatively, it might be beneficial to not interpolate the master integrals at all but to calculate a grid of form factors and then to interpolate on the level of form factors.

### Comparison with `pySecDec` and `Fiesta`

The strongest check is the comparison with completely independently calculated results. For this purpose, the results calculated previously are compared with numerical values obtained with `pySecDec` [76, 81–84, 248–252] and `Fiesta` [77–80].

Comparisons with `pySecDec` and `Fiesta` results were already shown in fig. 4.5 for the sunrise integral  $I_{3,0,3,0,1,0,0}$  and in fig. 4.7 for the double-box integral  $I_{1,1,1,1,1,1,1}$ . In both examples, `pySecDec` and `Fiesta` results exhibit very good agreement with the asymptotic expansions and the numerical ODE solutions.

#### 4. Evaluation of the master integrals

For a further, comparison 10 randomly selected values of  $(x, z)$ ,

$$\begin{aligned} & (0.7, 0.59), (0.69, 0.87), (0.8, 0.79), (0.08, 0.52), (0.8, 0.1), \\ & (0.98, 0.25), (0.52, 0.73), (0.81, 0.87), (0.84, 0.88), (0.26, 0.18), \end{aligned} \quad (4.75)$$

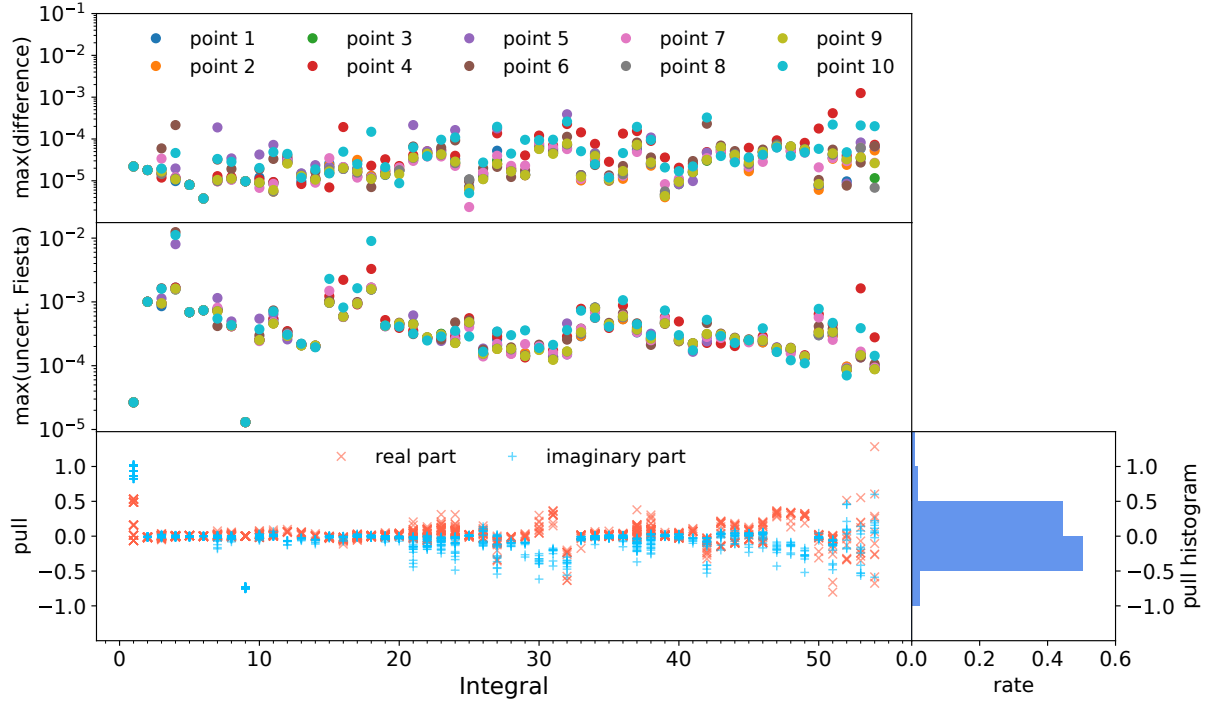
were chosen while keeping  $m = 289/2500$  constant. The maximal number of integrand evaluations was set to  $2.1 \cdot 10^9$ . The results of the comparison are plotted in fig. 4.23. The results agree within the numerical uncertainties for all integrals with maximal relative differences, which are shown in the upper panel, and maximal relative uncertainties, which are shown in the middle panel, typically ranging from  $10^{-4}$  to  $10^{-2}$ . The pull is plotted for all coefficients of the  $\epsilon$  expansion up to the order  $\epsilon^0$  in the lower panels. Only the uncertainties of the **pySecDec** and **Fiesta** results are relevant for the pull since the numerical ODE solutions have in comparison negligible uncertainties. A histogram of the pull results is shown on the right side. The pull is for all integrals smaller than 2, which means that the **pySecDec** and **Fiesta** results agree with the ODE results within the numerical uncertainties. The pull is very small for many integrals, which indicates that the corresponding uncertainties provided by **pySecDec** and **Fiesta** might be overestimated.

Higher accuracy would be desirable for the **pySecDec** and **Fiesta** results but would also increase the computational cost. Even the numerical computations for the 10 phase space points in eq. (4.75) were comparatively expensive. For example, calculating the three double-box integrals  $I_{1,1,1,1,1,1}$ ,  $I_{1,1,1,1,1,2,1}$ , and  $I_{1,1,1,1,2,1,1}$  with **Fiesta** took 2 to 5 days for each integral and phase space point<sup>5</sup>. Calculating the double-box integrals  $I_{1,1,1,1,1,2,1}$  and  $I_{1,1,1,1,2,1,1}$  with **pySecDec** also required several days for each phase space point. Increasing the precision and number of phase space points, e. g. to perform a Monte Carlo phase space integration, with this setup would require very large computational resources.

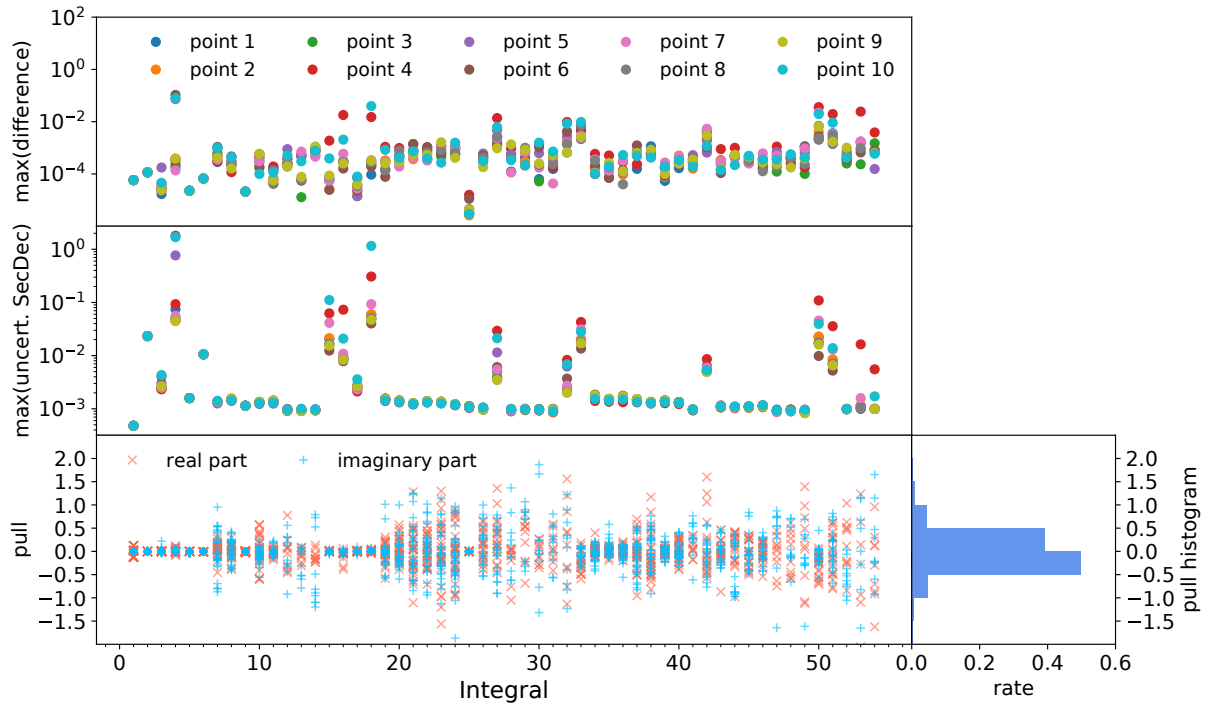
The calculations in sec. 4.3.5 in comparison, i. e. solving ODE systems numerically for a grid of phase space points, required on average less than 2 minutes to compute all 54 master integrals for one phase space point. The results on the grid also have relative uncertainties of less than  $10^{-9}$ .

---

<sup>5</sup>The calculation was performed on a computer with 24 physical Intel Xeon cores with 3GHz but **Fiesta** and **pySecDec** did not use all available resources during the entire computation time.



(a) Fiesta



(b) pySecDec

**Figure 4.23.:** Numerical comparison with values obtained from **Fiesta** and **pySecDec** for all 54 Integrals for 10 different phase space points. The upper panel shows the maximal relative difference of the ODE results and the sector decomposition results. The middle panel shows the maximal relative uncertainty of the **Fiesta** and **pySecDec** results. The lower panel shows the pull for the real part (red) and imaginary part (blue) of all coefficients in  $\epsilon$  up to order  $\epsilon^0$  for all 10 phase space points. A histogram of the pull is shown in the lower-right panel.





# 5. Amplitude evaluation and numerical results

## 5.1. Overview of the calculation

### 5.1.1. General work-flow

This chapter presents the calculation of the leading-order, one-loop, and leading-colour two-loop amplitudes. The following summary focuses mainly on the calculation of the vector current  $V_t$  since the evaluation of the axial-vector currents is almost identical.

The Feynman diagrams are generated with **qgraf** [253] and the resulting terms are translated into **FORM** [250–252] expressions. The colour factors are calculated by replacing the structure constants of the  $SU(N_c)$ , which occur in the gluon vertices, with

$$f^{a_1 a_2 a_3} = -2i [t^{a_1}, t^{a_2}] t^{a_3}, \quad (5.1)$$

where  $t^a$  denotes the generators of the  $SU(N_c)$  in the fundamental representation. The Fierz identity

$$t_{ij}^a t_{kl}^a = \frac{1}{2} \left( \delta_{il} \delta_{kj} - \frac{1}{N_c} \delta_{ij} \delta_{kl} \right) \quad (5.2)$$

is subsequently applied and the remaining sums are resolved. Then, the leading-colour term of the two-loop amplitude is extracted and the amplitudes are decomposed into vector and axial-vector currents. The coefficients of the form-factor decomposition, as defined in eq. (3.3), are extracted with projectors as described in sec. 3. All steps described so far, including the projection procedure, are implemented in **FORM**.

The tensor reduction is performed by replacing scalar products involving loop momenta with inverse propagators and subsequently reducing the scalar Feynman integrals to master integrals with **Kira** [104, 105, 186]. The master integrals are at this point still  $(4 - 2\epsilon)$ -dimensional. Hence, dimension-shift transformations, as explained in sec. 2.4, are applied to express the  $(4 - 2\epsilon)$ -dimensional integrals in the amplitude through the  $(6 - 2\epsilon)$ -dimensional integrals of the quasi-finite basis.

The evaluation of the form factors is performed numerically in **Mathematica** by inserting the numerically evaluated IBP reductions, dimension-shift transformations, and master integrals and expanding in  $\epsilon$ . This evaluation was performed for the benchmark phase space point. The evaluation of the amplitude for other phase space points is in principle possible but would benefit from an automatization of the last steps, which are currently implemented several **Mathematica** scripts.

The amplitudes are obtained by inserting the form factors and spinor structures back into eq. (3.3). At this point, the initial state is restored by substituting  $\epsilon_4$  and  $\tilde{\epsilon}_4$  with the expression given in eq. (2.10). The spinor structures are evaluated by virtue of the spinor helicity formalism as described in ref. [254, 255].

The renormalization of the one-loop and two-loop amplitudes is discussed in sec. 5.2.

Table 5.1.: One-loop integral families.

integral family	$P_1$	$P_2$	$P_3$	$P_4$
box A	$k^2$	$(k + p_1)^2 - m_t^2$	$(k - p_2)^2 - m_t^2$	$(k + p_1 + p_3)^2 - m_t^2$
box B	$k^2$	$(k - p_1)^2 - m_t^2$	$(k + p_2)^2 - m_t^2$	$(k + p_2 + p_3)^2 - m_t^2$
box C	$k^2$	$(k + p_3)^2$	$(k + p_2 + p_3)^2 - m_t^2$	$(k - p_1)^2 - m_t^2$

### 5.1.2. Leading-order and one-loop amplitudes

This section provides a summary of the leading-order and one-loop calculations. The one-loop calculation in particular shares many steps with the two-loop calculation and hence serves as an illustration of the previously summarized calculation steps. The squared one-loop amplitude also contributes to the NNLO cross section. Furthermore, the one-loop currents are also required to cross-check the two-loop IR singularities in sec. 5.3.2. Additionally, one-loop diagrams with counterterm insertions appear in the renormalization of the two-loop amplitude, as explained in sec. 5.2.

The leading-order vector current, to which only the two tree-level diagrams plotted in fig. 2.1 contribute, is given by

$$V^{(0)} = \bar{u}(p_1) \not{\epsilon}_3^* \frac{\not{p}_1 + \not{p}_3 + m_t}{(p_1 + p_3)^2 - m_t^2} \not{\epsilon}_4 v(p_2) + \bar{u}(p_1) \not{\epsilon}_4 \frac{-\not{p}_2 - \not{p}_3 + m_t}{(p_2 + p_3)^2 - m_t^2} \not{\epsilon}_3^* v(p_2). \quad (5.3)$$

When applying the projectors to the vector current, only the three coefficients

$$C_5 = \frac{2}{x}, \quad C_{10} = -\frac{x+z}{xz}, \quad C_{11} = -\frac{2}{xz} \quad (5.4)$$

yield non-zero values while the remaining coefficients vanish. The projection coefficients of the axial-vector current are the same apart from an additional minus sign in all coefficients, i. e.

$$\tilde{C}_5 = -\frac{2}{x}, \quad \tilde{C}_{10} = \frac{x+z}{xz}, \quad \tilde{C}_{11} = \frac{2}{xz}. \quad (5.5)$$

At the one-loop level, 11 Feynman diagrams contribute to the vector current. Three one-loop diagrams are exemplarily depicted in fig. 5.1. The three depicted diagrams also correspond to the box A, box B, and box C integral families as defined in tab. 5.1. The vector current does not receive any contributions from one-loop diagrams with a closed fermion line, as depicted in fig. 5.2. Contributions from Feynman diagrams involving closed fermion loops connected to one photon and two gluons cancel as a direct result of Furry's theorem. The remaining one-loop diagrams involving a closed fermion line have vanishing colour factors. Consequently, also the

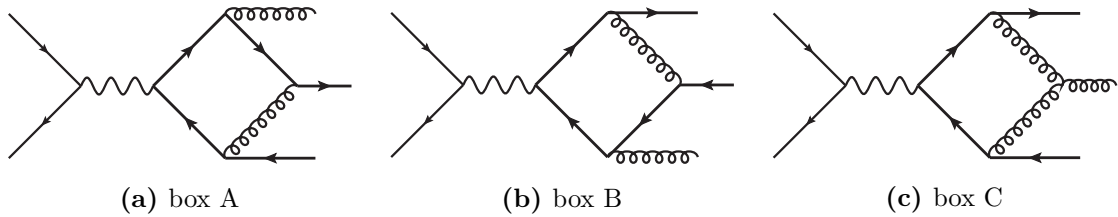
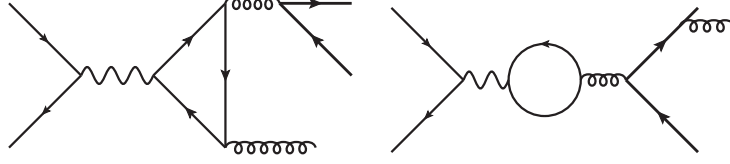


Figure 5.1.: Examples of one-loop Feynman diagrams corresponding to the one-loop integral families defined in tab. 5.1.



**Figure 5.2.:** Examples of one-loop Feynman diagrams with a closed fermion line.

vector current  $V_q$  vanishes at the one-loop level.

The integral families box A and box B are related by exchanging  $p_1 \leftrightarrow p_2$ . Once the projection is applied, the tensor structure of the integrals is resolved and only scalar products involving the loop momentum  $k$  remain. The scalar products are then replaced with inverse propagators as demonstrated in sec. 3.3. For example, for the box A integral family, the scalar products are replaced with

$$k^2 = P_1, \quad k \cdot p_1 = \frac{1}{2}(P_2 - P_1), \quad k \cdot p_2 = \frac{1}{2}(P_1 - P_3), \quad k \cdot p_3 = \frac{1}{2}(P_4 - P_2 - sx). \quad (5.6)$$

The resulting integrals are reduced with **Kira** to the one-loop master integrals

$$\begin{aligned} &I_{0,0,3,1}^{\text{box A}}, \quad I_{0,4,0,0}^{\text{box A}}, \quad I_{0,3,1,0}^{\text{box A}}, \quad I_{0,2,1,1}^{\text{box A}}, \quad I_{2,0,0,2}^{\text{box A}}, \quad I_{2,0,1,1}^{\text{box A}}, \quad I_{1,2,0,1}^{\text{box A}}, \quad I_{1,1,1,1}^{\text{box A}}, \\ &I_{2,0,0,2}^{\text{box B}}, \quad I_{1,0,2,1}^{\text{box B}}, \quad I_{2,1,0,1}^{\text{box B}}, \quad I_{1,1,1,1}^{\text{box B}}, \quad I_{1,1,1,1}^{\text{box C}}. \end{aligned} \quad (5.7)$$

The  $(4 - 2\epsilon)$ -dimensional integral basis in eq. (5.7) is expressed through the corresponding  $(6 - 2\epsilon)$ -dimensional integrals by a dimension-shift transformation. This yields quasi-finite master integrals. These one-loop master integrals were chosen in order to apply the same techniques as in the two-loop case.

In the next step, the master integrals are calculated. Numerical values for one-loop Feynman integrals up to order  $\epsilon^0$  can be calculated with **Collier** [256], **LoopTools** [257], **OneL0op** [258], and **QCDLoop** [259, 260], which partly rely on **ff** [261]. For this work, the one-loop master integrals were calculated using the same techniques as for the two-loop master integrals since the one-loop integrals are required up to order  $\epsilon^2$ . The calculation of the leading-colour two-loop master integrals is presented in detail in chapter 4 and hence is not repeated here for the one-loop integrals. Numerical reference values for the one-loop master integrals are given in tab. C.1.

The unrenormalized form factors are evaluated by inserting the IBP reductions, dimension-shift transformations, and master integrals and expanding in  $\epsilon$ . The renormalization is described in sec. 5.2. The renormalized one-loop form factors expanded up to  $\epsilon^2$  at the benchmark point  $x = 0.2$ ,  $z = 0.05$  and  $m = 289/2500$  are given in tab. C.3 in app. C.2.

## 5.2. Renormalization

The one-loop and two-loop currents still contain UV divergences which are cancelled by renormalization. The gluon field  $A_\mu^a$ , the ghost fields  $\chi_{1,2}^a$ , the massive top-quark field  $\psi^t$ , the massless quark fields  $\psi^q$ , the coupling constant of the strong interaction  $g_s$ , and the top-quark mass  $m_t$  are renormalized multiplicatively by defining

$$\begin{aligned} A_{0\mu}^a &= Z_g^{1/2} A_\mu^a, & \chi_{0,1,2}^a &= \tilde{Z}_g^{1/2} \chi_{1,2}^a, & \psi_0^t &= Z_t^{1/2} \psi^t, & \psi_0^q &= Z_q^{1/2} \psi^q, \\ g_{s0} &= Z_{g_s} g_s, & m_{t0} &= Z_m m_t. \end{aligned} \quad (5.8)$$

## 5. Amplitude evaluation and numerical results

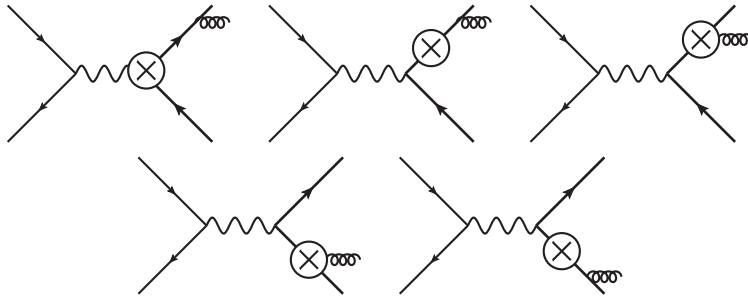


**Figure 5.3.:** One-loop counterterm diagrams.

In this formula, the unrenormalized quantities, which are also called ‘bare’ quantities, are indicated with index 0. The ghost field renormalization does not contribute in this calculation. The renormalized quantities are rendered finite as the  $Z_i$  factors absorb the divergences. The top-quark wave function, the top-quark mass, and the gluon wave function are renormalized in the on-shell scheme. The coupling constant of the strong interaction is renormalized in the  $\overline{\text{MS}}$  scheme with  $n_l = 5$  active quark flavours. The required renormalization constants are given in ref. [152, 262].

The renormalization constants taken from ref. [152] are defined with  $n_f = n_h + n_l = 6$  active quark flavours. The scheme with  $n_l$  active flavours can be obtained by applying the decoupling relation

$$\alpha_s^{(n_f)} = \zeta_{\alpha_s} \alpha_s^{(n_l)}, \quad (5.9)$$

where the decoupling constant is [152]

$$\begin{aligned} \zeta_{\alpha_s} = 1 + \left( \frac{\alpha_s^{(n_l)}}{2\pi} \right) T_F n_h \left( \frac{2}{3} \ln \left( \frac{\mu^2}{m_t^2} \right) + \frac{1}{3} \epsilon \ln \left( \frac{\mu^2}{m_t^2} \right)^2 + \frac{\pi^2}{18} \epsilon + \frac{1}{9} \epsilon^2 \ln \left( \frac{\mu^2}{m_t^2} \right)^3 \right. \\ \left. + \frac{\pi^2}{18} \epsilon^2 \ln \left( \frac{\mu^2}{m_t^2} \right) - \frac{2}{9} \epsilon^2 \zeta_3 \right) + \mathcal{O} \left( \left( \alpha_s^{(n_l)} \right)^2 \right). \end{aligned} \quad (5.10)$$

Both schemes yield the same results for the calculation at hand since the substitution in eq. (5.9) does not contribute to the one-loop amplitude and the leading-colour two-loop amplitude. The dependence of the coupling constant of the strong interaction on the number of active quark flavours is suppressed in the following.

The expansion of the renormalization constants in the coupling constant of the strong interaction is

$$Z_i = 1 + \delta_i = 1 + \left(\frac{\alpha_s}{2\pi}\right) \delta_i^{(1)} + \left(\frac{\alpha_s}{2\pi}\right)^2 \delta_i^{(2)} + \mathcal{O}(\alpha_s^3). \quad (5.11)$$

The  $\delta_i^{(1)}$  terms have to be expanded up to order  $\epsilon^2$  and the  $\delta_i^{(2)}$  terms contribute up to order  $\epsilon^0$  to the two-loop renormalization. Applying the definitions of eq. (5.8) and expanding in  $\alpha_s$  gives rise to the self-energy counterterm Feynman rules

$$\begin{aligned}
\mu, a \text{---} \text{oooo} \bigcirc \text{oooo} \nu, b \text{---}^p &= i(Z_g - 1) \delta_{ab} (p_\mu p_\nu - p^2 g_{\mu\nu}) \\
&= i \left( \left( \frac{\alpha_s}{2\pi} \right) \delta_g^{(1)} + \left( \frac{\alpha_s}{2\pi} \right)^2 \delta_g^{(2)} \right) \delta_{ab} (p_\mu p_\nu - p^2 g_{\mu\nu}) + \mathcal{O}(\alpha_s^3)
\end{aligned} \tag{5.12}$$

and

$$\begin{aligned}
\text{Diagram: } i \text{ --- } \text{circle with } \otimes \text{ --- } j \text{ with momentum } p \text{ entering from top} &= i \left[ (Z_t - 1) \not{p} - (Z_t Z_m - 1) m_t \right] \delta_{ij} \\
&= i \left( \left( \frac{\alpha_s}{2\pi} \right) \left[ \delta_t^{(1)} \not{p} - (\delta_t^{(1)} + \delta_m^{(1)}) m_t \right] \right. \\
&\quad \left. + \left( \frac{\alpha_s}{2\pi} \right)^2 \left[ \delta_t^{(2)} \not{p} - (\delta_t^{(2)} + \delta_m^{(2)} + \delta_t^{(1)} \delta_m^{(1)}) m_t \right] \right) \delta_{ij} + \mathcal{O}(\alpha_s^3). \quad (5.13)
\end{aligned}$$

Similarly, the counterterm Feynman rules for the interaction vertices are

$$\begin{aligned}
\text{Diagram: } \mu \text{ --- wavy line --- circle with } \otimes \text{ --- } i, j &= (Z_t - 1) i Q_t \gamma^\mu \delta_{ij} \\
&= \left( \left( \frac{\alpha_s}{2\pi} \right) \delta_t^{(1)} + \left( \frac{\alpha_s}{2\pi} \right)^2 \delta_t^{(2)} \right) i Q_t \gamma^\mu \delta_{ij} + \mathcal{O}(\alpha_s^3), \quad (5.14)
\end{aligned}$$

$$\begin{aligned}
\text{Diagram: } \mu, a_1 \text{ --- wavy line --- circle with } \otimes \text{ --- } \rho, a_3 \text{ and } \nu, a_2 \text{ with momenta } p_1, p_2, p_3 &= (Z_{g_s} Z_g^{3/2} - 1) g_s f^{a_1 a_2 a_3} (g^{\mu\nu} (p_1^\rho - p_2^\rho) + g^{\nu\rho} (p_2^\mu - p_3^\mu) + g^{\rho\mu} (p_3^\nu - p_1^\nu)) \\
&= \left( \frac{\alpha_s}{2\pi} \right) \left( \delta_{g_s}^{(1)} + \frac{3}{2} \delta_g^{(1)} \right) g_s f^{a_1 a_2 a_3} (g^{\mu\nu} (p_1^\rho - p_2^\rho) + g^{\nu\rho} (p_2^\mu - p_3^\mu) \\
&\quad + g^{\rho\mu} (p_3^\nu - p_1^\nu)) + \mathcal{O}(\alpha_s^2), \quad (5.15)
\end{aligned}$$

$$\begin{aligned}
\text{Diagram: } a, \mu \text{ --- wavy line --- circle with } \otimes \text{ --- } i, j &= (Z_{g_s} Z_g^{1/2} Z_t - 1) i g_s \gamma^\mu t_{ij}^a \\
&= \left( \left( \frac{\alpha_s}{2\pi} \right) \left( \delta_t^{(1)} + \frac{1}{2} \delta_g^{(1)} + \delta_{g_s}^{(1)} \right) \right. \\
&\quad + \left( \frac{\alpha_s}{2\pi} \right)^2 \left( \delta_t^{(2)} + \frac{1}{2} \delta_g^{(2)} + \delta_{g_s}^{(2)} - \frac{1}{8} (\delta_{g_s}^{(1)})^2 + \frac{1}{2} \delta_{g_s}^{(1)} \delta_g^{(1)} \right. \\
&\quad \left. \left. + \frac{1}{2} \delta_g^{(1)} \delta_t^{(1)} + \delta_{g_s}^{(1)} \delta_t^{(1)} \right) \right) i g_s \gamma^\mu t_{ij}^a + \mathcal{O}(\alpha_s^3). \quad (5.16)
\end{aligned}$$

For the one-loop renormalization, only tree-level Feynman diagrams with counterterm insertions as shown in fig. 5.3 contribute. Hence, the renormalized one-loop amplitude is given by

$$\mathcal{M}_{\text{ren}}^{(1)} = \mathcal{M}_{\text{bare}}^{(1)} + \mathcal{M}_{1 \text{ ct}}^{(0)}, \quad (5.17)$$

where  $\mathcal{M}_{\text{bare}}^{(1)}$  is the unrenormalized one-loop amplitude and  $\mathcal{M}_{1 \text{ ct}}^{(0)}$  is the corresponding counterterm amplitude. The upper index in brackets denotes the number of loops of each term, corresponding to the notation introduced in eq. (2.13).

## 5. Amplitude evaluation and numerical results

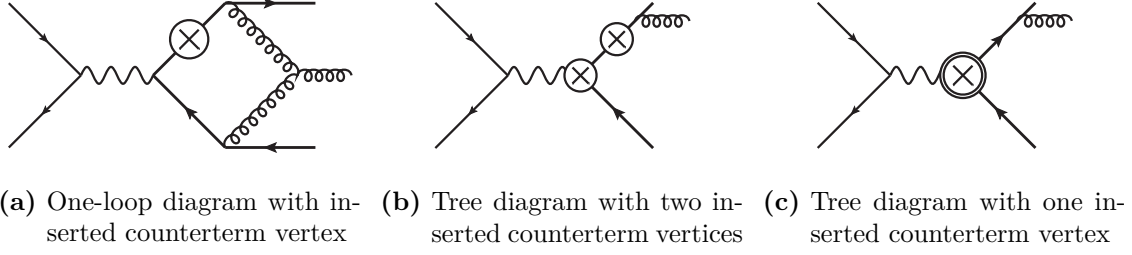


**Figure 5.4.:** Examples of counterterm Feynman diagrams. Counterterm vertices with a double circle, as in fig. c, indicate that the counterterm coefficient of order  $\alpha_s^2$  contributes, while in fig. a, b only the order  $\alpha_s$  coefficients contribute.

Applying the counterterm Feynman rules at the two-loop level gives rise to the three types of counterterm Feynman diagrams that are exemplarily illustrated in fig. 5.4. Correspondingly, the renormalized two-loop amplitude is given by

$$\mathcal{M}_{\text{ren}}^{(2)} = \mathcal{M}_{\text{bare}}^{(2)} + \mathcal{M}_{1 \text{ ct}}^{(1)} + \mathcal{M}_{2 \text{ ct}}^{(0)} + \mathcal{M}_{1 \text{ ct}}^{(0)}, \quad (5.18)$$

where the unrenormalized or ‘bare’ two-loop amplitude is  $\mathcal{M}_{\text{bare}}^{(2)}$ . The remaining three terms are:

- The term  $\mathcal{M}_{1 \text{ ct}}^{(1)}$ , exemplarily illustrated in fig. 5.4a, contains all one-loop diagrams with one counterterm vertex. In this term, the counterterm vertices given in eq. (5.13-5.16) contribute at order  $\alpha_s$  and both the one-loop integrals as well as the renormalization constants contribute up to order  $\epsilon^2$ .
- The term  $\mathcal{M}_{2 \text{ ct}}^{(0)}$  contains all tree-level Feynman diagrams with two counterterm vertices, each contributing at order  $\alpha_s$ . This term is illustrated in fig. 5.4b.
- The term  $\mathcal{M}_{1 \text{ ct}}^{(0)}$  contains all tree-level Feynman diagrams with one counterterm insertion, which are exemplarily depicted in fig. 5.4c. The counterterm symbol with two circles indicates that the counterterm coefficient of order  $\alpha_s^2$  contributes.

## 5.3. Cross-checks

### 5.3.1. Electroweak Ward identities

The electroweak Ward identities derived in sec. 3.5 serve as a strong cross-check for the one-loop and leading-colour two-loop projection coefficients. Inserting the one-loop projection coefficients

given in tab. C.3 into the four equations given in eq. (3.48) yields

$$\begin{aligned}
W_1 &= N_c \left( 0(0)\epsilon^{-2} + 0(0)\epsilon^{-1} + 0(1 \cdot 10^{-12})\epsilon^0 + 0(4 \cdot 10^{-11})\epsilon^1 + 0(2 \cdot 10^{-9})\epsilon^2 \right) \\
&\quad + N_c^{-1} \left( 0(0)\epsilon^{-2} + 0(0)\epsilon^{-1} + 0(1 \cdot 10^{-12})\epsilon^0 + 0(1 \cdot 10^{-10})\epsilon^1 + 0(7 \cdot 10^{-9})\epsilon^2 \right), \\
W_2 &= N_c \left( 0(2 \cdot 10^{-12})\epsilon^{-2} + 0(2 \cdot 10^{-11})\epsilon^{-1} + 0(6 \cdot 10^{-11})\epsilon^0 + 0(2 \cdot 10^{-10})\epsilon^1 + 0(5 \cdot 10^{-10})\epsilon^2 \right) \\
&\quad + N_c^{-1} \left( 0(0)\epsilon^{-2} + 0(4 \cdot 10^{-10})\epsilon^{-1} + 0(2 \cdot 10^{-9})\epsilon^0 + 0(4 \cdot 10^{-9})\epsilon^1 + 0(1 \cdot 10^{-8})\epsilon^2 \right), \\
W_3 &= N_c \left( 0(2 \cdot 10^{-12})\epsilon^{-2} + 0(2 \cdot 10^{-11})\epsilon^{-1} + 0(8 \cdot 10^{-11})\epsilon^0 + 0(2 \cdot 10^{-10})\epsilon^1 + 0(8 \cdot 10^{-10})\epsilon^2 \right) \\
&\quad + N_c^{-1} \left( 0(0)\epsilon^{-2} + 0(3 \cdot 10^{-9})\epsilon^{-1} + 0(2 \cdot 10^{-8})\epsilon^0 + 0(5 \cdot 10^{-8})\epsilon^1 + 0(1 \cdot 10^{-7})\epsilon^2 \right), \\
W_4 &= N_c \left( 0(0)\epsilon^{-2} + 0(0)\epsilon^{-1} + 0(1 \cdot 10^{-13})\epsilon^0 + 0(2 \cdot 10^{-12})\epsilon^1 + 0(1 \cdot 10^{-10})\epsilon^2 \right) \\
&\quad + N_c^{-1} \left( 0(0)\epsilon^{-2} + 0(0)\epsilon^{-1} + 0(3 \cdot 10^{-13})\epsilon^0 + 0(3 \cdot 10^{-12})\epsilon^1 + 0(1 \cdot 10^{-10})\epsilon^2 \right). \tag{5.19}
\end{aligned}$$

Numerical zeros are here denoted with a zero followed by the rounded uncertainty in brackets. The results in eq. (5.19) are numerically compatible with zero and at least 11 decimal digits cancel in the calculation.

Correspondingly, inserting the leading-colour two-loop coefficients of the vector current given in tab. C.6 into the Ward identities in eq. (3.48) yields

$$\begin{aligned}
W_1 &= 0(2 \cdot 10^{-18})\epsilon^{-4} + 0(5 \cdot 10^{-16})\epsilon^{-3} + 0(1 \cdot 10^{-14})\epsilon^{-2} \\
&\quad + 0(8 \cdot 10^{-12})\epsilon^{-1} + 0(3 \cdot 10^{-10})\epsilon^0, \\
W_2 &= 0(1 \cdot 10^{-19})\epsilon^{-4} + 0(2 \cdot 10^{-16})\epsilon^{-3} + 0(2 \cdot 10^{-15})\epsilon^{-2} \\
&\quad + 0(6 \cdot 10^{-13})\epsilon^{-1} + 0(2 \cdot 10^{-11})\epsilon^0, \\
W_3 &= 0(9 \cdot 10^{-19})\epsilon^{-4} + 0(5 \cdot 10^{-16})\epsilon^{-3} + 0(8 \cdot 10^{-15})\epsilon^{-2} \\
&\quad + 0(5 \cdot 10^{-12})\epsilon^{-1} + 0(2 \cdot 10^{-10})\epsilon^0, \\
W_4 &= 0(9 \cdot 10^{-20})\epsilon^{-4} + 0(2 \cdot 10^{-16})\epsilon^{-3} + 0(2 \cdot 10^{-15})\epsilon^{-2} \\
&\quad + 0(1 \cdot 10^{-13})\epsilon^{-1} + 0(6 \cdot 10^{-11})\epsilon^0. \tag{5.20}
\end{aligned}$$

The results in eq. (5.20) are numerically compatible with zero and at least 15 decimal digits cancel in the calculation.

The leading-colour two-loop axial-vector current projection coefficients are given in tab. C.7. The Ward identities for the axial-vector current in eq. (3.53) require the corresponding coefficients of the Goldstone current  $A_t^{\text{Goldstone}}$ . The projection coefficients of the Goldstone current were calculated separately and the results are given in tab. C.8 in the appendix. The differences of the left- and right-hand sides of eq. (3.53) are

$$\begin{aligned}
C_1^{\text{Goldstone}} - \tilde{W}_1 &= 0(3 \cdot 10^{-20})\epsilon^{-4} + 0(6 \cdot 10^{-17})\epsilon^{-3} + 0(3 \cdot 10^{-16})\epsilon^{-2} \\
&\quad + 0(1 \cdot 10^{-13})\epsilon^{-1} + 0(6 \cdot 10^{-12})\epsilon^0, \\
C_2^{\text{Goldstone}} - \tilde{W}_2 &= 0(6 \cdot 10^{-20})\epsilon^{-4} + 0(5 \cdot 10^{-17})\epsilon^{-3} + 0(2 \cdot 10^{-17})\epsilon^{-2} \\
&\quad + 0(3 \cdot 10^{-13})\epsilon^{-1} + 0(1 \cdot 10^{-11})\epsilon^0, \\
C_3^{\text{Goldstone}} - \tilde{W}_3 &= 0(9 \cdot 10^{-19})\epsilon^{-4} + 0(1 \cdot 10^{-15})\epsilon^{-3} + 0(2 \cdot 10^{-14})\epsilon^{-2} \\
&\quad + 0(4 \cdot 10^{-12})\epsilon^{-1} + 0(2 \cdot 10^{-10})\epsilon^0, \\
C_4^{\text{Goldstone}} - \tilde{W}_4 &= 0(4 \cdot 10^{-21})\epsilon^{-4} + 0(3 \cdot 10^{-16})\epsilon^{-3} + 0(2 \cdot 10^{-16})\epsilon^{-2} \\
&\quad + 0(1 \cdot 10^{-15})\epsilon^{-1} + 0(3 \cdot 10^{-12})\epsilon^0, \tag{5.21}
\end{aligned}$$

## 5. Amplitude evaluation and numerical results

where  $\tilde{W}_i$  denotes the right-hand sides of the expressions in eq. (3.53). The results in eq. (5.21) are also numerically compatible with zero and also at least 15 decimal digits cancel in the calculation.

In conclusion, the numerical results obey the Ward identities.

### 5.3.2. Analytic structure of the singularity

The general analytic structure of the IR singularities of renormalized QCD amplitudes is understood at the two-loop level [263–270]. In the following, the poles of the leading-colour two-loop amplitude are calculated for the process at hand and used to cross-check the previously obtained amplitude.

The following paragraphs summarize the notation and general formulas for a generic QCD process involving  $n$  external QCD partons, for which momenta and masses are denoted with  $\{p\} = \{p_1, p_2, \dots, p_n\}$  and  $\{m\} = \{m_1, m_2, \dots, m_n\}$  with  $m_i^2 = p_i^2$ .

The colour-space formalism used in ref. [271, 272], in which the  $n$ -parton amplitude  $|\mathcal{M}_n\rangle$  is an  $n$ -dimensional vector in colour space, is adopted. An orthonormal basis in the colour space  $\{|c_1, \dots, c_n\rangle\}$  is introduced with the  $n$  colour indices  $c_i$  being  $c_i = 1, \dots, N_c$  for quarks and antiquarks and with  $c_i = 1, \dots, N_c^2 - 1$  for gluons. The amplitude is then written as

$$\mathcal{M}_n^{c_1, \dots, c_n} = \langle c_1, \dots, c_n | \mathcal{M}_n \rangle. \quad (5.22)$$

The colour generator  $\mathbf{T}_i$  associated with the  $i$ th particle is applied on vectors in colour space as

$$\langle c_1, \dots, c_i, \dots, c_n | \mathbf{T}_i^a | b_1, \dots, b_i, \dots, b_n \rangle = \delta_{c_1 b_1} \dots T_{c_i b_i}^a \dots \delta_{c_n b_n}. \quad (5.23)$$

The colour generators are  $(T^a)_{cb} = t_{cb}^a$  for external quarks and  $(T^a)_{cb} = -t_{bc}^a$  for external antiquarks, where  $t_{cb}^a$  are the generators of the  $SU(N_c)$  in the fundamental representation. For external gluons, the generators are  $(T^a)_{bc} = -if^{abc}$ , where  $f^{abc}$  is the structure constant of the  $SU(N_c)$ . Furthermore, the shorthand notation  $\mathbf{T}_i \cdot \mathbf{T}_j = \sum_{a=1}^{N_c^2-1} \mathbf{T}_i^a \cdot \mathbf{T}_j^a$  is applied. The colour algebra is

$$\mathbf{T}_i \cdot \mathbf{T}_j = \mathbf{T}_j \cdot \mathbf{T}_i \quad \text{if } i \neq j, \quad \mathbf{T}_i^2 = C_i \quad (5.24)$$

with  $C_q = C_{\bar{q}} = C_F = \frac{N_c^2-1}{2N_c}$  and  $C_g = C_A = N_c$ .

The IR singularities of the renormalized QCD amplitude  $|\mathcal{M}_{\text{ren}}\rangle$  can be cancelled through IR renormalization, i. e.

$$|\mathcal{M}_{\text{fin}}\rangle = \mathbf{Z}^{-1}(\epsilon, \{p\}, \{m\}, \mu) |\mathcal{M}_{\text{ren}}\rangle, \quad (5.25)$$

where the renormalization factor  $\mathbf{Z}$  obeys the differential equation

$$\mathbf{Z}^{-1}(\epsilon, \{p\}, \{m\}, \mu) \frac{d}{d \ln \mu} \mathbf{Z}(\epsilon, \{p\}, \{m\}, \mu) = -\mathbf{\Gamma}(\{p\}, \{m\}, \mu). \quad (5.26)$$

Hence, the singularity structure of QCD amplitudes is governed by the anomalous-dimension



matrix  $\Gamma(\{p\}, \{m\}, \mu)$ , which is for two-loop amplitudes involving massive quarks given by [267]

$$\begin{aligned}
\Gamma(\{p\}, \{m\}, \mu) = & \sum_{(i,j)} \frac{\mathbf{T}_i \cdot \mathbf{T}_j}{2} \gamma_{\text{cusp}}(\alpha_s) \ln \left( \frac{\mu^2}{-s_{ij}} \right) + \sum_i \gamma^i(\alpha_s) \\
& - \sum_{(I,J)} \frac{\mathbf{T}_I \cdot \mathbf{T}_J}{2} \gamma_{\text{cusp}}(\beta_{IJ}, \alpha_s) + \sum_I \gamma^I(\alpha_s) \\
& + \sum_{(I,j)} \mathbf{T}_I \cdot \mathbf{T}_j \gamma_{\text{cusp}}(\alpha_s) \ln \left( \frac{m_I \mu}{-s_{Ij}} \right) \\
& + \sum_{(I,J,K)} i f^{abc} \mathbf{T}_I^a \mathbf{T}_J^b \mathbf{T}_K^c F_1(\beta_{IJ}, \beta_{JK}, \beta_{KI}) \\
& + \sum_{(I,J)} \sum_k i f^{abc} \mathbf{T}_I^a \mathbf{T}_J^b \mathbf{T}_k^c f_2 \left( \beta_{IJ}, \ln \left( \frac{-\sigma_{Jk} v_J \cdot p_k}{-\sigma_{Ik} v_I \cdot p_k} \right) \right). \quad (5.27)
\end{aligned}$$

In this formula, lower case indices, e. g.  $i, j, k$ , denote massless particles while upper case indices, e. g.  $I, J, K$ , denote massive particles. Sums denoted by  $(i, j, \dots)$  are performed over tuples of distinct parton indices, i. e. the configuration  $i = j$  is excluded. This means, for example, that the summation over  $(I, J)$  excludes the cases  $(I, J) = (t, t)$  and  $(I, J) = (\bar{t}, \bar{t})$  but includes both the configurations  $(I, J) = (t, \bar{t})$  and  $(I, J) = (\bar{t}, t)$  [270]. Scalar products of massless as well as massive particles are denoted with

$$s_{ij} = 2\sigma_{ij} p_i \cdot p_j + i\varepsilon, \quad (5.28)$$

where the sign factor  $\sigma_{ij}$  is  $\sigma_{ij} = +1$  if the respective momenta  $p_i, p_j$  are both incoming or both outgoing and  $\sigma_{ij} = -1$  if one momentum is incoming and the other momentum is outgoing. Furthermore, the velocity  $v_I = p_I/m_I$ , the recoil variable  $w_{IJ} = -\sigma_{IJ} v_I \cdot v_J - i\varepsilon$ , and the cusp angle

$$\cosh \beta_{IJ} = -\frac{s_{IJ}}{2m_I m_J} = w_{IJ} \quad (5.29)$$

are defined for massive particles. The functions  $F_1$  and  $f_2$  were computed in ref. [268] and the required anomalous dimensions can be found in ref. [152].

The colour vector for the process at hand is relatively simple as the only appearing colour structure is  $|c\rangle = t_{ij}^a$ . Note that the colour indices  $i, j$ , and  $a$  are used for the external particles in the following for simplicity. The resulting anomalous-dimension matrix hence only has one entry. In general, i. e. for processes with multiple independent colour structures, this is not the case. For example, the top-quark pair production channel  $q\bar{q} \rightarrow t\bar{t}$  has two independent colour structures while the  $gg \rightarrow t\bar{t}$  process has three, which give rise to  $2 \times 2$  and  $3 \times 3$  anomalous-dimension matrices correspondingly [268].

For the process at hand, the application of the colour correlators yields

$$\begin{aligned}
\mathbf{T}_t \cdot \mathbf{T}_g |c\rangle &= t_{ik}^b t_{kj}^c (-i f^{bac}) = -\frac{N_c}{2} |c\rangle, \\
\mathbf{T}_t \cdot \mathbf{T}_g |c\rangle &= t_{ik}^c (-t_{kj}^b) (-i f^{bac}) = -\frac{N_c}{2} |c\rangle, \\
\mathbf{T}_t \cdot \mathbf{T}_{\bar{t}} |c\rangle &= t_{ik}^b t_{kl}^a (-t_{lj}^b) = \frac{1}{2N_c} |c\rangle, \\
i f^{bce} \mathbf{T}_t^b \mathbf{T}_{\bar{t}}^c \mathbf{T}_g^e |c\rangle &= i f^{bce} t_{ik}^b t_{kl}^f (-t_{lj}^c) (-i f^{eaf}) = 0. \quad (5.30)
\end{aligned}$$

## 5. Amplitude evaluation and numerical results

The three-particle correlators vanish for this process. Additionally, the correlator  $\mathbf{T}_t \cdot \mathbf{T}_{\bar{t}}$  only contributes to sub-leading-colour terms.

Hence, the anomalous-dimension matrix for this process is

$$\begin{aligned} \mathbf{\Gamma}(\{x_i\}, \mu, \alpha_s) = & 2\gamma^t(\alpha_s) + \gamma^g(\alpha_s) - \frac{1}{2N_c} \gamma_{\text{cusp}}(\beta_{t\bar{t}}, \alpha_s) \\ & - \frac{N_c}{2} \gamma_{\text{cusp}}(\alpha_s) \left( \ln \left( \frac{m_t \mu}{-2sx} \right) + \ln \left( \frac{m_t \mu}{-2sz} \right) \right) \end{aligned} \quad (5.31)$$

with

$$\beta_{t\bar{t}} = \cosh^{-1} \left( \frac{2m + x + z - 1}{2m} \right). \quad (5.32)$$

According to ref. [268], the general  $\mathbf{Z}$  factor at two-loop order is

$$\begin{aligned} \mathbf{Z} = & 1 + \left( \frac{\alpha_s}{4\pi} \right) \mathbf{Z}^{(1)} + \left( \frac{\alpha_s}{4\pi} \right)^2 \mathbf{Z}^{(2)} + \mathcal{O}(\alpha_s^3) \\ = & 1 + \left( \frac{\alpha_s}{4\pi} \right) \left( \frac{\mathbf{\Gamma}'_0}{4\epsilon^2} + \frac{\mathbf{\Gamma}_0}{2\epsilon} \right) \\ & + \left( \frac{\alpha_s}{4\pi} \right)^2 \left( \frac{(\mathbf{\Gamma}'_0)^2}{32\epsilon^4} + \frac{\mathbf{\Gamma}'_0}{8\epsilon^3} \left( \mathbf{\Gamma}_0 - \frac{3\beta_0}{2} \right) + \frac{\mathbf{\Gamma}_0}{8\epsilon^2} (\mathbf{\Gamma}_0 - 2\beta_0) + \frac{\mathbf{\Gamma}'_1}{16\epsilon^2} + \frac{\mathbf{\Gamma}_1}{4\epsilon} \right. \\ & \quad \left. - \frac{2T_F}{3} \sum_{I=1}^{n_h} \left[ \mathbf{\Gamma}'_0 \left( \frac{1}{2\epsilon^2} \ln \left( \frac{\mu^2}{m_I^2} \right) + \frac{1}{4\epsilon} \left[ \ln^2 \left( \frac{\mu^2}{m_I^2} \right) + \frac{\pi^2}{6} \right] \right) \right. \right. \\ & \quad \left. \left. + \frac{\mathbf{\Gamma}_0}{\epsilon} \ln \left( \frac{\mu^2}{m_I^2} \right) \right] \right) + \mathcal{O}(\alpha_s^3). \end{aligned} \quad (5.34)$$

The expansion coefficients  $\mathbf{\Gamma}_n$  are defined by

$$\mathbf{\Gamma} = \sum_{n \geq 0} \mathbf{\Gamma}_n \left( \frac{\alpha_s}{4\pi} \right)^{n+1} \quad (5.35)$$

and a similar expansion holds for  $\Gamma'$  which is defined as

$$\Gamma'(\{x_i\}, \mu, \alpha_s) = \frac{\partial}{\partial \ln(\mu)} \mathbf{\Gamma}(\{x_i\}, \mu, \alpha_s) = \sum_{n \geq 0} \mathbf{\Gamma}'_n \left( \frac{\alpha_s}{4\pi} \right)^{n+1}. \quad (5.36)$$

Inserting  $\mathbf{\Gamma}$  from eq. (5.31) into eq. (5.34) yields

$$\begin{aligned} \mathbf{Z}^{(1)} = & N_c \left( -\frac{1}{\epsilon^2} - \frac{1}{\epsilon} \left( \frac{17}{6} + \ln \left( -\frac{m}{x} \right) + \ln \left( -\frac{m}{z} \right) \right) \right) + \frac{5}{3\epsilon} \\ & + N_c^{-1} \frac{1}{\epsilon} \left( 1 - \frac{1 - 2m - x - z}{1 - x - z} \sqrt{\frac{1 - x - z}{1 - 4m - x - z}} \text{sech}^{-1} \left( \frac{2m}{2m + x + z - 1} \right) \right) \end{aligned} \quad (5.37)$$

and

$$\begin{aligned}
\mathbf{Z}_{\text{LC}}^{(2)} = & N_c^2 \left( \frac{1}{2\epsilon^4} + \frac{1}{\epsilon^3} \left( \frac{67}{12} + \ln \left( -\frac{m}{x} \right) + \ln \left( -\frac{m}{z} \right) \right) \right. \\
& + \frac{1}{72\epsilon^2} \left( 2 \left( 3\pi^2 - 67 \right) + 22 \left( 6 \ln \left( -\frac{m}{x} \right) + 6 \ln \left( -\frac{m}{z} \right) + 17 \right) \right. \\
& \quad \left. \left. + \left( 6 \ln \left( -\frac{m}{x} \right) + 6 \ln \left( -\frac{m}{z} \right) + 17 \right)^2 \right) \right. \\
& \left. + \frac{1}{\epsilon} \left( \frac{-108\zeta_3 + 69\pi^2 - 1972}{216} + \frac{1}{18} \left( 3\pi^2 - 67 \right) \left( \ln \left( -\frac{m}{x} \right) + \ln \left( -\frac{m}{z} \right) \right) \right) \right). \tag{5.38}
\end{aligned}$$

For the latter coefficient, only the leading-colour term is stated. The IR singularities of the one-loop and two-loop amplitudes are given by

$$\begin{aligned}
|\mathcal{M}_n^{(1),\text{sing}}\rangle &= \mathbf{Z}^{(1)} |\mathcal{M}_n^{(0)}\rangle, \\
|\mathcal{M}_n^{(2),\text{sing}}\rangle &= \left[ \mathbf{Z}^{(2)} - \left( \mathbf{Z}^{(1)} \right)^2 \right] |\mathcal{M}_n^{(0)}\rangle + \left( \mathbf{Z}^{(1)} |\mathcal{M}_n^{(1)}\rangle \right)_{\text{poles}}. \tag{5.39}
\end{aligned}$$

The IR singularities obtained from these equations agree numerically with the poles of the one-loop vector current, the leading-colour one-loop axial-vector current, and the leading-colour two-loop vector and axial-vector currents within their numerical uncertainties. This was checked for the projection coefficients given in tab. C.3, tab. C.5, tab. C.6, and tab. C.7.

The  $\epsilon^{-2}$  and  $\epsilon^{-1}$  poles of the one-loop currents agree for at least 12 digits with the analytical results. The maximal relative difference of the numerical and analytical results for the poles of the leading-colour two-loop vector current coefficients is

$$0(4 \cdot 10^{-22})\epsilon^{-4} + 0(3 \cdot 10^{-18})\epsilon^{-3} + 0(2 \cdot 10^{-12})\epsilon^{-2} + 0(2 \cdot 10^{-12})\epsilon^{-1}. \tag{5.40}$$

The corresponding maximal relative difference for the poles of the axial-vector current is

$$0(5 \cdot 10^{-22})\epsilon^{-4} + 0(3 \cdot 10^{-18})\epsilon^{-3} + 0(1 \cdot 10^{-14})\epsilon^{-2} + 0(4 \cdot 10^{-14})\epsilon^{-1}. \tag{5.41}$$

Note that also the two-loop singularity structure given in eq. (5.39) acquires a non-vanishing numerical uncertainty originating from the one-loop uncertainties. The relative uncertainties stated in eq. (5.40) and eq. (5.41) include these uncertainties as well as the uncertainties of the leading-colour two-loop currents.

Also note that only the coefficients which contribute at leading-order have non-vanishing  $\epsilon^{-4}$  and  $\epsilon^{-3}$  coefficients in tab. C.6 and tab. C.7. All remaining  $\epsilon^{-4}$  and  $\epsilon^{-3}$  coefficients agree numerically with zero and have uncertainties below  $10^{-15}$ .

## 5.4. Numerical results

In this section, numerical results for the leading-colour one-loop and two-loop amplitudes are presented for the benchmark phase space point defined in eq. (2.7). Furthermore, the  $Z$  boson mass  $m_Z = 91.1876$  and the electroweak mixing angle  $\sin^2 \theta_w = 0.2229$  are used.

In the here applied notation, all significant digits of non-zero results are stated. The digit in brackets behind the result indicates the uncertainty of the last stated digit. The same notation is used in app. B and app. C.

## 5. Amplitude evaluation and numerical results

The interference term of the leading-order subamplitude  $\mathcal{M}_\gamma^{(0)}$  and one-loop subamplitude  $\mathcal{M}_\gamma^{(1)}$  summed over all helicities is

$$\begin{aligned} \frac{\sum_{\text{pol}} 2\text{Re}(\mathcal{M}_\gamma^{(0)} \cdot \mathcal{M}_\gamma^{(1)})}{\sum_{\text{pol}} |\mathcal{M}_\gamma^{(0)}|^2} = & N_c \left( + 2.00000000000(1)\epsilon^{-2} + 6.24652974767(1)\epsilon^{-1} \right. \\ & - 1648.1798847751(1)\epsilon^0 - 11068.796935404(1)\epsilon^1 \\ & - 26588.482406286(8)\epsilon^2 \Big) \\ & + N_c^0 \left( - 3.3333333333333333(1)\epsilon^{-1} \right. \\ & + 0.54831135561607547882(1)\epsilon^1 \\ & - 0.26712375625768761898(1)\epsilon^2 \Big) \\ & + N_c^{-1} \left( + 1.234022321(1)\epsilon^{-1} + 73.679059347(1)\epsilon^0 \right. \\ & \left. - 1175.75638908(1)\epsilon^1 - 5119.33855720(6)\epsilon^2 \right). \end{aligned} \quad (5.42)$$

Note that the  $N_c^0$  term originates solely from the renormalization and hence has technically no uncertainty. The stated uncertainty in the 20th digit is only the rounding error.

In the context of this work, the squared leading-colour one-loop amplitude is of particular interest since it also contributes to the leading-colour NNLO corrections. The corresponding leading-colour contribution is

$$\begin{aligned} \frac{\sum_{\text{pol}} |\mathcal{M}^{(1)}|^2}{\sum_{\text{pol}} |\mathcal{M}^{(0)}|^2} = & N_c^2 \left( + 1.00000000000(1)\epsilon^{-4} + 6.24652974767(1)\epsilon^{-3} - 1602.51827251(1)\epsilon^{-2} \right. \\ & \left. - 8235.4565195(1)\epsilon^{-1} + 12466447.351047(1)\epsilon^0 \right). \end{aligned} \quad (5.43)$$

The corresponding contribution involving only the photon yields

$$\begin{aligned} \frac{\sum_{\text{pol}} |\mathcal{M}_\gamma^{(1)}|^2}{\sum_{\text{pol}} |\mathcal{M}_\gamma^{(0)}|^2} = & N_c^2 \left( + 1.00000000000(1)\epsilon^{-4} + 6.24652974767(1)\epsilon^{-3} - 1598.94668370(1)\epsilon^{-2} \right. \\ & \left. - 8201.3884772(1)\epsilon^{-1} + 12468170.294056(1)\epsilon^0 \right) \end{aligned} \quad (5.44)$$

and the contribution involving only the  $Z$  boson yields

$$\begin{aligned} \frac{\sum_{\text{pol}} |\mathcal{M}_Z^{(1)}|^2}{\sum_{\text{pol}} |\mathcal{M}_Z^{(0)}|^2} = & N_c^2 \left( + 1.00000000000(1)\epsilon^{-4} + 6.24652974767(1)\epsilon^{-3} - 1317.36751511(1)\epsilon^{-2} \right. \\ & \left. - 5515.5107062(1)\epsilon^{-1} + 12604004.760224(1)\epsilon^0 \right). \end{aligned} \quad (5.45)$$

The leading-colour two-loop amplitude at the benchmark phase space point is

$$\begin{aligned} \frac{\sum_{\text{pol}} 2\text{Re} \left( \mathcal{M}^{(0)} \cdot \mathcal{M}^{(2)\text{LC}} \right)}{\sum_{\text{pol}} |\mathcal{M}^{(0)}|^2} = & N_c^2 \left( -1.0000000000000000(4)\epsilon^{-4} - 11.7465297476674096(4)\epsilon^{-3} \right. \\ & + 1672.1004246743386908(7)\epsilon^{-2} + 24248.83906708939(4)\epsilon^{-1} \\ & \left. - 3648989.230879838(2)\epsilon^0 \right). \end{aligned} \quad (5.46)$$

The subprocess involving only the photon yields

$$\begin{aligned} \frac{\sum_{\text{pol}} 2\text{Re} \left( \mathcal{M}_{\gamma}^{(0)} \cdot \mathcal{M}_{\gamma}^{(2)\text{LC}} \right)}{\sum_{\text{pol}} |\mathcal{M}_{\gamma}^{(0)}|^2} = & N_c^2 \left( -1.0000000000000000(4)\epsilon^{-4} - 11.7465297476674096(4)\epsilon^{-3} \right. \\ & + 1668.5288358586071638(7)\epsilon^{-2} + 24245.97035161149(4)\epsilon^{-1} \\ & \left. - 3679648.614339240(2)\epsilon^0 \right) \end{aligned} \quad (5.47)$$

and the subprocess involving only the  $Z$  boson yields

$$\begin{aligned} \frac{\sum_{\text{pol}} 2\text{Re} \left( \mathcal{M}_Z^{(0)} \cdot \mathcal{M}_Z^{(2)\text{LC}} \right)}{\sum_{\text{pol}} |\mathcal{M}_Z^{(0)}|^2} = & N_c^2 \left( -1.0000000000000000(1)\epsilon^{-4} - 11.746529747667410(1)\epsilon^{-3} \right. \\ & + 1386.949667274629371(1)\epsilon^{-2} + 24019.80475393273(9)\epsilon^{-1} \\ & \left. - 6096792.398016293(4)\epsilon^0 \right). \end{aligned} \quad (5.48)$$



## 6. Conclusion

In this work, the calculation of the leading-colour two-loop QCD amplitude for top-quark pair production in association with a jet at a lepton collider was presented and numerical results for one benchmark phase space point with a centre-of-mass energy of  $\sqrt{s} = 500$  GeV corresponding to a proposed ILC setup were provided. This is the first time that any two-loop results for this process have been presented. The two-loop amplitude is an essential building block of the full NNLO QCD corrections, which will be crucial for future lepton collider experiments. Improving theoretical predictions for top-quark pair production in association with a jet contributes to more accurate top-quark mass and coupling measurements at lepton colliders.

This five-parton reaction is effectively a 1-to-3 process due to its purely electroweak initial state producing a virtual photon or  $Z$  boson. The two-loop QCD process can be treated as an off-shell photon or  $Z$  boson decaying into a top-quark pair and a gluon. The vector and axial-vector coupling structure of the photon and  $Z$  boson to quarks leads to a straightforward decomposition of the amplitude into vector and axial-vector currents. The currents depend on four independent kinematic variables, which are effectively reduced to three independent variables by setting the centre-of-mass energy  $s$  to one.

The currents were decomposed into spinor structures and scalar form factors. The spinor structures depend on the helicities of the external particles and are relatively compact expressions composed of Dirac spinors, Dirac matrices, polarization vectors, masses, and external momenta. The form factors are scalar quantities, independent of the external helicities, and absorb all complicated parts of the remaining calculation, in particular the Feynman integrals.

The form factors were extracted with projectors. The projection procedure was implemented in  $d$  dimensions in this work, corresponding to the adoption of conventional dimensional regularization. The spinor structures were determined by making a general ansatz for the process at hand on which the QCD Ward identity for the gluon was imposed. This yielded for the vector and axial-vector current 18 independent spinor structures in each case. Electroweak Ward identities for the off-shell photon and  $Z$  boson give rise to relations between the form factors which were later used to check the results.

The tensor Feynman integrals in the extracted form factors only contain scalar products involving loop momenta in the numerator. These scalar products were subsequently replaced with linear combinations of inverse propagators, giving rise to scalar Feynman integrals with negative propagator exponents. The Feynman integrals were then reduced to master integrals using the program Kira.

The calculation of the 90 master integrals of the leading-colour two-loop amplitude constituted the largest part of this work. Accounting for crossed kinematics, it was sufficient to calculate the 54 master integrals of one two-loop integral family and 5 remaining integrals that are products of one-loop integrals. The most complicated Feynman integrals appearing in this calculation were double-box integrals involving internal masses. Quasi-finite Feynman integrals, i.e. Feynman integrals free of subdivergences, in  $6 - 2\epsilon$  dimensions were chosen as integral basis.

In this work, a seminumerical evaluation method was applied, where the Feynman integrals were calculated by numerically solving differential equations in the kinematic variables. However, one drawback of this technique is that the Feynman integrals are not calculated ‘from scratch’ but require initial conditions.

## 6. Conclusion

Consequently, asymptotic expansions, i. e. power-logarithmic expansions, in  $m = m_t^2/s$  were calculated at least up to the 13th order for all master integrals. The leading expansion coefficients were calculated with the expansion by regions. The higher order expansions were obtained by applying the differential equation in  $m$  onto an ansatz for the asymptotic expansions and solving the resulting system of equations. This expansion provided high-precision initial conditions in the small-mass limit at  $m = 0.001$ .

The contributions of the expansion by regions were calculated in large parts with **HyperInt**. Spurious singularities, which prevented a direct evaluation with **HyperInt**, were resolved by applying partial integrations. This step was in fact a bottleneck of this calculation since it was done individually ‘by hand’ for each integral. This was also one major motivation for adopting a quasi-finite basis in this work.

The Feynman integrals for the mass value  $m_t = 170 \text{ GeV}$  were obtained by numerically solving the differential equation in  $m$  while using the asymptotic expansions as initial conditions. Furthermore, the Feynman integrals were calculated for a grid in the two kinematical variables  $x$  and  $z$  ranging from 0.01 to 1.00 with a step size of 0.01 by subsequently solving the respective differential equations. Results for in-between phase space points were obtained by using a Clough-Tocher interpolation scheme.

Solving differential equations numerically is a very well studied technique in physics, mathematics, and computer science and hence a comprehensive infrastructure is readily available: very efficient numerical methods to solve ordinary differential equations which are already implemented in easy-to-apply libraries. In this work, the Bulirsch-Stoer algorithm implemented in the **Boost Library** was used. Singularities of the differential equations were circumvented by contour deformation into the complex plane, which made a detailed study of singularities necessary. For each integration step, a single elliptic contour with a small deformation parameter was used to avoid all singularities. The uncertainties of the solutions of the differential equations were studied extensively. An uncertainty band approach was applied, where the initial conditions were varied according to their uncertainties. Furthermore, initial conditions at a second phase space point were used for a second uncertainty estimate. Both uncertainty estimates agree well for most phase space points although the uncertainty band might underestimate uncertainties close to certain singularities. The master integrals in the physical phase space were obtained for at least 15 decimal digits, but in phase space regions close to certain singularities a loss of precision was observed. The obtained precision is sufficient for all practical purposes.

Internal cross-checks were also performed using IBP relations for special phase space points. This revealed for the interpolated results only accuracy at the permille level. The interpolated master integrals might hence not be sufficiently accurate for a Monte Carlo phase space integration. Possible solutions might be the calculation of a denser grid or interpolation on the level of amplitudes instead.

Furthermore, a comparison with numerical results obtained with **Fiesta** and **pySecDec** showed agreement within their numerical uncertainties.

The renormalized leading-colour two-loop amplitude was numerically evaluated at a benchmark phase space point with an accuracy of at least 15 decimal digits. The results were numerically cross-checked with electroweak Ward identities and by comparing the singularities with the expected two-loop IR singularities obtained from general factorization formulas. Both cross-checks agree within the numerical uncertainties.

The leading-colour two-loop amplitude is, of course, only a small part of the full NNLO QCD corrections. Sub-leading-colour contributions, i. e. contributions of order  $N_c$ ,  $N_c^0$ ,  $N_c^{-1}$ , and  $N_c^{-2}$ , might contribute substantially to the full amplitude. The calculation of the full two-loop amplitude for this process is naturally very involved and might require a refinement of the presented



techniques or possibly completely different approaches.

Furthermore, the two-loop amplitude is only one building block of the NNLO corrections which also include the one-loop real corrections, i.e. one-loop diagrams with one additional soft or collinear parton, and the double-real corrections, i.e. contributions with two additional partons which simultaneously become soft or collinear. The combination of all three parts is a non-trivial task in itself.



## A. Additional calculations

### A.1. Determination of the benchmark phase space point

Most calculations in this work are performed in terms of the variables  $x$ ,  $z$ ,  $m$ , and  $s$  as defined in eq. (2.4). This includes the calculation of the master integrals and the evaluation of projector coefficients. Moreover, the calculations are often performed for the benchmark point  $x = 0.2$ ,  $z = 0.05$ ,  $m = 289/2500$ , and  $s = (500 \text{ GeV})^2$ . In this section, the external momenta  $p_1$ ,  $p_2$ , and  $p_3$  are expressed in terms of the variables  $x$ ,  $z$ ,  $m$ , and  $s$  by adjusting a parameterization for a three-particle phase space taken from ref. [176] to the process at hand. The obtained momenta are then used as a benchmark phase space point for the numerical evaluation of the one-loop and leading-colour two-loop amplitudes.

First, general formulas from ref. [176] are reproduced. The final-state momenta of a general 1-to-3 process are in the following denoted by  $p_1$ ,  $p_2$ , and  $p_3$  and the initial-state momentum is  $p = p_1 + p_2 + p_3$ . The final-state particles can have arbitrary masses, i. e.  $p_i^2 = m_i^2$ . This process possesses the invariant variables

$$s_{12} = s_1 = (p_1 + p_2)^2, \quad s_{23} = s_2 = (p_2 + p_3)^2, \quad s_{31} = s_3 = (p_3 + p_1)^2. \quad (\text{A.1})$$

Momentum conservation yields

$$s = p^2 = s_1 + s_2 + s_3 - m_1^2 - m_2^2 - m_3^2. \quad (\text{A.2})$$

The energies of the final-state particles are

$$E_1 = \frac{s + m_1^2 - s_2}{2\sqrt{s}}, \quad E_2 = \frac{s + m_2^2 - s_3}{2\sqrt{s}}, \quad E_3 = \frac{s + m_3^2 - s_1}{2\sqrt{s}} \quad (\text{A.3})$$

and the absolute values of the spatial components are

$$|\vec{p}_1| = \frac{\lambda^{\frac{1}{2}}(s, m_1^2, s_2)}{2\sqrt{s}}, \quad |\vec{p}_2| = \frac{\lambda^{\frac{1}{2}}(s, m_2^2, s_3)}{2\sqrt{s}}, \quad |\vec{p}_3| = \frac{\lambda^{\frac{1}{2}}(s, m_3^2, s_1)}{2\sqrt{s}} \quad (\text{A.4})$$

with

$$\lambda(x, y, z) = (x - y - z)^2 - 4yz. \quad (\text{A.5})$$

The angles between two particles are given by

$$\begin{aligned} \cos \theta_{12} &= \frac{(s + m_1^2 - s_2)(s + m_2^2 - s_3) + 2s(m_1^2 + m_2^2 - s_2)}{\lambda^{\frac{1}{2}}(s, m_1^2, s_2)\lambda^{\frac{1}{2}}(s, m_2^2, s_3)}, \\ \cos \theta_{23} &= \frac{(s + m_2^2 - s_3)(s + m_3^2 - s_1) + 2s(m_2^2 + m_3^2 - s_3)}{\lambda^{\frac{1}{2}}(s, m_2^2, s_3)\lambda^{\frac{1}{2}}(s, m_3^2, s_1)}, \\ \cos \theta_{31} &= \frac{(s + m_3^2 - s_1)(s + m_1^2 - s_2) + 2s(m_3^2 + m_1^2 - s_1)}{\lambda^{\frac{1}{2}}(s, m_3^2, s_1)\lambda^{\frac{1}{2}}(s, m_1^2, s_2)}. \end{aligned} \quad (\text{A.6})$$

### A. Additional calculations

The last two angles were obtained from the first formula with the permutation

$$p_1 \rightarrow p_2, \quad p_2 \rightarrow p_3, \quad p_3 \rightarrow p_1, \quad s_1 \rightarrow s_2, \quad s_2 \rightarrow s_3, \quad s_3 \rightarrow s_1. \quad (\text{A.7})$$

Now, these formulas are applied to the process  $Z \rightarrow t\bar{t}g$  using the kinematic definitions from sec. 2.1. For this process, the energies are

$$E_1 = \frac{1}{2} \sqrt{s}(1-z), \quad E_2 = \frac{1}{2} \sqrt{s}(1-x), \quad E_3 = \frac{1}{2} \sqrt{s}(x+z) \quad (\text{A.8})$$

and the absolute spatial momenta are

$$|\vec{p}_1| = \frac{1}{2} \sqrt{s((1-z)^2 - 4m)}, \quad |\vec{p}_2| = \frac{1}{2} \sqrt{s((1-x)^2 - 4m)}, \quad |\vec{p}_3| = \frac{1}{2} \sqrt{s(x+z)^2} \quad (\text{A.9})$$

and the angles are

$$\begin{aligned} \cos \theta_{12} &= \frac{4m + x + z + xz - 1}{\sqrt{(1-x)^2 - 4m} \sqrt{(1-z)^2 - 4m}}, \\ \cos \theta_{23} &= -\frac{z + x(x+z-1)}{(x+z) \sqrt{(1-x)^2 - 4m}}, \\ \cos \theta_{31} &= -\frac{x + z(x+z-1)}{(x+z) \sqrt{(1-z)^2 - 4m}}. \end{aligned} \quad (\text{A.10})$$

These relations define all three momenta relative to each other with the spatial orientation of the whole system remaining undefined.

The orientation is fixed by imposing that the spatial vector  $\vec{p}_1$  is parallel to the  $x$  direction, which yields

$$p_1 = \sqrt{s} \left( \frac{1}{2}(1-z), \frac{1}{2} \sqrt{(1-z)^2 - 4m}, 0, 0 \right). \quad (\text{A.11})$$

Furthermore, restricting  $\vec{p}_2$  to the xy-plane yields

$$\begin{aligned} p_2 &= (E_2, |\vec{p}_2| \cos \theta_{12}, |\vec{p}_2| \sin \theta_{12}, 0) \\ &= \sqrt{s} \left( \frac{1}{2}(1-x), \frac{4m + x + z + xz - 1}{2 \sqrt{(1-z)^2 - 4m}}, \sqrt{\frac{xz(x+z-1) + m(x+z)^2}{4m - (1-z)^2}}, 0 \right). \end{aligned} \quad (\text{A.12})$$

This already determines  $p_3$ , which can be calculated by computing the scalar products

$$\begin{aligned} \vec{p}_1 \cdot \vec{p}_3 &= |\vec{p}_1| |\vec{p}_3| \cos \theta_{13} = |\vec{p}_1| p_3^x, \\ \vec{p}_2 \cdot \vec{p}_3 &= |\vec{p}_2| |\vec{p}_3| \cos \theta_{23} = |\vec{p}_2| (p_3^x \cos \theta_{12} - p_3^y \sin \theta_{13}) \\ &= |\vec{p}_2| (|\vec{p}_3| \cos \theta_{12} \cos \theta_{13} - p_3^y \sin \theta_{13}). \end{aligned} \quad (\text{A.13})$$

The results is

$$\begin{aligned} p_3 &= \left( E_3, |\vec{p}_3| \cos \theta_{13}, \frac{|\vec{p}_3| \cos \theta_{23} - |\vec{p}_2| \cos \theta_{12} \cos \theta_{13}}{\sin \theta_{13}}, 0 \right) \\ &= \sqrt{s} \left( \frac{1}{2}(x+z), -\frac{x + z(x+z-1)}{2 \sqrt{(1-z)^2 - 4m}}, -\sqrt{\frac{xz(x+z-1) + m(x+z)^2}{4m - (1-z)^2}}, 0 \right). \end{aligned} \quad (\text{A.14})$$

The spatial components of all three particles lie in the xy-plane because the momenta are defined in the centre-of-momentum frame. Other orientations can be obtained by applying

spatial rotations.

## A.2. Brief overview of the Tarasov method

In this section, a tensor reduction method which was introduced in ref. [189] by Tarasov is very briefly discussed. This method is hence referred to as Tarasov method in this work. This review contributes to the general discussion on tensor reduction procedures given in sec. 2.4.2 even though this method was not used in this work. The following discussion follows the notations of ref. [273]. In this method, tensor integrals are expressed in terms of scalar integrals with increased propagator exponents in shifted space-time dimensions.

The Tarasov method makes use of the Schwinger parameter representation. This parameterization is obtained by applying the Schwinger transformation in eq. (2.27) to each propagator  $P_j$ . This yields for a generic scalar  $L$ -loop Feynman integral in  $d$  dimensions composed of  $N$  propagators

$$\left( \prod_{i=1}^L \int \frac{d^d k_i}{i\pi^{d/2}} \right) \prod_{j=1}^N \frac{1}{P_j^{n_j}} = \left( \prod_{i=1}^L \int \frac{d^d k_i}{i\pi^{d/2}} \right) \left( \prod_{i=1}^N \frac{(-1)^{n_i}}{\Gamma(n_i)} \int_0^\infty dx_i x_i^{n_i-1} \right) \exp \left( \sum_{j=1}^N x_j P_j \right). \quad (\text{A.15})$$

In the next step, the loop momenta  $k_i$  are integrated out in a universal way. Consider, for example, a generic one-loop four point function with the propagators

$$\begin{aligned} P_1 &= k^2 - m_1^2, & P_2 &= (k + p_1)^2 - m_2^2, \\ P_3 &= (k + p_1 + p_2)^2 - m_3^2, & P_4 &= (k + p_1 + p_2 + p_3)^2 - m_4^2. \end{aligned} \quad (\text{A.16})$$

The argument of the exponential function in eq. (A.15) is then expressed as a quadratic polynomial, i. e.

$$\begin{aligned} \sum_{j=1}^n x_j P_j &= a \cdot k^2 + 2b \cdot k + c = a \cdot \left( k^2 + \frac{2b \cdot k}{a} + \frac{c}{a} \right) \\ &= a \cdot \left( \left( k + \frac{b}{a} \right)^2 - \frac{b^2}{a^2} + \frac{c}{a} \right) = \mathcal{U} \cdot q^2 - \frac{\mathcal{F}}{\mathcal{U}}, \end{aligned} \quad (\text{A.17})$$

where the loop momentum  $k$  is shifted and replaced with  $q$ . For the one-loop four point function, the coefficients are

$$\begin{aligned} a &= x_1 + x_2 + x_3 + x_4, \\ b &= p_3 x_4 + p_2(x_3 + x_4) + p_1(x_2 + x_3 + x_4), \\ c &= -m_1^2 x_1 - m_2^2 x_2 + p_1^2 x_2 - m_3^2 x_3 + p_1^2 x_3 + 2p_1 p_2 x_3 + p_2^2 x_3 \\ &\quad + (-m_4^2 + (p_1 + p_2 + p_3)^2) x_4 \end{aligned} \quad (\text{A.18})$$

and the Symanzik polynomials are

$$\mathcal{U} = a = x_1 + x_2 + x_3 + x_4, \quad \mathcal{F} = b^2 - ca. \quad (\text{A.19})$$

Integration over  $q$  yields the Schwinger representation, i. e.

$$\prod_{i=1}^N \left( \int_0^\infty dx_i \frac{(-1)^{n_i} x_i^{n_i-1}}{\Gamma(n_i)} \right) \mathcal{U}^{-d/2} e^{-\mathcal{F}/\mathcal{U}}. \quad (\text{A.20})$$

### A. Additional calculations

The calculation of tensor integrals also follows the outlined steps but differs in the integration of the loop momenta. At one-loop, a generic tensor integral is given by

$$\int \frac{d^d k}{i\pi^{d/2}} (k_{\mu_1} k_{\mu_2} \dots k_{\mu_t}) \prod_{j=1}^N \frac{1}{P_j^{n_j}} = \left( \prod_{i=1}^N \frac{(-1)^{n_i}}{\Gamma(n_i)} \int_0^\infty dx_i x_i^{n_i-1} \right) J_d[k_{\mu_1} k_{\mu_2} \dots k_{\mu_t}], \quad (\text{A.21})$$

where the integrand of the Schwinger parameter integration including the tensor structure is

$$J_d[k_{\mu_1} k_{\mu_2} \dots k_{\mu_t}] = (k_{\mu_1} k_{\mu_2} \dots k_{\mu_t}) \exp \left( \sum_{j=1}^N x_j P_j \right). \quad (\text{A.22})$$

Applying the same loop-momentum shift as for the scalar integrals, i.e.  $k \rightarrow q - \frac{b}{a}$ , yields for the integrand

$$\begin{aligned} J_d[\dots] &= \left( \left( q_{\mu_1} - \frac{b_{\mu_1}}{a} \right) \left( q_{\mu_2} - \frac{b_{\mu_2}}{a} \right) \dots \left( q_{\mu_t} - \frac{b_{\mu_t}}{a} \right) \right) \exp \left( \mathcal{U} q^2 - \frac{\mathcal{F}}{\mathcal{U}} \right) \\ &= \left( \left( q_{\mu_1} - \frac{b_{\mu_1}}{a} \right) \left( q_{\mu_2} - \frac{b_{\mu_2}}{a} \right) \dots \left( q_{\mu_t} - \frac{b_{\mu_t}}{a} \right) \right) \exp(\mathcal{U} q^2) \cdot \exp \left( -\frac{\mathcal{F}}{\mathcal{U}} \right). \end{aligned} \quad (\text{A.23})$$

The term  $\exp(-\mathcal{F}/\mathcal{U})$  is the same as for scalar integrals and is independent of the shifted loop momentum  $q$ . The tensor structure gives rise to factors containing  $b_{\mu_i}$ , which are a linear combination of external momenta and Schwinger parameters. The remaining tensor integrals are resolved by applying relations such as

$$\begin{aligned} \int \frac{d^d q}{i\pi^{d/2}} q^\mu \exp(\mathcal{U} q^2) &= 0, \\ \int \frac{d^d q}{i\pi^{d/2}} q^\mu q^\nu \exp(\mathcal{U} q^2) &= -\frac{1}{2\mathcal{U}} g^{\mu\nu} \frac{1}{\mathcal{U}^{d/2}}, \\ \int \frac{d^d q}{i\pi^{d/2}} q^\mu q^\nu q^\rho q^\sigma \exp(\mathcal{U} q^2) &= \frac{1}{4\mathcal{U}^2} (g^{\mu\nu} g^{\rho\sigma} + g^{\mu\rho} g^{\nu\sigma} + g^{\mu\sigma} g^{\nu\rho}) \frac{1}{\mathcal{U}^{d/2}}. \end{aligned} \quad (\text{A.24})$$

Only the metric tensor can appear in the results of these integrals since the integrand is independent of  $q$  and the external momenta. For example, for the tensor integrals of rank 1 and 2, the integrands are effectively replaced with

$$\begin{aligned} J_d[k^\mu] &= J_d[q^\mu] - \frac{b^\mu}{\mathcal{U}} J_d[1] = -b^\mu J_{d+2}[1], \\ J_d[k^\mu k^\nu] &= J_d[q^\mu q^\nu] + \frac{b^\mu b^\nu}{a^2} J_d[1] = \left( -\frac{1}{2\mathcal{U}} g^{\mu\nu} + \frac{b^\mu b^\nu}{\mathcal{U}^2} \right) J_d[1] \\ &= -\frac{1}{2} g^{\mu\nu} J_{d+2}[1] + b^\mu b^\nu J_{d+4}[1]. \end{aligned} \quad (\text{A.25})$$

The dimension-shift operator  $\mathbf{D}^+ = U^{-1}$  is applied at this step. Furthermore, the factors  $b_{\mu_i}$  contain Schwinger parameters which act as  $\mathbf{i}^+$  operators.

As a result, this tensor reduction yields Feynman integrals in increased space-time dimensions and with increased exponents of the propagators.

For example, the tensor integral of rank 1 for the generic box integral defined in eq. (A.16) yields

$$I_{1,1,1,1}^{(d)}[k^\mu] = p_1^\mu \left( I_{1,2,1,1}^{(d+2)} + I_{1,1,2,1}^{(d+2)} + I_{1,1,1,2}^{(d+2)} \right) + p_2^\mu \left( I_{1,1,2,1}^{(d+2)} + I_{1,1,1,2}^{(d+2)} \right) + p_3^\mu I_{1,1,1,2}^{(d+2)}, \quad (\text{A.26})$$

where  $[k^\mu]$  indicates the tensor structure similarly to eq. (A.22).

The tensor reduction for two-loop integrals can be done in a similar fashion. After introducing Schwinger parameters, the argument of the exponential function is

$$\sum_{j=1}^N x_j P_j = a \cdot k_1^2 + b \cdot k_2^2 + 2c \cdot k_1 k_2 + 2d \cdot k_1 + 2e \cdot k_2 + f, \quad (\text{A.27})$$

where the coefficients  $a, b$ , etc. are linear combinations of the Schwinger parameters  $x_i$ , external momenta, and kinematical variables. The substitution, also taken from ref. [273],

$$k_1^\mu \rightarrow q_1^\mu - \frac{c}{a} q_2^\mu + X^\mu, \quad k_2^\mu \rightarrow q_2^\mu + Y^\mu \quad (\text{A.28})$$

is applied to the loop momenta. The two auxiliary vectors are

$$X^\mu = \frac{bd^\mu - ce^\mu}{\mathcal{U}}, \quad Y^\mu = \frac{ad^\mu - cd^\mu}{\mathcal{U}} \quad (\text{A.29})$$

and the Symanzik polynomials for this two-loop integral are

$$\mathcal{U} = c^2 - ab, \quad \mathcal{F} = -bd^2 + 2cde - ae^2 + abf - c^2 f. \quad (\text{A.30})$$

Applying this substitution to the argument of the exponential function yields

$$\sum_{j=1}^N x_j P_j = a q_1^2 - \frac{\mathcal{U}}{a} q_2^2 - \frac{\mathcal{F}}{\mathcal{U}}. \quad (\text{A.31})$$

The  $q_1$  and  $q_2$  integrations factorize as a result. Integrating over  $q_1$  and  $q_2$  yields for scalar integrals again the Schwinger representation in eq. (A.20).

Tensor integrals are calculated in the same manner as in the one-loop case by substituting  $k_1$  and  $k_2$  with eq. (A.28) and then applying the same relations as in eq. (A.24). Two-loop tensor integrals with tensor rank  $t$  are expressed with scalar integrals with maximal space-time dimensionality  $d + 2t$  since each tensor momentum gives rise to one  $\mathbf{D}^+$  operator when applying the substitution in eq. (A.28). The sum of all positive propagator exponents  $r$  is increased by  $2t$  since  $X^\mu$  and  $Y^\mu$  in eq. (A.29) are polynomials of order 2 in the Schwinger parameters.

## A.3. Calculating derivatives of Feynman integrals

### A.3.1. Derivatives in the parametric representation

The derivatives with respect to the invariants  $x, z, m$ , and  $s$  of the master integrals have to be calculated in order to determine the differential equations. In one possible approach, the derivatives are calculated using parametric representations of Feynman integrals, such as the Schwinger or Feynman parameterization. Differentiation with respect to invariants is straight forward in this case since the loop momenta are integrated out and the remaining integrand depends explicitly on scalar invariants.

Consider a generic scalar Feynman integral in Schwinger representation as defined in eq. (2.28).

### A. Additional calculations

The invariants only enter in  $\mathcal{F}$  and hence differentiation with respect to some invariant  $s_i$  yields

$$\begin{aligned} & \frac{\partial}{\partial s_i} \prod_{i=1}^N \left( \int_0^\infty dx_i \frac{(-1)^{n_i} x_i^{n_i-1}}{\Gamma(n_i)} \right) \mathcal{U}^{-d/2} e^{-\mathcal{F}/\mathcal{U}} \\ &= \prod_{i=1}^N \left( \int_0^\infty dx_i \frac{(-1)^{n_i} x_i^{n_i-1}}{\Gamma(n_i)} \right) \left( -\frac{\partial \mathcal{F}}{\partial s_i} \right) \mathcal{U}^{-(d+2)/2} e^{-\mathcal{F}/\mathcal{U}}. \end{aligned} \quad (\text{A.32})$$

On the right-hand side of this equation, Feynman integrals in dimension  $d+2$  occur. The term  $\partial \mathcal{F} / \partial s_i$  is a polynomial in the Schwinger parameters of order  $L+1$ . The  $x_i$  factors can be identified as  $\mathbf{i}^+$  operators, which increase propagator exponents, as defined in eq. (2.33). The integrals on the right-hand side are typically reduced to master integrals with IBP relations and the space-time dimension is reduced by applying a dimension-shift transformation.

For example, consider the sunrise topology given by sector 21. The corresponding Symanzik polynomials are

$$\begin{aligned} \mathcal{U} &= x_1 x_2 + x_1 x_3 + x_2 x_3, \\ \mathcal{F} &= -x_1 x_2 x_3 + m(x_1 + x_2)(x_1 x_2 + x_1 x_3 + x_2 x_3) = -x_1 x_2 x_3 + m(x_1 + x_2)\mathcal{U}. \end{aligned} \quad (\text{A.33})$$

Differentiating the Schwinger representation with respect to  $m$  gives

$$\begin{aligned} \frac{\partial}{\partial m} I_{n_1,0,n_2,0,n_3,0,0}^{(d)} &= \frac{\partial}{\partial m} \prod_{i=1}^3 \left( \int_0^\infty dx_i \frac{(-1)^{n_i} x_i^{n_i-1}}{\Gamma(n_i)} \right) \mathcal{U}^{-d/2} e^{-\mathcal{F}/\mathcal{U}} \\ &= \int \prod_{i=1}^3 \left( \int_0^\infty dx_i \frac{(-1)^{n_i} x_i^{n_i-1}}{\Gamma(n_i)} \right) (x_1 + x_2) \mathcal{U}^{-d/2} e^{-\mathcal{F}/\mathcal{U}} \\ &= -n_1 I_{n_1+1,0,n_2,0,n_3,0,0}^{(d)} - n_2 I_{n_1,0,n_2+1,0,n_3,0,0}^{(d)}. \end{aligned} \quad (\text{A.34})$$

The  $\mathcal{U}^{-1}$  term cancels in this example since the derivative of  $\mathcal{F}$  is proportional to  $\mathcal{U}$ . Hence, the integrals on the right-hand side are  $d$ -dimensional. Reducing the integrals on the right-hand side with Kira to master integrals yields, for example,

$$\begin{aligned} \frac{\partial}{\partial m} I_{3,0,3,0,1,0,0}^{(6-2\epsilon)} &= + \frac{9m}{d(m-1) - 7m + 6} I_{4,0,4,0,0,0,0}^{(6-2\epsilon)} \\ &+ \frac{(3d^2 - 37d + 112)(2m-1)}{4ms(d(m-1) - 7m + 6)} I_{3,0,3,0,1,0,0}^{(6-2\epsilon)} \\ &- \frac{(d-4)(4m-1)}{4m(d(m-1) - 7m + 6)} I_{3,0,3,0,2,0,0}^{(6-2\epsilon)}. \end{aligned} \quad (\text{A.35})$$

#### A.3.2. Derivatives in the momentum representation

Another approach to calculate the derivatives of Feynman integrals uses the momentum representation. In this case, derivatives assume, for example, the form

$$\frac{\partial}{\partial m} = \sum_{i,j} c_{i,j} p_i^\mu \frac{\partial}{\partial p_j^\mu} + c_{m_t^2} \frac{\partial}{\partial m_t^2}. \quad (\text{A.36})$$

This approach is, for example, discussed in ref. [118].

In the following, the derivatives in momentum representation with respect to the invariants  $x$ ,  $z$ ,  $m$ , and  $z$  are derived for the process at hand. The calculation is divided into two steps for the



sake of clarity. In the first step, the derivatives with respect to the invariants  $s_{ij} = (p_i + p_j)^2$  and  $m_t^2$  are calculated. In the second step, these derivatives are expressed with derivatives with respect to  $x, z, m$ , and  $s$ .

In the first step, the chain rule yields equations of the form

$$p_l^\mu \frac{\partial}{\partial p_k^\mu} = \sum_{s_{ij}} p_l^\mu \frac{\partial s_{ij}}{\partial p_k^\mu} \frac{\partial}{\partial s_{ij}}, \quad m_t^2 \frac{\partial}{\partial m_t^2} = \sum_{s_{ij}} m_t^2 \frac{\partial s_{ij}}{\partial m_t^2} \frac{\partial}{\partial s_{ij}} + m_t^2 \frac{\partial}{\partial m_t^2}, \quad (\text{A.37})$$

where the sums are performed over the invariants  $s_{ij} = \{s, s_{11}, s_{22}, s_{33}, s_{13}, s_{23}, m_t^2\}$  and the external momenta are  $p_i \in \{p_1, p_2, p_3\}$ . Note that  $s_{12}$  is not an independent variable and hence is not included. Eq. (A.37) gives rise to a system of equations of rank 7. Removing linearly dependent equations yields the system

$$\underbrace{\begin{pmatrix} p_1 \partial_{p_1} \\ p_1 \partial_{p_2} \\ p_1 \partial_{p_3} \\ p_2 \partial_{p_1} \\ p_2 \partial_{p_2} \\ p_3 \partial_{p_1} \\ m_t^2 \partial_{m_t^2} \end{pmatrix}}_{\partial_{\vec{p}}} = \underbrace{\begin{pmatrix} p_1 \frac{\partial s}{\partial p_1} & p_1 \frac{\partial s_{11}}{\partial p_1} & p_1 \frac{\partial s_{22}}{\partial p_1} & p_1 \frac{\partial s_{33}}{\partial p_1} & p_1 \frac{\partial s_{13}}{\partial p_1} & p_1 \frac{\partial s_{23}}{\partial p_1} & p_1 \frac{\partial m_t^2}{\partial p_1} \\ p_1 \frac{\partial s}{\partial p_2} & p_1 \frac{\partial s_{11}}{\partial p_2} & p_1 \frac{\partial s_{22}}{\partial p_2} & p_1 \frac{\partial s_{33}}{\partial p_2} & p_1 \frac{\partial s_{13}}{\partial p_2} & p_1 \frac{\partial s_{23}}{\partial p_2} & p_1 \frac{\partial m_t^2}{\partial p_2} \\ p_1 \frac{\partial s}{\partial p_3} & p_1 \frac{\partial s_{11}}{\partial p_3} & p_1 \frac{\partial s_{22}}{\partial p_3} & p_1 \frac{\partial s_{33}}{\partial p_3} & p_1 \frac{\partial s_{13}}{\partial p_3} & p_1 \frac{\partial s_{23}}{\partial p_3} & p_1 \frac{\partial m_t^2}{\partial p_3} \\ p_2 \frac{\partial s}{\partial p_1} & p_2 \frac{\partial s_{11}}{\partial p_1} & p_2 \frac{\partial s_{22}}{\partial p_1} & p_2 \frac{\partial s_{33}}{\partial p_1} & p_2 \frac{\partial s_{13}}{\partial p_1} & p_2 \frac{\partial s_{23}}{\partial p_1} & p_2 \frac{\partial m_t^2}{\partial p_1} \\ p_2 \frac{\partial s}{\partial p_2} & p_2 \frac{\partial s_{11}}{\partial p_2} & p_2 \frac{\partial s_{22}}{\partial p_2} & p_2 \frac{\partial s_{33}}{\partial p_2} & p_2 \frac{\partial s_{13}}{\partial p_2} & p_2 \frac{\partial s_{23}}{\partial p_2} & p_2 \frac{\partial m_t^2}{\partial p_2} \\ p_3 \frac{\partial s}{\partial p_1} & p_3 \frac{\partial s_{11}}{\partial p_1} & p_3 \frac{\partial s_{22}}{\partial p_1} & p_3 \frac{\partial s_{33}}{\partial p_1} & p_3 \frac{\partial s_{13}}{\partial p_1} & p_3 \frac{\partial s_{23}}{\partial p_1} & p_3 \frac{\partial m_t^2}{\partial p_1} \\ m_t^2 \frac{\partial s}{\partial m_t^2} & m_t^2 \frac{\partial s_{11}}{\partial m_t^2} & m_t^2 \frac{\partial s_{22}}{\partial m_t^2} & m_t^2 \frac{\partial s_{33}}{\partial m_t^2} & m_t^2 \frac{\partial s_{13}}{\partial m_t^2} & m_t^2 \frac{\partial s_{23}}{\partial m_t^2} & m_t^2 \frac{\partial m_t^2}{\partial m_t^2} \end{pmatrix}}_{=\hat{D}} \cdot \underbrace{\begin{pmatrix} \partial_s \\ \partial_{s_{11}} \\ \partial_{s_{22}} \\ \partial_{s_{33}} \\ \partial_{s_{13}} \\ \partial_{s_{23}} \\ \partial_{m_t^2} \end{pmatrix}}_{\partial_{\vec{s}}}. \quad (\text{A.38})$$

Inverting the matrix  $\hat{D}$  yields

$$\partial_{\vec{s}} = \hat{D}^{-1} \partial_{\vec{p}}, \quad (\text{A.39})$$

i. e. derivatives with respect to the invariants expressed through derivatives with respect to external momenta.

In the next step, these results are used to obtain derivatives with respect to  $x, z, m$ , and  $s$ . Applying the chain rule yields

$$\begin{aligned} \frac{\partial f}{\partial x} &= \sum_{s_{ij}} \frac{\partial f}{\partial s_{ij}} \frac{\partial s_{ij}}{\partial x} = \frac{\partial s_{13}}{\partial x} \frac{\partial f}{\partial s_{13}} = \frac{\partial(x+m)s}{\partial x} \frac{\partial f}{\partial s_{13}} = s \frac{\partial f}{\partial s_{13}}, \\ \frac{\partial f}{\partial z} &= \sum_{s_{ij}} \frac{\partial f}{\partial s_{ij}} \frac{\partial s_{ij}}{\partial z} = \frac{\partial s_{23}}{\partial z} \frac{\partial f}{\partial s_{23}} = s \frac{\partial f}{\partial s_{23}}, \\ \frac{\partial f}{\partial m} &= \sum_{s_{ij}} \frac{\partial f}{\partial s_{ij}} \frac{\partial s_{ij}}{\partial m} = \frac{\partial s_{11}}{\partial m} \frac{\partial f}{\partial s_{11}} + \frac{\partial s_{22}}{\partial m} \frac{\partial f}{\partial s_{22}} + \frac{\partial s_{13}}{\partial m} \frac{\partial f}{\partial s_{13}} + \frac{\partial s_{23}}{\partial m} \frac{\partial f}{\partial s_{23}} + \frac{\partial m_t^2}{\partial m} \frac{\partial f}{\partial m_t^2} \\ &= s \left( \frac{\partial f}{\partial s_{11}} + \frac{\partial f}{\partial s_{22}} + \frac{\partial f}{\partial s_{13}} + \frac{\partial f}{\partial s_{23}} + \frac{\partial f}{\partial m_t^2} \right), \\ \frac{\partial f}{\partial s} &= \sum_{s_{ij}} \frac{\partial f}{\partial s_{ij}} \frac{\partial s_{ij}}{\partial s} = m \frac{\partial f}{\partial s_{11}} + m \frac{\partial f}{\partial s_{22}} + (x+m) \frac{\partial f}{\partial s_{13}} + (z+m) \frac{\partial f}{\partial s_{23}} + m \frac{\partial f}{\partial m_t^2}, \end{aligned} \quad (\text{A.40})$$

where  $f$  is a generic function. Inserting the results of the first step, given in eq. (A.39), yields

### A. Additional calculations

for the derivative with respect to  $x$

$$\begin{aligned}\partial_x = & \frac{1}{2(m(x+z)^2 + xy(x+z-1))} \left[ p_1(2m(x+z) + y(2x+z-1)) \right. \\ & + p_2(x(2m+z-1) + 2mz) \\ & \left. + p_3(2m(x+z-2) + (z-1)(x+z-1)) \right] \partial_{p_1}, \quad (\text{A.41})\end{aligned}$$

for the derivative with respect to  $z$

$$\begin{aligned}\partial_z = & \frac{1}{2(2m^2(x+z)^3 + mz(3x^3 + x^2(7z-3) + xz(5z-4) + (z-1)z^2) + xz^2(x+z-1)^2)} \times \\ & \times \left[ + p_1xz(2m(x+z-2) + (x-1)(x+z-1)) \right. \\ & + p_2x^2(2m(x+z-2) + (x-1)(x+z-1)) \\ & + p_3 \left( x(2m+z-1) + 2mz + x^2 \right) (2m(x+z-2) + (x-1)(x+z-1)) \left. \right] \partial_{p_1} \\ & + \frac{2m(p_1+p_2) + p_2(x+z-1)}{2m(x+z) + z(x+z-1)} \partial_{p_2}, \quad (\text{A.42})\end{aligned}$$

for the derivative with respect to  $m$

$$\begin{aligned}\partial_m = & \frac{1}{2(2m(x+z) + z(x+z-1))(m(x+z)^2 + xz(x+z-1))} \times \\ & \times \left[ p_1z \left( x^2(2m+z+1) + xz(4m+3z-2) + z^2(2m+z-1) - x^3 \right) \right. \\ & + p_2x \left( -x^2(2m+z+1) + xz(-4m-3z+2) - z^2(2m+z-1) + x^3 \right) \\ & + p_3 \left( -x^2 + x + (z-1)z \right)^2 \left. \right] \cdot \partial_{p_1} \\ & + \frac{p_2x - p_1z}{2m(x+z) + z(x+z-1)} \cdot \partial_{p_2} \\ & + s\partial_{m_t^2}, \quad (\text{A.43})\end{aligned}$$

and for the derivative with respect to  $s$

$$\begin{aligned}\partial_s = & \frac{1}{2s(z(-1+x+z) + 2m(x+z))} \left[ \left( p_1(2m(2x+z) + z(x+z-1)) \right. \right. \\ & + p_2x(-1+2m+x+z) \\ & + p_3(x+z-1)(4m+x+z-1) \left. \right) \partial_{p_1} \\ & + 2 \left( p_1mz + p_2(z(-1+x+z) + m(x+2z)) \right) \partial_{p_2} \left. \right] \\ & + m\partial_{m_t^2}. \quad (\text{A.44})\end{aligned}$$

When calculating the derivatives in the momentum representation, scalar products involving loop momenta occur in intermediate expressions. These scalar products are then replaced with inverse propagators. The here derived expressions do not give rise to integrals in shifted dimensions in contrast to the differentiation in the Schwinger representation.

### A.4. Axial-vector current spinor structures

$$\begin{aligned}
\tilde{S}_1 &= \frac{2}{s^2} \bar{u}(p_1) \gamma^5 \left( \not{p}_3 (p_1 \cdot \epsilon_3^*) - \frac{sx}{2} \not{\epsilon}_3^* \right) v(p_2) (p_1 \cdot \epsilon_4), \\
\tilde{S}_2 &= \frac{2}{s^2} \bar{u}(p_1) \gamma^5 \left( \not{p}_3 (p_1 \cdot \epsilon_3^*) - \frac{sx}{2} \not{\epsilon}_3^* \right) v(p_2) (p_2 \cdot \epsilon_4), \\
\tilde{S}_3 &= \frac{2}{s^2} \bar{u}(p_1) \gamma^5 \left( \not{p}_3 (p_2 \cdot \epsilon_3^*) - \frac{sz}{2} \not{\epsilon}_3^* \right) v(p_2) (p_1 \cdot \epsilon_4), \\
\tilde{S}_4 &= \frac{2}{s^2} \bar{u}(p_1) \gamma^5 \left( \not{p}_3 (p_2 \cdot \epsilon_3^*) - \frac{sz}{2} \not{\epsilon}_3^* \right) v(p_2) (p_2 \cdot \epsilon_4), \\
\tilde{S}_5 &= \frac{1}{s} \bar{u}(p_1) \gamma^5 \left( \not{p}_3 (\epsilon_3^* \cdot \epsilon_4) - \not{\epsilon}_3^* (p_3 \cdot \epsilon_4) \right) v(p_2), \\
\tilde{S}_6 &= \frac{m_t}{s^2} \bar{u}(p_1) \gamma^5 \not{\epsilon}_3^* \not{p}_3 v(p_2) (p_1 \cdot \epsilon_4), \\
\tilde{S}_7 &= \frac{m_t}{s^2} \bar{u}(p_1) \gamma^5 \not{\epsilon}_3^* \not{p}_3 v(p_2) (p_2 \cdot \epsilon_4), \\
\tilde{S}_8 &= \frac{2m_t}{s^2} \bar{u}(p_1) \gamma^5 \left( \not{\epsilon}_4 \not{p}_3 (p_1 \cdot \epsilon_3^*) - \frac{sx}{2} \not{\epsilon}_4 \not{\epsilon}_3^* \right) v(p_2), \\
\tilde{S}_9 &= 2 \frac{m_t}{s^2} \bar{u}(p_1) \gamma^5 \left( \not{\epsilon}_4 \not{p}_3 (p_2 \cdot \epsilon_3^*) - \frac{sz}{2} \not{\epsilon}_4 \not{\epsilon}_3^* \right) v(p_2), \\
\tilde{S}_{10} &= \frac{1}{s} \bar{u}(p_1) \gamma^5 \not{\epsilon}_4 \not{\epsilon}_3^* \not{p}_3 v(p_2), \\
\tilde{S}_{11} &= \frac{1}{s} \bar{u}(p_1) \gamma^5 \left( \not{\epsilon}_4 (p_1 \cdot \epsilon_3^*) z - \not{\epsilon}_4 (p_2 \cdot \epsilon_3^*) x \right) v(p_2), \\
\tilde{S}_{12} &= \frac{m_t}{s^2} \bar{u}(p_1) \gamma^5 v(p_2) \left( (p_1 \cdot \epsilon_3^*) z - (p_2 \cdot \epsilon_3^*) x \right) (p_1 \cdot \epsilon_4), \\
\tilde{S}_{13} &= \frac{m_t}{s^2} \bar{u}(p_1) \gamma^5 \not{\epsilon}_3^* \not{p}_3 v(p_2) (p_3 \cdot \epsilon_4), \\
\tilde{S}_{14} &= \frac{1}{s^2} \bar{u}(p_1) \gamma^5 \left( \not{p}_3 (p_2 \cdot \epsilon_3^*) - \frac{sz}{2} \not{\epsilon}_3^* \right) v(p_2) (p_3 \cdot \epsilon_4), \\
\tilde{S}_{15} &= \frac{1}{s^2} \bar{u}(p_1) \gamma^5 \left( \not{p}_3 (p_1 \cdot \epsilon_3^*) - \frac{sx}{2} \not{\epsilon}_3^* \right) v(p_2) (p_3 \cdot \epsilon_4), \\
\tilde{S}_{16} &= \frac{m_t}{s^2} \bar{u}(p_1) \gamma^5 v(p_2) \left( (p_1 \cdot \epsilon_3^*) (p_3 \cdot \epsilon_4) - \frac{sx}{2} (\epsilon_3^* \cdot \epsilon_4) \right), \\
\tilde{S}_{17} &= \frac{m_t}{s^2} \bar{u}(p_1) \gamma^5 v(p_2) \left( (p_2 \cdot \epsilon_3^*) (p_3 \cdot \epsilon_4) - \frac{sz}{2} (\epsilon_3^* \cdot \epsilon_4) \right), \\
\tilde{S}_{18} &= \frac{m_t}{s^2} \bar{u}(p_1) \gamma^5 v(p_2) \left( (p_1 \cdot \epsilon_3^*) z - (p_2 \cdot \epsilon_3^*) x \right) (p_2 \cdot \epsilon_4). \tag{A.45}
\end{aligned}$$

### A.5. Restoring the renormalization scale dependence of the finite remainder

The renormalization scale dependence of the finite remainder

$$|\mathcal{M}_{\text{fin}}(\alpha_s, \{x_i\}, \mu)\rangle = \mathbf{Z}^{-1} |\mathcal{M}_{\text{ren}}(\alpha_s, \{x_i\}, \mu)\rangle, \tag{A.46}$$

### A. Additional calculations

can be determined as described in ref. [274] by calculating the derivative

$$\begin{aligned} & \mu^2 \frac{d}{d\mu^2} \left[ \frac{Z_{UV}}{\mathbf{Z}} Z_{g_s} g_s \left( |\mathcal{M}_0^{(0)}(\{x_i^0\})\rangle + \left( \frac{N^\epsilon Z_{\alpha_s} \alpha_s(\mu)}{4\pi} \right) |\mathcal{M}_0^{(1)}(\{x_i^0\})\rangle \right. \right. \\ & \quad \left. \left. + \left( \frac{N^\epsilon Z_{\alpha_s} \alpha_s(\mu)}{4\pi} \right)^2 |\mathcal{M}_0^{(2)}(\{x_i^0\})\rangle + \mathcal{O}(\alpha_s^3) \right) \right] \\ & = \mu^2 \frac{d}{d\mu^2} \left[ g_s \left( |\mathcal{M}_{\text{fin}}^{(0)}(\{x_i\}, \mu)\rangle + \left( \frac{\alpha_s}{4\pi} \right) |\mathcal{M}_{\text{fin}}^{(1)}(\{x_i\}, \mu)\rangle + \left( \frac{\alpha_s}{4\pi} \right)^2 |\mathcal{M}_{\text{fin}}^{(2)}(\{x_i\}, \mu)\rangle \right) + \mathcal{O}(\alpha_s^3) \right] \end{aligned} \quad (\text{A.47})$$

using

$$\begin{aligned} \mu^2 \frac{d\alpha_s}{d\mu^2} &= -\alpha_s \left( \epsilon + \beta_0 + \frac{\alpha_s}{4\pi} \beta_1 \right) + \mathcal{O}(\alpha_s^3), \quad \mu^2 \frac{dZ_{\alpha_s}}{d\mu^2} = Z_{\alpha_s} \left( \beta_0 + \frac{\alpha_s}{4\pi} \beta_1 \right) + \mathcal{O}(\alpha_s^3), \\ \mu^2 \frac{d}{d\mu^2} \frac{1}{\mathbf{Z}} &= \frac{1}{2} \frac{\mathbf{\Gamma}}{\mathbf{Z}}, \end{aligned} \quad (\text{A.48})$$

and the factor  $N^\epsilon = \left( \frac{\mu^2 e^{\gamma_E}}{4\pi} \right)^\epsilon$ . The derivative of the factor  $Z_{UV}$ , which absorbs the remaining UV renormalization, vanishes due to the choice of the on-shell renormalization scheme for the wave functions and top-quark mass. The anomalous-dimension matrix is decomposed as

$$\mathbf{\Gamma} = \frac{\alpha_s}{4\pi} \left( K_1 + D_1 \ln \left( \frac{\mu^2}{\mu_0^2} \right) \right) + \left( \frac{\alpha_s}{4\pi} \right)^2 \left( K_2 + D_2 \ln \left( \frac{\mu^2}{\mu_0^2} \right) \right) + \mathcal{O}(\alpha_s^3). \quad (\text{A.49})$$

Expanding in  $\alpha_s$  yields differential equations, which are at order  $\epsilon^0$

$$\begin{aligned} \mu^2 \frac{d}{d\mu^2} |\mathcal{M}_{\text{fin}}^{(0)}(\{x_i\}, \mu)\rangle &= 0, \\ \mu^2 \frac{d}{d\mu^2} |\mathcal{M}_{\text{fin}}^{(1)}(\{x_i\}, \mu)\rangle &= \frac{1}{2} \left( K_1 + D_1 \ln \left( \frac{\mu^2}{\mu_0^2} \right) \right) |\mathcal{M}_{\text{fin}}^{(0)}(\{x_i\}, \mu)\rangle, \\ \mu^2 \frac{d}{d\mu^2} |\mathcal{M}_{\text{fin}}^{(2)}(\{x_i\}, \mu)\rangle &= \frac{1}{2} \left( K_2 |\mathcal{M}_{\text{fin}}^{(0)}(\{x_i\}, \mu)\rangle + (2\beta_0 + K_1) |\mathcal{M}_{\text{fin}}^{(1)}(\{x_i\}, \mu)\rangle \right. \\ & \quad \left. + \left( D_2 |\mathcal{M}_{\text{fin}}^{(0)}(\{x_i\}, \mu)\rangle + D_1 |\mathcal{M}_{\text{fin}}^{(1)}(\{x_i\}, \mu)\rangle \right) \ln \left( \frac{\mu^2}{\mu_0^2} \right) \right). \end{aligned} \quad (\text{A.50})$$

Hence, the renormalization scale dependence of the leading-order term is

$$|\mathcal{M}_{\text{fin}}^{(0)}(\{x_i\}, \mu)\rangle = |\mathcal{M}_{\text{fin}}^{(0)}(\{x_i\}, \mu_0)\rangle. \quad (\text{A.51})$$

The renormalization scale dependence of the finite remainder of the one-loop amplitude is given by

$$\begin{aligned} |\mathcal{M}_{\text{fin}}^{(1)}(\{x_i\}, \mu)\rangle &= |\mathcal{M}_{\text{fin}}^{(1)}(\{x_i\}, \mu_0)\rangle \\ & \quad + \frac{1}{4} \ln \left( \frac{\mu^2}{\mu_0^2} \right) \left( 2(\beta_0 + K_1) + D_1 \ln \left( \frac{\mu^2}{\mu_0^2} \right) \right) |\mathcal{M}_{\text{fin}}^{(0)}(\{x_i\}, \mu_0)\rangle. \end{aligned} \quad (\text{A.52})$$

The corresponding leading-colour term is

$$|\mathcal{M}_{\text{fin}}^{(1),\text{LC}}(\{x_i\}, \mu)\rangle = |\mathcal{M}_{\text{fin}}^{(1),\text{LC}}(\{x_i\}, \mu_0)\rangle - N_c \left( \ln \left( \frac{\mu^2}{\mu_0^2} \right) \left( \ln \left( -\frac{m}{x} \right) + \ln \left( -\frac{m}{z} \right) + 1 \right) - \frac{1}{2} \ln^2 \left( \frac{\mu^2}{\mu_0^2} \right) \right) |\mathcal{M}_{\text{fin}}^{(0)}(\{x_i\}, \mu_0)\rangle. \quad (\text{A.53})$$

The renormalization scale dependence of the finite remainder of the two-loop amplitude is given by

$$\begin{aligned} |\mathcal{M}_{\text{fin}}^{(2)}(\{x_i\}, \mu)\rangle &= |\mathcal{M}_{\text{fin}}^{(2)}(\{x_i\}, \mu_0)\rangle + \frac{1}{4} \ln \left( \frac{\mu^2}{\mu_0^2} \right) \left( 6\beta_0 + 2K_1 + D_1 \ln \left( \frac{\mu^2}{\mu_0^2} \right) \right) |\mathcal{M}_{\text{fin}}^{(1)}(\{x_i\}, \mu_0)\rangle \\ &+ \left( \frac{1}{2} (\beta_1 + K_2) \ln \left( \frac{\mu^2}{\mu_0^2} \right) + \frac{1}{8} ((\beta_0 + K_1)(3\beta_0 + K_1) + 2D_2) \ln^2 \left( \frac{\mu^2}{\mu_0^2} \right) \right. \\ &\quad \left. + \frac{1}{24} D_1 (5\beta_0 + 3K_1) \ln^3 \left( \frac{\mu^2}{\mu_0^2} \right) + \frac{1}{32} D_1^2 \ln^4 \left( \frac{\mu^2}{\mu_0^2} \right) \right) |\mathcal{M}_{\text{fin}}^{(0)}(\{x_i\}, \mu_0)\rangle. \end{aligned} \quad (\text{A.54})$$

The corresponding leading-colour term is then

$$\begin{aligned} |\mathcal{M}_{\text{fin}}^{(2),\text{LC}}(\{x_i\}, \mu)\rangle &= |\mathcal{M}_{\text{fin}}^{(2),\text{LC}}(\{x_i\}, \mu_0)\rangle \\ &- N_c \left( \ln \left( \frac{\mu^2}{\mu_0^2} \right) \left( \ln \left( -\frac{m}{x} \right) + \ln \left( -\frac{m}{z} \right) - \frac{8}{3} \right) + \frac{1}{2} \ln^2 \left( \frac{\mu^2}{\mu_0^2} \right) \right) |\mathcal{M}_{\text{fin}}^{(1),\text{LC}}(\{x_i\}, \mu_0)\rangle \\ &+ N_c^2 \left( \ln \left( \frac{\mu^2}{\mu_0^2} \right) \left( \frac{3\pi^2 - 67}{9} \left( \ln \left( -\frac{m}{x} \right) + \ln \left( -\frac{m}{z} \right) \right) - \zeta_3 + \frac{69\pi^2 - 1972}{108} \right) \right. \\ &\quad \left. + \frac{1}{72} \ln^2 \left( \frac{\mu^2}{\mu_0^2} \right) \left( \left( 6 \ln \left( -\frac{m}{x} \right) + 6 \ln \left( -\frac{m}{z} \right) + 17 \right)^2 + 12\pi^2 - 268 \right) \right. \\ &\quad \left. + \frac{1}{12} \ln^3 \left( \frac{\mu^2}{\mu_0^2} \right) \left( 6 \ln \left( -\frac{m}{x} \right) + 6 \ln \left( -\frac{m}{z} \right) + 17 \right) \right. \\ &\quad \left. + \frac{1}{8} \ln^4 \left( \frac{\mu^2}{\mu_0^2} \right) \right) |\mathcal{M}_{\text{fin}}^{(0)}(\{x_i\}, \mu_0)\rangle. \end{aligned} \quad (\text{A.55})$$



## B. Master integral calculation

### B.1. Leading-colour two-loop master integrals

Table B.1.: Leading-colour two-loop master integrals. All integrals are  $(6 - 2\epsilon)$ -dimensional.

double-box integral family					
$I_{4,0,4,0,0,0,0}$	$I_{3,0,4,1,0,0,0}$	$I_{3,2,0,0,2,0,0}$	$I_{4,2,0,0,2,0,0}$	$I_{3,0,3,0,1,0,0}$	$I_{3,0,3,0,2,0,0}$
$I_{3,2,1,0,1,0,0}$	$I_{3,1,2,0,1,0,0}$	$I_{0,2,0,3,2,0,0}$	$I_{2,2,0,1,2,0,0}$	$I_{1,2,0,2,2,0,0}$	$I_{2,2,1,1,1,0,0}$
$I_{2,1,2,1,1,0,0}$	$I_{1,2,1,2,1,0,0}$	$I_{0,0,4,3,0,1,0}$	$I_{2,0,4,1,0,1,0}$	$I_{0,0,3,0,2,2,0}$	$I_{0,0,4,0,2,2,0}$
$I_{2,0,3,0,1,1,0}$	$I_{2,0,2,0,2,1,0}$	$I_{2,2,1,0,1,1,0}$	$I_{2,1,2,0,1,1,0}$	$I_{2,1,1,0,2,1,0}$	$I_{1,2,1,0,2,1,0}$
$I_{0,2,0,2,2,1,0}$	$I_{1,2,0,1,2,1,0}$	$I_{2,2,0,1,2,1,0}$	$I_{0,2,1,2,1,1,0}$	$I_{0,2,1,1,2,1,0}$	$I_{1,2,1,1,1,1,0}$
$I_{1,1,2,1,1,1,0}$	$I_{2,2,1,1,1,1,0}$	$I_{3,0,3,1,0,0,1}$	$I_{3,0,2,0,1,0,1}$	$I_{3,0,1,0,2,0,1}$	$I_{3,0,1,0,1,0,2}$
$I_{3,1,1,0,1,0,1}$	$I_{2,1,1,0,2,0,1}$	$I_{2,0,0,1,2,0,2}$	$I_{1,0,0,2,2,0,2}$	$I_{2,1,0,1,2,0,1}$	$I_{3,1,0,1,2,0,1}$
$I_{2,0,2,1,1,0,1}$	$I_{2,0,1,1,2,0,1}$	$I_{2,0,1,1,1,0,2}$	$I_{1,0,2,2,1,0,1}$	$I_{2,1,1,1,1,0,1}$	$I_{1,1,1,2,1,0,1}$
$I_{1,1,1,1,2,0,1}$	$I_{0,0,3,3,0,1,1}$	$I_{2,0,3,1,0,1,1}$	$I_{1,1,1,1,1,1,1}$	$I_{1,1,1,1,1,2,1}$	$I_{1,1,1,1,2,1,1}$
'crossed' double-box integral family					
$I_{2,2,1,1,1,0,0}^c$	$I_{2,1,2,1,1,0,0}^c$	$I_{1,2,1,2,1,0,0}^c$	$I_{0,0,4,3,0,1,0}^c$	$I_{2,0,4,1,0,1,0}^c$	$I_{0,2,0,2,2,1,0}^c$
$I_{1,2,0,1,2,1,0}^c$	$I_{2,2,0,1,2,1,0}^c$	$I_{0,2,1,2,1,1,0}^c$	$I_{0,2,1,1,2,1,0}^c$	$I_{1,2,1,1,1,1,0}^c$	$I_{1,1,2,1,1,1,0}^c$
$I_{2,2,1,1,1,1,0}^c$	$I_{3,0,3,1,0,0,1}^c$	$I_{3,0,2,0,1,0,1}^c$	$I_{3,0,1,0,2,0,1}^c$	$I_{3,0,1,0,1,0,2}^c$	$I_{3,1,1,0,1,0,1}^c$
$I_{2,1,1,0,2,0,1}^c$	$I_{2,0,2,1,1,0,1}^c$	$I_{2,0,1,1,2,0,1}^c$	$I_{2,0,1,1,1,0,2}^c$	$I_{1,0,2,2,1,0,1}^c$	$I_{2,1,1,1,1,0,1}^c$
$I_{1,1,1,2,1,0,1}^c$	$I_{1,1,1,1,2,0,1}^c$	$I_{0,0,3,3,0,1,1}^c$	$I_{2,0,3,1,0,1,1}^c$	$I_{1,1,1,1,1,1,1}^c$	$I_{1,1,1,1,1,2,1}^c$
$I_{1,1,1,1,2,1,1}^c$					
auxiliary family 1					
$I_{1,4,1,1,0,0,1,0,0}^{a1}$	$I_{0,3,2,1,0,1,1,0,0}^{a1}$	$I_{1,3,1,1,0,1,1,0,0}^{a1}$			
auxiliary family 2					
$I_{0,3,3,1,0,1,0,0,0}^{a2}$	$I_{0,3,2,1,0,1,0,1,0}^{a2}$				

## B.2. Asymptotic expansions

**Table B.2.:** Summary of properties of the leading-colour two-loop master integrals of the double-box integral family and the two auxiliary integral families. The summary includes the sector,  $t$ ,  $r$ , the minimal  $\epsilon$  order  $e_{\min}$ , and the maximal calculated  $\epsilon$  order  $e_{\max}$ . Also stated is the maximal calculated order in  $m$  of the asymptotic expansion  $i_m^{\max}$  and the number of significant digits of the asymptotic expansion evaluated at  $m = 0.01$  and  $m = 0.001$ . The full asymptotic expansions of the integrals  $I_{4,0,4,0,0,0,0}$  and  $I_{0,2,0,3,2,0,0}$  only involve their leading-order terms in  $m$ .

sector	integral	$t$	$r$	$e_{\min}$	$e_{\max}$	$i_m^{\max}$	digits@ $m = 0.01$	digits@ $m = 0.001$
5	$I_{4,0,4,0,0,0,0}$	2	8	-4	0	-2	-	-
13	$I_{3,0,4,1,0,0,0}$	3	8	-2	0	16	24	41
19	$I_{3,2,0,0,2,0,0}$	3	7	-4	0	16	9	25
	$I_{4,2,0,0,2,0,0}$	3	8	-4	0	16	10	26
21	$I_{3,0,3,0,1,0,0}$	3	7	-2	0	13	20	34
	$I_{3,0,3,0,2,0,0}$	3	8	-2	0	13	18	32
23	$I_{3,2,1,0,1,0,0}$	4	7	-2	0	13	8	22
	$I_{3,1,2,0,1,0,0}$	4	7	-2	0	13	10	23
26	$I_{0,2,0,3,2,0,0}$	3	7	-4	0	-1	-	-
27	$I_{2,2,0,1,2,0,0}$	4	7	-2	1	16	11	26
	$I_{1,2,0,2,2,0,0}$	4	7	-2	1	16	13	29
31	$I_{2,2,1,1,1,0,0}$	5	7	0	1	14	11	25
	$I_{2,1,2,1,1,0,0}$	5	7	0	1	14	13	27
	$I_{1,2,1,2,1,0,0}$	5	7	0	1	14	13	27
44	$I_{0,0,4,3,0,1,0}$	3	8	-2	1	16	20	37
45	$I_{2,0,4,1,0,1,0}$	4	8	-2	0	16	24	41
52	$I_{0,0,3,0,2,2,0}$	3	7	-4	0	16	19	35
	$I_{0,0,4,0,2,2,0}$	3	8	-4	0	16	20	37
53	$I_{2,0,3,0,1,1,0}$	4	7	-2	0	13	18	31
	$I_{2,0,2,0,2,1,0}$	4	7	-2	0	13	17	30
55	$I_{2,2,1,0,1,1,0}$	5	7	-2	0	13	10	23
	$I_{2,1,2,0,1,1,0}$	5	7	-2	0	13	11	25
	$I_{2,1,1,0,2,1,0}$	5	7	-2	0	13	10	23
	$I_{1,2,1,0,2,1,0}$	5	7	-2	0	13	10	22
58	$I_{0,2,0,2,2,1,0}$	4	7	-1	2	16	20	36
59	$I_{1,2,0,1,2,1,0}$	5	7	-1	1	16	12	28
	$I_{2,2,0,1,2,1,0}$	5	8	-1	1	16	12	28
62	$I_{0,2,1,2,1,1,0}$	5	7	0	1	16	20	36
	$I_{0,2,1,1,2,1,0}$	5	7	0	1	16	21	37
63	$I_{1,2,1,1,1,1,0}$	6	7	0	0	15	13	28
	$I_{1,1,2,1,1,1,0}$	6	7	0	0	15	15	30
	$I_{2,2,1,1,1,1,0}$	6	8	0	0	15	13	28
77	$I_{3,0,3,1,0,0,1}$	4	8	-1	0	16	19	35
85	$I_{3,0,2,0,1,0,1}$	4	7	-2	0	13	16	29
	$I_{3,0,1,0,2,0,1}$	4	7	-2	0	13	18	31





### B. Master integral calculation

integral	value
$I_{3,2,0,0,2,0,0}$	$\begin{aligned} & (27.7972222743958675376658091879(2) \\ & -30.1960078199710999467766568943(2)\mathrm{i})\epsilon^{-4} \\ & + (391.724801150063559908514472143(2) \\ & -149.3136071599598927645105252984(4)\mathrm{i})\epsilon^{-3} \\ & + (2207.27156208018374808983962562(1) \\ & +115.409671544639681935198797983(4)\mathrm{i})\epsilon^{-2} \\ & + (7223.61292174935114717335114534(2) \\ & +3444.11087265373144611732713463(3)\mathrm{i})\epsilon^{-1} \\ & + (15138.443170916059414781802477167(8) \\ & +16226.62890556738677379216738494(7)\mathrm{i}) \end{aligned}$
$I_{4,2,0,0,2,0,0}$	$\begin{aligned} & (-3518.648148495972450251105394586(1) \\ & +201.306718799807332978511045962(1)\mathrm{i})\epsilon^{-4} \\ & + (-38141.42941608860602881348699977(1) \\ & -9875.1387674565300290761929799467(6)\mathrm{i})\epsilon^{-3} \\ & + (-192024.38943595392190011116347499(2) \\ & -116336.97455672136058813504166616(3)\mathrm{i})\epsilon^{-2} \\ & + (-593184.25931962260632465778776322(7) \\ & -634796.91030089586664017773559163(9)\mathrm{i})\epsilon^{-1} \\ & + (-1.2144593839823254798466369(4) \cdot 10^6 \\ & -2.26226437225227021523850681(3) \cdot 10^6\mathrm{i}) \end{aligned}$
$I_{3,0,3,0,1,0,0}$	$\begin{aligned} & (6.49007914201374243337005954471802798074(1) \\ & -9.258183656225205164855057696558411357258(2)\mathrm{i})\epsilon^{-2} \\ & + (71.06533930083802312240961747079802830572(3) \\ & -41.5899135814734797976571896166944777261(1)\mathrm{i})\epsilon^{-1} \\ & + (301.1816591616686384565861677391444437963(2) \\ & -89.6492865222768617996461385960395376938(2)\mathrm{i}) \end{aligned}$
$I_{3,0,3,0,2,0,0}$	$\begin{aligned} & (5.9951498363364590071670206765167894653(5) \\ & -9.2735829273283564241871830647898148387(3)\mathrm{i})\epsilon^{-2} \\ & + (76.176417954298629434538333168097805554(7) \\ & -48.0253516413715291746523753731454463910(3)\mathrm{i})\epsilon^{-1} \\ & + (352.04003593334545904655522214942045628(4) \\ & -83.24566206205916235859744291500788337(4)\mathrm{i}) \end{aligned}$
$I_{3,2,1,0,1,0,0}$	$\begin{aligned} & (29.5219971895806602682712462(8) \\ & -45.830196778215286662429499(1)\mathrm{i})\epsilon^{-2} \\ & + (462.55627057479565432167934(1) \\ & -417.90579266918457289585515(1)\mathrm{i})\epsilon^{-1} \\ & + (3288.9634377035298147852450(1) \\ & -2107.54314621320608764875591(8)\mathrm{i}) \end{aligned}$
$I_{3,1,2,0,1,0,0}$	$\begin{aligned} & (11.462353218207000113278917295(2) \\ & -16.648024055118956718751610820(3)\mathrm{i})\epsilon^{-2} \\ & + (143.84637009398424379318757688(4) \\ & -101.49639245146199503707522342(3)\mathrm{i})\epsilon^{-1} \\ & + (756.8706658583507580014534856(3) \\ & -324.8286189864459118518012894(2)\mathrm{i}) \end{aligned}$
$I_{0,2,0,3,2,0,0}$	$\begin{aligned} & (-500.00000000000000000000000000000000000000(1) \\ & +0(0)\mathrm{i})\epsilon^{-4} \\ & + (-8830.539614080604191447462273970690191761(1) \\ & +0(0)\mathrm{i})\epsilon^{-3} \\ & + (-85340.76504296739209845004617243136374998(1) \\ & +0(0)\mathrm{i})\epsilon^{-2} \\ & + (-599328.7360440269123202060290322796568177(1) \\ & +0(0)\mathrm{i})\epsilon^{-1} \\ & + (-3.446360763044423438123383039152207(1) \cdot 10^6 \\ & +0(0)\mathrm{i}) \end{aligned}$
$I_{2,2,0,1,2,0,0}$	$\begin{aligned} & (3.237044189271630763449367731739(1) \\ & -0.0642256754524799225317006383959(8)\mathrm{i})\epsilon^{-2} \\ & + (21.18811210387487437363446925855(1) \\ & +19.567238956341826601387044186582(2)\mathrm{i})\epsilon^{-1} \\ & + (31.76087152110813364447353552532(5) \\ & +127.10325911898495931038096717446(2)\mathrm{i}) \\ & + (-94.4748441549143946616759695(3) \\ & +431.7716920912757767225225991(3)\mathrm{i})\epsilon^1 \end{aligned}$

integral	value
$I_{1,2,0,2,2,0,0}$	$(6.053817430682806044247615400349841(3)$ $-2.787782733285729473634650915525825(2)i)\epsilon^{-2}$ $+(71.26876462255855805321797679343159(3)$ $-8.886053420148723179601512359704559(5)i)\epsilon^{-1}$ $+(452.3639054846672762612228684550924(1)$ $-13.85623253439926363847171482730160(5)i)$ $+(2274.5492267433631373850538466401(8)$ $-9.287650079726786811800643037(1)i)\epsilon^{-1}$
$I_{2,2,1,1,1,0,0}$	$(7.653714368360222526781830501445(2)$ $-2.893609618780655620355003305268(2)i)$ $+(73.939601423164616566328684(5)$ $+12.825003129665806188991275(4)i)\epsilon^{-1}$
$I_{2,1,2,1,1,0,0}$	$(4.264629814805857405150999032846475(5)$ $-2.017160256679987470589447964369463(6)i)$ $+(33.17975519101001802629042193(2)$ $+8.07586512331554321976777377(1)i)\epsilon^{-1}$
$I_{1,2,1,2,1,0,0}$	$(11.543566907798982758958158957031838(5)$ $-9.820373209388924816976509004988606(6)i)$ $+(144.21172124550668234062350975(2)$ $-62.47107819862774607013925186(1)i)\epsilon^{-1}$
$I_{0,0,4,3,0,1,0}$	$(-1771.126690984561717718709533108464717572(1)$ $+1296.00449394395899378012234980961811349(1)i)\epsilon^{-2}$ $+(-20717.89512089967975519982104063915736754(1)$ $+10844.6408306458577135101196652423956448(1)i)\epsilon^{-1}$ $+(-119739.3349314498339740540444185220180661(1)$ $+45184.7832169057850097341314049930093661(1)i)$ $+(-461738.517132741034558500314858975507720(4)$ $+123853.496421736915587945725861120693392(1)i)\epsilon^{-1}$
$I_{2,0,4,1,0,1,0}$	$(-848.7800071960334765340241806762636530859(1)$ $+391.391529696807297793625473782724283231(1)i)\epsilon^{-2}$ $+(-9737.831026511969515755374274936075571072(1)$ $+2822.76185918563552228425668949540802028(1)i)\epsilon^{-1}$ $+(-56873.59255831332601997575413490033667703(1)$ $+10145.3091912606671512935889476428709303(1)i)$
$I_{0,0,3,0,2,2,0}$	$(10.62676014590737030631225719865078830543(1)$ $-7.77602696366375396268073409885770868097(1)i)\epsilon^{-4}$ $+(111.1329185684439095853391014667207015161(1)$ $-5.9962084662154749967518299746134943053(1)i)\epsilon^{-3}$ $+(436.3107141642636915283241152281182327017(1)$ $+201.474014221889365893592344646848985435(1)i)\epsilon^{-2}$ $+(930.471018499460760315616518424563045529(1)$ $+1099.290747550425580182851691591005385881(1)i)\epsilon^{-1}$ $+(983.724859630280758218436196051119176161(1)$ $+3161.295585052746126105345598344088483816(1)i)$
$I_{0,0,4,0,2,2,0}$	$(-851.0446002431789505105204286644179805091(1)$ $+12.960044939439589937801223498096181135(1)i)\epsilon^{-4}$ $+(-7956.355771473240930908501511521083464948(1)$ $-2633.85548686865055565019654365393179435(1)i)\epsilon^{-3}$ $+(-34388.65126393856838055410408040912216949(1)$ $-24932.6024014035056967159360044481788570(1)i)\epsilon^{-2}$ $+(-90103.3083062731127776853650225572653876(1)$ $-116898.4962958999962353056054231206151182(1)i)\epsilon^{-1}$ $+(-149081.345428498420922595244977860002721(1)$ $-365828.0166691566404461517736296109952652(1)i)$
$I_{2,0,3,0,1,1,0}$	$(10.402252539494370457318743704950989829(8)$ $-14.345229797245715625498652239939852715(8)i)\epsilon^{-2}$ $+(125.1273081193061484281585437574391255(1)$ $-80.35902925039748859362470228514207405(7)i)\epsilon^{-1}$ $+(625.1188543878396380380496132087098749(8)$ $-230.0669048824000616683729095797092182(3)i)$

## B. Master integral calculation

integral	value
$I_{2,0,2,0,2,1,0}$	$(5.12649165149262354153270015453577104(2)$ $-2.39786879828713692490396035700446035(2)i)\epsilon^{-2}$ $+(43.1384382909484253787782201805652478(2)$ $+9.1341172236538057274008858311651787(1)i)\epsilon^{-1}$ $+(135.718994336864940526291080488278390(2)$ $+108.6649426667132432945486271698197560(5)i)$
$I_{2,2,1,0,1,1,0}$	$(57.6734388505725719455230823(1)$ $-77.1896655394704099189526669(1)i)\epsilon^{-2}$ $+(973.971142941339456802493352(2)$ $-798.500698487214456333540921(1)i)\epsilon^{-1}$ $+(7786.74308408804792237470238(2)$ $-4503.53630475190424554467555(1)i)$
$I_{2,1,2,0,1,1,0}$	$(19.4062122064900530561990259341(3)$ $-26.2140392043579812629983115801(4)i)\epsilon^{-2}$ $+(264.300162580220667577703060437(5)$ $-188.359258060110421268894876817(4)i)\epsilon^{-1}$ $+(1590.44313249687489294233477328(4)$ $-714.10255783372903943787323640(2)i)$
$I_{2,1,1,0,2,1,0}$	$(13.162534599117637003632795289(8)$ $-7.873123399619770344968884083(6)i)\epsilon^{-2}$ $+(149.0655250969421242880608796(1)$ $-6.50921223327200026918254598(2)i)\epsilon^{-1}$ $+(724.9459418143662970772723239(4)$ $+255.3771913443671642515902549(2)i)$
$I_{1,2,1,0,2,1,0}$	$(48.2590164403780686449685451(1)$ $-18.6333983817561933462295789(1)i)\epsilon^{-2}$ $+(719.187093654641546056020141(2)$ $-5.847914378317309199852258(2)i)\epsilon^{-1}$ $+(5314.48966732850763701536112(2)$ $+1384.12333941950822759585419(1)i)$
$I_{0,2,0,2,2,1,0}$	$(26.35978789327381431568763696928808449392(1)$ $-15.6298141969641454649882755387039944487(1)i)\epsilon^{-1}$ $+(391.6624233232694123430221833662171114550(1)$ $-110.571863556868624565654732648083607456(1)i)$ $+(3041.0904076263704880629487556512624166(1)$ $-415.579628953133529413147038419460340662(4)i)\epsilon^1$ $+(17752.9342343181057430646055510799119212(3)$ $-1114.8919193137183166127109438063008483(1)i)\epsilon^2$
$I_{1,2,0,1,2,1,0}$	$(7.68703603980620427081183077546397(5)$ $-0.06035627207628029354034089427181(4)i)\epsilon^{-1}$ $+(70.0128064225360568378100525015565(7)$ $+47.3958979498079244861299799725087(1)i)$ $+(250.340727450474131778908547051(8)$ $+431.608218030737487778856296084(3)i)\epsilon^1$
$I_{2,2,0,1,2,1,0}$	$(211.176680230009271873109150590297(1)$ $-125.6320560422318000007809172816634(9)i)\epsilon^{-1}$ $+(3481.65670949815433210492059762191(1)$ $-581.8378570274732124059852526844247(4)i)$ $+(26618.03978805584175676539564497(6)$ $+3989.59700633486387676042343947(8)i)\epsilon^1$
$I_{0,2,1,2,1,1,0}$	$(35.5123537865915438035939939368450271926(1)$ $-41.40640145790152669538293805301505606439(1)i)$ $+(536.2866497588244933017599219627679228(2)$ $-373.39546128377042868166630197294524969(7)i)\epsilon^1$
$I_{0,2,1,1,2,1,0}$	$(77.1931247647508488971887683668851742772(1)$ $-77.29633677481677507872642339165608017738(1)i)$ $+(1417.26749613802551022809655401224437678(2)$ $-877.63904945360346748843624039013773012(1)i)\epsilon^1$
$I_{1,2,1,1,1,1,0}$	$(14.3469946386848490584503197504650(1)$ $-5.9110561447297520043240139521545(1)i)$
$I_{1,1,2,1,1,1,0}$	$(7.5661883763641641147905139525466162(3)$ $-4.0414148256198952334058354219457418(3)i)$

integral	value
$I_{2,2,1,1,1,1,0}$	( 123.448368780499985905570157543746(2) -145.894064022690534123097806910204(2)i)
$I_{3,0,3,1,0,0,1}$	( 19.1650010010752141880583898052118191905(1) -39.65420769189096007125888448488170232143(1)i) $\epsilon^{-1}$ +( 271.3342103025257208719998705577617396042(1) -240.772814068792435228767384008977327359(1)i)
$I_{3,0,2,0,1,0,1}$	( 5.6353434048468061993364604421164674(5) -3.2254746747864649288415059417860592(6)i) $\epsilon^{-2}$ +( 45.285938657087681584574763690989328(4) +7.731756063648849975009525988876820(1)i) $\epsilon^{-1}$ +( 125.51478782993090482519962255328947(1) +100.8041720066283889328114925092024823(1)i)
$I_{3,0,1,0,2,0,1}$	( 6.197654728933413109156869152717302380(5) -7.207269902172504244857669489444425615(6)i) $\epsilon^{-2}$ +( 70.84089619330629807688687599901961715(4) -34.71365938080273424523357918825985499(1)i) $\epsilon^{-1}$ +( 344.7132861320938507016105769402412003(1) -81.645622160988167323016851586366393777(5)i)
$I_{3,0,1,0,1,0,2}$	( 9.9178352106575937062768860835368286(4) -11.6254187347803946922837185016602550(5)i) $\epsilon^{-2}$ +( 116.557096310307450011121548465599770(4) -61.115963188642961813934299035043565(1)i) $\epsilon^{-1}$ +( 593.80198520407661933204663155027056(1) -163.3243899369700810400245062875216427(3)i)
$I_{3,1,1,0,1,0,1}$	( 14.2682668588555252375964224621(5) -11.5057579723304825251846486315(2)i) $\epsilon^{-2}$ +( 161.891316481480402152191164640(5) -30.543791632101886500905586718(3)i) $\epsilon^{-1}$ +( 768.22815142127768834244428771(1) +147.49153341719194492069938172(4)i)
$I_{2,1,1,0,2,0,1}$	( 7.875199237842743709382167813(1) -0.5408893457125379975500203582(5)i) $\epsilon^{-2}$ +( 64.13777468906711059557734189(1) +41.992004404581737404090895674(5)i) $\epsilon^{-1}$ +( 179.46712885091786979076841611(3) +339.45937733104817059878528661(8)i)
$I_{2,0,0,1,2,0,2}$	( 5.092680043176200859204145084057581918516(1) -2.34834917818084378676175284269634569939(1)i) $\epsilon^{-2}$ +( 56.32229647415513733751038536329259595919(1) -5.96300003706608703397694847471146348576(1)i) $\epsilon^{-1}$ +( 332.6920332300623757000369276504465775143(1) -5.5377313835037484480909187243077963993(1)i) +( 1573.524521694381974200100881674959238213(1) +3.372511034931439270303914450069641229(1)i) $\epsilon^1$
$I_{1,0,0,2,2,0,2}$	( 2.042800388456276164266038611986847480737(1) -0.017590264991183329273020431739395270631(1)i) $\epsilon^{-2}$ +( 9.96880923572943088480602991800408033439(1) +12.63913772468013760643302663486701239647(1)i) $\epsilon^{-1}$ +( -2.5791177598825203281095071710746280062(1) +61.13138897649507357545520723718983833691(1)i) +( -92.58392625111734846245585886597823220(1) +143.94428231186044270079388967871192445(5)i) $\epsilon^1$
$I_{2,1,0,1,2,0,1}$	( 3.70803854994086519555654855998437(6) -0.23844949107277436245487895342875(5)i) +( 27.985277946643772720137497526(2) +19.9941340602904860140697687938(3)i) $\epsilon^1$
$I_{3,1,0,1,2,0,1}$	( 43.8171936197303967437025546346140(5) -111.5127641508116461668950250335634(4)i) $\epsilon^{-1}$ +( 927.509880612332186197023162009544(5) -1152.6456520510807760786206852334734(3)i) +( 7681.61675845847637346103143138(3) -5743.20005369445283724949272225(4)i) $\epsilon^1$

## B. Master integral calculation

integral	value
$I_{2,0,2,1,1,0,1}$	( 1.6170594195943819446812334495741223833(7) −0.0221542772000165343848990431432593307(4)i) $\epsilon^{-1}$ +( 4.537924390020428807192468358690171794(2) +9.96071993450880656056354378083004431(1)i)
$I_{2,0,1,1,2,0,1}$	( 1.25643183302747245263936253309624607(2) −0.01657494384268934827939940373222405(2)i) $\epsilon^{-1}$ +( 4.5349170368901024562166202380730864(2) +7.69786551137275614286741181477507234(7)i)
$I_{2,0,1,1,1,0,2}$	( 2.0429859690732942657839736885781459073(6) −0.0268782019487011136089479295090443320(4)i) $\epsilon^{-1}$ +( 7.575046804965183098452601316843626470(2) +12.50674932104938898797721308545330973(1)i)
$I_{1,0,2,2,1,0,1}$	( 2.16438237847467652496443541775953(1) −0.103118010854412934537297789332147(2)i) $\epsilon^{-1}$ +( 8.81377386476325033579282798371617(2) +12.430404725829744331685997892826827(7)i)
$I_{2,1,1,1,1,0,1}$	( 2.78217539093380451477585927413662(5) −0.03339642699071255185162873958418(2)i) +( 12.3587027512868085075987822(1) +17.10906450151247642837528497(6)i) $\epsilon^1$
$I_{1,1,1,2,1,0,1}$	( 3.3493903737394035013485179932750195(2) −0.12011147805770139355767260601692690(6)i) +( 17.6102955683643041175505474658(4) +19.5090544213655352113395654131(2)i) $\epsilon^1$
$I_{1,1,1,1,2,0,1}$	( 4.21917795363762170931992773799539(6) −0.05987204805510559886802449906268(2)i) +( 26.5554926740215583714166509(1) +25.66213027164904137002608397(5)i) $\epsilon^1$
$I_{0,0,3,3,0,1,1}$	( 52.4614358590194934509268567703238115679(5) −165.267946861926159519226788383233115907(1)i) $\epsilon^{-1}$ +( 965.812196176029490959530560379790149323(6) −1223.685127700746419315565022072768624529(4)i) +( 5752.1139566977682547660890676209809(7) −4100.4982067318332858597702254572829(2)i) $\epsilon^1$
$I_{2,0,3,1,0,1,1}$	( 35.8578627890508185051064810479742347426(1) −64.55616078841694526916325764443322438043(1)i) $\epsilon^{-1}$ +( 515.4467380808836486419399629782398523420(1) −440.246860216652022986859715388427384203(1)i)
$I_{1,1,1,1,1,1,1}$	( 4.4010558557694406850689904297647(2) −0.03361590896548148544159251786030(6)i)
$I_{1,1,1,1,1,2,1}$	( 167.8810238246235255376142819235725(2) −74.4325041023953689599557085240962(1)i)
$I_{1,1,1,1,2,1,1}$	( 49.0745359649025571838433570199(3) −1.1477549244480465116662588097(1)i)
$I_{1,4,1,1,0,0,1,0,0}^{a1}$	(−1281.1726733010340451353051292440(5) +10.0593786793800489233901490453(4)i) +(−13574.752262793192541368064058476(5) −3873.055756423793274530907243784(3)i) $\epsilon^1$
$I_{0,3,2,1,0,1,1,0,0}^{a1}$	( 9.457727324470883771803545223(4) −5.27439824216496124734458002(1)i) +( 84.57102951127698665263138182(6) +10.30204662606587106979410418(5)i) $\epsilon^1$
$I_{1,3,1,1,0,1,1,0,0}^{a1}$	( 22.6041109767130782637870655531(3) −12.2530172357251915386069330221(6)i) +( 230.075382169749333110876740616(4) +12.364439324225702449322922427(3)i) $\epsilon^1$
$I_{0,3,3,1,0,1,0,0,0}^{a2}$	( 6.25210741338324794026437693336204008512(1) −9.276774386458589110969224479081621018618(9)i) +( 71.8128092898418535442607814317351630221(1) −43.2569260597965242322816569368409481615(1)i) $\epsilon^1$

integral	value
$I_{0,3,2,1,0,1,0,1,0}^{a2}$	( 6.004519902583655613671638490013729901(2) − 3.260771785658951040603924712299624944(2)i) +( 49.19720796965677703133042185192592690(2) + 9.655647278279117240325316167548194315(8)i) $\epsilon^1$

**Table B.4.:** Numerical results for the one-loop master integrals at the point  $x = 0.2$ ,  $z = 0.05$ ,  $m = 0.001$ , and  $s = 1$ .

[illegible]

## B. Master integral calculation

integral	value
$I_{1,1,1,1}^{\text{box A}}$	$(-3.29341280000677824246287745062130(2)$ $+0.10849492255047109340158902897349(2)\text{i})$ $+(-10.3004937740793241750983328501296(1)$ $-9.5334786846670136514592840849555(1)\text{i}) \epsilon^1$ $+(-6.8398834629654813102068584749275(5)$ $-28.7961690563716481338122143760938(3)\text{i}) \epsilon^2$
$I_{2,0,0,2}^{\text{box B}}$	$(-21.11188889097583470151(8)$ $+1.20784031279884399787(7)\text{i})$ $+(-97.2882468805152390173(4)$ $-57.44691537129055885531(9)\text{i}) \epsilon^1$ $+(-151.8448600686526640635(7)$ $-267.42872391079420755581(3)\text{i}) \epsilon^2$ $+(-24.5995471836486005228(7)$ $-574.3303227875950694272(1)\text{i}) \epsilon^3$
$I_{1,0,2,1}^{\text{box B}}$	$(-10.4905403617881122851722(6)$ $+131.2619399340341442062066(5)\text{i})$ $+(-220.389609956283148669844(3)$ $+776.0505410655329425303857(5)\text{i}) \epsilon^1$ $+(-1095.606061033664620488256(4)$ $+2314.1825843109280599012359(3)\text{i}) \epsilon^2$
$I_{2,1,0,1}^{\text{box B}}$	$(-20.3708686115440641608733(3)$ $+7.1287147960760528693654(2)\text{i})$ $+(-157.070329955792958565286(1)$ $+15.8167898124675369908974(3)\text{i}) \epsilon^1$ $+(-683.450322481514915039954(2)$ $+12.53865253992443146190289(6)\text{i}) \epsilon^2$
$I_{1,1,1,1}^{\text{box B}}$	$(-4.7787934283744859498136871(5)$ $+0.3114516551610548344667942(4)\text{i})$ $+(-18.343841254420443716364557(2)$ $-12.6711383547989776289276137(4)\text{i}) \epsilon^1$ $+(-24.123720460347704199557088(3)$ $-47.3340142852470091205085628(2)\text{i}) \epsilon^2$
$I_{1,1,1,1}^{\text{box C}}$	$(-7.6870360398062042708118308(4)$ $+0.0603562720762802935403409(3)\text{i})$ $+(-32.785427411900690904242024(2)$ $-23.6204223098798790437196114(4)\text{i}) \epsilon^1$ $+(-50.140698178495198200782471(3)$ $-100.3475339608545766368170733(2)\text{i}) \epsilon^2$



### B.3. Singularities of the differential equations

**Table B.5.:** Singularities of the differential equations of the double-box integral family.

Singularity	DE	Interpretation
$m = 0$	$A_x, A_z, A_m$	massless limit
$m = 1/4$	$A_x, A_z, A_m$	production threshold
$m = 1/2$	$A_x, A_z, A_m$	
$x = 0$	$A_x, A_z, A_m$	
$z = 0$	$A_x, A_z, A_m$	
$m + x = 0$	$A_x, A_m$	
$m + z = 0$	$A_z, A_m$	
$x + z = 0$	$A_x, A_z$	
$1 - x - z = 0$	$A_x, A_z$	
$2m + x = 0$	$A_x, A_z, A_m$	
$2m - (1 - x) = 0$	$A_x, A_z, A_m$	
$2m - (1 - z) = 0$	$A_x, A_z, A_m$	
$4m - (1 - x)^2 = 0$	$A_x, A_m$	
$4m - (1 - z)^2 = 0$	$A_z, A_m$	
$m^2 - mx + x = 0$	$A_x, A_z, A_m$	
$4m + xz = 0$	$A_x, A_z, A_m$	
$4m - (1 - x - z) = 0$	$A_x, A_z, A_m$	
$4m(1 - 2x - 4m) + xz = 0$	$A_x, A_z, A_m$	
$4m(1 - 2x - 4m) + xz(1 - x - 2m) = 0$	$A_x, A_z, A_m$	
$m(x + z)^2 - xz = 0$	$A_x, A_z, A_m$	
$m(x + z)^2 - xz(1 - x - z) = 0$	$A_x, A_z, A_m$	boundary of physical phase space



## C. Numerical results

### C.1. Numerical results for the master integrals at the benchmark phase space point

**Table C.1.:** Numerical values for the one-loop master integrals at the benchmark point  $x = 0.2$ ,  $z = 0.05$ ,  $m = 289/2500$ , and  $s = 1$ .

integral	value
$I_{0,0,3,1}^{\text{box A}}$	$-0.481051948718639672(3) + 1.647038009335536233(2)i$ $+ (-3.473955240960911533(7) + 1.223249228135763085(3)i)\epsilon^1$ $+ (-3.260387067683624358(2) - 1.708883153353645054(7)i)\epsilon^2$
$I_{0,4,0,0}^{\text{box A}}$	$1.441753171856978085(2) + 0(2 \cdot 10^{-18})i$ $+ (2.278551986508545410(3) + 0(3 \cdot 10^{-18})i)\epsilon^1$ $+ (2.986310401218017396(4) + 0(4 \cdot 10^{-18})i)\epsilon^2$ $+ (2.244858104782409163(3) + 0(3 \cdot 10^{-18})i)\epsilon^3$ $+ (1.820389870967189175(3) + 0(3 \cdot 10^{-18})i)\epsilon^4$
$I_{0,3,1,0}^{\text{box A}}$	$-0.411340773796563501(4) + 2.339556342086690189(3)i$ $+ (-4.98531426868027702(1) + 2.862038218079440258(3)i)\epsilon^1$ $+ (-6.993102746440117556(7) - 1.78761247424332808(1)i)\epsilon^2$ $+ (-3.730336829322852153(4) - 6.29381739669472563(1)i)\epsilon^3$
$I_{0,2,1,1}^{\text{box A}}$	$-0.443696748247589373(4) + 2.059395394550822008(2)i$ $+ (-4.365877968747799624(9) + 2.160747810820682499(3)i)\epsilon^1$ $+ (-5.362191709509864132(5) - 1.80754082201655012(1)i)\epsilon^2$
$I_{2,0,0,2}^{\text{box A}}$	$-3.80478902550886042(1) + 3.6461431698185693572(2)i$ $+ (-19.59465614794808260(3) - 0.88135789153436103(3)i)\epsilon^1$ $+ (-28.315504933053821093(2) - 26.96331339419949376(8)i)\epsilon^2$ $+ (-8.82580059827601412(7) - 57.04643204101818615(9)i)\epsilon^3$
$I_{2,0,1,1}^{\text{box A}}$	$-5.75190039815061123(1) + 4.703345789615881179(1)i$ $+ (-32.17353796831732699(5) + 6.65611830468976022(4)i)\epsilon^1$ $+ (-82.1850952726611045(1) - 2.6912788873706998(1)i)\epsilon^2$
$I_{1,2,0,1}^{\text{box A}}$	$3.392347831320988319(1) + 2.597409872432067470(8)i$ $+ (6.158534757173375845(7) + 10.94791689305203590(2)i)\epsilon^1$ $+ (3.43687165733518715(3) + 22.49878453364155016(4)i)\epsilon^2$
$I_{1,1,1,1}^{\text{box A}}$	$-3.080896347916169957(9) + 3.1991723080595289652(2)i$ $+ (-15.91249858579344338(2) + 1.11356776154783343(2)i)\epsilon^1$ $+ (-26.40327292795157624(2) - 15.02016964920329350(6)i)\epsilon^2$
$I_{2,0,0,2}^{\text{box B}}$	$-2.50567920511377352(2) + 13.24302021178222138(2)i$ $+ (-46.3478529429305264(2) + 42.15972288526383763(2)i)\epsilon^1$ $+ (-162.667092800096266(6) + 21.7381571209837982(8)i)\epsilon^2$ $+ (-285.4951117238158(3) - 138.59245540041183(4)i)\epsilon^3$
$I_{1,0,2,1}^{\text{box B}}$	$4.5678091967489664(1) + 1.35003930332489817(1)i$ $+ (13.773617313259506(6) + 8.4923908775111097(8)i)\epsilon^1$ $+ (23.4679151747593(3) + 26.38378174724278(4)i)\epsilon^2$
$I_{2,1,0,1}^{\text{box B}}$	$-11.36339347383403118(3) + 10.123354851135646533(2)i$ $+ (-78.3554102236169545(3) + 24.49512991117622366(7)i)\epsilon^1$ $+ (-249.93269335018518(1) + 12.149633498096507(2)i)\epsilon^2$

### C. Numerical results

integral	value
$I_{1,1,1,1}^{\text{box B}}$	$-3.17962875108424836(8) + 4.425350373137667900(7)i$ $+ (-20.007820106247942(4) + 5.9843070353671266(5)i)\epsilon^1$ $+ (-43.2680826586445(2) - 9.54720330587401(3)i)\epsilon^2$
$I_{1,1,1,1}^{\text{box C}}$	$-8.66852344336730530(3) + 4.399885074763291166(6)i$ $+ (-46.798730333785023(2) - 6.8928888642525010(2)i)\epsilon^1$ $+ (-99.99489253629838(8) - 74.83931582092854(1)i)\epsilon^2$

**Table C.2.:** Numerical values for the two-loop master integrals at the benchmark point  $x = 0.2$ ,  $z = 0.05$ ,  $m = 289/2500$ , and  $s = 1$ .

integral	value
$I_{4,0,4,0,0,0,0}$	$(2.078652208559656985801309(3) + 0(3 \cdot 10^{-24})i)\epsilon^{-4}$ $+ (6.570219107579427363460488(9) + 0(9 \cdot 10^{-24})i)\epsilon^{-3}$ $+ (13.80284414143316132976818(2) + 0(2 \cdot 10^{-23})i)\epsilon^{-2}$ $+ (20.08198957993065536075399(3) + 0(3 \cdot 10^{-23})i)\epsilon^{-1}$ $+ (24.39720734155296971341952(3) + 0(3 \cdot 10^{-23})i)\epsilon^0$
$I_{3,0,4,1,0,0,0}$	$(-0.693558172893079111731066(4) + 2.374622274128512447256156(2)i)\epsilon^{-2}$ $+ (-6.10468786091123014010305(2) + 5.5164851826629028715574278(8)i)\epsilon^{-1}$ $+ (-14.05283144963226478965663(3) + 5.24201599056334527131195(1)i)\epsilon^0$
$I_{3,2,0,0,2,0,0}$	$(-3.783373874326606072976462(1) - 2.863974959295463100129455(9)i)\epsilon^{-4}$ $+ (-15.52966934695094918992457(2) - 31.13913597085513608405862(7)i)\epsilon^{-3}$ $+ (-4.7675566106874185862637(2) - 158.0573914585248234652427(2)i)\epsilon^{-2}$ $+ (228.406167472504411249066(1) - 478.9702905199366323958504(4)i)\epsilon^{-1}$ $+ (1148.391744220882199557748(3) - 871.5632391229058226583729(4)i)\epsilon^0$
$I_{4,2,0,0,2,0,0}$	$(-3.61257094162885455385934(3) + 19.09316639530308733419637(2)i)\epsilon^{-4}$ $+ (-128.2453664671136286949123(4) + 122.963284261122170634996756(7)i)\epsilon^{-3}$ $+ (-896.073333079925456814237(1) + 123.130211548489142088425(1)i)\epsilon^{-2}$ $+ (-2952.210587139624783047429(2) - 1613.825461958468240360006(6)i)\epsilon^{-1}$ $+ (-4283.449748114193677961526(7) - 9219.77443829406314930894(2)i)\epsilon^0$
$I_{3,0,3,0,1,0,0}$	$(-1.4099367413420776481287956(4) - 1.108080930636926778082162(4)i)\epsilon^{-2}$ $+ (-0.920632768532596181973368(6) - 5.55679365294295782990032(2)i)\epsilon^{-1}$ $+ (2.515253083956218707042(4) - 11.94384732458145778584(3)i)\epsilon^0$
$I_{3,0,3,0,2,0,0}$	$(-2.868063126893464638364896(3) - 0.797047102399561924254405(5)i)\epsilon^{-2}$ $+ (-7.98791744382488069445814(1) - 16.42852181647373564890305(4)i)\epsilon^{-1}$ $+ (22.104585354635706656077(6) - 55.91465303475725121885(4)i)\epsilon^0$
$I_{3,2,1,0,1,0,0}$	$(-5.368538718040736994867971(5) - 3.370378871861364203374619(3)i)\epsilon^{-2}$ $+ (-26.24873969222245484439902(6) - 30.4247116661581688241519(4)i)\epsilon^{-1}$ $+ (-79.1361002319131714443(1) - 142.2458130777469442483(7)i)\epsilon^0$
$I_{3,1,2,0,1,0,0}$	$(-2.3939132912203584263337337(7) - 1.799394194387369730757061(5)i)\epsilon^{-2}$ $+ (-5.12023565842171450613744(2) - 11.5164505573440084831992(1)i)\epsilon^{-1}$ $+ (-3.86245922041100019949(4) - 35.2146129555726290517(3)i)\epsilon^0$
$I_{0,2,0,3,2,0,0}$	$(-4.325259515570934256055363(6) + 0(6 \cdot 10^{-24})i)\epsilon^{-4}$ $+ (-35.29760949690594373816540(5) + 0(5 \cdot 10^{-23})i)\epsilon^{-3}$ $+ (-207.7165153810865819012483(3) + 0(3 \cdot 10^{-22})i)\epsilon^{-2}$ $+ (-1000.130815167729631064071(1) + 0(1 \cdot 10^{-21})i)\epsilon^{-1}$ $+ (-4425.171628498583896399563(6) + 0(6 \cdot 10^{-21})i)\epsilon^0$
$I_{2,2,0,1,2,0,0}$	$(2.943458085451554619452169(8) - 2.98848176406093818433949417(6)i)\epsilon^{-2}$ $+ (33.18322577558473143322179(5) - 3.30103352691433971629770(4)i)\epsilon^{-1}$ $+ (134.0680456378317831437544(1) + 59.5462466514309830447660(3)i)\epsilon^0$ $+ (322.66779128911579053341159(8) + 379.063721094683710417211(1)i)\epsilon^1$
$I_{1,2,0,2,2,0,0}$	$(2.122234984582881128855329(8) - 3.430862528022813236432156(2)i)\epsilon^{-2}$ $+ (26.43982535047013380354646(5) - 12.41135648747758526745752(2)i)\epsilon^{-1}$ $+ (116.9113240202218961179817(2) - 12.0918345874416712304719(1)i)\epsilon^0$ $+ (367.4512625229782886361815(5) + 42.9773513945082020897528(6)i)\epsilon^1$
$I_{2,2,1,1,1,0,0}$	$(1.6207766391930502360822(1) - 5.84904548090065984389143(1)i)\epsilon^0$ $+ (30.508340935695989273277(6) - 27.3967554430545040491886(1)i)\epsilon^1$

*C.1. Numerical results for the master integrals at the benchmark phase space point*

integral	value
$I_{2,1,2,1,1,0,0}$	$(0.1872160481915144306223(1) - 2.97179025574148867176968(2)i)\epsilon^0$ $+ (10.702328881706250821686(8) - 9.6865745071424100472404(2)i)\epsilon^1$
$I_{1,2,1,2,1,0,0}$	$(0.3026645537449615916677(1) - 5.37660463166395365358814(1)i)\epsilon^0$ $+ (18.279064000268748191585(7) - 28.0442394703816426616759(5)i)\epsilon^1$
$I_{0,0,4,3,0,1,0}$	$(1.490656759092448280316844(4) + 4.547438131600846589930800(9)i)\epsilon^{-2}$ $+ (-1.92151279325605485702344(3) + 18.50254409200354170577641(2)i)\epsilon^{-1}$ $+ (-17.58730555285321028128051(8) + 36.98235016056506212740318(3)i)\epsilon^0$ $+ (-46.4172507468145607038543(1) + 44.403911052120363979146797(3)i)\epsilon^1$
$I_{2,0,4,1,0,1,0}$	$(-2.425325904394164264127012(9) + 3.885977811961802154393640(2)i)\epsilon^{-2}$ $+ (-16.58330324297619792700050(4) + 10.220211653532146305020179(9)i)\epsilon^{-1}$ $+ (-44.19884480602518639889034(8) + 11.14991117502423953867350(5)i)\epsilon^0$
$I_{0,0,3,0,2,2,0}$	$(-1.033919528106522127227763(3) - 3.154103088078347194776003(6)i)\epsilon^{-4}$ $+ (7.83821025967097570505795(4) - 18.83763248827838569088623(2)i)\epsilon^{-3}$ $+ (60.4476350286270257604011(1) - 40.75515457936101755152594(3)i)\epsilon^{-2}$ $+ (197.6754188382385971078718(3) + 1.9965114519514722644638(3)i)\epsilon^{-1}$ $+ (344.599095203468537626899(2) + 238.3342690801926614271566(8)i)\epsilon^0$
$I_{0,0,4,0,2,2,0}$	$(-5.48556664577402021471267(2) + 5.2568384801305786579600049(3)i)\epsilon^{-4}$ $+ (-52.93207986271701477382194(8) + 1.27382396340663500644210(7)i)\epsilon^{-3}$ $+ (-152.35490799567253287740589(3) - 128.7645333559813866782910(4)i)\epsilon^{-2}$ $+ (-72.8445002137058557246168(7) - 537.4852216313562727193796(9)i)\epsilon^{-1}$ $+ (683.533580282257326756447(2) - 979.8622803959722417649340(4)i)\epsilon^0$
$I_{2,0,3,0,1,1,0}$	$(-2.1002726939758899941038249(2) - 1.946173016838776321202506(6)i)\epsilon^{-2}$ $+ (-2.73002001462274249751501(5) - 11.4219053231008273766159(3)i)\epsilon^{-1}$ $+ (4.04021379649353679113(8) - 30.7731080749037934231(6)i)\epsilon^0$
$I_{2,0,2,0,2,1,0}$	$(0.199193524249726614723674(5) - 3.358730188673610121988528(4)i)\epsilon^{-2}$ $+ (14.31665561216199321250629(3) - 13.4641354671954418897663(2)i)\epsilon^{-1}$ $+ (61.47564243606201348831(5) - 9.9971411011165999631(3)i)\epsilon^0$
$I_{2,2,1,0,1,1,0}$	$(-9.389450494521746726733(2) - 11.0268694575670401119586(2)i)\epsilon^{-2}$ $+ (-45.22413370693602057051(4) - 115.225559434239177163302(2)i)\epsilon^{-1}$ $+ (-72.166230469134071149(4) - 627.87906850169687708(2)i)\epsilon^0$
$I_{2,1,2,0,1,1,0}$	$(-3.6921162135735822925962(5) - 3.89988848976218820357311(6)i)\epsilon^{-2}$ $+ (-8.938661321549967563831(7) - 28.69988485558428767473430(7)i)\epsilon^{-1}$ $+ (2.435828710858997226(1) - 103.595273796578848536(7)i)\epsilon^0$
$I_{2,1,1,0,2,1,0}$	$(-0.0212947246348681018227(8) - 6.23440536853113163302786(8)i)\epsilon^{-2}$ $+ (26.15250364294111339252(1) - 39.05592444886478737116313(2)i)\epsilon^{-1}$ $+ (175.455075488100296133(1) - 98.195224859292210584(9)i)\epsilon^0$
$I_{1,2,1,0,2,1,0}$	$(10.5163412151011942500044(7) - 26.74263046907044737865912(8)i)\epsilon^{-2}$ $+ (251.37459587481481594446(5) - 231.833715143736793219071(6)i)\epsilon^{-1}$ $+ (2133.845115664248568939(3) - 845.06715494733483760(2)i)\epsilon^0$
$I_{0,2,0,2,2,1,0}$	$(1.73694996929581616646918(2) - 9.95434934597526374671307(1)i)\epsilon^{-1}$ $+ (59.7411480525214857893681(2) - 79.40346504521902476871604(3)i)\epsilon^0$ $+ (487.328934431697699302672(1) - 332.2717549245353183064151(2)i)\epsilon^1$ $+ (2620.142507782282659065223(5) - 978.770262566856435738736(2)i)\epsilon^2$
$I_{1,2,0,1,2,1,0}$	$(8.66852344336730530362368(2) - 4.399885074763291165914653(6)i)\epsilon^{-1}$ $+ (100.7201543763787601479937(1) + 11.8132989686471057174807(2)i)\epsilon^0$ $+ (490.8170658525522334245258(2) + 316.906983356891803230297(1)i)\epsilon^1$
$I_{2,2,0,1,2,1,0}$	$(25.0155827025969922431229(2) - 92.8777684866825089716301(1)i)\epsilon^{-1}$ $+ (926.931374902771235377093(3) - 953.00022140872008213669167(4)i)\epsilon^0$ $+ (9299.87971092151498150340(2) - 3461.192623666048873852604(8)i)\epsilon^1$
$I_{0,2,1,2,1,1,0}$	$(-4.074032636063980238694697(6) - 8.57174770577329512502127(2)i)\epsilon^0$ $+ (-2.93453456075008044245055(9) - 69.2669480060537283297693(1)i)\epsilon^1$
$I_{0,2,1,1,2,1,0}$	$(-0.90231877863951689315101(3) - 23.35119799628597008584045(3)i)\epsilon^0$ $+ (95.7993934959786181954306(5) - 259.6692848780394739889165(2)i)\epsilon^1$
$I_{1,2,1,1,1,1,0}$	$(3.903532028991533223491(2) - 8.9765758080371977193602(3)i)\epsilon^0$
$I_{1,1,2,1,1,1,0}$	$(0.375949828356908527554(4) - 4.1843448095863002349318(5)i)\epsilon^0$
$I_{2,2,1,1,1,1,0}$	$(-25.65867786386626897063(1) - 42.573829879266823448400(1)i)\epsilon^0$
$I_{3,0,3,1,0,0,1}$	$(-5.692296675241527280930977(8) + 0.185617324406135105448449(8)i)\epsilon^{-1}$ $+ (-18.9498296910939196027691695(8) - 18.35444550265516918591303(5)i)\epsilon^0$

## C. Numerical results

integral	value
$I_{3,0,2,0,1,0,1}$	$(-0.965045477812790708998864(2) - 2.545828323467531536117390(5)i)\epsilon^{-2}$ $+(5.05374692381561363259600(3) - 10.6863749933564257321306(2)i)\epsilon^{-1}$ $+(24.29431075364005058386(5) - 16.0906007095104081579(3)i)\epsilon^0$
$I_{3,0,1,0,2,0,1}$	$(-0.570891555874676270433932(2) - 2.179797929323353264519984(4)i)\epsilon^{-2}$ $+(5.29069480998744864805208(3) - 9.9157666091794918238375(2)i)\epsilon^{-1}$ $+(26.12455935200131965458(5) - 16.9434883970457729602(3)i)\epsilon^0$
$I_{3,0,1,0,1,0,2}$	$(-0.687529515839652630455102(4) - 3.378349330952861594630522(6)i)\epsilon^{-2}$ $+(8.06267520088530606740411(8) - 14.8563152203564331320961(5)i)\epsilon^{-1}$ $+(37.1461014198389956516(1) - 27.629279274337110889(1)i)\epsilon^0$
$I_{3,1,1,0,1,0,1}$	$(-1.940394369461363788902375(3) - 4.265698610082124170669848(9)i)\epsilon^{-2}$ $+(3.7793387839224458189534(1) - 25.688083903795273567194(1)i)\epsilon^{-1}$ $+(43.9533518956062202415(2) - 73.779964867889612414(3)i)\epsilon^0$
$I_{2,1,1,0,2,0,1}$	$(2.80129779562052200421549(1) - 6.73353289405667550558101(6)i)\epsilon^{-2}$ $+(47.0917032287518641402995(1) - 30.120713288411122976845(1)i)\epsilon^{-1}$ $+(234.6128673606650257074(2) - 20.644898254368405374(2)i)\epsilon^0$
$I_{2,0,0,1,2,0,2}$	$(1.682206047287792333598495(6) - 2.695314210376705974287429(1)i)\epsilon^{-2}$ $+(18.85883901814948712499155(4) - 7.49603075437049494872420(2)i)\epsilon^{-1}$ $+(68.8156102698855901519614(1) - 2.04659498140836946407749(9)i)\epsilon^0$ $+(182.8670046200825533225222(2) + 29.8633516843826847373446(3)i)\epsilon^1$
$I_{1,0,0,2,2,0,2}$	$(2.485196133058751347284105(6) - 1.645113499104829460822134(1)i)\epsilon^{-2}$ $+(20.84524684621531594442709(2) + 5.41973376759840287976992(4)i)\epsilon^{-1}$ $+(49.27183193743445476347004(2) + 63.0617249014673468454902(2)i)\epsilon^0$ $+(26.6821880593150347539200(3) + 222.8419346817291604085598(4)i)\epsilon^1$
$I_{2,1,0,1,2,0,1}$	$(2.302527768989571638166752(7) - 2.8380288478684819682537791(8)i)\epsilon^0$ $+(25.94403692332447998582960(4) - 5.48469283335280975923486(3)i)\epsilon^1$
$I_{3,1,0,1,2,0,1}$	$(-9.149972621633102847123584(2) - 7.84442844852820320991232(2)i)\epsilon^{-1}$ $+( -38.0332933143947607140084(1) - 106.0576011598782040925515(2)i)\epsilon^0$ $+(53.3156706081796772627197(8) - 591.604074586138953664735(1)i)\epsilon^1$
$I_{2,0,2,1,1,0,1}$	$(1.35468288080330928203776(3) - 2.14161352588354822155908(1)i)\epsilon^{-1}$ $+(13.261373963883967886549(7) - 0.143264778107999125046(8)i)\epsilon^0$
$I_{2,0,1,1,2,0,1}$	$(1.6874409039083587010147(5) - 1.2572019221380717536990(2)i)\epsilon^{-1}$ $+(12.5159106589813372819(1) + 3.8192057591744221935(2)i)\epsilon^0$
$I_{2,0,1,1,1,0,2}$	$(2.54516345541249395156110(2) - 1.795334288641831093776512(6)i)\epsilon^{-1}$ $+(18.064762274113116911391(3) + 6.335825893124126963232(5)i)\epsilon^0$
$I_{1,0,2,2,1,0,1}$	$(0.80635830988826140436898(4) - 2.20742438823104755039239(2)i)\epsilon^{-1}$ $+(10.734321441183216312226(3) - 2.503147053281732562505(5)i)\epsilon^0$
$I_{2,1,1,1,1,0,1}$	$(2.93002674462100690567891(4) - 3.05937036555429544419532(2)i)\epsilon^0$ $+(27.24286014503540197696(1) + 0.55332292942249101266(1)i)\epsilon^1$
$I_{1,1,1,2,1,0,1}$	$(2.3615738066448575522525(2) - 3.2247479167932383190810(1)i)\epsilon^0$ $+(24.20672156293772468976(1) - 2.68000636416035537925(3)i)\epsilon^1$
$I_{1,1,1,1,2,0,1}$	$(4.520710969589522290272(6) - 3.620578190624512346726(3)i)\epsilon^0$ $+(45.522587159836769842(2) + 1.850777097115065880(2)i)\epsilon^1$
$I_{0,0,3,3,0,1,1}$	$(-8.87937669962535260294328(2) + 6.522177552850577858161383(3)i)\epsilon^{-1}$ $+( -55.64544670124480246597834(8) - 2.48534691374122351949977(8)i)\epsilon^0$ $+( -115.10904329170002583237719(3) - 93.5699889292279833809679(3)i)\epsilon^1$
$I_{2,0,3,1,0,1,1}$	$(-10.24056455688035236049962(1) - 2.51911329204300880257938(2)i)\epsilon^{-1}$ $+( -34.23046004991631788320548(2) - 46.1680154174523951192807(1)i)\epsilon^0$
$I_{1,1,1,1,1,1,1}$	$(5.029627152473532173573(6) - 3.66871945901777544363(3)i)\epsilon^0$
$I_{1,1,1,1,1,2,1}$	$(45.320198923648579185(5) - 92.68568243119606428(3)i)\epsilon^0$
$I_{1,1,1,1,2,1,1}$	$(46.1594587849386946(1) - 43.9309251938021438(1)i)\epsilon^0$
$I_{2,2,1,1,1,0,0}^c$	$(1.9614467572590914903782(5) - 4.894756734073404398646(4)i)\epsilon^0$ $+(29.11681179843566356160(3) - 17.653530885735489342598(7)i)\epsilon^1$
$I_{2,1,2,1,1,0,0}^c$	$(0.2978948626206104743747(1) - 2.82238900780845171483977(1)i)\epsilon^0$ $+(10.788811952304601117009(9) - 8.238731808427991740776(2)i)\epsilon^1$
$I_{1,2,1,2,1,0,0}^c$	$(0.370679108274706560683(1) - 4.91753966731921105141(1)i)\epsilon^0$ $+(16.98005224753033835758(6) - 23.68721061301598404255(4)i)\epsilon^1$

C.1. Numerical results for the master integrals at the benchmark phase space point

integral	value
$I_{0,0,4,3,0,1,0}^C$	$(5.454691283631208294372061(2) + 4.12914498168319362763762(1)i)\epsilon^{-2}$ $+(18.07472613336040167831794(4) + 25.58613333997384050900173(2)i)\epsilon^{-1}$ $+(25.8854957894539754712301(2) + 78.673432075046133262678454(7)i)\epsilon^0$ $+(-1.9335939762431181632073(4) + 156.42581029601492601942026(2)i)\epsilon^1$
$I_{2,0,4,1,0,1,0}^C$	$(-3.059739020448213853597649(5) + 4.946456931982141344337018(6)i)\epsilon^{-2}$ $+(-22.59370857747207822379193(2) + 14.70267273251023338022528(1)i)\epsilon^{-1}$ $+(-66.888138051843759159481945(9) + 18.80340858861520287539028(2)i)\epsilon^0$
$I_{0,2,0,2,2,1,0}^C$	$(-5.06106854353943862739608(4) - 18.97097013037314757525751(1)i)\epsilon^{-1}$ $+(41.1608746236522212536320(6) - 232.05551875425931729352564(2)i)\epsilon^0$ $+(863.828870218169996264654(5) - 1448.9608493055503953107686(8)i)\epsilon^1$ $+(6950.11821540260495146890(3) - 6173.79644002718924460747(1)i)\epsilon^2$
$I_{1,2,0,1,2,1,0}^C$	$(8.668523443367305303624(2) - 4.399885074763291165914(2)i)\epsilon^{-1}$ $+(97.66748709441583144305(2) + 12.988543950287174355331(3)i)\epsilon^0$ $+(450.52233739582698358700(1) + 308.44351159462852526213(6)i)\epsilon^1$
$I_{2,2,0,1,2,1,0}^C$	$(38.802815502505808146124(8) - 60.714070342280533941307(9)i)\epsilon^{-1}$ $+(812.53182058831081924585(8) - 424.35643260108859556988(1)i)\epsilon^0$ $+(6231.7114786874866890390(3) - 314.2552027879229865800(3)i)\epsilon^1$
$I_{0,2,1,2,1,1,0}^C$	$(-10.9176830458666877065178(6) - 7.4306661975268063889499(5)i)\epsilon^0$ $+(-70.576159679486214547906(3) - 87.887956796827534709399(5)i)\epsilon^1$
$I_{0,2,1,1,2,1,0}^C$	$(-16.5163732884190570578344(3) - 38.3725208222934887039574(4)i)\epsilon^0$ $+(-20.967051436146608088005(4) - 585.6482618640538673365786(5)i)\epsilon^1$
$I_{1,2,1,1,1,1,0}^C$	$(3.46810543770102184645(4) - 10.4972124022601790320(2)i)\epsilon^0$
$I_{1,1,2,1,1,1,0}^C$	$(-0.318761279541891745611(8) - 4.862635248103019368665(1)i)\epsilon^0$
$I_{2,2,1,1,1,1,0}^C$	$(-25.29574389323399997251(2) - 53.293272001660817933(1)i)\epsilon^0$
$I_{3,0,3,1,0,0,1}^C$	$(-6.53707499072082655695487(2) + 4.853639839292499244614042(2)i)\epsilon^{-1}$ $+(-41.57540909232405137473819(6) - 0.88072426208776470426459(6)i)\epsilon^0$
$I_{3,0,2,0,1,0,1}^C$	$(-2.201203497799253031111299(2) - 2.460689313947990855947058(4)i)\epsilon^{-2}$ $+(-1.6921365681185437701151(1) - 15.14104758329367702055683(4)i)\epsilon^{-1}$ $+(14.24713337880373015101(1) - 42.01443212555013605113(8)i)\epsilon^0$
$I_{3,0,1,0,2,0,1}^C$	$(-0.89409218106490247644053(1) - 2.493658696797914212805826(6)i)\epsilon^{-2}$ $+(4.7776368335269798293367(1) - 13.43247572865186649621466(6)i)\epsilon^{-1}$ $+(32.641836027142534478855(5) - 29.94840842175951878960(2)i)\epsilon^0$
$I_{3,0,1,0,1,0,2}^C$	$(-2.941877194926537369756246(1) - 4.815435616371413854766392(8)i)\epsilon^{-2}$ $+(-0.29529454040276649462607(9) - 33.2111950382684482815249(5)i)\epsilon^{-1}$ $+(44.90489401349237158497(9) - 106.6151041157274514297(7)i)\epsilon^0$
$I_{3,1,1,0,1,0,1}^C$	$(-3.142634342230047071813(1) - 4.95999301672790038551292(5)i)\epsilon^{-2}$ $+(-0.739844358012812627288(4) - 35.60793732149674633753(3)i)\epsilon^{-1}$ $+(51.007444739252365235(9) - 118.35162094551799889(7)i)\epsilon^0$
$I_{2,1,1,0,2,0,1}^C$	$(3.284835565185729818327(8) - 8.142563801847218692830(3)i)\epsilon^{-2}$ $+(59.84990818615841858372(1) - 36.5200702556542745396(3)i)\epsilon^{-1}$ $+(304.19408233116236356(7) - 1.4055267626913064(5)i)\epsilon^0$
$I_{2,0,2,1,1,0,1}^C$	$(0.8021852846264809974438(4) - 3.0075920494067946410077(2)i)\epsilon^{-1}$ $+(14.71502607944883970828(1) - 7.232297742791658046356(9)i)\epsilon^0$
$I_{2,0,1,1,2,0,1}^C$	$(1.9193842708646316622440(4) - 1.7335201682299046258509(3)i)\epsilon^{-1}$ $+(16.69801524431494493571(1) + 1.93330058395712616635(1)i)\epsilon^0$
$I_{2,0,1,1,1,0,2}^C$	$(3.2769313843021135187249(4) - 3.9334950400179183648533(3)i)\epsilon^{-1}$ $+(34.304455465226281337071(8) - 2.961639291145203364820(6)i)\epsilon^0$
$I_{1,0,2,2,1,0,1}^C$	$(0.0348319355590401631230(2) - 2.7476206713127811162922(1)i)\epsilon^{-1}$ $+(9.448000396592772513387(9) - 8.440045968636669794458(8)i)\epsilon^0$
$I_{2,1,1,1,1,0,1}^C$	$(2.96384517323843279779(5) - 4.38197793282387441512(1)i)\epsilon^0$ $+(34.738148793246224666(2) - 7.7706297762994866832(8)i)\epsilon^1$
$I_{1,1,1,2,1,0,1}^C$	$(1.7701306457788465239(1) - 4.63044744794959914730(2)i)\epsilon^0$ $+(27.332625016396995126(3) - 14.607945745806468133(2)i)\epsilon^1$

## C. Numerical results

integral	value
$I_{1,1,1,1,2,0,1}^c$	$(4.5809825979192144722(1) - 6.0179208078438957804(2)i)\epsilon^0$ $+ (59.359681766062049179(3) - 15.983565463570657153(4)i)\epsilon^1$
$I_{0,0,3,3,0,1,1}^c$	$(6.11156530546566412203860(1) + 21.67097607544812030863848(4)i)\epsilon^{-1}$ $+ (-26.1072674395728288517596(3) + 137.5950166997233416823782(1)i)\epsilon^0$ $+ (-292.542564822901844479302(1) + 381.8929824167400021916357(5)i)\epsilon^1$
$I_{2,0,3,1,0,1,1}^c$	$(-17.85511276489526625332980(3) + 6.902207801341480271035070(5)i)\epsilon^{-1}$ $+ (-119.55045675765061543963848(9) - 22.76677703120654305896378(8)i)\epsilon^0$
$I_{1,1,1,1,1,1,1}^c$	$(6.1217805875813911339(6) - 8.426882406085824005(4)i)\epsilon^0$
$I_{1,1,1,1,1,2,1}^c$	$(139.9185004432642812(8) - 491.066576860794480(7)i)\epsilon^0$
$I_{1,1,1,1,2,1,1}^c$	$(94.9310103519581456(7) - 144.244157364640101(6)i)\epsilon^0$
$I_{1,4,1,1,0,0,1,0,0}^{a1}$	$(-12.49787116979138596(3) + 6.343548262346152200(9)i)\epsilon^0$ $+ (-87.2238992095944015(1) + 0.0875224942175103(1)i)\epsilon^1$
$I_{0,3,2,1,0,1,1,0,0}^{a1}$	$(-3.506186807636372734(4) - 6.28560232193634948(1)i)\epsilon^0$ $+ (12.71477727119858309(7) - 39.14237743783716525(4)i)\epsilon^1$
$I_{1,3,1,1,0,1,1,0,0}^{a1}$	$(-3.07676785989821335(2) - 16.39396088539505331(3)i)\epsilon^0$ $+ (58.5973768040630418(2) - 99.65221845421363373(6)i)\epsilon^1$
$I_{0,3,3,1,0,1,0,0,0}^{a2}$	$(-2.481323226829965208(1) - 1.584621688009057491(6)i)\epsilon^0$ $+ (-0.68717007040876102(2) - 12.62036549911258700(2)i)\epsilon^1$
$I_{0,3,2,1,0,1,0,1,0}^{a2}$	$(-1.514056019940696717(5) - 4.884597546409176542(9)i)\epsilon^0$ $+ (15.76683698388269690(5) - 23.02597689816930463(1)i)\epsilon^1$

## C.2. Numerical results for the projection coefficients at the benchmark phase space point

**Table C.3.:** Numerical results for the one-loop vector current projection coefficients proportional to  $N_c$  and  $N_c^{-1}$  at the benchmark phase space point.

	$\epsilon^{-2}, N_c$		$\epsilon^{-2}, N_c^{-1}$	
$C_1$	0(0)	+0(0)i	0(0)	+0(0)i
$C_2$	0(0)	+0(0)i	0(0)	+0(0)i
$C_3$	0(0)	+0(0)i	0(0)	+0(0)i
$C_4$	0(0)	+0(0)i	0(0)	+0(0)i
$C_5$	10.000000000000(3)	+0(3 · 10 <sup>-12</sup> )i	0(0)	+0(0)i
$C_6$	0(0)	+0(0)i	0(0)	+0(0)i
$C_7$	0(0)	+0(0)i	0(0)	+0(0)i
$C_8$	0(0)	+0(0)i	0(0)	+0(0)i
$C_9$	0(0)	+0(0)i	0(0)	+0(0)i
$C_{10}$	-25.000000000000(2)	+0(2 · 10 <sup>-13</sup> )i	0(0)	+0(0)i
$C_{11}$	-200.000000000000(4)	+0(4 · 10 <sup>-12</sup> )i	0(0)	+0(0)i
$C_{12}$	0(0)	+0(0)i	0(0)	+0(0)i
$C_{13}$	0(0)	+0(0)i	0(0)	+0(0)i
$C_{14}$	0(0)	+0(0)i	0(0)	+0(0)i
$C_{15}$	0(0)	+0(0)i	0(0)	+0(0)i
$C_{16}$	0(0)	+0(0)i	0(0)	+0(0)i
$C_{17}$	0(0)	+0(0)i	0(0)	+0(0)i
$C_{18}$	0(0)	+0(0)i	0(0)	+0(0)i



## C.2. Numerical results for the projection coefficients at the benchmark phase space point

$\epsilon^{-1}, N_c$			$\epsilon^{-1}, N_c^{-1}$		
$C_1$	0(0)	+0(0)i	0(0)	+0(0)i	
$C_2$	0(0)	+0(0)i	0(0)	+0(0)i	
$C_3$	0(0)	+0(0)i	0(0)	+0(0)i	
$C_4$	0(0)	+0(0)i	0(0)	+0(0)i	
$C_5$	31.23264873830(3)	+62.83185307180(3)i	6.1701116070(5)	-35.0933451310(5)i	
$C_6$	0(0)	+0(0)i	0(0)	+0(0)i	
$C_7$	0(0)	+0(0)i	0(0)	+0(0)i	
$C_8$	0(0)	+0(0)i	0(0)	+0(0)i	
$C_9$	0(0)	+0(0)i	0(0)	+0(0)i	
$C_{10}$	-78.081621845840(2)	-157.079632679490(2)i	-15.4252790170(2)	+87.7333628280(2)i	
$C_{11}$	-624.65297476670(4)	-1256.63706143590(4)i	-123.402232140(6)	+701.866902630(6)i	
$C_{12}$	0(0)	+0(0)i	0(0)	+0(0)i	
$C_{13}$	0(0)	+0(0)i	0(0)	+0(0)i	
$C_{14}$	0(0)	+0(0)i	0(0)	+0(0)i	
$C_{15}$	0(0)	+0(0)i	0(0)	+0(0)i	
$C_{16}$	0(0)	+0(0)i	0(0)	+0(0)i	
$C_{17}$	0(0)	+0(0)i	0(0)	+0(0)i	
$C_{18}$	0(0)	+0(0)i	0(0)	+0(0)i	

$\epsilon^0, N_c$			$\epsilon^0, N_c^{-1}$		
$C_1$	-34.39009167557150(2)	+22.05263566861510(2)i	-7.72287497544663(2)	+13.916378512665710(2)i	
$C_2$	26.93605841404294(5)	-14.998255988455620(4)i	-5.00723078091639(9)	+11.316017972108770(2)i	
$C_3$	-49.77462167280340(1)	+60.12479593828650(1)i	12.48111052315832(8)	+3.175846477480160(2)i	
$C_4$	63.7349240320747(2)	-60.46808510021190(1)i	6.1334723221193(4)	-29.741702723979200(4)i	
$C_5$	-75.65042368990(8)	+76.68006207570(8)i	79.398829500(2)	+12.021798670(2)i	
$C_6$	58.00755743540200(2)	+1.62693832046390(2)i	-39.0898734635210(1)	+252.1060269366540(1)i	
$C_7$	-57.554116198470080(8)	-3.981709279954830(8)i	38.12717716576490(4)	-252.05309644279820(4)i	
$C_8$	42.2398048473806(1)	-141.2918070204922(1)i	-21.3681889420170(1)	-113.8113835803010(1)i	
$C_9$	-8.7626029555790(2)	+398.9268710890900(2)i	76.40830867754440(7)	+153.15110739677390(7)i	
$C_{10}$	176.127485941620(7)	-177.098809218050(7)i	-179.6222643190(7)	+3.0129824330(7)i	
$C_{11}$	1442.7229303610(2)	-469.5875600340(2)i	-1135.32991540(3)	+303.27097400(3)i	
$C_{12}$	501.3606976274090(1)	-614.3698374915550(1)i	-491.1972666137180(2)	+1028.6518747140280(2)i	
$C_{13}$	-100.33419299300080(2)	+73.05524687524420(2)i	30.16033106714231(7)	-30.595222972559690(6)i	
$C_{14}$	98.3185347922719(7)	-76.86263119394490(2)i	5.477450179640(2)	-59.474662156841860(8)i	
$C_{15}$	-39.1653458318958(2)	+25.449987182693740(7)i	-11.2733385376886(5)	+25.341299411336270(4)i	
$C_{16}$	-413.5776745240080(9)	+641.9934308082690(1)i	548.138340689228(2)	-1062.4364736504140(2)i	
$C_{17}$	340.0323144500370(1)	-545.6874854867920(1)i	-131.499540936581(1)	-139.48244501271950(6)i	
$C_{18}$	25.64257193368130(7)	+89.53634356553780(7)i	-17.90005443686500(8)	+188.49298725048670(8)i	

$\epsilon^1, N_c$			$\epsilon^1, N_c^{-1}$		
$C_1$	-190.4034528019576(8)	-22.36984760705100(9)i	-56.174308435070(2)	+17.20079623568640(1)i	
$C_2$	142.755549240827(2)	+31.00579646220870(3)i	-46.439768701047(9)	+32.93235535552550(1)i	
$C_3$	-412.420001768464(3)	+81.24363933778570(9)i	15.939977003037(7)	+46.85913113075340(1)i	
$C_4$	454.039848061719(8)	-57.2781926090270(1)i	99.10116333918(4)	-84.40498343074260(3)i	
$C_5$	-137.3084459870(2)	+103.3203681110(2)i	66.813021100(5)	+31.820360170(5)i	
$C_6$	146.0562353651589(1)	+86.9403356700153(1)i	-806.5134163412580(5)	+695.4952218500970(5)i	
$C_7$	-133.127304230927(1)	-83.13979562970920(5)i	811.347176430962(2)	-691.0546643816470(3)i	
$C_8$	537.8959829108340(3)	-419.0050350340670(3)i	235.9779102430940(4)	-388.9088372755860(4)i	
$C_9$	-976.739436848720(1)	+1554.727149377000(1)i	-96.3626443146440(2)	+535.0533801492560(2)i	
$C_{10}$	237.38476931900(2)	-248.08263313920(2)i	-216.211892900(2)	+84.428379190(2)i	
$C_{11}$	-290.1381775100(5)	+1748.9811289560(5)i	-1460.56301290(8)	+2009.62431380(8)i	
$C_{12}$	2828.39677200290(2)	-771.0257267265890(7)i	-4067.77580140916(4)	+3167.222545241850(1)i	
$C_{13}$	-598.944118766486(3)	-15.8087332272800(1)i	129.420418854612(3)	-23.27412942786310(4)i	
$C_{14}$	677.78168541636(3)	-60.9889055808180(1)i	189.0587202428(2)	-185.22501292666650(6)i	
$C_{15}$	-241.831254926637(8)	-4.59822642058570(5)i	-99.06918537297(4)	+38.74583828161900(3)i	
$C_{16}$	-2546.10758830329(4)	+1154.8047998973530(7)i	4382.6253670219(2)	-3126.696157320700(1)i	
$C_{17}$	2765.72088973811(2)	-1062.4841792059770(6)i	196.5150466942(1)	-534.1043697945170(2)i	
$C_{18}$	-35.953904665349(4)	+422.1665614026680(2)i	-389.10987655697(3)	+514.0264871846320(2)i	

$\epsilon^2, N_c$			$\epsilon^2, N_c^{-1}$		
$C_1$	-358.43534861548(4)	-310.0326710368110(3)i	-105.17024119606(9)	-46.05851980061040(5)i	
$C_2$	252.8190391507(1)	+259.4543497646230(1)i	-133.7405219767(5)	-0.29858264633090(5)i	
$C_3$	-1109.8754807117(1)	-462.1675338813370(4)i	-77.0065072006(4)	+112.36714461368500(4)i	
$C_4$	1159.1063636496(4)	+539.5615499051150(4)i	309.442292942(2)	-38.3624481085580(1)i	
$C_5$	-318.7270448430(5)	+37.9028864300(5)i	163.67289820(1)	+78.83502990(1)i	
$C_6$	81.89916026948(2)	+361.6386120453370(3)i	-2254.81627679751(2)	+391.886936912700(2)i	
$C_7$	-54.08491188093(6)	-308.3186660862880(1)i	2273.83695236244(8)	-367.4440819095470(9)i	
$C_8$	1736.5114787343240(7)	-324.0487112297130(7)i	950.00827976206(1)	-474.130402756870(1)i	
$C_9$	-4230.692597434420(4)	+2790.409096719320(4)i	-847.23399557468(4)	+757.5055359350350(6)i	
$C_{10}$	535.58443079220(5)	-225.53394704360(5)i	-754.572447130(5)	+140.788900470(5)i	
$C_{11}$	-5526.5859394580(9)	+4873.0877171810(9)i	-7418.1016170(2)	+3870.1640450(2)i	
$C_{12}$	4663.2395215386(8)	+2690.795417891040(2)i	-11987.284537071(2)	+3241.172302849960(5)i	
$C_{13}$	-1224.2864180062(1)	-985.2926950163460(5)i	110.9039548813(2)	+142.2571318792850(1)i	
$C_{14}$	1804.878945419(2)	+839.2584162673380(6)i	633.72015714(1)	-101.6752847336640(2)i	
$C_{15}$	-557.1857286915(4)	-357.9967243464960(2)i	-201.179993431(2)	-72.88699227438060(9)i	
$C_{16}$	-4561.140300055(2)	-1407.072497534320(2)i	12612.03470735(1)	-2726.031397247780(5)i	
$C_{17}$	7129.3662446428(8)	+1187.704150412030(2)i	1213.556955808(6)	-598.6416774241240(8)i	
$C_{18}$	-597.8449757122(2)	+1053.3013463618440(7)i	-1288.183618901(1)	+399.5913636941210(5)i	

## C. Numerical results

**Table C.4.:** Non-zero one-loop vector current coefficients of order  $N_c^0$  up to order  $\epsilon^2$ . All other coefficients vanish. These contributions originate purely from the renormalization.

	$\epsilon^{-1}$	$\epsilon^1$	$\epsilon^2$
$C_5$	-16.66666666666666667(1)	2.7415567780803773941(1)	-1.3356187812884380949(1)
$C_{10}$	41.66666666666666667(1)	-6.8538919452009434853(1)	3.3390469532210952372(1)
$C_{11}$	333.3333333333333333(1)	-54.831135561607547882(1)	26.712375625768761898(1)

**Table C.5.:** Numerical results for the leading-colour one-loop axial-vector current projection coefficients at the benchmark phase space point.

	$\epsilon^{-2}$		$\epsilon^{-1}$	
$\tilde{C}_1$	0(0)	+0(0)i	0(0)	+0(0)i
$\tilde{C}_2$	0(0)	+0(0)i	0(0)	+0(0)i
$\tilde{C}_3$	0(0)	+0(0)i	0(0)	+0(0)i
$\tilde{C}_4$	0(0)	+0(0)i	0(0)	+0(0)i
$\tilde{C}_5$	-10.0000000000000000(1)	+0(1 · 10 <sup>-17</sup> )i	-31.23264873833704788(2)	-62.8318530717958648(2)i
$\tilde{C}_6$	0(0)	+0(0)i	0(0)	+0(0)i
$\tilde{C}_7$	0(0)	+0(0)i	0(0)	+0(0)i
$\tilde{C}_8$	0(0)	+0(0)i	0(2 · 10 <sup>-16</sup> )	+0(2 · 10 <sup>-16</sup> )i
$\tilde{C}_9$	0(0)	+0(0)i	0(2 · 10 <sup>-16</sup> )	+0(2 · 10 <sup>-16</sup> )i
$\tilde{C}_{10}$	25.0000000000000000(4)	+0(4 · 10 <sup>-17</sup> )i	78.0816218458426197(1)	+157.0796326794896619(3)i
$\tilde{C}_{11}$	200.0000000000000000(3)	+0(3 · 10 <sup>-16</sup> )i	624.6529747667409576(9)	+1256.637061435917295(3)i
$\tilde{C}_{12}$	0(0)	+0(0)i	0(0)	+0(0)i
$\tilde{C}_{13}$	0(0)	+0(0)i	0(0)	+0(0)i
$\tilde{C}_{14}$	0(0)	+0(0)i	0(0)	+0(0)i
$\tilde{C}_{15}$	0(0)	+0(0)i	0(0)	+0(0)i
$\tilde{C}_{16}$	0(0)	+0(0)i	0(0)	+0(0)i
$\tilde{C}_{17}$	0(0)	+0(0)i	0(2 · 10 <sup>-16</sup> )	+0(2 · 10 <sup>-16</sup> )i
$\tilde{C}_{18}$	0(0)	+0(0)i	0(2 · 10 <sup>-16</sup> )	+0(2 · 10 <sup>-16</sup> )i
	$\epsilon^0$		$\epsilon^1$	
$\tilde{C}_1$	34.390091675571540(6)	-22.05263566861509(1)i	190.40345280195762(9)	+22.3698476070510(7)i
$\tilde{C}_2$	-26.93605841404294(2)	+14.99825598845562(4)i	-142.7555492408268(3)	-31.005796462209(2)i
$\tilde{C}_3$	49.77462167280342(2)	-60.12479593828653(5)i	412.4200017684639(3)	-81.243639337786(3)i
$\tilde{C}_4$	-63.73492403207472(7)	+60.4680851002119(2)i	-454.039848061719(1)	+57.278192609027(8)i
$\tilde{C}_5$	85.2854575308906949(1)	-86.7151309400435840(3)i	164.440550249582683(1)	-87.56360951337624(2)i
$\tilde{C}_6$	-106.665169274345021(2)	+222.668009305153666(3)i	-555.89283114269089(2)	-71.8114589764244(2)i
$\tilde{C}_7$	-57.480564157202262(6)	+239.40922715615711(1)i	-438.97791344978311(9)	+117.5664271159078(7)i
$\tilde{C}_8$	22.429491712891181(3)	+25.272475805395816(5)i	-66.04782497526846(3)	+217.4305319135133(3)i
$\tilde{C}_9$	-14.057711593048798(9)	-342.20502754337045(2)i	769.9241648581443(2)	-1364.690745576463(1)i
$\tilde{C}_{10}$	-204.368767617941746(1)	+211.799391656800991(3)i	-340.61202526270618(1)	+218.48874675235456(5)i
$\tilde{C}_{11}$	-1666.58820801522448(2)	+803.57857871600952(4)i	-669.7017422844488(2)	-1852.627916359368(1)i
$\tilde{C}_{12}$	-894.06632997699788(9)	+1885.5463616081282(2)i	-4893.200509133524(1)	-455.43388679561(1)i
$\tilde{C}_{13}$	-30.28384606760816(1)	+321.49147844493458(3)i	-518.5755282228875(2)	+699.292584055388(2)i
$\tilde{C}_{14}$	-98.3185347922719(3)	+76.8626311939449(6)i	-677.781685416359(4)	+60.98890558082(3)i
$\tilde{C}_{15}$	39.16534583189576(7)	-25.4499871826937(2)i	241.831254926637(1)	+4.598226420586(8)i
$\tilde{C}_{16}$	-836.1431845019487(2)	+1919.8914608337251(5)i	-4705.203635368519(3)	-133.04073892441(2)i
$\tilde{C}_{17}$	211.84243726907142(8)	-444.4250214319400(2)i	1209.872769007002(1)	-209.103233459857(9)i
$\tilde{C}_{18}$	-151.28423041348620(2)	+280.05847249315241(4)i	-995.9677131986800(3)	+317.651160869855(2)i
	$\epsilon^2$			
$\tilde{C}_1$	358.435348615485(5)	+310.03267103681(4)i		
$\tilde{C}_2$	-252.81903915070(2)	-259.4543497646(1)i		
$\tilde{C}_3$	1109.87548071169(2)	+462.1675338813(1)i		
$\tilde{C}_4$	-1159.10636364958(6)	-539.5615499051(4)i		
$\tilde{C}_5$	313.9931787576301(1)	-12.444866459178(1)i		
$\tilde{C}_6$	-277.644093457682(1)	-441.834809618452(9)i		
$\tilde{C}_7$	-316.694563703151(5)	+59.79040619545(4)i		
$\tilde{C}_8$	-636.180869340823(2)	+454.47809938642(1)i		
$\tilde{C}_9$	3552.534471060474(8)	-2302.45778602109(6)i		
$\tilde{C}_{10}$	-580.0155059020637(3)	+130.839505740823(2)i		
$\tilde{C}_{11}$	4846.883384466256(9)	-5595.91211694132(7)i		
$\tilde{C}_{12}$	-3082.45560988524(7)	-3974.3098758183(6)i		
$\tilde{C}_{13}$	-1474.71226083154(1)	+1983.66852440014(8)i		
$\tilde{C}_{14}$	-1804.8789454185(2)	-839.258416267(2)i		
$\tilde{C}_{15}$	557.18572869152(6)	+357.9967243465(4)i		
$\tilde{C}_{16}$	-3023.5448928791(2)	-2897.999716494(1)i		
$\tilde{C}_{17}$	1557.94171262599(6)	-345.6491005308(5)i		
$\tilde{C}_{18}$	-1983.88046656304(1)	-308.4708418434(1)i		

## C.2. Numerical results for the projection coefficients at the benchmark phase space point

**Table C.6.:** Numerical results for projection coefficients of the leading-colour two-loop vector current at the benchmark phase space point.

$\epsilon^{-4}$			$\epsilon^{-3}$		
$C_1$	$0(2 \cdot 10^{-20})$	$+0(2 \cdot 10^{-20})i$	$0(2 \cdot 10^{-18})$	$+0(2 \cdot 10^{-18})i$	
$C_2$	$0(7 \cdot 10^{-20})$	$+0(7 \cdot 10^{-20})i$	$0(7 \cdot 10^{-18})$	$+0(6 \cdot 10^{-18})i$	
$C_3$	$0(9 \cdot 10^{-20})$	$+0(9 \cdot 10^{-20})i$	$0(7 \cdot 10^{-18})$	$+0(6 \cdot 10^{-18})i$	
$C_4$	$0(3 \cdot 10^{-19})$	$+0(3 \cdot 10^{-19})i$	$0(2 \cdot 10^{-17})$	$+0(2 \cdot 10^{-17})i$	
$C_5$	$-5.000000000000000000(1)$	$+0(1 \cdot 10^{-21})i$	$-58.73264873833704788(8)$	$-62.83185307179586477(8)i$	
$C_6$	$0(1 \cdot 10^{-20})$	$+0(1 \cdot 10^{-20})i$	$0(1 \cdot 10^{-18})$	$+0(8 \cdot 10^{-19})i$	
$C_7$	$0(4 \cdot 10^{-20})$	$+0(4 \cdot 10^{-20})i$	$0(4 \cdot 10^{-18})$	$+0(3 \cdot 10^{-18})i$	
$C_8$	$0(5 \cdot 10^{-22})$	$+0(5 \cdot 10^{-22})i$	$0(2 \cdot 10^{-16})$	$+0(2 \cdot 10^{-16})i$	
$C_9$	$0(7 \cdot 10^{-21})$	$+0(7 \cdot 10^{-21})i$	$0(6 \cdot 10^{-16})$	$+0(6 \cdot 10^{-16})i$	
$C_{10}$	$12.500000000000000000(2)$	$+0(2 \cdot 10^{-22})i$	$146.8316218458426197(3)$	$+157.0796326794896619(3)i$	
$C_{11}$	$100.000000000000000000(5)$	$+0(5 \cdot 10^{-21})i$	$1174.652974766740958(4)$	$+1256.637061435917295(4)i$	
$C_{12}$	$0(5 \cdot 10^{-19})$	$+0(5 \cdot 10^{-19})i$	$0(4 \cdot 10^{-17})$	$+0(4 \cdot 10^{-17})i$	
$C_{13}$	$0(9 \cdot 10^{-20})$	$+0(9 \cdot 10^{-20})i$	$0(9 \cdot 10^{-18})$	$+0(7 \cdot 10^{-18})i$	
$C_{14}$	$0(1 \cdot 10^{-18})$	$+0(1 \cdot 10^{-18})i$	$0(9 \cdot 10^{-17})$	$+0(8 \cdot 10^{-17})i$	
$C_{15}$	$0(3 \cdot 10^{-19})$	$+0(3 \cdot 10^{-19})i$	$0(3 \cdot 10^{-17})$	$+0(2 \cdot 10^{-17})i$	
$C_{16}$	$0(1 \cdot 10^{-18})$	$+0(1 \cdot 10^{-18})i$	$0(1 \cdot 10^{-16})$	$+0(1 \cdot 10^{-16})i$	
$C_{17}$	$0(5 \cdot 10^{-19})$	$+0(5 \cdot 10^{-19})i$	$0(7 \cdot 10^{-16})$	$+0(7 \cdot 10^{-16})i$	
$C_{18}$	$0(1 \cdot 10^{-19})$	$+0(1 \cdot 10^{-19})i$	$0(6 \cdot 10^{-17})$	$+0(6 \cdot 10^{-17})i$	
$\epsilon^{-2}$			$\epsilon^{-1}$		
$C_1$	$34.390091675571540341(6)$	$-22.052635668615086668(2)i$	$436.3736145578179(1)$	$+169.57294397632336(5)i$	
$C_2$	$-26.93605841404293597(3)$	$+14.99825598845561843(2)i$	$-321.1208159849225(4)$	$-153.4065168251449(2)i$	
$C_3$	$49.77462167280342009(2)$	$-60.124795938286530913(3)i$	$945.6545636841054(4)$	$+43.7138690267257(2)i$	
$C_4$	$-63.7349240320747159(1)$	$+60.46808510021193009(5)i$	$-1033.033081382494(2)$	$-154.3222994420328(7)i$	
$C_5$	$177.3951791076847100(8)$	$-388.11231236436841436(8)i$	$927.18118779032684(1)$	$+263.032982260747849(6)i$	
$C_6$	$-58.007557435402019641(6)$	$-1.626938320463862713(4)i$	$-317.006846969215152(8)$	$-456.49392756170799(2)i$	
$C_7$	$57.55411619847007959(2)$	$+3.98170927995483322(2)i$	$287.86623645287897(4)$	$+457.19890562754362(7)i$	
$C_8$	$-42.2398048473806029(3)$	$+141.291807020492159(2)i$	$-1557.58468756425843(2)$	$+594.896251666465752(5)i$	
$C_9$	$8.76260295557899(1)$	$-398.926871089090174(5)i$	$3510.63882192932496(7)$	$-2745.62437493479626(4)i$	
$C_{10}$	$-430.4893744860099707(3)$	$+955.679434939660420(3)i$	$-2079.72567400911941(1)$	$-631.732169106807291(4)i$	
$C_{11}$	$-3477.61803871603007(2)$	$+6698.23256580698790(2)i$	$-8602.4011594749452(2)$	$-11957.62759921159564(8)i$	
$C_{12}$	$-501.3606976274092501(2)$	$+614.36983749155453467(5)i$	$-8254.478564124592(3)$	$-460.276709222962(1)i$	
$C_{13}$	$100.334192993000788(2)$	$-73.055246875244173(2)i$	$1371.3340331648884(1)$	$+418.0561740339241(2)i$	
$C_{14}$	$-98.3185347922718829(4)$	$+76.8626311939448872(2)i$	$-1467.798666568817(8)$	$-316.702311530926(3)i$	
$C_{15}$	$39.1653458318957589(1)$	$-25.44998718269373940(6)i$	$524.061989369156(2)$	$+171.1943008949349(8)i$	
$C_{16}$	$413.5776745240075071(6)$	$-641.9934308082692114(3)i$	$7871.58390350628(1)$	$-561.335163626064(4)i$	
$C_{17}$	$-340.03231445003650(1)$	$+545.687485486792294(1)i$	$-7256.387464550672(4)$	$+630.324692598777(2)i$	
$C_{18}$	$-25.642571933681309(4)$	$-89.536343565537783(3)i$	$518.438798819698(1)$	$-862.9293094044211(4)i$	
$\epsilon^0$					
$C_1$	$-40.107882844428(5)$	$+1831.4848563593947(6)i$			
$C_2$	$420833.33195088415(1)$	$+3667.4622531409147(7)i$			
$C_3$	$-419103.36993232946(3)$	$-1427.169322978936(5)i$			
$C_4$	$-1178.81920613765(8)$	$-4309.49348100966(1)i$			
$C_5$	$-13178.1690300339339(1)$	$-1126.09984800773147(1)i$			
$C_6$	$533505.997618679724(9)$	$+12211.496291227070(3)i$			
$C_7$	$-2.07817354864 \cdot 10^6(3)$	$+8003.50564104692(1)i$			
$C_8$	$-270571.123453530908(4)$	$-11885.741799955149(1)i$			
$C_9$	$1.05334198405 \cdot 10^6(2)$	$+5867.809983392475(5)i$			
$C_{10}$	$12277.32613007092649(1)$	$-610.30656900787797(2)i$			
$C_{11}$	$-397479.12422426227(1)$	$-14388.710941236483(4)i$			
$C_{12}$	$-4268.5952410965(1)$	$-26570.11157108272(1)i$			
$C_{13}$	$4.63440956861 \cdot 10^6(8)$	$-55344.84107144175(2)i$			
$C_{14}$	$-1.4307710776 \cdot 10^6(4)$	$+12472.80882474580(5)i$			
$C_{15}$	$-1.42771480277 \cdot 10^6(6)$	$+21340.975898517279(3)i$			
$C_{16}$	$7424.2906255255(4)$	$+23179.59792244033(5)i$			
$C_{17}$	$-853589.6323304906(2)$	$-35665.49158421301(3)i$			
$C_{18}$	$226810.59446225434(5)$	$+18575.403270183907(7)i$			

**Table C.7.:** Numerical results for projection coefficients of the leading-colour two-loop axial-vector current at the benchmark phase space point.

$\epsilon^{-4}$			$\epsilon^{-3}$		
$\tilde{C}_1$	$0(7 \cdot 10^{-21})$	$+0(7 \cdot 10^{-21})i$	$0(4 \cdot 10^{-19})$	$+0(3 \cdot 10^{-19})i$	
$\tilde{C}_2$	$0(2 \cdot 10^{-20})$	$+0(2 \cdot 10^{-20})i$	$0(1 \cdot 10^{-18})$	$+0(1 \cdot 10^{-18})i$	
$\tilde{C}_3$	$0(3 \cdot 10^{-20})$	$+0(3 \cdot 10^{-20})i$	$0(2 \cdot 10^{-18})$	$+0(1 \cdot 10^{-18})i$	
$\tilde{C}_4$	$0(9 \cdot 10^{-20})$	$+0(9 \cdot 10^{-20})i$	$0(5 \cdot 10^{-18})$	$+0(4 \cdot 10^{-18})i$	
$\tilde{C}_5$	$1.25000000000000000000(4)$	$+0(4 \cdot 10^{-22})i$	$14.68316218458426197(2)$	$+15.70796326794896619(2)i$	
$\tilde{C}_6$	$0(1 \cdot 10^{-21})$	$+0(1 \cdot 10^{-21})i$	$0(1 \cdot 10^{-19})$	$+0(1 \cdot 10^{-19})i$	
$\tilde{C}_7$	$0(5 \cdot 10^{-21})$	$+0(5 \cdot 10^{-21})i$	$0(5 \cdot 10^{-19})$	$+0(4 \cdot 10^{-19})i$	
$\tilde{C}_8$	$0(1 \cdot 10^{-21})$	$+0(1 \cdot 10^{-21})i$	$0(5 \cdot 10^{-17})$	$+0(5 \cdot 10^{-17})i$	
$\tilde{C}_9$	$0(5 \cdot 10^{-21})$	$+0(5 \cdot 10^{-21})i$	$0(5 \cdot 10^{-17})$	$+0(5 \cdot 10^{-17})i$	
$\tilde{C}_{10}$	$-3.12500000000000000000(5)$	$+0(5 \cdot 10^{-23})i$	$-36.70790546146065492(7)$	$-39.26990816987241548(7)i$	
$\tilde{C}_{11}$	$-25.00000000000000000000(4)$	$+0(4 \cdot 10^{-21})i$	$-293.6632436916852394(9)$	$-314.1592653589793238(9)i$	
$\tilde{C}_{12}$	$0(1 \cdot 10^{-19})$	$+0(1 \cdot 10^{-19})i$	$0(7 \cdot 10^{-18})$	$+0(6 \cdot 10^{-18})i$	
$\tilde{C}_{13}$	$0(1 \cdot 10^{-20})$	$+0(1 \cdot 10^{-20})i$	$0(1 \cdot 10^{-16})$	$+0(1 \cdot 10^{-16})i$	
$\tilde{C}_{14}$	$0(4 \cdot 10^{-19})$	$+0(4 \cdot 10^{-19})i$	$0(2 \cdot 10^{-17})$	$+0(2 \cdot 10^{-17})i$	
$\tilde{C}_{15}$	$0(9 \cdot 10^{-20})$	$+0(9 \cdot 10^{-20})i$	$0(5 \cdot 10^{-18})$	$+0(4 \cdot 10^{-18})i$	
$\tilde{C}_{16}$	$0(3 \cdot 10^{-19})$	$+0(3 \cdot 10^{-19})i$	$0(1 \cdot 10^{-17})$	$+0(1 \cdot 10^{-17})i$	
$\tilde{C}_{17}$	$0(1 \cdot 10^{-19})$	$+0(1 \cdot 10^{-19})i$	$0(2 \cdot 10^{-16})$	$+0(2 \cdot 10^{-16})i$	
$\tilde{C}_{18}$	$0(3 \cdot 10^{-20})$	$+0(3 \cdot 10^{-20})i$	$0(2 \cdot 10^{-17})$	$+0(2 \cdot 10^{-17})i$	
$\epsilon^{-2}$			$\epsilon^{-1}$		
$\tilde{C}_1$	$-8.597522918892885086(1)$	$+5.5131589171537716670(3)i$	$-109.09340363945448(3)$	$-42.39323599408084(1)i$	
$\tilde{C}_2$	$6.734014603510733994(5)$	$-3.7495639971139046082(8)i$	$80.2802039962306(1)$	$+38.35162920628621(5)i$	
$\tilde{C}_3$	$-12.443655418200855023(3)$	$+15.031198984571632729(2)i$	$-236.4136409210264(1)$	$-10.92846725668142(5)i$	
$\tilde{C}_4$	$15.93373100801867898(2)$	$-15.11702127505298252373(6)i$	$258.2582703456234(4)$	$+38.5805748605082(2)i$	
$\tilde{C}_5$	$-46.7575532371614797(2)$	$+99.53684530717243107(2)i$	$-261.864563012740778(3)$	$-76.996566458029283(1)i$	
$\tilde{C}_6$	$26.6662923185862551667(9)$	$-55.6670023262884164920(6)i$	$572.025193010961953(5)$	$+11.639327839887375(2)i$	
$\tilde{C}_7$	$14.370141039300565435(4)$	$-59.852306789039277594(2)i$	$530.68936972022600(1)$	$-126.03595515087020(1)i$	
$\tilde{C}_8$	$-5.6073729282227953(3)$	$-6.3181189513489540(9)i$	$38.696557506741459(4)$	$-109.322955162315584(3)i$	
$\tilde{C}_9$	$3.514427898262200(2)$	$+85.551256885842613(1)i$	$-719.03895228414526(2)$	$+630.45372367149488(2)i$	
$\tilde{C}_{10}$	$114.68266404058245153(7)$	$-247.5950043446040854(8)i$	$622.297030683571794(3)$	$+182.598037836416053(1)i$	
$\tilde{C}_{11}$	$925.370829092582240(4)$	$-1758.055896122233080(4)i$	$3089.98977468752370(5)$	$+3106.17974828381808(2)i$	
$\tilde{C}_{12}$	$223.51658249424946917(2)$	$-471.386590402032052896(2)i$	$4883.2109169225535(4)$	$+45.9893989388630(2)i$	
$\tilde{C}_{13}$	$7.570961516902039(2)$	$-80.3728696112336446(6)i$	$658.28763365977269(2)$	$-378.27915231560847(2)i$	
$\tilde{C}_{14}$	$24.57963369806797073(6)$	$-19.215657798486221799(1)i$	$366.949666642204(2)$	$+79.1755778827316(8)i$	
$\tilde{C}_{15}$	$-9.79133645797393973(2)$	$+6.362496795673434848(4)i$	$-131.0154973422891(5)$	$-42.7985752237337(2)i$	
$\tilde{C}_{16}$	$209.03579612548717773(4)$	$-479.972865208431265145(3)i$	$4844.933522777231(1)$	$-152.4115626774606(6)i$	
$\tilde{C}_{17}$	$-52.960609317267855(2)$	$+111.1062553579849978(3)i$	$-1165.9793942302377(6)$	$+66.5287506662209(3)i$	
$\tilde{C}_{18}$	$37.821057603371549(1)$	$-70.0146181232881031(8)i$	$807.0319288835549(2)$	$-60.45027422131332(7)i$	
$\epsilon^0$					
$\tilde{C}_1$	$34.463211163189(1)$	$-453.8889032245627(2)i$			
$\tilde{C}_2$	$-56816.077862557407(3)$	$-8678.0860819996628(2)i$			
$\tilde{C}_3$	$56320.743623925221(7)$	$+8095.412438429639(1)i$			
$\tilde{C}_4$	$165.81850617429(2)$	$+1061.001935527068(2)i$			
$\tilde{C}_5$	$4055.07742980377662(2)$	$+70.172019174376264(4)i$			
$\tilde{C}_6$	$-47340.058116129494(1)$	$-5472.5961255544885(4)i$			
$\tilde{C}_7$	$152570.065173594233(4)$	$+26280.029712196229(1)i$			
$\tilde{C}_8$	$24179.1233229337806(4)$	$+3791.1341631314068(2)i$			
$\tilde{C}_9$	$-79528.394464859820(1)$	$-14105.0630456657011(6)i$			
$\tilde{C}_{10}$	$-3869.743788317160433(4)$	$+573.632508153165017(6)i$			
$\tilde{C}_{11}$	$50219.325715053084(2)$	$+13796.6591534091791(8)i$			
$\tilde{C}_{12}$	$-3601.65082608213(2)$	$+14866.467407359821(2)i$			
$\tilde{C}_{13}$	$-380734.415950966356(9)$	$-60032.286394715905(3)i$			
$\tilde{C}_{14}$	$-307349.29968204729(8)$	$-48110.952257626809(8)i$			
$\tilde{C}_{15}$	$307487.59107137777(1)$	$+49066.3054630638677(5)i$			
$\tilde{C}_{16}$	$-3026.18334822615(6)$	$+14184.808723951771(8)i$			
$\tilde{C}_{17}$	$-113799.76060038346(3)$	$-21771.484041572459(3)i$			
$\tilde{C}_{18}$	$20048.121740313765(6)$	$+5917.9824381401940(6)i$			



### C. Numerical results

are below  $10^{-16}$  for all coefficients up to order  $\epsilon^0$ .

**Table C.9.:** Numerical values for some two-loop master integrals at the phase space point  $x = z = m = 289/2500$  and  $s = 1$ .

integral	value
$I_{4,0,4,0,0,0,0}$	$(2.078652208559656986(2) + 0(3 \cdot 10^{-24})i) \epsilon^{-4}$ $+ (6.570219107579427363(7) + 0(9 \cdot 10^{-24})i) \epsilon^{-3}$ $+ (13.80284414143316133(1) + 0(2 \cdot 10^{-23})i) \epsilon^{-2}$ $+ (20.08198957993065536(2) + 0(3 \cdot 10^{-23})i) \epsilon^{-1}$ $+ (24.39720734155296971(2) + 0(3 \cdot 10^{-23})i) \epsilon^0$
$I_{2,2,0,1,2,0,0}$	$(2.763497344885674096(3) - 2.187689190010290673(2)i) \epsilon^{-2}$ $+ (26.43230679419105819(3) + 2.822891659036842250(3)i) \epsilon^{-1}$ $+ (81.27312135968845723(8) + 68.70025467847656357(7)i) \epsilon^0$
$I_{1,2,0,2,2,0,0}$	$(1.873152895628368976(2) - 3.011856071206025785(3)i) \epsilon^{-2}$ $+ (21.98014017263183268(2) - 9.430219854150125426(9)i) \epsilon^{-1}$ $+ (87.17672560054666128(9) - 5.272259003634755705(5)i) \epsilon^0$
$I_{0,0,3,0,2,2,0}$	$(-2.162629757785467128(2) - 3.397050879746748744(3)i) \epsilon^{-4}$ $+ (1.027457904992505621(1) - 26.68028303095864959(3)i) \epsilon^{-3}$ $+ (56.32677742941012565(6) - 89.87039692128182526(9)i) \epsilon^{-2}$ $+ (281.9105698387693922(3) - 138.7370573487527360(1)i) \epsilon^{-1}$ $+ (737.0268780425461068(7) + 64.49168362831650646(6)i) \epsilon^0$
$I_{0,0,4,0,2,2,0}$	$(-6.235956625678970957(6) + 9.79541776166882568(1)i) \epsilon^{-4}$ $+ (-86.03569241217430212(9) + 27.95567656350895580(3)i) \epsilon^{-3}$ $+ (-359.9490542763335962(4) - 140.6576258092432336(1)i) \epsilon^{-2}$ $+ (-577.2258255834204541(6) - 1051.381337111411663(1)i) \epsilon^{-1}$ $+ (593.4688122222393216(6) - 2965.195844042988107(3)i) \epsilon^0$
$I_{2,0,3,0,1,1,0}$	$(-2.257454804119177900(2) - 1.886219863445238394(2)i) \epsilon^{-2}$ $+ (-3.915306717367840388(4) - 11.61854696487315544(1)i) \epsilon^{-1}$ $+ (0.5421001201460687601(5) - 33.51384153016527507(3)i) \epsilon^0$
$I_{2,0,2,0,2,1,0}$	$(0.006712851207298924330(7) - 3.665667088168171970(4)i) \epsilon^{-2}$ $+ (14.45906123773678721(1) - 16.54003268430997070(2)i) \epsilon^{-1}$ $+ (69.33371847434661383(7) - 20.97674984524004457(2)i) \epsilon^0$
$I_{2,2,1,0,1,1,0}$	$(-7.465927050084259117(7) - 11.22169571735170823(1)i) \epsilon^{-2}$ $+ (-23.03851477578925928(2) - 108.4534205700704758(1)i) \epsilon^{-1}$ $+ (45.35783723949059610(5) - 537.1045066725525650(5)i) \epsilon^0$
$I_{2,1,2,0,1,1,0}$	$(-3.724822437658699349(4) - 3.932457430485097542(4)i) \epsilon^{-2}$ $+ (-8.971110547133893803(9) - 29.11731338083836246(3)i) \epsilon^{-1}$ $+ (3.592292917822887715(6) - 105.3100197929409337(1)i) \epsilon^0$
$I_{2,1,1,0,2,1,0}$	$(0.3337392296703365378(3) - 6.200346365572559716(6)i) \epsilon^{-2}$ $+ (29.08330535780810964(3) - 36.64179951461972767(4)i) \epsilon^{-1}$ $+ (181.8528336546817851(2) - 77.80716592107028308(8)i) \epsilon^0$
$I_{1,2,1,0,2,1,0}$	$(10.45284260697314155(1) - 21.32903507509364087(2)i) \epsilon^{-2}$ $+ (216.2607082599166582(2) - 158.4615203262954675(2)i) \epsilon^{-1}$ $+ (1648.582453457273170(2) - 408.4744365869250567(4)i) \epsilon^0$

integral	value
$I_{3,2,0,0,2,0,0}$	$(-2.162629757785467128(2) - 3.397050879746748744(3)i) \epsilon^{-4}$ $+(1.027457904992505621(1) - 26.68028303095864959(3)i) \epsilon^{-3}$ $+(56.32677742941012565(6) - 89.87039692128182526(9)i) \epsilon^{-2}$ $+(281.9105698387693922(3) - 138.7370573487527360(1)i) \epsilon^{-1}$ $+(737.0268780425461068(7) + 64.49168362831650646(6)i) \epsilon^0$
$I_{2,0,0,1,2,0,2}$	$(1.873152895628368976(2) - 3.011856071206025785(3)i) \epsilon^{-2}$ $+(21.98014017263183268(2) - 9.430219854150125426(9)i) \epsilon^{-1}$ $+(87.17672560054666128(9) - 5.272259003634755705(5)i) \epsilon^0$
$I_{4,2,0,0,2,0,0}$	$(-6.235956625678970957(6) + 9.79541776166882568(1)i) \epsilon^{-4}$ $+(-86.03569241217430212(9) + 27.95567656350895580(3)i) \epsilon^{-3}$ $+(-359.9490542763335962(4) - 140.6576258092432336(1)i) \epsilon^{-2}$ $+(-577.2258255834204541(6) - 1051.381337111411663(1)i) \epsilon^{-1}$ $+(593.4688122222393216(6) - 2965.195844042988107(3)i) \epsilon^0$
$I_{1,0,0,2,2,0,2}$	$(2.763497344885674096(3) - 2.187689190010290673(2)i) \epsilon^{-2}$ $+(26.43230679419105819(3) + 2.822891659036842250(3)i) \epsilon^{-1}$ $+(81.27312135968845723(8) + 68.70025467847656357(7)i) \epsilon^0$
$I_{3,0,3,0,1,0,0}$	$(-1.409936741342077648(1) - 1.108080930636926778(1)i) \epsilon^{-2}$ $+(-0.9206327685325961820(9) - 5.556793652942957830(6)i) \epsilon^{-1}$ $+(2.515253083956218707(3) - 11.94384732458145779(1)i) \epsilon^0$
$I_{3,0,3,0,2,0,0}$	$(-2.868063126893464638(3) - 0.7970471023995619243(8)i) \epsilon^{-2}$ $+(-7.987917443824880694(8) - 16.42852181647373565(2)i) \epsilon^{-1}$ $+(22.10458535463570666(2) - 55.91465303475725122(6)i) \epsilon^0$
$I_{3,2,1,0,1,0,0}$	$(-4.524964575272350187(5) - 3.994540222364581135(4)i) \epsilon^{-2}$ $+(-16.58397358460685181(2) - 32.92183861734267093(3)i) \epsilon^{-1}$ $+(-29.02978617163272324(3) - 137.6991174728067040(1)i) \epsilon^0$
$I_{3,1,2,0,1,0,0}$	$(-2.257454804119177900(2) - 1.886219863445238394(2)i) \epsilon^{-2}$ $+(-3.915306717367840388(4) - 11.61854696487315544(1)i) \epsilon^{-1}$ $+(0.5421001201460687601(5) - 33.51384153016527507(3)i) \epsilon^0$





# Bibliography

- [1] G. Arnison et al. Experimental Observation of Isolated Large Transverse Energy Electrons with Associated Missing Energy at  $\sqrt{s} = 540$  GeV. *Phys. Lett. B*, 122:103–116, 1983.
- [2] M. Banner et al. Observation of Single Isolated Electrons of High Transverse Momentum in Events with Missing Transverse Energy at the CERN anti-p p Collider. *Phys. Lett. B*, 122:476–485, 1983.
- [3] G. Arnison et al. Experimental Observation of Lepton Pairs of Invariant Mass Around 95-GeV/c\*\*2 at the CERN SPS Collider. *Phys. Lett. B*, 126:398–410, 1983.
- [4] P. Bagnaia et al. Evidence for  $Z^0 \rightarrow e^+e^-$  at the CERN  $\bar{p}p$  Collider. *Phys. Lett. B*, 129:130–140, 1983.
- [5] F. Abe et al. Observation of top quark production in  $\bar{p}p$  collisions. *Phys. Rev. Lett.*, 74:2626–2631, 1995.
- [6] S. Abachi et al. Observation of the top quark. *Phys. Rev. Lett.*, 74:2632–2637, 1995.
- [7] Georges Aad et al. Observation of a new particle in the search for the Standard Model Higgs boson with the ATLAS detector at the LHC. *Phys. Lett. B*, 716:1–29, 2012.
- [8] Serguei Chatrchyan et al. Observation of a New Boson at a Mass of 125 GeV with the CMS Experiment at the LHC. *Phys. Lett. B*, 716:30–61, 2012.
- [9] S. L. Glashow. Partial Symmetries of Weak Interactions. *Nucl. Phys.*, 22:579–588, 1961.
- [10] Steven Weinberg. A Model of Leptons. *Phys. Rev. Lett.*, 19:1264–1266, 1967.
- [11] Abdus Salam. Weak and Electromagnetic Interactions. *Conf. Proc. C*, 680519:367–377, 1968.
- [12] F. Englert and R. Brout. Broken Symmetry and the Mass of Gauge Vector Mesons. *Phys. Rev. Lett.*, 13:321–323, 1964.
- [13] Peter W. Higgs. Broken symmetries, massless particles and gauge fields. *Phys. Lett.*, 12:132–133, 1964.
- [14] Peter W. Higgs. Broken Symmetries and the Masses of Gauge Bosons. *Phys. Rev. Lett.*, 13:508–509, 1964.
- [15] G. S. Guralnik, C. R. Hagen, and T. W. B. Kibble. Global Conservation Laws and Massless Particles. *Phys. Rev. Lett.*, 13:585–587, 1964.
- [16] G. W. Bennett et al. Final Report of the Muon E821 Anomalous Magnetic Moment Measurement at BNL. *Phys. Rev. D*, 73:072003, 2006.
- [17] B. Abi et al. Measurement of the Positive Muon Anomalous Magnetic Moment to 0.46 ppm. *Phys. Rev. Lett.*, 126(14):141801, 2021.
- [18] Roel Aaij et al. Angular analysis of the  $B^0 \rightarrow K^{*0}\mu^+\mu^-$  decay using 3 fb<sup>-1</sup> of integrated luminosity. *JHEP*, 02:104, 2016.
- [19] Albert M Sirunyan et al. Measurement of angular parameters from the decay  $B^0 \rightarrow K^{*0}\mu^+\mu^-$  in proton-proton collisions at  $\sqrt{s} = 8$  TeV. *Phys. Lett. B*, 781:517–541, 2018.
- [20] Morad Aaboud et al. Angular analysis of  $B_d^0 \rightarrow K^{*}\mu^+\mu^-$  decays in  $pp$  collisions at  $\sqrt{s} = 8$  TeV with the ATLAS detector. *JHEP*, 10:047, 2018.
- [21] S. Wehle et al. Lepton-Flavor-Dependent Angular Analysis of  $B \rightarrow K^{*}\ell^+\ell^-$ . *Phys. Rev. Lett.*, 118(11):111801, 2017.
- [22] Bernard Aubert et al. Measurements of branching fractions, rate asymmetries, and angular distributions in the rare decays  $B \rightarrow K\ell^+\ell^-$  and  $B \rightarrow K^{*}\ell^+\ell^-$ . *Phys. Rev. D*, 73:092001, 2006.
- [23] T. Aaltonen et al. Measurements of the Angular Distributions in the Decays  $B \rightarrow$

- $K^{(*)}\mu^+\mu^-$  at CDF. *Phys. Rev. Lett.*, 108:081807, 2012.
- [24] Roel Aaij et al. Angular moments of the decay  $\Lambda_b^0 \rightarrow \Lambda\mu^+\mu^-$  at low hadronic recoil. *JHEP*, 09:146, 2018.
  - [25] Roel Aaij et al. Angular analysis and differential branching fraction of the decay  $B_s^0 \rightarrow \phi\mu^+\mu^-$ . *JHEP*, 09:179, 2015.
  - [26] Roel Aaij et al. Measurements of the S-wave fraction in  $B^0 \rightarrow K^+\pi^-\mu^+\mu^-$  decays and the  $B^0 \rightarrow K^*(892)^0\mu^+\mu^-$  differential branching fraction. *JHEP*, 11:047, 2016. [Erratum: *JHEP* 04, 142 (2017)].
  - [27] Roel Aaij et al. Differential branching fraction and angular analysis of  $\Lambda_b^0 \rightarrow \Lambda\mu^+\mu^-$  decays. *JHEP*, 06:115, 2015. [Erratum: *JHEP* 09, 145 (2018)].
  - [28] R. Aaij et al. Differential branching fractions and isospin asymmetries of  $B \rightarrow K^{(*)}\mu^+\mu^-$  decays. *JHEP*, 06:133, 2014.
  - [29] S. Choudhury et al. Test of lepton flavor universality and search for lepton flavor violation in  $B \rightarrow K\ell\ell$  decays. *JHEP*, 03:105, 2021.
  - [30] J. P. Lees et al. Measurement of Branching Fractions and Rate Asymmetries in the Rare Decays  $B \rightarrow K^{(*)}l^+l^-$ . *Phys. Rev. D*, 86:032012, 2012.
  - [31] R. Aaij et al. Test of lepton universality with  $B^0 \rightarrow K^{*0}\ell^+\ell^-$  decays. *JHEP*, 08:055, 2017.
  - [32] A. Abdesselam et al. Test of Lepton-Flavor Universality in  $B \rightarrow K^*\ell^+\ell^-$  Decays at Belle. *Phys. Rev. Lett.*, 126(16):161801, 2021.
  - [33] T. Aaltonen et al. High-precision measurement of the W boson mass with the CDF II detector. *Science*, 376(6589):170–176, 2022.
  - [34] P. Lebrun, L. Linssen, A. Lucaci-Timoce, D. Schulte, F. Simon, S. Stapnes, N. Toge, H. Weerts, and J. Wells. The CLIC Programme: Towards a Staged e+e- Linear Collider Exploring the Terascale : CLIC Conceptual Design Report. 9 2012.
  - [35] Muhammd Ahmad et al. CEPC-SPPC Preliminary Conceptual Design Report. 1. Physics and Detector. 3 2015.
  - [36] CEPC-SPPC Preliminary Conceptual Design Report. 2. Accelerator. 1 2015.
  - [37] A. Abada et al. FCC-ee: The Lepton Collider: Future Circular Collider Conceptual Design Report Volume 2. *Eur. Phys. J. ST*, 228(2):261–623, 2019.
  - [38] The International Linear Collider Technical Design Report - Volume 1: Executive Summary. 6 2013.
  - [39] A. Abada et al. FCC-hh: The Hadron Collider: Future Circular Collider Conceptual Design Report Volume 3. *Eur. Phys. J. ST*, 228(4):755–1107, 2019.
  - [40] S. Amoroso et al. Les Houches 2019: Physics at TeV Colliders: Standard Model Working Group Report. In *11th Les Houches Workshop on Physics at TeV Colliders: PhysTeV Les Houches*, 3 2020.
  - [41] I. Zurbano Fernandez et al. High-Luminosity Large Hadron Collider (HL-LHC): Technical design report. 10/2020, 12 2020.
  - [42] A. Arbey et al. Physics at the e+ e- Linear Collider. *Eur. Phys. J. C*, 75(8):371, 2015.
  - [43] Frank Simon. Perspectives for Top Quark Physics at the (I)LC. In *7th International Workshop on Top Quark Physics*, 11 2014.
  - [44] M.S. Amjad, M. Boronat, T. Frisson, I. Garcia, R. Poschl, E. Ros, F. Richard, J. Rouene, P. Ruiz Femenia, and M. Vos. A precise determination of top quark electro-weak couplings at the ILC operating at  $\sqrt{s} = 500$  GeV. 7 2013.
  - [45] M.S. Amjad et al. A precise characterisation of the top quark electro-weak vertices at the ILC. *Eur. Phys. J. C*, 75(10):512, 2015.
  - [46] Thomas G. Rizzo. Anomalous chromoelectric and chromomagnetic moments of the top quark at the NLC. In *1996 DPF / DPB Summer Study on New Directions for High-Energy Physics (Snowmass 96)*, 5 1996.
  - [47] Thomas G. Rizzo. Using final state gluons as probes of anomalous top quark couplings at

- the NLC. *eConf*, C960625:STC123, 1996.
- [48] Reza Jafari, Parvin Eslami, Mojtaba Mohammadi Najafabadi, and Hamzeh Khanpour. Constraining the top quark effective field theory using the top quark pair production in association with a jet at future lepton colliders. *Phys. Lett. B*, 806:135469, 2020.
  - [49] Arnd Brandenburg. Production of top quark pairs in association with a hard gluon to order  $\alpha^2(s)$ . *Eur. Phys. J. C*, 11:127–135, 1999.
  - [50] L.W. Garland, T. Gehrmann, E.W.Nigel Glover, A. Koukoutsakis, and E. Remiddi. The Two loop QCD matrix element for  $e^+ e^- \rightarrow i$  3 jets. *Nucl. Phys. B*, 627:107–188, 2002.
  - [51] L.W. Garland, T. Gehrmann, E.W.Nigel Glover, A. Koukoutsakis, and E. Remiddi. Two loop QCD helicity amplitudes for  $e^+ e^- \rightarrow i$  three jets. *Nucl. Phys. B*, 642:227–262, 2002.
  - [52] Sven Moch, Peter Uwer, and Stefan Weinzierl. Two loop amplitudes for  $e^+ e^- \rightarrow i$  q anti-q g: The n(f) contribution. *Acta Phys. Polon. B*, 33:2921–2926, 2002.
  - [53] Sven Moch, Peter Uwer, and Stefan Weinzierl. Two loop amplitudes with nested sums: Fermionic contributions to  $e^+ e^- \rightarrow i$  q anti-q g. *Phys. Rev. D*, 66:114001, 2002.
  - [54] A. Gehrmann-De Ridder, T. Gehrmann, E.W.N. Glover, and G. Heinrich. Second-order QCD corrections to the thrust distribution. *Phys. Rev. Lett.*, 99:132002, 2007.
  - [55] A. Gehrmann-De Ridder, T. Gehrmann, E.W.N. Glover, and G. Heinrich. NNLO corrections to event shapes in  $e^+ e^-$  annihilation. *JHEP*, 12:094, 2007.
  - [56] A. Gehrmann-De Ridder, T. Gehrmann, E.W.N. Glover, and G. Heinrich. Jet rates in electron-positron annihilation at  $O(\alpha(s)^3)$  in QCD. *Phys. Rev. Lett.*, 100:172001, 2008.
  - [57] Stefan Weinzierl. NNLO corrections to 3-jet observables in electron-positron annihilation. *Phys. Rev. Lett.*, 101:162001, 2008.
  - [58] A. Gehrmann-De Ridder, T. Gehrmann, E.W.N. Glover, and G. Heinrich. NNLO moments of event shapes in  $e^+e^-$  annihilation. *JHEP*, 05:106, 2009.
  - [59] Stefan Weinzierl. Event shapes and jet rates in electron-positron annihilation at NNLO. *JHEP*, 06:041, 2009.
  - [60] Stefan Weinzierl. Moments of event shapes in electron-positron annihilation at NNLO. *Phys. Rev. D*, 80:094018, 2009.
  - [61] Stefan Weinzierl. Jet algorithms in electron-positron annihilation: Perturbative higher order predictions. *Eur. Phys. J. C*, 71:1565, 2011. [Erratum: *Eur.Phys.J.C* 71, 1717 (2011)].
  - [62] G. Dissertori, A. Gehrmann-De Ridder, T. Gehrmann, E.W.N. Glover, G. Heinrich, and H. Stenzel. First determination of the strong coupling constant using NNLO predictions for hadronic event shapes in  $e^+ e^-$  annihilations. *JHEP*, 02:040, 2008.
  - [63] K.G. Chetyrkin, Johann H. Kuhn, and M. Steinhauser. Three loop polarization function and  $O(\alpha_s^2)$  corrections to the production of heavy quarks. *Nucl. Phys. B*, 482:213–240, 1996.
  - [64] K.G. Chetyrkin, Johann H. Kuhn, and M. Steinhauser. Heavy quark current correlators to  $O(\alpha_s^2)$ . *Nucl. Phys. B*, 505:40–64, 1997.
  - [65] R. Harlander and M. Steinhauser.  $O(\alpha_s^2)$  corrections to top quark production at  $e^+ e^-$  colliders. *Eur. Phys. J. C*, 2:151–158, 1998.
  - [66] W. Bernreuther, R. Bonciani, T. Gehrmann, R. Heinesch, T. Leineweber, P. Mastrolia, and E. Remiddi. Two-Parton Contribution to the Heavy-Quark Forward-Backward Asymmetry in NNLO QCD. *Nucl. Phys. B*, 750:83–107, 2006.
  - [67] Y. Kiyo, A. Maier, P. Maierhofer, and P. Marquard. Reconstruction of heavy quark current correlators at  $O(\alpha(s)^3)$ . *Nucl. Phys. B*, 823:269–287, 2009.
  - [68] Andre H. Hoang, Vicent Mateu, and S. Mohammad Zebarjad. Heavy Quark Vacuum Polarization Function at  $O(\alpha^2(s))$   $O(\alpha^3(s))$ . *Nucl. Phys. B*, 813:349–369, 2009.

- [69] J. Fleischer, A. Leike, T. Riemann, and A. Werthenbach. Electroweak one loop corrections for  $e^+e^-$  annihilation into  $t$  anti-top including hard bremsstrahlung. *Eur. Phys. J. C*, 31:37–56, 2003.
- [70] Martin Beneke, Yuichiro Kiyo, Peter Marquard, Alexander Penin, Jan Piclum, and Matthias Steinhauser. Next-to-Next-to-Next-to-Leading Order QCD Prediction for the Top Antitop  $S$ -Wave Pair Production Cross Section Near Threshold in  $e^+e^-$  Annihilation. *Phys. Rev. Lett.*, 115(19):192001, 2015.
- [71] German Rodrigo, Arcadi Santamaria, and Mikhail S. Bilenky. Do the quark masses run? Extracting  $m(b)$  ( $m(z)$ ) from LEP data. *Phys. Rev. Lett.*, 79:193–196, 1997.
- [72] Werner Bernreuther, Arnd Brandenburg, and Peter Uwer. Next-to-leading order QCD corrections to three jet cross-sections with massive quarks. *Phys. Rev. Lett.*, 79:189–192, 1997.
- [73] Arnd Brandenburg and Peter Uwer. Next-to-leading order QCD corrections and massive quarks in  $e^+e^- \rightarrow 3$  jets. *Nucl. Phys. B*, 515:279–320, 1998.
- [74] Paolo Nason and Carlo Oleari. Next-to-leading order corrections to the production of heavy flavor jets in  $e^+e^-$  collisions. *Nucl. Phys. B*, 521:237–273, 1998.
- [75] German Rodrigo, Mikhail S. Bilenky, and Arcadi Santamaria. Quark mass effects for jet production in  $e^+e^-$  collisions at the next-to-leading order: Results and applications. *Nucl. Phys. B*, 554:257–297, 1999.
- [76] T. Binoth and G. Heinrich. An automatized algorithm to compute infrared divergent multiloop integrals. *Nucl. Phys. B*, 585:741–759, 2000.
- [77] A.V. Smirnov and M.N. Tentyukov. Feynman Integral Evaluation by a Sector decomposition Approach (FIESTA). *Comput. Phys. Commun.*, 180:735–746, 2009.
- [78] A.V. Smirnov, V.A. Smirnov, and M. Tentyukov. FIESTA 2: Parallelizeable multiloop numerical calculations. *Comput. Phys. Commun.*, 182:790–803, 2011.
- [79] Alexander V. Smirnov. FIESTA 3: cluster-parallelizable multiloop numerical calculations in physical regions. *Comput. Phys. Commun.*, 185:2090–2100, 2014.
- [80] Alexander V. Smirnov. FIESTA4: Optimized Feynman integral calculations with GPU support. *Comput. Phys. Commun.*, 204:189–199, 2016.
- [81] Gudrun Heinrich. Sector Decomposition. *Int. J. Mod. Phys. A*, 23:1457–1486, 2008.
- [82] S. Borowka, G. Heinrich, S.P. Jones, M. Kerner, J. Schlenk, and T. Zirke. SecDec-3.0: numerical evaluation of multi-scale integrals beyond one loop. *Comput. Phys. Commun.*, 196:470–491, 2015.
- [83] S. Borowka, G. Heinrich, S. Jahn, S.P. Jones, M. Kerner, J. Schlenk, and T. Zirke. pySecDec: a toolbox for the numerical evaluation of multi-scale integrals. *Comput. Phys. Commun.*, 222:313–326, 2018.
- [84] S. Borowka, G. Heinrich, S. Jahn, S.P. Jones, M. Kerner, and J. Schlenk. A GPU compatible quasi-Monte Carlo integrator interfaced to pySecDec. *Comput. Phys. Commun.*, 240:120–137, 2019.
- [85] G. Heinrich, S. Jahn, S. P. Jones, M. Kerner, F. Langer, V. Magerya, A. Pöldaru, J. Schlenk, and E. Villa. Expansion by regions with pySecDec. 8 2021.
- [86] Gudrun Heinrich. Collider Physics at the Precision Frontier. *Phys. Rept.*, 922:1–69, 2021.
- [87] M. Czakon. Automatized analytic continuation of Mellin-Barnes integrals. *Comput. Phys. Commun.*, 175:559–571, 2006.
- [88] A.V. Smirnov and V.A. Smirnov. On the Resolution of Singularities of Multiple Mellin-Barnes Integrals. *Eur. Phys. J. C*, 62:445–449, 2009.
- [89] J. Gluza, K. Kajda, and T. Riemann. AMBRE: A Mathematica package for the construction of Mellin-Barnes representations for Feynman integrals. *Comput. Phys. Commun.*, 177:879–893, 2007.
- [90] Michal Ochman and Tord Riemann. MBsums - a Mathematica package for the repre-

- sentation of Mellin-Barnes integrals by multiple sums. *Acta Phys. Polon. B*, 46(11):2117, 2015.
- [91] S. Moch and P. Uwer. XSummer: Transcendental functions and symbolic summation in form. *Comput. Phys. Commun.*, 174:759–770, 2006.
  - [92] C. Schneider. Symbolic Summation Assists Combinatorics. *Sem. Lothar. Combin.*, 56:1–36, 2007. Article B56b.
  - [93] F.V. Tkachov. A Theorem on Analytical Calculability of Four Loop Renormalization Group Functions. *Phys. Lett. B*, 100:65–68, 1981.
  - [94] K.G. Chetyrkin and F.V. Tkachov. Integration by Parts: The Algorithm to Calculate beta Functions in 4 Loops. *Nucl. Phys. B*, 192:159–204, 1981.
  - [95] S. Laporta. High precision calculation of multiloop Feynman integrals by difference equations. *Int. J. Mod. Phys. A*, 15:5087–5159, 2000.
  - [96] Charalampos Anastasiou and Achilleas Lazopoulos. Automatic integral reduction for higher order perturbative calculations. *JHEP*, 07:046, 2004.
  - [97] A.V. Smirnov. Algorithm FIRE – Feynman Integral REduction. *JHEP*, 10:107, 2008.
  - [98] A.V. Smirnov and V.A. Smirnov. FIRE4, LiteRed and accompanying tools to solve integration by parts relations. *Comput. Phys. Commun.*, 184:2820–2827, 2013.
  - [99] Alexander V. Smirnov. FIRE5: a C++ implementation of Feynman Integral REduction. *Comput. Phys. Commun.*, 189:182–191, 2015.
  - [100] A.V. Smirnov and F.S. Chuharev. FIRE6: Feynman Integral REduction with Modular Arithmetic. 1 2019.
  - [101] C. Studerus. Reduze-Feynman Integral Reduction in C++. *Comput. Phys. Commun.*, 181:1293–1300, 2010.
  - [102] A. von Manteuffel and C. Studerus. Reduze 2 - Distributed Feynman Integral Reduction. 2012.
  - [103] R.N. Lee. Presenting LiteRed: a tool for the Loop InTEgrals REDuction. 12 2012.
  - [104] Philipp Maierhoefer, Johann Usovitsch, and Peter Uwer. Kira - A Feynman integral reduction program. *Comput. Phys. Commun.*, 230:99–112, 2018.
  - [105] Philipp Maierhoefer and Johann Usovitsch. Kira 1.2 Release Notes. 2018.
  - [106] A.V. Kotikov. Differential equations method: New technique for massive Feynman diagrams calculation. *Phys. Lett. B*, 254:158–164, 1991.
  - [107] A.V. Kotikov. Differential equations method: The Calculation of vertex type Feynman diagrams. *Phys. Lett. B*, 259:314–322, 1991.
  - [108] A.V. Kotikov. Differential equation method: The Calculation of N point Feynman diagrams. *Phys. Lett. B*, 267:123–127, 1991. [Erratum: *Phys.Lett.B* 295, 409–409 (1992)].
  - [109] Ettore Remiddi. Differential equations for Feynman graph amplitudes. *Nuovo Cim. A*, 110:1435–1452, 1997.
  - [110] T. Gehrmann and E. Remiddi. Differential equations for two loop four point functions. *Nucl. Phys. B*, 580:485–518, 2000.
  - [111] Johannes M. Henn. Multiloop integrals in dimensional regularization made simple. *Phys. Rev. Lett.*, 110:251601, 2013.
  - [112] Roman N. Lee. Reducing differential equations for multiloop master integrals. *JHEP*, 04:108, 2015.
  - [113] O. Gituliar and V. Magerya. Fuchsia and master integrals for splitting functions from differential equations in QCD. *PoS*, LL2016:030, 2016.
  - [114] Christoph Meyer. Transforming differential equations of multi-loop Feynman integrals into canonical form. *JHEP*, 04:006, 2017.
  - [115] Kuo-Tsai Chen. Iterated path integrals. *Bull. Am. Math. Soc.*, 83:831–879, 1977.
  - [116] Alexander B. Goncharov. Multiple polylogarithms, cyclotomy and modular complexes. *Math. Res. Lett.*, 5:497–516, 1998.

- [117] Mario Argeri and Pierpaolo Mastrolia. Feynman Diagrams and Differential Equations. *Int. J. Mod. Phys. A*, 22:4375–4436, 2007.
- [118] Johannes M. Henn. Lectures on differential equations for Feynman integrals. *J. Phys. A*, 48:153001, 2015.
- [119] Andrey Levin and Georges Racinet. Towards multiple elliptic polylogarithms. *arXiv Mathematics e-prints*, page math/0703237, March 2007.
- [120] Francis C. S. Brown and Andrey Levin. Multiple Elliptic Polylogarithms. *arXiv e-prints*, page arXiv:1110.6917, October 2011.
- [121] Johannes Broedel, Claude Duhr, Falko Dulat, and Lorenzo Tancredi. Elliptic polylogarithms and iterated integrals on elliptic curves. Part I: general formalism. *JHEP*, 05:093, 2018.
- [122] Johannes Broedel, Claude Duhr, Falko Dulat, and Lorenzo Tancredi. Elliptic polylogarithms and iterated integrals on elliptic curves II: an application to the sunrise integral. *Phys. Rev. D*, 97(11):116009, 2018.
- [123] Johannes Broedel, Claude Duhr, Falko Dulat, Brenda Penante, and Lorenzo Tancredi. Elliptic symbol calculus: from elliptic polylogarithms to iterated integrals of Eisenstein series. *JHEP*, 08:014, 2018.
- [124] Claude Duhr and Lorenzo Tancredi. Algorithms and tools for iterated Eisenstein integrals. 2019.
- [125] David J. Broadhurst. The Master Two Loop Diagram With Masses. *Z. Phys. C*, 47:115–124, 1990.
- [126] S. Bauberger, Frits A. Berends, M. Bohm, and M. Buza. Analytical and numerical methods for massive two loop selfenergy diagrams. *Nucl. Phys. B*, 434:383–407, 1995.
- [127] S. Bauberger and M. Bohm. Simple one-dimensional integral representations for two loop selfenergies: The Master diagram. *Nucl. Phys. B*, 445:25–48, 1995.
- [128] Michele Caffo, H. Czyz, S. Laporta, and E. Remiddi. The Master differential equations for the two loop sunrise selfmass amplitudes. *Nuovo Cim. A*, 111:365–389, 1998.
- [129] S. Laporta and E. Remiddi. Analytic treatment of the two loop equal mass sunrise graph. *Nucl. Phys. B*, 704:349–386, 2005.
- [130] Spencer Bloch and Pierre Vanhove. The elliptic dilogarithm for the sunset graph. *J. Number Theor.*, 148:328–364, 2015.
- [131] Spencer Bloch, Matt Kerr, and Pierre Vanhove. A Feynman integral via higher normal functions. *Compos. Math.*, 151(12):2329–2375, 2015.
- [132] Spencer Bloch, Matt Kerr, and Pierre Vanhove. Local mirror symmetry and the sunset Feynman integral. *Adv. Theor. Math. Phys.*, 21:1373–1453, 2017.
- [133] B.A. Kniehl, A.V. Kotikov, A. Onishchenko, and O. Veretin. Two-loop sunset diagrams with three massive lines. *Nucl. Phys. B*, 738:306–316, 2006.
- [134] Luise Adams, Christian Bogner, and Stefan Weinzierl. The two-loop sunrise graph in two space-time dimensions with arbitrary masses in terms of elliptic dilogarithms. *J. Math. Phys.*, 55(10):102301, 2014.
- [135] Luise Adams, Christian Bogner, and Stefan Weinzierl. The two-loop sunrise integral around four space-time dimensions and generalisations of the Clausen and Glaisher functions towards the elliptic case. *J. Math. Phys.*, 56(7):072303, 2015.
- [136] Luise Adams, Christian Bogner, and Stefan Weinzierl. The iterated structure of the all-order result for the two-loop sunrise integral. *J. Math. Phys.*, 57(3):032304, 2016.
- [137] Luise Adams, Christian Bogner, Armin Schweitzer, and Stefan Weinzierl. The kite integral to all orders in terms of elliptic polylogarithms. *J. Math. Phys.*, 57(12):122302, 2016.
- [138] Stefan Müller-Stach, Stefan Weinzierl, and Raphael Zayadeh. A Second-Order Differential Equation for the Two-Loop Sunrise Graph with Arbitrary Masses. *Commun. Num. Theor. Phys.*, 6:203–222, 2012.

- [139] Christian Bogner, Stefan Müller-Stach, and Stefan Weinzierl. The unequal mass sunrise integral expressed through iterated integrals on  $\overline{\mathcal{M}}_{1,3}$ . *Nucl. Phys. B*, 954:114991, 2020.
- [140] Ettore Remiddi and Lorenzo Tancredi. Differential equations and dispersion relations for Feynman amplitudes. The two-loop massive sunrise and the kite integral. *Nucl. Phys. B*, 907:400–444, 2016.
- [141] M. Czakon and A. Mitov. Inclusive Heavy Flavor Hadroproduction in NLO QCD: The Exact Analytic Result. *Nucl. Phys. B*, 824:111–135, 2010.
- [142] Luise Adams, Ekta Chaubey, and Stefan Weinzierl. Planar Double Box Integral for Top Pair Production with a Closed Top Loop to all orders in the Dimensional Regularization Parameter. *Phys. Rev. Lett.*, 121(14):142001, 2018.
- [143] Luise Adams, Ekta Chaubey, and Stefan Weinzierl. Analytic results for the planar double box integral relevant to top-pair production with a closed top loop. *JHEP*, 10:206, 2018.
- [144] Andreas von Manteuffel and Lorenzo Tancredi. A non-planar two-loop three-point function beyond multiple polylogarithms. *JHEP*, 06:127, 2017.
- [145] Bernhard Mistlberger. Higgs boson production at hadron colliders at N<sup>3</sup>LO in QCD. *JHEP*, 05:028, 2018.
- [146] Roberto Bonciani, Vittorio Del Duca, Hjalte Frellesvig, Johannes M. Henn, Francesco Moriello, and Vladimir A. Smirnov. Two-loop planar master integrals for Higgs → 3 partons with full heavy-quark mass dependence. *JHEP*, 12:096, 2016.
- [147] R. Bonciani, V. Del Duca, H. Frellesvig, J.M. Henn, M. Hidding, L. Maestri, F. Moriello, G. Salvatori, and V.A. Smirnov. Evaluating a family of two-loop non-planar master integrals for Higgs + jet production with full heavy-quark mass dependence. *JHEP*, 01:132, 2020.
- [148] Francesco Moriello. Generalised power series expansions for the elliptic planar families of Higgs + jet production at two loops. *JHEP*, 01:150, 2020.
- [149] Hjalte Frellesvig, Martijn Hidding, Leila Maestri, Francesco Moriello, and Giulio Salvatori. The complete set of two-loop master integrals for Higgs + jet production in QCD. *JHEP*, 06:093, 2020.
- [150] R. Boughezal, M. Czakon, and T. Schutzmeier. NNLO fermionic corrections to the charm quark mass dependent matrix elements in  $\bar{B} \rightarrow X_s \gamma$ . *JHEP*, 09:072, 2007.
- [151] M. Czakon. Tops from Light Quarks: Full Mass Dependence at Two-Loops in QCD. *Phys. Lett.*, B664:307–314, 2008.
- [152] P. Bärnreuther, M. Czakon, and P. Fiedler. Virtual amplitudes and threshold behaviour of hadronic top-quark pair-production cross sections. *JHEP*, 02:078, 2014.
- [153] Manoj K. Mandal and Xiaoran Zhao. Evaluating multi-loop Feynman integrals numerically through differential equations. *JHEP*, 03:190, 2019.
- [154] M. Misiak, A. Rehman, and M. Steinhauser. Towards  $B \rightarrow X_s \gamma$  at the NNLO in QCD without interpolation in  $m_c$ . 2020.
- [155] Micha L. Czakon and Marco Niggetiedt. Exact quark-mass dependence of the Higgs-gluon form factor at three loops in QCD. 2020.
- [156] Joshua Davies, Go Mishima, Matthias Steinhauser, and David Wellmann. Double-Higgs boson production in the high-energy limit: planar master integrals. *JHEP*, 03:048, 2018.
- [157] Joshua Davies, Go Mishima, Matthias Steinhauser, and David Wellmann. Double Higgs boson production at NLO in the high-energy limit: complete analytic results. *JHEP*, 01:176, 2019.
- [158] Vladimir A. Smirnov. Applied asymptotic expansions in momenta and masses. *Springer Tracts Mod. Phys.*, 177:1–262, 2002.
- [159] Vladimir A. Smirnov. Analytic tools for Feynman integrals. *Springer Tracts Mod. Phys.*, 250:1–296, 2012.
- [160] J. A. M. Vermaseren. Harmonic sums, Mellin transforms and integrals. *Int. J. Mod. Phys.*,

- A14:2037–2076, 1999.
- [161] Sven Moch, Peter Uwer, and Stefan Weinzierl. Nested sums, expansion of transcendental functions and multiscale multiloop integrals. *J. Math. Phys.*, 43:3363–3386, 2002.
  - [162] Volker Pilipp. Semi-numerical power expansion of Feynman integrals. *JHEP*, 09:135, 2008.
  - [163] Feng Feng, Yi-Fan Xie, Qiu-Chen Zhou, and Shan-Rong Tang. HepLib: A C++ Library for High Energy Physics. *Comput. Phys. Commun.*, 265:107982, 2021.
  - [164] K. G. Chetyrkin. Operator Expansions in the Minimal Subtraction Scheme. 1: The Gluing Method. *Theor. Math. Phys.*, 75:346–356, 1988.
  - [165] K. G. Chetyrkin. Operator Expansions in the Minimal Subtraction Scheme. 2: Explicit Formulas for Coefficient Functions. *Theor. Math. Phys.*, 76:809–817, 1988.
  - [166] S.G. Gorishny. Construction of operator expansions and effective theories in the  $\overline{ms}$  scheme. *Nuclear Physics B*, 319(3):633–666, 1989.
  - [167] Vladimir A. Smirnov. Asymptotic expansions in limits of large momenta and masses. *Commun. Math. Phys.*, 134:109–137, 1990.
  - [168] Vladimir A. Smirnov. Asymptotic expansions in momenta and masses and calculation of Feynman diagrams. *Mod. Phys. Lett. A*, 10:1485–1500, 1995.
  - [169] Bernd Jantzen. Foundation and generalization of the expansion by regions. *JHEP*, 12:076, 2011.
  - [170] Tatiana Yu Semenova, Alexander V. Smirnov, and Vladimir A. Smirnov. On the status of expansion by regions. *Eur. Phys. J.*, C79(2):136, 2019.
  - [171] A. Pak and A. Smirnov. Geometric approach to asymptotic expansion of Feynman integrals. *Eur. Phys. J.*, C71:1626, 2011.
  - [172] Bernd Jantzen, Alexander V. Smirnov, and Vladimir A. Smirnov. Expansion by regions: revealing potential and Glauber regions automatically. *Eur. Phys. J.*, C72:2139, 2012.
  - [173] C. Bradford Barber, David P. Dobkin, and Hannu Huhdanpaa. The quickhull algorithm for convex hulls. *ACM Trans. Math. Softw.*, 22(4):469–483, dec 1996.
  - [174] B. Ananthanarayan, Abhishek Pal, S. Ramanan, and Ratan Sarkar. Unveiling Regions in multi-scale Feynman Integrals using Singularities and Power Geometry. *Eur. Phys. J. C*, 79(1):57, 2019.
  - [175] B. Ananthanarayan, Abhijit B. Das, and Ratan Sarkar. Asymptotic analysis of Feynman diagrams and their maximal cuts. *Eur. Phys. J. C*, 80(12):1131, 2020.
  - [176] Eero Byckling and K. Kajantie. *Particle Kinematics*. University of Jyväskylä, Jyväskylä, Finland, 1971.
  - [177] Jorge C. Romao and Joao P. Silva. A resource for signs and Feynman diagrams of the Standard Model. *Int. J. Mod. Phys. A*, 27:1230025, 2012.
  - [178] P. Bärnreuther, M. Czakon, and P. Fiedler. Virtual amplitudes and threshold behaviour of hadronic top-quark pair-production cross sections. *JHEP*, 02:078, 2014.
  - [179] Ernst Carl Gerlach Stueckelberg de Breidenbach and Andreas Petermann. Normalization of constants in the quanta theory. *Helv. Phys. Acta*, 26:499–520, 1953.
  - [180] Murray Gell-Mann and F. E. Low. Quantum electrodynamics at small distances. *Phys. Rev.*, 95:1300–1312, 1954.
  - [181] William E. Caswell. Asymptotic Behavior of Nonabelian Gauge Theories to Two Loop Order. *Phys. Rev. Lett.*, 33:244, 1974.
  - [182] D. R. T. Jones. Two Loop Diagrams in Yang-Mills Theory. *Nucl. Phys. B*, 75:531, 1974.
  - [183] Ansgar Denner and S. Dittmaier. Reduction schemes for one-loop tensor integrals. *Nucl. Phys. B*, 734:62–115, 2006.
  - [184] Ayres Freitas. Numerical multi-loop integrals and applications. *Prog. Part. Nucl. Phys.*, 90:201–240, 2016.
  - [185] Ansgar Denner and Stefan Dittmaier. Electroweak Radiative Corrections for Collider Physics. *Phys. Rept.*, 864:1–163, 2020.



- [186] Jonas Klappert, Fabian Lange, Philipp Maierhöfer, and Johann Usovitsch. Integral reduction with Kira 2.0 and finite field methods. *Comput. Phys. Commun.*, 266:108024, 2021.
- [187] G. Passarino and M. J. G. Veltman. One Loop Corrections for  $e^+ e^-$  Annihilation Into  $\mu^+ \mu^-$  in the Weinberg Model. *Nucl. Phys. B*, 160:151–207, 1979.
- [188] R. Keith Ellis, Zoltan Kunszt, Kirill Melnikov, and Giulia Zanderighi. One-loop calculations in quantum field theory: from Feynman diagrams to unitarity cuts. *Phys. Rept.*, 518:141–250, 2012.
- [189] O. V. Tarasov. Connection between Feynman integrals having different values of the space-time dimension. *Phys. Rev.*, D54:6479–6490, 1996.
- [190] Roman N. Lee and Andrei A. Pomeransky. Critical points and number of master integrals. *JHEP*, 11:165, 2013.
- [191] P. A. Baikov. Explicit solutions of the multiloop integral recurrence relations and its application. *Nucl. Instrum. Meth. A*, 389:347–349, 1997.
- [192] Hj. Mellin. Om definitiva integraler, hvilka för obegränsadt växande värden af vissa heltaliga parametrar hafva till gränser hypergeometrisk funktioner. *Acta Soc. Sc. Fennicae* 20, No. 7, 1-39 (1895)., 1895.
- [193] E. W. Barnes. A new development of the theory of the hypergeometric functions. *Proc. Lond. Math. Soc. (2)*, 6:141–177, 1908.
- [194] N. I. Usyukina. On a Representation for Three Point Function. *Teor. Mat. Fiz.*, 22:300–306, 1975.
- [195] R. N. Lee. Group structure of the integration-by-part identities and its application to the reduction of multiloop integrals. *JHEP*, 07:031, 2008.
- [196] Andreas von Manteuffel, Erik Panzer, and Robert M. Schabinger. A quasi-finite basis for multi-loop Feynman integrals. *JHEP*, 02:120, 2015.
- [197] Erik Panzer. Algorithms for the symbolic integration of hyperlogarithms with applications to Feynman integrals. *Comput. Phys. Commun.*, 188:148–166, 2015.
- [198] T. Binoth and G. Heinrich. Numerical evaluation of multiloop integrals by sector decomposition. *Nucl. Phys. B*, 680:375–388, 2004.
- [199] Andreas von Manteuffel, Robert M. Schabinger, and Hua Xing Zhu. The Complete Two-Loop Integrated Jet Thrust Distribution In Soft-Collinear Effective Theory. *JHEP*, 03:139, 2014.
- [200] T. Binoth, E. W. Nigel Glover, P. Marquard, and J. J. van der Bij. Two loop corrections to light by light scattering in supersymmetric QED. *JHEP*, 05:060, 2002.
- [201] E. W. Nigel Glover and M. E. Tejeda-Yeomans. Two loop QCD helicity amplitudes for massless quark massless gauge boson scattering. *JHEP*, 06:033, 2003.
- [202] E. W. Nigel Glover. Two loop QCD helicity amplitudes for massless quark quark scattering. *JHEP*, 04:021, 2004.
- [203] Stefano Actis, Andrea Ferroglia, Giampiero Passarino, Massimo Passera, and Sandro Uccirati. Two-loop tensor integrals in quantum field theory. *Nucl. Phys. B*, 703:3–126, 2004.
- [204] Thomas Gehrmann, Andreas von Manteuffel, and Lorenzo Tancredi. The two-loop helicity amplitudes for  $q\bar{q}' \rightarrow V_1 V_2 \rightarrow 4$  leptons. *JHEP*, 09:128, 2015.
- [205] Tiziano Peraro and Lorenzo Tancredi. Physical projectors for multi-leg helicity amplitudes. *JHEP*, 07:114, 2019.
- [206] Long Chen. A prescription for projectors to compute helicity amplitudes in D dimensions. *Eur. Phys. J. C*, 81(5):417, 2021.
- [207] Tiziano Peraro and Lorenzo Tancredi. Tensor decomposition for bosonic and fermionic scattering amplitudes. *Phys. Rev. D*, 103(5):054042, 2021.
- [208] Robert H. Lewis. Computer algebra system fermat. <https://home.bway.net/lewis>, 1992, 1995 – 2021.

- [209] Gerard 't Hooft and M. J. G. Veltman. Regularization and Renormalization of Gauge Fields. *Nucl. Phys. B*, 44:189–213, 1972.
- [210] Ansgar Denner. Techniques for calculation of electroweak radiative corrections at the one loop level and results for W physics at LEP-200. *Fortsch. Phys.*, 41:307–420, 1993.
- [211] P. Breitenlohner and D. Maison. Dimensionally Renormalized Green's Functions for Theories with Massless Particles. 1. *Commun. Math. Phys.*, 52:39, 1977.
- [212] P. Breitenlohner and D. Maison. Dimensionally Renormalized Green's Functions for Theories with Massless Particles. 2. *Commun. Math. Phys.*, 52:55, 1977.
- [213] Dirk Kreimer. The  $\gamma(5)$  Problem and Anomalies: A Clifford Algebra Approach. *Phys. Lett. B*, 237:59–62, 1990.
- [214] J. G. Korner, D. Kreimer, and K. Schilcher. A Practicable  $\gamma(5)$  scheme in dimensional regularization. *Z. Phys. C*, 54:503–512, 1992.
- [215] S. A. Larin. The Renormalization of the axial anomaly in dimensional regularization. *Phys. Lett. B*, 303:113–118, 1993.
- [216] F. Jegerlehner. Facts of life with  $\gamma(5)$ . *Eur. Phys. J. C*, 18:673–679, 2001.
- [217] Nikolai Zerf. Fermion Traces Without Evanescence. *Phys. Rev. D*, 101(3):036002, 2020.
- [218] William A. Bardeen, R. Gastmans, and B. E. Lautrup. Static quantities in Weinberg's model of weak and electromagnetic interactions. *Nucl. Phys. B*, 46:319–331, 1972.
- [219] Michael S. Chanowitz, M. Furman, and I. Hinchliffe. The Axial Current in Dimensional Regularization. *Nucl. Phys. B*, 159:225–243, 1979.
- [220] Michael E. Peskin and Daniel V. Schroeder. *An Introduction to quantum field theory*. Addison-Wesley, Reading, USA, 1995.
- [221] M. Bohm, Ansgar Denner, and H. Joos. *Gauge theories of the strong and electroweak interaction*. Vieweg+Teubner Verlag, 3. edition, 2001.
- [222] H. Czyz, A. Grzelinska, and R. Zabawa. The Analytical values of the sunrise master integrals for one of the masses equal to zero. *Phys. Lett.*, B538:52–58, 2002.
- [223] T. Gehrmann and E. Remiddi. Two loop master integrals for  $\gamma^* \rightarrow 3$  jets: The Planar topologies. *Nucl. Phys. B*, 601:248–286, 2001.
- [224] Johannes Blümlein. Analytic integration methods in quantum field theory: an Introduction. 3 2021.
- [225] Go Mishima. High-Energy Expansion of Two-Loop Massive Four-Point Diagrams. *JHEP*, 02:080, 2019.
- [226] Erik Panzer. On hyperlogarithms and Feynman integrals with divergences and many scales. *JHEP*, 03:071, 2014.
- [227] Hung Cheng and T. T. Wu. *EXPANDING PROTONS: SCATTERING AT HIGH-ENERGIES*. 1987.
- [228] Vladimir A. Smirnov. Asymptotic expansions of two loop Feynman diagrams in the Sudakov limit. *Phys. Lett. B*, 404:101–107, 1997.
- [229] Thomas Becher and Matthias Neubert. Drell-Yan Production at Small  $q_T$ , Transverse Parton Distributions and the Collinear Anomaly. *Eur. Phys. J. C*, 71:1665, 2011.
- [230] Michał Czakon, Paul Fiedler, Tobias Huber, Mikołaj Misiak, Thomas Schutzmeier, and Matthias Steinhauser. The  $(Q_7, Q_{1,2})$  contribution to  $\overline{B} \rightarrow X_s \gamma$  at  $\mathcal{O}(\alpha_s^2)$ . *JHEP*, 04:168, 2015.
- [231] Kirill Melnikov, Lorenzo Tancredi, and Christopher Wever. Two-loop  $gg \rightarrow Hg$  amplitude mediated by a nearly massless quark. *JHEP*, 11:104, 2016.
- [232] Kirill Kudashkin, Kirill Melnikov, and Christopher Wever. Two-loop amplitudes for processes  $gg \rightarrow Hg, qg \rightarrow Hq$  and  $q\bar{q} \rightarrow Hg$  at large Higgs transverse momentum. *JHEP*, 02:135, 2018.
- [233] Claude Duhr and Falko Dulat. PolyLogTools — polylogs for the masses. *JHEP*, 08:135, 2019.

- [234] D Maitre. HPL, a mathematica implementation of the harmonic polylogarithms. *Comput. Phys. Commun.*, 174:222–240, 2006.
- [235] Daniel Maitre. Extension of HPL to complex arguments. *Comput. Phys. Commun.*, 183:846, 2012.
- [236] Christian W. Bauer, Alexander Frink, and Richard Kreckel. Introduction to the GiNaC framework for symbolic computation within the C++ programming language. *J. Symb. Comput.*, 33:1, 2000.
- [237] Karsten Ahnert and Mario Mulansky. Odeint – Solving Ordinary Differential Equations in C++. *AIP Conference Proceedings*, 1389(1):1586–1589, 2011.
- [238] Boost C++ Libraries. <http://www.boost.org>. (19.04.2022).
- [239] R. Bulirsch and J. Stoer. Numerical treatment of ordinary differential equations by extrapolation methods. *Numer. Math.*, 8:1–13, 1966.
- [240] Ernst Hairer. *Solving Ordinary Differential Equations I Nonstiff Problems / by Ernst Hairer, Syvert Paul Nørsett, Gerhard Wanner*. Springer Series in Computational Mathematics, 8. Berlin, Heidelberg, 1987.
- [241] Michele Caffo, H. Czyz, and E. Remiddi. Numerical evaluation of the general massive 2 loop sunrise selfmass master integrals from differential equations. *Nucl. Phys.*, B634:309–325, 2002.
- [242] Michele Caffo, Henryk Czyz, Michal Gunia, and Ettore Remiddi. BOKASUN: A Fast and precise numerical program to calculate the Master Integrals of the two-loop sunrise diagrams. *Comput. Phys. Commun.*, 180:427–430, 2009.
- [243] William H. Press, Saul A. Teukolsky, William T. Vetterling, and Brian P. Flannery. *Numerical Recipes in C*. Cambridge University Press, Cambridge, USA, second edition, 1992.
- [244] R. Bulirsch and J. Stoer. *Introduction to Numerical Analysis*. Texts in Applied Mathematics. Springer, New York, NY, 3rd edition, 2002.
- [245] R. W. Clough and J. L. Tocher. Finite element stiffness matrices for the analysis of plate bending. In *Proc. Matrix Methods in Structural Analysis*, Wright-Patterson Air Force Base, Ohio, October 26-28 1965.
- [246] Gilbert Strang and George J Fix. *An analysis of the finite element method*. Prentice-Hall series in automatic computation. Prentice-Hall, Englewood Cliffs, NJ, 1973.
- [247] G. Heinrich, S. P. Jones, M. Kerner, G. Luisoni, and E. Vryonidou. NLO predictions for Higgs boson pair production with full top quark mass dependence matched to parton showers. *JHEP*, 08:088, 2017.
- [248] T. Hahn. CUBA: A Library for multidimensional numerical integration. *Comput. Phys. Commun.*, 168:78–95, 2005.
- [249] T. Hahn. Concurrent Cuba. *J. Phys. Conf. Ser.*, 608(1):012066, 2015.
- [250] J.A.M. Vermaseren. New features of FORM. 10 2000.
- [251] J. Kuipers, T. Ueda, and J.A.M. Vermaseren. Code Optimization in FORM. *Comput. Phys. Commun.*, 189:1–19, 2015.
- [252] Ben Ruijl, Takahiro Ueda, and Jos Vermaseren. FORM version 4.2. 7 2017.
- [253] Paulo Nogueira. Automatic Feynman graph generation. *J. Comput. Phys.*, 105:279–289, 1993.
- [254] R. Kleiss and W. James Stirling. Spinor Techniques for Calculating  $p$  anti- $p \rightarrow W^{+-} / Z^0 + \text{Jets}$ . *Nucl. Phys. B*, 262:235–262, 1985.
- [255] Lance J. Dixon. Calculating scattering amplitudes efficiently. In *Theoretical Advanced Study Institute in Elementary Particle Physics (TASI 95): QCD and Beyond*, pages 539–584, 1 1996.
- [256] Ansgar Denner, Stefan Dittmaier, and Lars Hofer. Collier: a fortran-based Complex One-Loop Library in Extended Regularizations. *Comput. Phys. Commun.*, 212:220–238, 2017.
- [257] T. Hahn and M. Perez-Victoria. Automatized one loop calculations in four-dimensions

- and D-dimensions. *Comput. Phys. Commun.*, 118:153–165, 1999.
- [258] A. van Hameren. OneLOop: For the evaluation of one-loop scalar functions. *Comput. Phys. Commun.*, 182:2427–2438, 2011.
  - [259] R. Keith Ellis and Giulia Zanderighi. Scalar one-loop integrals for QCD. *JHEP*, 02:002, 2008.
  - [260] Stefano Carrazza, R. Keith Ellis, and Giulia Zanderighi. QCDDLoop: a comprehensive framework for one-loop scalar integrals. *Comput. Phys. Commun.*, 209:134–143, 2016.
  - [261] G. J. van Oldenborgh and J. A. M. Vermaseren. New Algorithms for One Loop Integrals. *Z. Phys. C*, 46:425–438, 1990.
  - [262] David J. Broadhurst, N. Gray, and K. Schilcher. Gauge invariant on-shell  $Z(2)$  in QED, QCD and the effective field theory of a static quark. *Z. Phys. C*, 52:111–122, 1991.
  - [263] Stefano Catani. The Singular behavior of QCD amplitudes at two loop order. *Phys. Lett. B*, 427:161–171, 1998.
  - [264] S. Mert Aybat, Lance J. Dixon, and George F. Sterman. The Two-loop soft anomalous dimension matrix and resummation at next-to-next-to leading pole. *Phys. Rev. D*, 74:074004, 2006.
  - [265] Alexander Mitov, George F. Sterman, and Ilmo Sung. The Massive Soft Anomalous Dimension Matrix at Two Loops. *Phys. Rev. D*, 79:094015, 2009.
  - [266] Thomas Becher and Matthias Neubert. On the Structure of Infrared Singularities of Gauge-Theory Amplitudes. *JHEP*, 06:081, 2009. [Erratum: *JHEP* 11, 024 (2013)].
  - [267] Thomas Becher and Matthias Neubert. Infrared singularities of QCD amplitudes with massive partons. *Phys. Rev. D*, 79:125004, 2009. [Erratum: *Phys.Rev.D* 80, 109901 (2009)].
  - [268] Andrea Ferroglia, Matthias Neubert, Ben D. Pecjak, and Li Lin Yang. Two-loop divergences of massive scattering amplitudes in non-abelian gauge theories. *JHEP*, 11:062, 2009.
  - [269] Michal Czakon, Alexander Mitov, and George F. Sterman. Threshold Resummation for Top-Pair Hadroproduction to Next-to-Next-to-Leading Log. *Phys. Rev. D*, 80:074017, 2009.
  - [270] Thomas Becher, Alessandro Broggio, and Andrea Ferroglia. *Introduction to Soft-Collinear Effective Theory*, volume 896. Springer, 2015.
  - [271] S. Catani and M. H. Seymour. The Dipole formalism for the calculation of QCD jet cross-sections at next-to-leading order. *Phys. Lett. B*, 378:287–301, 1996.
  - [272] S. Catani and M. H. Seymour. A General algorithm for calculating jet cross-sections in NLO QCD. *Nucl. Phys. B*, 485:291–419, 1997. [Erratum: *Nucl.Phys.B* 510, 503–504 (1998)].
  - [273] C. Anastasiou, E. W. Nigel Glover, and C. Oleari. The two-loop scalar and tensor pentabox graph with light-like legs. *Nucl. Phys.*, B575:416–436, 2000. [Erratum: *Nucl. Phys.B*585,763(2000)].
  - [274] John M. Campbell, R. Keith Ellis, Michal Czakon, and Sebastian Kirchner. Two loop correction to interference in  $gg \rightarrow ZZ$ . *JHEP*, 08:011, 2016.

# Danksagung

Ich bedanke mich bei Prof. Peter Uwer, der meine Forschung und mein Promotionsstudium betreut hat. Darüber hinaus bedanke ich mich bei Manfred Kraus, mit dem ich intensiv und lange an diesem Projekt gearbeitet hatte. Ich bedanke mich auch bei Lina Alasfar, Till Martini, Markus Schulze, Bas Tausk, Nikolai Zerf und allen anderen Mitgliedern der Arbeitsgruppe "Phänomenologie der Elementarteilchenphysik jenseits des Standardmodells", die ich während meiner Promotion kennen gelernt habe und die mich auf unterschiedliche Weise unterstützt haben. Insbesondere bedanke ich mich bei Lina Alasfar, Till Martini und Peter Uwer für das Probelesen dieser Arbeit und konstruktive Kritik.